

December 2013

Applying Computational Methods to Interpret Experimental Results in Tribology and Enantioselective Catalysis

Michael Garvey

University of Wisconsin-Milwaukee

Follow this and additional works at: <https://dc.uwm.edu/etd>



Part of the [Materials Science and Engineering Commons](#), and the [Physical Chemistry Commons](#)

Recommended Citation

Garvey, Michael, "Applying Computational Methods to Interpret Experimental Results in Tribology and Enantioselective Catalysis" (2013). *Theses and Dissertations*. 460.
<https://dc.uwm.edu/etd/460>

This Dissertation is brought to you for free and open access by UWM Digital Commons. It has been accepted for inclusion in Theses and Dissertations by an authorized administrator of UWM Digital Commons. For more information, please contact open-access@uwm.edu.

APPLYING COMPUTATIONAL METHODS TO INTERPRET
EXPERIMENTAL RESULTS IN TRIBOLOGY AND
ENANTIOSELECTIVE CATALYSIS

by

Michael T. Garvey

A Dissertation Submitted in
Partial Fulfillment of the
Requirements for the Degree of

Doctor of Philosophy
in Chemistry

at

The University of Wisconsin-Milwaukee

December 2013

ABSTRACT

APPLYING COMPUTATIONAL METHODS TO INTERPRET EXPERIMENTAL RESULTS IN TRIBOLOGY AND ENANTIOSELECTIVE CATALYSIS

by

Michael T. Garvey

The University of Wisconsin-Milwaukee, 2013
Under the Supervision of Distinguished Professor Wilfred T. Tysoe

Computational methods are rapidly becoming a mainstay in the field of chemistry. Advances in computational methods (both theory and implementation), increasing availability of computational resources and the advancement of parallel computing are some of the major forces driving this trend.

It is now possible to perform density functional theory (DFT) calculations with chemical accuracy for model systems that can be interrogated experimentally. This allows computational methods to supplement or complement experimental methods. There are even cases where DFT calculations can give insight into processes and interactions that cannot be interrogated directly by current experimental methods.

This work presents several examples of the application of computational methods to the interpretation and analysis of experimentally obtained results. First, triobological systems were investigated primarily with full-potential linearized augmented plane wave (FLAPW) method DFT calculations. Second, small organic molecules adsorbed on Pd(111) were studied using projector-augmented wave (PAW) method DFT calculations

and scanning tunneling microscopy (STM) image simulations to investigate molecular interactions involved in enantioselective heterogeneous catalysis.

A method for method for calculating pressure-dependent shear properties of model boundary-layer lubricants is demonstrated. The calculated values are compared with experimentally obtained results.

For the case of methyl pyruvate adsorbed on Pd(111), DFT-calculated adsorption energies and structures are used along with STM simulations to identify species observed by STM imaging. A previously unobserved enol species is discovered to be present along with the expected keto species.

The information about methyl pyruvate species on Pd(111) is combined with previously published studies of S- α -(1-naphthyl)-ethylamine (NEA) to understand the nature of their interaction upon coadsorption on Pd(111). DFT calculated structures and energies are used to identify potential docking complexes and STM simulations are compared to the experimental STM images.

© Copyright by Michael T. Garvey, 2013
All Rights Reserved

To my wife Sarah and my parents Michael and Carol.

TABLE OF CONTENTS

Abstract	ii
Table of Contents	vi
List of Figures	ix
List of Tables	xvi
Acknowledgments.....	xviii
Chapter 1: Introduction	1
1.1 Background	1
1.2 Applications	3
1.3 Organization of This Dissertation	5
1.4 References	7
Chapter 2: Theoretical Methods.....	9
2.1 Introduction.....	9
2.2 Density Functional Theory	9
2.3 Flair	11
2.4 VASP	13
2.5 bSKAN.....	16
2.6 References.....	19
Chapter 3: Shear Properties of Potassium Chloride Films on Iron Obtained using Density Functional Theory	22
3.1 Introduction.....	22
3.2 Theoretical Methods	25
3.3 Results and Discussion	26
3.3.1 KCl(100)	26
3.3.2 KCl/Fe(100)	30
3.4 Conclusions.....	40
3.5 References.....	41
Chapter 4: Pressure Dependence of Shear Strengths in Sliding, Boundary-Layer Friction	47
4.1 Introduction.....	47
4.2 Theoretical Methods	50
4.3 Results and Discussion	53
4.4 Conclusions.....	60
4.5 References.....	61

Chapter 5: Film Thickness Dependence of Shear Strengths in Sliding, Boundary-Layer Friction	66
5.1 Introduction.....	66
5.2 Theoretical Methods	70
5.3 Results and Discussion	73
5.4 Conclusions.....	80
5.5 References.....	81
Chapter 6: Pressure Dependence of the Shear Strengths of the Tungsten Carbide– Potassium Chloride Interface.....	85
6.1 Introduction.....	85
6.2 Theoretical Methods	89
6.3 Results.....	91
6.4 Discussion	94
6.5 Conclusions.....	105
6.6 References.....	105
Chapter 7: Identifying Molecular Species on Surfaces by Scanning Tunneling Microscopy: Methyl Pyruvate on Pd(111).....	112
7.1 Introduction.....	112
7.2 Experimental Methods	114
7.3 Theoretical Methods	115
7.4 Results.....	116
7.4.1 STM Images.....	116
7.4.2 DFT Calculations of Methyl Pyruvate Derived Surface Species.....	120
7.4.3 Simulations of the STM Images	127
7.5 Discussion	133
7.6 Conclusions.....	135
7.7 Supporting Figures.....	136
7.8 References.....	145
Chapter 8: Studying Enantioselectivity on Chirally Modified Surfaces using Computational Methods: Identifying NEA and Methyl Pyruvate Docking Complexes on Pd(111).....	156
8.1 Introduction.....	156
8.2 Experimental Methods	157
8.3 Theoretical Methods	158
8.4 Results.....	158
8.4.1 STM Images.....	158
8.4.2 Calculations of NEA/Methyl Pyruvate Docking Complexes	160
8.4.3 STM Simulations of NEA/Methyl Pyruvate Docking Complexes	168
8.5 Discussion	169
8.6 Conclusions.....	171
8.7 References.....	172

Chapter 9: Conclusions	176
9.1 Summary	176
9.2 References	179
Appendix.....	180
Sample <i>flair</i> Input File	181
Sample VASP Input Files	182
Sample bSKAN Input Files	184
Example Job Submission Files	186
Useful Shell Scripts.....	189
Curriculum Vitae	198

LIST OF FIGURES

Figure 1.1: Number of publications where “DFT” or “density functional theory” appear in the title, abstract or keywords from Web of Science searches of the even numbered years from 1992 to 2012.	2
Figure 2.1: Regions in a <i>flair</i> calculation.....	12
Figure 2.2: Regions in a VASP calculation.	14
Figure 2.3: Theoretical modeling of the STM current within a perturbation approach. The surface and the tip are treated as separate systems, and their electronic structure is determined by DFT calculations. The current through the separation surface is then determined by numerical integration at the plane of the surface.	18
Figure 3.1: A depiction of the equilibrium geometry of a distorted KCl(100) slab (solid circles) for a displacement $\alpha = 0.2$ along $\langle 10 \rangle$ compared to the undistorted lattice (open circles). Cl (K) ions are large red (small blue) circles.....	28
Figure 3.2: Plot of the calculated change in energy as a function of displacement of the outer layer of the slab α for shear along the $\langle 10 \rangle$ direction. Shown as an inset is a plot of calculated energy change as a function of α^2 to indicate the elastic region.	29
Figure 3.3: Schematic of the location of the ions above the Fe(100) lattice. Also indicated are the paths used for the sliding calculations.	31
Figure 3.4: A depiction of the equilibrium geometry of a distorted KCl/Fe(100) slab (solid circles) for a displacement $\alpha = 0.2$ along $\langle 10 \rangle$ compared to the undistorted lattice (open circles). Cl (K) ions are depicted as large red (small blue) circles; Fe substrate atoms are depicted by green circles.....	32
Figure 3.5: The change in energy as a function of the surface KCl layer displacement along the $\langle 10 \rangle$ direction, along Path A in Figure 3.3.	33
Figure 3.6: Displacements of the (■) middle KCl, (●) bottom KCl and (▲) top Fe layers along the $\langle 10 \rangle$ direction as a function of the surface KCl layer displacement along Path A (Figure 3.2), corresponding to the potential energy curve shown in Figure 3.5.	34
Figure 3.7: The change in energy as a function of the surface KCl layer displacement along the $\langle 11 \rangle$ direction, along Path B (Figure 3.3).....	34

Figure 3.8: Displacements of the (■) middle KCl, (●) bottom KCl and (▲) top Fe layers along the $\langle 11 \rangle$ direction as a function of the surface KCl layer displacement along Path B (Figure 3.3), corresponding to the potential energy curve shown in Figure 3.6.	35
Figure 4.1: A schematic depiction of the KCl bilayer enclosed between two, four-atom thick iron slabs where the surfaces have a (100) orientation. Application of an external pressure is simulated by changing the distance d between the outermost iron layers in the composite slab.	51
Figure 4.2: Plot of the total energy of the KCl+iron composite slab as a function of half of the separation between the outermost iron layers $d/2$ for the chlorine and potassium ions located (a) above iron atoms in the substrate (designated <i>atop</i>), (b) above a site between iron atoms in the substrate (designated <i>bridge</i>) and (c) above the four-fold hollow between four iron atoms (designated <i>hollow</i>). The energy is plotted versus $d/2$ to take into account the existence of two surfaces.	54
Figure 4.3: Plots of the fits to harmonic potentials to the data displayed in Figure 4.2.	55
Figure 4.4: Plot of the height of the sliding potentials ΔE versus pressure for sliding along the $\langle 11 \rangle$ direction from an <i>atop</i> to a <i>hollow</i> to an <i>atop</i> site (in red, upper traces), or for sliding along the $\langle 10 \rangle$ direction from an <i>atop</i> to a <i>bridge</i> to an <i>atop</i> site (in black, lower traces). The portion of the data that vary linearly with P , calculated for a KCl film on iron are shown as solid squares (■), while the effect of adding a quadratic pressure dependence is shown by the solid circles (●).	57
Figure 4.5: Calculated values of the pressure-dependent shear strength S for a bilayer KCl film on Fe(100) plotted as a function of pressure P for sliding along the $\langle 10 \rangle$ (●) and $\langle 11 \rangle$ (▲) directions.	59
Figure 5.1: Depiction of the structure used for the density functional theory calculations showing four layers of KCl sandwiched between iron.	72
Figure 5.2: Plot of the energy of a four-layer KCl slab sandwiched between iron as a function of $d/2$, where d is the distance between the outermost edges of the slab. Results are shown for potassium and chloride ions on the KCl located on atop (top), bridge (middle), and hollow (bottom) sites on the iron substrate. Lines are harmonic potential fits to the data. (Fitting parameters are given in Table 5.1.)	75

Figure 5.3: Plots of the fits to the results of the calculations shown in Figure 5.2 for the potassium and chloride ions on the KCl located on <i>atop</i> , <i>bridge</i> and <i>hollow</i> sites on the iron substrate. (Fitting parameters are given in Table 5.1.).....	76
Figure 6.1: Locations of the $(\bar{1}\bar{1}00)$ and $(10\bar{1}0)$ planes of WC shown with respect to the basal plane of WC. Larger silver and smaller yellow spheres indicate W and C atoms respectively.	89
Figure 6.2: A schematic depiction of a KCl bilayer enclosed between two, tungsten carbide slabs where the KCl slab has the (100) plane in contact with the WC layers, and the WC surface exposes either the $(\bar{1}\bar{1}00)$ or $(10\bar{1}0)$ planes. The application of an external load is simulated by changing the distance d between the outermost tungsten layers in the composite slab.....	90
Figure 6.3: Top view of (a) the $(\bar{1}\bar{1}00)$ and (b) the $(10\bar{1}0)$ tungsten carbide faces. The high-symmetry sites for potassium and chloride ions for which the calculations are performed are indicated as A(W) for an atop tungsten site, B(C) for a bridge site that has a carbon atom below it in the lattice, B(W) for a bridge site that has a tungsten atom below it, and H for a hollow site. Each atom is numbered from 1 to 4 to indicate the layer in which the atom is located (e.g. tungsten atoms labeled as 1 are at the surface, atoms with 2, 3 or 4 are in the second, third or fourth layer below the surface respectively). Larger silver and smaller yellow spheres indicate W and C atoms respectively.	92
Figure 6.4: Plot of the total energy of the KCl+tungsten carbide composite slab as a function of half of the separation between the outermost tungsten carbide layers $d/2$ for a KCl(100) slab located on various sites with respect to the WC $(\bar{1}\bar{1}00)$ surface.	95
Figure 6.5: Plot of the total energy of the KCl+tungsten carbide composite slab as a function of half of the separation between the outermost tungsten carbide layers $d/2$ for the KCl(100) slab located on various sites with respect to the WC $(10\bar{1}0)$ surface.	96
Figure 6.6: Plots of the fits to harmonic potentials to the data displayed in Figure 6.4.....	98
Figure 6.7: Plots of the fits to harmonic potentials to the data displayed in Figure 6.5.....	99

Figure 7.1: Methyl pyruvate on Pd(111) imaged at 120K ($I_t = 8.35$ nA, $V_b = -94$ mV). Two species, designated A and B are identified on the surface, and line profiles along the long axes of the images are shown on the figure.	116
Figure 7.2: A coverage of ~ 0.03 ML of methyl pyruvate on Pd(111) imaged at 120K ($I_t = 8.13$ nA, $V_b = -91$ mV). Species A are identified by solid rectangles and species B by dashed ovals. The $\langle 1\bar{1}0 \rangle$ directions of the underlying Pd(111) lattice are indicated.....	117
Figure 7.3: Structures of various forms of methyl pyruvate: <i>cis</i> keto (1), <i>trans</i> keto (2), <i>cis syn</i> -enol (3), <i>trans syn</i> -enol (4), <i>cis anti</i> -enol (5), <i>trans anti</i> -enol (6), <i>cis</i> enolate (7), and <i>trans</i> enolate (8).	121
Figure 7.4: Depictions of the most stable structures of the various tips used to simulate the STM images of methyl-pyruvate derived species on Pd(111) showing (a) a gold pyramid on a W(110) substrate, (b) a gold pyramid on a W(111) substrate, (c) a CO functionalized gold pyramid on a W(110) substrate, (d) a CO functionalized gold pyramid on a W(111) substrate, (e) a CH ₃ functionalized gold pyramid on a W(110) substrate, and (f) a CH ₃ functionalized gold pyramid on a W(111) substrate.	128
Figure 7.5: (A) Simulated STM images of the keto form of methyl pyruvate (1) with the carbonyl groups located on atop sites oriented at 30° with respect to the $\langle 1\bar{1}0 \rangle$ directions (A30cis) using the Bardeen method with the following tips: (a) Au on W(110), (b) CH ₃ on Au on W(110), (c) CO on Au on W(110), (d) Au on W(111), (e) CH ₃ on Au on W(111), and (f) CO on Au on W(111). (B) STM images of the keto form of methyl pyruvate (1) with the carbonyl groups located on atop sites oriented at 0° with respect to the $\langle 1\bar{1}0 \rangle$ directions (A0cis) simulated by the Bardeen method with the following tips: (a) Au on W(110), (b) CH ₃ on Au on W(110), (c) CO on Au on W(110), (d) Au on W(111), (e) CH ₃ on Au on W(111), and (f) CO on Au on W(111). (g) Profile measured along the long axis of the simulated image.....	130
Figure 7.6: STM images of the enol form of methyl pyruvate (3) with the carbonyl and alcohol groups located on atop and bridge sites (AB cis) simulated by the Bardeen method with the following tips: (a) Au on W(110), (b) CH ₃ on Au on W(110), (c) CO on Au on W(110), (d) Au on W(111), (e) CH ₃ on Au on W(111), (f) CO on Au on W(111). (g) Profile measured along the long axis of the simulated image.....	131
Figure 7.7: Proposed structure of flat-lying AB <i>syn,cis</i> enol (3) form of methyl pyruvate on Pd(111).	132

- Figure 7.8: STM images of the keto form of methyl pyruvate with the carbonyl groups located on atop sites oriented at 30° with respect to the $\langle \bar{1}\bar{1}0 \rangle$ direction imaged with Au on W(110) tip at varied bias: a) -0.1 V, b) -0.2 V, c) -0.3 V, d) -0.4 V e) +0.1 V, f) +0.2 V, g) +0.3 V, h) +0.4 V136
- Figure 7.9: STM images of the keto form of methyl pyruvate with the carbonyl groups located on atop sites oriented at 30° with respect to the $\langle \bar{1}\bar{1}0 \rangle$ direction imaged with a CH_3 group on Au on W(110) tip at varied bias: a) -0.1 V, b) -0.2 V, c) -0.3 V, d) -0.4 V e) +0.1 V, f) +0.2 V, g) +0.3 V, h) +0.4 V137
- Figure 7.10: STM images of the keto form of methyl pyruvate with the carbonyl groups located on atop sites oriented at 30° with respect to the $\langle \bar{1}\bar{1}0 \rangle$ direction imaged with a CO group Au on W(110) tip at varied bias: a) -0.1 V, b) -0.2 V, c) -0.3 V, d) -0.4 V, e) +0.1 V, f) +0.2 V, g) +0.3 V, h) +0.4 V137
- Figure 7.11: STM images of the keto form of methyl pyruvate with the carbonyl groups located on atop sites oriented at 30° with respect to the $\langle \bar{1}\bar{1}0 \rangle$ direction imaged with Au on W(111) tip at varied bias: a) -0.1 V, b) -0.2 V, c) -0.3 V, d) -0.4 V, e) +0.1 V, f) +0.2 V, g) +0.3 V, h) +0.4 V138
- Figure 7.12: STM images of the keto form of methyl pyruvate with the carbonyl groups located on atop sites oriented at 30° with respect to the $\langle \bar{1}\bar{1}0 \rangle$ direction imaged with a CH_3 group on Au on W(110) tip at varied bias: a) -0.1 V, b) -0.2 V, c) -0.3 V, d) -0.4 V, e) +0.1 V, f) +0.2 V, g) +0.3 V, h) +0.4 V138
- Figure 7.13: STM images of the keto form of methyl pyruvate with the carbonyl groups located on atop sites oriented at 30° with respect to the $\langle \bar{1}\bar{1}0 \rangle$ direction imaged with a CO group on Au on W(111) tip at varied bias: a) -0.1 V, b) -0.2 V, c) -0.3 V, d) -0.4 V, e) +0.1 V, f) +0.2 V, g) +0.3 V, h) +0.4 V139
- Figure 7.14: STM images of the most stable enol form of methyl pyruvate with the carbonyl groups located on bridge and atop sites (AB cis) imaged with a Au on W(110) tip at varied bias: a) -0.1 V, b) -0.2 V, c) -0.3 V, d) -0.4 V, e) +0.1 V, f) +0.2 V, g) +0.3 V, h) +0.4 V139
- Figure 7.15: STM images of the enol form of methyl pyruvate with the carbonyl groups located on bridge and atop sites (AB cis) imaged with a CH_3 group on Au on W(110) tip at varied bias: a) -0.1 V, b) -0.2 V, c) -0.3 V, d) -0.4 V, e) +0.1 V, f) +0.2 V, g) +0.3 V, h) +0.4 V140

Figure 7.16: STM images of the enol form of methyl pyruvate with the carbonyl groups located on bridge and atop sites (AB cis) imaged with a CO group on Au on W(110) tip at varied bias: a) -0.1 V, b) -0.2 V, c) -0.3 V, d) -0.4 V, e) +0.1 V, f) +0.2 V, g) +0.3 V, h) +0.4 V	140
Figure 7.17: STM images of the enol form of methyl pyruvate with the carbonyl groups located on bridge and atop sites (AB cis) imaged with a Au on W(111) tip at varied bias: a) -0.1 V, b) -0.2 V, c) -0.3 V, d) -0.4 V, e) +0.1 V, f) +0.2 V, g) +0.3 V, h) +0.4 V	141
Figure 7.18: STM images of the enol form of methyl pyruvate with the carbonyl groups located on bridge and atop sites (AB cis) imaged with a CH ₃ group on Au on W(111) tip at varied bias: a) -0.1 V, b) -0.2 V, c) -0.3 V, d) -0.4 V, e) +0.1 V, f) +0.2 V, g) +0.3 V, h) +0.4 V	141
Figure 7.19: STM images of the enol form of methyl pyruvate with the carbonyl groups located on bridge and atop sites (AB cis) imaged with a CO group on Au on W(111) tip at varied bias: a) -0.1 V, b) -0.2 V, c) -0.3 V, d) -0.4 V, e) +0.1 V, f) +0.2 V, g) +0.3 V, h) +0.4 V	142
Figure 7.20: STM images of the enolate form of methyl pyruvate with the carbonyl groups located on bridge and atop sites (BA cis) imaged with a Au on W(110) tip at varied bias: a) -0.1 V, b) -0.2 V, c) -0.3 V, d) -0.4 V, e) +0.1 V, f) +0.2 V, g) +0.3 V, h) +0.4 V	142
Figure 7.21: STM images of the enolate form of methyl pyruvate with the carbonyl groups located on bridge and atop sites (BA cis) imaged with a CH ₃ group on Au on W(110) tip at varied bias: a) -0.1 V, b) -0.2 V, c) -0.3 V, d) -0.4 V, e) +0.1 V, f) +0.2 V, g) +0.3 V, h) +0.4 V	143
Figure 7.22: STM images of the of the enolate form of methyl pyruvate with the carbonyl groups located on bridge and atop sites (BA cis) imaged with a CO group on Au on W(110) tip at varied bias: a) -0.1 V, b) -0.2 V, c) -0.3 V, d) -0.4 V, e) +0.1 V, f) +0.2 V, g) +0.3 V, h) +0.4 V	143
Figure 7.23: STM images of the enolate form of methyl pyruvate with the carbonyl groups located on bridge and atop sites (BA cis) imaged with a Au on W(111) tip at varied bias: a) -0.1 V, b) -0.2 V, c) -0.3 V, d) -0.4 V, e) +0.1 V, f) +0.2 V, g) +0.3 V, h) +0.4 V	144
Figure 7.24: STM images of the enolate form of methyl pyruvate with the carbonyl groups located on bridge and atop sites (BA cis) imaged with a CH ₃ group on Au on W(111) tip at varied bias: a) -0.1 V, b) -0.2 V, c) -0.3 V, d) -0.4 V, e) +0.1 V, f) +0.2 V, g) +0.3 V, h) +0.4 V	144

Figure 7.25: STM images of the enolate form of methyl pyruvate with the carbonyl groups located on bridge and atop sites (BA cis) imaged with a CO group on Au on W(111) tip at varied bias: a) -0.1 V, b) -0.2 V, c) -0.3 V, d) -0.4 V, e) +0.1 V, f) +0.2 V, g) +0.3 V, h) +0.4 V	145
Figure 8.1: NEA and methyl pyruvate on Pd(111) imaged at 120K ($I_t = 183$ pA, $V_b = -154$ mV). Solid and dashed white circles are used to identify <i>exo</i> -NEA and <i>endo</i> -NEA, respectively. Two intersecting lines are drawn through the long axes of an <i>exo</i> -NEA molecule and a methyl pyruvate molecule.	159
Figure 8.2: NEA and methyl pyruvate on Pd(111) imaged at 120K ($I_t = 280$ pA, $V_b = -154$ mV). Solid and dashed white circles are used to identify <i>exo</i> -NEA and <i>endo</i> -NEA, respectively. Three lines are drawn through the long axes of an <i>exo</i> -NEA molecule and two methyl pyruvate molecules....	160
Figure 8.3: Converged geometries for the eight combinations of R-endo NEA and keto methyl pyruvate on Pd(111) calculated with DFT. They are identified as: (a) Geo01, (b) Geo02, (c) Geo03, (d) Geo04, (e) Geo05, (f) Geo06, (g) Geo07, and (h) Geo08.....	163
Figure 8.4: Converged geometries for the eight combinations of R-exo NEA and keto methyl pyruvate on Pd(111) calculated with DFT. They are identified as: (a) Geo01, (b) Geo02, (c) Geo03, (d) Geo04, (e) Geo05, (f) Geo06, (g) Geo07, and (h) Geo08.....	164
Figure 8.5: Converged geometries for the seven combinations of R-endo NEA and enol syn methyl pyruvate on Pd(111) calculated with DFT. They are identified as: (a) Geo01, (b) Geo02, (c) Geo03, (d) Geo04, (e) Geo05, (f) Geo06, and (g) Geo07.	165
Figure 8.6: Converged geometries for the seven combinations of R-exo NEA and enol syn methyl pyruvate on Pd(111) calculated with DFT. They are identified as: (a) Geo01, (b) Geo02, (c) Geo03, (d) Geo04, (e) Geo05, (f) Geo06, and (g) Geo07.	166
Figure 8.7: STM simulation of R-exo NEA and enol syn methyl pyruvate on Pd(111) obtained from the DFT calculated structure Geo07 in Figure 8.6. Intersecting lines are drawn through the long axes of the NEA and methyl pyruvate molecules and the angle between those lines is indicated.	168
Figure 8.8: STM simulation of R-exo NEA and enol syn methyl pyruvate on Pd(111) obtained from the DFT calculated structure Geo04 in Figure 8.6. Lines are drawn through the long axes of the NEA and methyl pyruvate molecules and the angle between those lines is indicated.....	169

LIST OF TABLES

Table 3.1: Energy differences for KCl slabs adsorbed on a Fe(100) substrate at various sites (see Figure 3.3) relative to the atop site calculated using <i>flair</i> and VASP.....	36
Table 4.1: The parameters of the fits to harmonic potentials to the data displayed in Figure 4.2.	55
Table 5.1: Harmonic potential fitting parameters to the data displayed in Figures 5.2 and 5.3.....	74
Table 6.1: The lattice parameters of hexagonal tungsten carbide calculated using DFT compared with the results of previous DFT calculations and the experimental values.	92
Table 6.2: Parameters of the harmonic fitting potentials for the data displayed in Figures 6.4 and 6.5.....	97
Table 6.3: Vertical distances between planes containing interfacial tungsten and potassium, and chlorine atoms.....	101
Table 6.4: Calculated values of S_0 and α for several paths on the WC($\bar{1}\bar{1}00$) and WC($\bar{1}\bar{1}00$) surfaces.	103
Table 7.1: Adsorption energies of flat-lying <i>cis</i> -methyl pyruvate (1) on Pd(111) calculated using density functional theory, the relaxed azimuthal angles with respect to the close-packed $\langle \bar{1}\bar{1}0 \rangle$ directions, and the Boltzmann population calculated from the relative energies at a sample temperature of 120 K. The most stable species are highlighted.	122
Table 7.2: Adsorption energies of the enol form of flat-lying and perpendicular <i>syn,cis</i> - (3) and <i>syn,trans</i> - (4) methyl pyruvate on Pd(111) calculated using DFT.	123
Table 7.3: Adsorption energies of the enol form of flat-lying and perpendicular <i>anti,cis</i> - (5) and <i>anti,trans</i> - (6) methyl pyruvate on Pd(111) calculated using DFT.	124
Table 7.4: The relaxed azimuthal angles with respect to the close-packed $\langle \bar{1}\bar{1}0 \rangle$ directions and the Boltzmann population calculated from the relative energies at a sample temperature of 120 K for the flat-lying enol form of <i>syn, cis</i> methyl pyruvate (3) on Pd(111).....	125

Table 7.5: Adsorption energies of the enolate form of flat-lying and perpendicular <i>cis</i> (7) and <i>trans</i> (8) methyl pyruvate on Pd(111) calculated using density functional theory.....	125
Table 8.1: Adsorption and interaction energies of R-endo NEA and keto methyl pyruvate on Pd(111) calculated using DFT for the geometries shown in Figure 8.3.	163
Table 8.2: Adsorption and interaction energies of R-exo NEA and keto methyl pyruvate on Pd(111) calculated using DFT for the geometries shown in Figure 8.4.	164
Table 8.3: Adsorption and interaction energies of R-endo NEA and enol syn methyl pyruvate on Pd(111) calculated using DFT for the geometries shown in Figure 8.5.....	165
Table 8.4: Adsorption and interaction energies of R-exo NEA and enol syn methyl pyruvate on Pd(111) calculated using DFT for the geometries shown in Figure 8.6.....	166

ACKNOWLEDGMENTS

There are numerous people who have influenced and contributed to this work through their impact on my life. I will attempt to thank as many of them by name as possible and recognize their contribution. However, it is very likely that I will overlook one or more and for that I apologize.

First, I would like to thank my research advisor, Professor Wilfred Tysoe, for his invaluable advice and experience. Also, his dogged determination to get as much work out of me as humanly possible was the catalyst required to overcome my occasional procrastination or lack of motivation. His energy and excitement when approaching a problem are a measure to which all scientists should aspire.

Many members of Professor Tysoe's research group have helped shape my work and my identity as a scientist. Dr. Octavio Furlong taught me how to do tribology; Dr. Florencia Calaza taught me how to do TPD; Dr. J. Anibal Boscoboinik taught me how to look at the world on the atomic level; all three taught me how to relax Argentinian-style. Dr. Zhenjun Li taught me what it means to work hard. Dr. Luke Burkholder taught me how much of what I know about UHV technology. Dr. Brendan Miller taught me that "Better is the enemy of good enough." John Kestell has been an example of hard work and dedication and has been my source of knowledge of "real" chemistry on many occasions. (Thanks for not graduating before me John.) Mausumi Mahapatra has been an example of hard work and quiet perseverance and is one of the nicest people I have met in my life. Heather Adams has been an eager and motivated apprentice in tribology and DFT calculations. Other members also touched my work and life in their own unique

way: Rasha Abuflaha, Dr. Yun Bai, Dr. Sunil Devarajan, Dr. Zeeshan Habeeb, Ted Thuening, and Josh Walker.

I would like to thank the members of my doctoral committee: Professor Dennis Bennett, Dr. Peter Kotvis, Distinguished Professor Michael Weinert, and Professor Jorg Woehl. Their time, interest, and insight were extremely helpful. Also, numerous members of the Department of Chemistry and Biochemistry have helped me during my time at UWM: Kevin Blackburn, Michael Conway, Wendy Grober, Shelley Hagen, Neal Korfhage, Elise Nicks, Dan Shurilla, and Alan Thompson.

I would like to thank Professor Michael Weinert for helping me to understand how *flair* works on the inside and for providing practical advice regarding calculations countless times. I would also like to thank Professor Werner Hofer for numerous communications regarding usage of the Bardeen method in bSKAN and for allowing me to use Figure 2.2.

Dr. Thomas Sorensen and Dan Siercks have been my go-to guys for Linux questions. I would like to thank Dr. Sorensen for helping me compile code, install software/hardware, and generally maintaining the departmental cluster. I would like to thank Dan Siercks for installing multiple software packages on the UWM Avi cluster, being available whenever I have problems running jobs on Avi, and not yelling at me too much when I go over my usage limit.

During my undergraduate education, I was fortunate to meet many excellent professors that helped me get started down this long path I have taken. Dr. Sandra Neuendorf was an excellent advisor and kept me from straying too far from the path. Professor William “Wild Bill” Wacholtz was the first chemistry professor I met and kept

me entertained during general chemistry. Professor Jonathan Gutow taught me physical chemistry and encouraged me to start taking my education seriously. I did my undergraduate research under the guidance of Professor Charles Gibson. His brilliance and passion for research strongly influenced my decision to pursue a PhD in chemistry. I was fortunate to take many of my physics courses with Professor Dennis Rioux; he was always entertaining and an excellent teacher.

My parents, Michael Garvey and Carol Stinski, have always encouraged and supported me in whatever I have chosen to do. Thank you both for all you have done for me.

My wife, Sarah, has been at my side through graduate school and before. Thank you for putting up with the long hours, highs and lows of research and the stress of writing. We have gone through this experience together and are stronger because of it.

I would lastly like to recognize myself for the hard work and dedication I have applied to this work.

I swear by my life and my love of it that I will never live for the sake of another man, nor ask another man to live for mine.

—John Galt

Chapter 1

Introduction

1.1 Background

Over the past few decades, density functional theory (DFT) has evolved from the postulates set forth by Hohenberg and Kohn [1] in 1964 and expanded upon by Kohn and Sham [2] in 1965 to a robust and dependable theoretical tool. The capabilities of DFT have grown beyond the limits of atoms and small molecules to the point where it is now possible to calculate the properties of realistic systems of interest. In particular, DFT calculations can be performed with chemical accuracy for model systems that can be interrogated experimentally. Figure 1.1 illustrates the rapid increase in the usage of the DFT method over the last ~20 years. One reason that DFT is able to model large systems is the fact that it uses a single electron density distribution to define an external potential that is a functional of that density instead of using a wavefunction for each individual electron. This is different from other approaches such as the Hartree-Fock method which attempts to solve the exact Schrödinger equation. The advantage of using a functional that depends only on the spatial coordinates of the electron density distribution, not the spatial coordinates of each electron, is that it reduces the problem of N_e electrons with $3N_e$ spatial coordinates to just three spatial coordinates. This leads to DFT calculations scaling as $\sim N_b^3$, where N_b is the number of basis functions. This is more efficient than Hartree-Fock and post-Hartree-Fock methods which scale as N_b^4 or higher.

It is important to note that, in DFT calculations, if the exact form of the exchange-correlation energy and potential were known, the Kohn-Sham approach would give the exact energy [3]. It is important to stress the point that, unlike Hartree-Fock and many other methods, the Kohn-Sham approach is in principle exact [3]! In reality, however approximations are made since the exact form of the exchange-correlation energy and potential are not known. These approximations are made when a so-called exchange-correlation functional is defined explicitly.

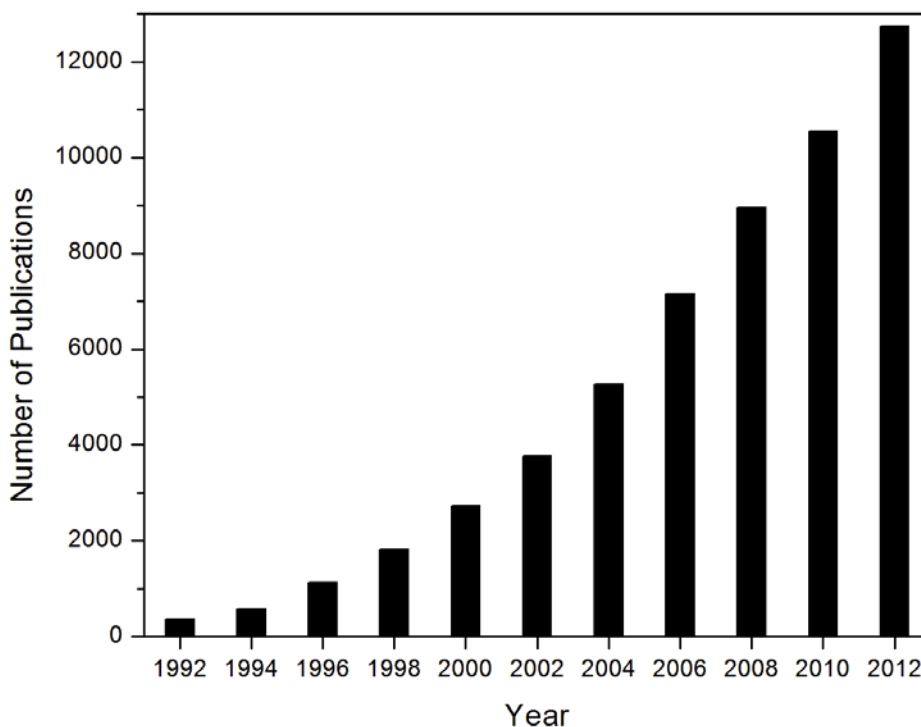


Figure 1.1: Number of publications where “DFT” or “density functional theory” appear in the title, abstract or keywords from Web of Science searches of the even numbered years from 1992 to 2012.

Development of more accurate exchange-correlation potentials has been one of the most active areas in the advancement of DFT. While a “perfect” functional has not

been found, many of the current functionals can achieve or exceed so-called chemical accuracy (~ 8 kJ/mol).

Advances in computational resources have also driven the development and usage of DFT. Beyond the general advances in hardware (e.g. increased speed and component density and decreased cost), parallel computing has been extremely important in allowing large systems to be calculated with DFT on relatively short time scales. The Kohn-Sham approach is ideal for parallelization because the one-electron bands can be evaluated individually at the same time, which is known as parallelization over bands. DFT calculations for periodic systems can also be parallelized over k-points.

Due to the advances in theory and computational resources, it is now possible to perform DFT calculations of complex systems that can be compared with experimental results. This opens nearly endless possibilities for performing computationally guided research. Properties such as surface adsorption energies and vibrational frequencies can be calculated and used to confirm models based on surface chemistry experimental results. With the nudged elastic band (NEB) method, energy barriers between two stable structures can be found. This method can be used to calculate activation energies for activated processes.

1.2 Applications

One of the general areas where DFT calculations can be of assistance is in tribology. Specifically, the following chapters present calculations that calculate energy profiles during sliding events. The calculations of a model lubricant film (KCl) are used

to determine parameters that can be compared with previous experimental results. This is more challenging than typical chemistry problems due to the small differences in energy (<30 meV) in the surface energy profile during sliding and therefore requires computationally-expensive, full-potential DFT calculations.

Another application that is presented is the determination of surface species adsorbed on a Pd(111) single crystal. The potential surface structures of various methyl pyruvate species are calculated on a Pd(111) surface. Scanning tunneling microscope (STM) image simulations are then calculated for the most likely structures (determined by analysis of the energetics). These are compared to experimentally obtained STM images of methyl pyruvate on Pd(111) to determine the identity of the observed species. This is particularly important since STM images have molecular, but not always atomic, resolution so that assigning a particular image shape to an adsorbed species is a challenge. This is particularly important when chemical changes occur following surface adsorption.

Finally, chemical interactions are investigated in a model enantioselective heterogeneous catalytic system. DFT calculations of S- α -(1-naphthyl)-ethylamine (NEA) and methyl pyruvate on Pd(111) are used to identify potential docking complexes. STM image simulations are calculated for the best candidates identified from the DFT calculations. The appearance and relative orientations of the two species are compared to experimentally obtained STM images of docking complexes.

These studies illustrate how the application of quantum mechanics based DFT calculations can help to gain an understanding of processes and interactions that cannot be interrogated directly via current experimental methods. For example, the structure of

a sliding interface can be extrapolated from calculations that give agreement with experimentally measured properties. Also, calculations that reproduce trends (energies, bond lengths, etc.) in systems of interest can be used to gain a basic understanding of those systems.

1.3 Organization of This Dissertation

The background theory used for the computational chemistry results is presented in Chapter 2. Density functional theory in general and its implementation in two software packages (*flair* [4-7] and VASP [8-11]) are introduced. Software that is used to simulate STM images (bSKAN [12-13]) is also summarized.

Chapters 3-8 present computational chemistry results and comparison with experimental results. These chapters are categorized by the general type of system they explore. Chapters 3-6 involve tribological systems investigated primarily with *flair* calculations. Chapters 7 and 8 are concerned with organic molecules adsorbed on Pd(111) to study enantioselective heterogeneous catalysis with VASP calculations and STM simulations.

The first part of the tribological work is presented in Chapter 3. First it is shown that DFT is capable of reproducing the mechanical properties of bulk potassium chloride. Then it is demonstrated that the height of the sliding potential for a KCl thin film on an iron surface can be calculated from the values at high-symmetry sites, greatly reducing the computational cost of the calculations. The calculated zero-pressure shear strength is compared to the experimental results.

In Chapter 4, the method is expanded by calculating sliding potentials as a function of compression at the high-symmetry sites defined in Chapter 3. This allows experimentally observed pressure dependence to be explored computationally. The pressure dependence parameter is compared to the experimentally obtained value.

In an attempt to improve the agreement of the model with experimental results, the effect of varying the KCl film thickness is explored in Chapter 5. It is shown that the film thickness does not have an appreciable effect on the tribological properties of the interface and suggests that the local interactions at the interface play an important role.

In Chapter 6, the iron is exchanged for tungsten carbide in an effort to more accurately model the expected sliding interface. Again, potentials are calculated as a function of compression for various high-symmetry sites on the tungsten carbide face. The pressure dependence parameter is again compared to experimental results.

In the latter part of the dissertation, the focus shifts to a small organic molecule, methyl pyruvate, adsorbed on Pd(111) in Chapter 7. DFT-calculated adsorption energies and structures are used along with STM simulations to identify species observed by STM imaging. Specifically, a previously unobserved enol species is discovered to be present along with the expected keto species.

Chapter 8 combines the knowledge obtained about methyl pyruvate in Chapter 7 with previously published studies of S- α -(1-naphthyl)-ethylamine (NEA) to understand the nature of their interaction upon coadsorption on Pd(111). DFT calculated structures and energies are used to identify potential docking complexes and STM simulations are compared to the experimental STM images.

1.4 References

- [1] Hohenberg, P.; Kohn, W., Inhomogeneous Electron Gas. *Physical Review* **1964**, *136* (3B), B864-B871.
- [2] Kohn, W.; Sham, L. J., Self-Consistent Equations Including Exchange and Correlation Effects. *Physical Review* **1965**, *140* (4A), A1133-A1138.
- [3] Koch, W.; Holthausen, M. C., *A Chemist's Guide to Density Functional Theory*. Wiley-VCH Verlag GmbH: 2001.
- [4] Weinert, M.; Schneider, G.; Podloucky, R.; Redinger, J. *Flair*. <http://www.uwm.edu/~weinert/flair.html>.
- [5] Weinert, M.; Schneider, G.; Podloucky, R.; Redinger, J., FLAPW: applications and implementations. *Journal of Physics-Condensed Matter* **2009**, *21* (8).
- [6] Weinert, M.; Wimmer, E.; Freeman, A. J., Total-energy all-electron density functional method for bulk solids and surfaces. *Physical Review B* **1982**, *26* (8), 4571-4578.
- [7] Wimmer, E.; Krakauer, H.; Weinert, M.; Freeman, A. J., Full-potential self-consistent linearized-augmented-plane-wave method for calculating the electronic structure of molecules and surfaces: O₂ molecule. *Physical Review B* **1981**, *24* (2), 864-875.
- [8] Kresse, G.; Furthmüller, J., Efficient iterative schemes for ab initio total-energy calculations using a plane-wave basis set. *Physical Review B* **1996**, *54* (16), 11169-11186.

- [9] Kresse, G.; Furthmüller, J., Efficiency of ab-initio total energy calculations for metals and semiconductors using a plane-wave basis set. *Computational Materials Science* **1996**, 6 (1), 15-50.
- [10] Kresse, G.; Hafner, J., Ab initio molecular dynamics for liquid metals. *Physical Review B* **1993**, 47 (1), 558-561.
- [11] Kresse, G.; Hafner, J., Ab initio molecular-dynamics simulation of the liquid-metal–amorphous-semiconductor transition in germanium. *Physical Review B* **1994**, 49 (20), 14251-14269.
- [12] Hofer, W. A.; Foster, A. S.; Shluger, A. L., Theories of scanning probe microscopes at the atomic scale. *Reviews of Modern Physics* **2003**, 75 (4), 1287-1331.
- [13] Palotás, K.; Hofer, W. A., Multiple scattering in a vacuum barrier obtained from real-space wavefunctions. *Journal of Physics: Condensed Matter* **2005**, 17 (17), 2705.

Chapter 2

Theoretical Methods

2.1 Introduction

The following sections present the background theory used for the computational chemistry results. All too often, computational methods are treated as a “black box” where some information is fed in to a computer and results are produced. While it is not necessary to have a strong theoretical background to perform calculations, it is advisable to have some familiarity with the foundations that the computational methods are built upon. Therefore, this chapter will introduce the underlying theories and methods involved in performing such calculations.

2.2 Density Functional Theory

Density functional theory (DFT) is based on the Thomas-Fermi model [1-2] of a non-uniform electron gas and was first postulated by Hohenberg and Kohn [3] and later expanded by Kohn and Sham [4]. The main concept of DFT is that the electronic ground state of a system can be determined from a functional of the total electron density distribution. This functional depends only on the spatial coordinates of the electron density function. In contrast, methods which attempt to solve the exact Schrödinger equation depend on the spatial coordinates of all the individual electrons. This leads to DFT calculations scaling as $\sim N^3$, where N is the number of basis functions, which is a

key advantage of the DFT method over Hartree-Fock and post-Hartree-Fock methods which scale as N^4 or higher.

The first Hohenberg-Kohn theorem is described in their 1964 paper in section I.1., entitled *The Density as Basic Variable* [3]. They describe a system of electrons in a large box which are in an external potential $v(\mathbf{r})$. The ground state electronic density, $n(\mathbf{r})$, is obviously a functional of $v(\mathbf{r})$. They go on to prove by *reductio ad absurdum* that the converse is true [3]. In other words, the external potential, $v(\mathbf{r})$, is a unique functional of the ground state electronic density $n(\mathbf{r})$. This external potential $v(\mathbf{r})$ can then be used to define the Hamiltonian of the system.

The second Hohenberg-Kohn theorem involves the variational principle. They define a universal functional, $F[n(\mathbf{r})]$, which includes kinetic and interaction energy and is valid for any external potential and any number of particles [3]. From this, they define the energy functional

$$E_v[n] \equiv \int v(\mathbf{r})n(\mathbf{r})d\mathbf{r} + F[n] \quad (2.2.1)$$

where $v(\mathbf{r})$ and $n(\mathbf{r})$ are the external potential and ground state electronic density, respectively, mentioned above. They state that for the correct $n(\mathbf{r})$, $E_v[n]$ is equal to the ground state energy and go on to show that this is the case if the functions are restricted by the condition

$$N[n] \equiv \int n(\mathbf{r})d\mathbf{r} = N. \quad (2.2.2)$$

In other words, the energy of any trial density will be larger than the true ground state energy and only the exact ground state electronic density will give the true ground state energy. Therefore, according to the variational principle, one can iteratively change the trial density until the lowest energy is reached. This is not always easy since

determining the form of the universal functional, $F[n]$, is far from trivial. In fact finding improved forms of density functionals is still a very active area of research nearly 50 years after Hohenberg and Kohn stated their famous theorems.

The following sections will describe the all-electron full-potential linearized augmented plane wave (FLAPW) method as implemented in *flair* [5-8] and the projector augmented-wave (PAW) method [9-10] as implemented in VASP [11-14]. Results from both methods will be presented in later chapters.

2.3 Flair

Flair is an all-electron implementation of the full-potential linearized augmented plane wave (FLAPW) method for bulk and thin films [5]. In this method space is divided into regions (shown in Figure 2.1); spheres (often called “muffin-tin” spheres) around the atoms and an interstitial region [6]. The wavefunctions, density and potential are defined in a piece-wise manner, consisting of some analytic form in the interstitial and numerical solutions inside the spheres [6].

In this case, the basis functions are plane waves in the interstitial region because they have the necessary translational properties and are well-suited to describe the wave functions in that region.

Inside the sphere, the potential is more atomic-like. This can be represented by a radial function multiplied by a spherical harmonic. The Hamiltonian can then be solved for any energy to get radial functions, $u_l(r; \epsilon_l)$, that depend on the radius and energy for each angular momentum quantum number l [6]. The energy derivative $\dot{u}_l(r) \equiv$

$du_\ell(r)/d\epsilon$, which can be shown to be orthogonal to $u_\ell(r)$, is also calculated. The basis functions inside the sphere are described by these two functions.

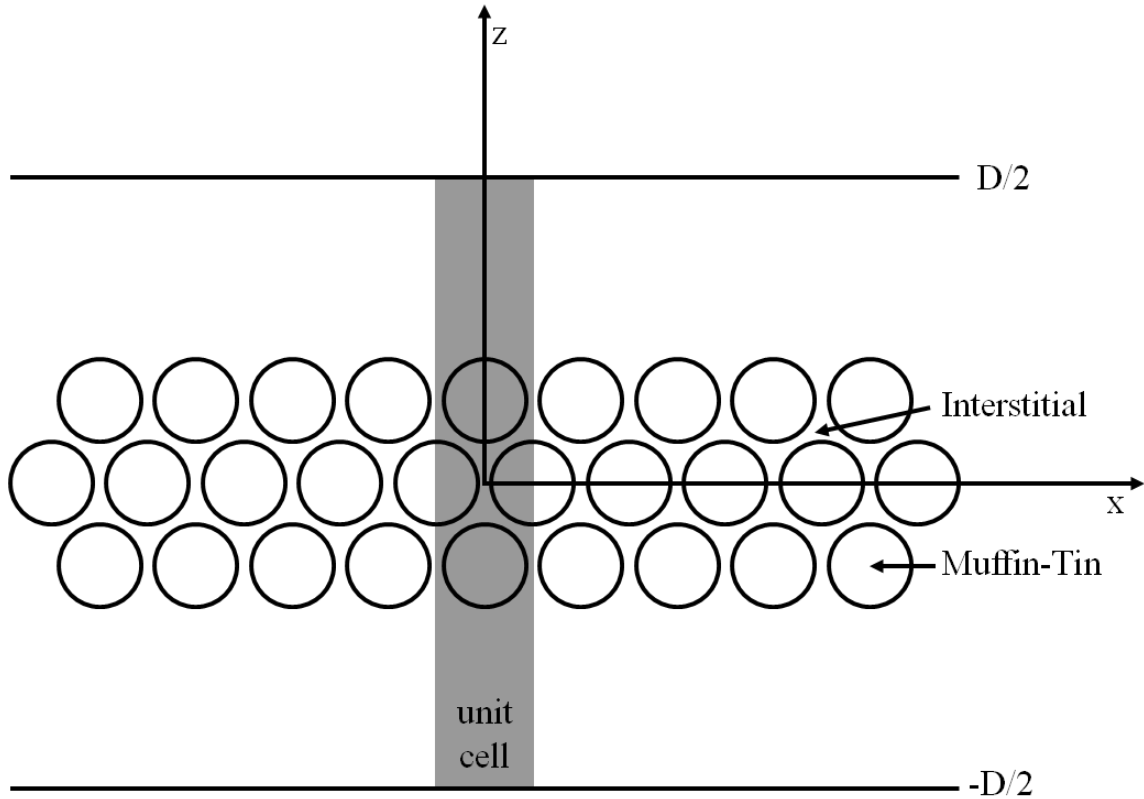


Figure 2.1: Regions in a *flair* calculation.

Additionally, a continuity condition is imposed such that the values and derivatives of the “inner” and “outer” portions of the basis functions must match at the sphere boundary.

In practice, *flair* uses the FLAPW method as described above to calculate the ground state energy iteratively. From the ground state energy, forces on the atoms are calculated and used to determine which direction to move the atoms for the next geometry optimization step. Simply, there are two “loops”, the electronic “loop” and the

geometric “loop”. Both loops continue until certain convergence criteria (defined by the user in the input file `inp`) are met.

In an electronic step, trial wavefunctions are used to generate a charge density distribution. The parameters are varied until the total energy and charge density are converged. The convergence criteria for these are set with the parameters **evar_delta** and **cdist_eps** in the input file.

For each geometric step, a full electronic “loop” is performed. In other words, the ground state energy is calculated, as described above, for each set of atomic positions. This energy and charge density distribution are then used to calculate the forces on all of the atoms. The atoms that have been allowed to relax are then moved in an attempt to minimize the forces and the entire process is repeated for this new geometry. The geometric relaxation is stopped when the forces on all atoms that have been allowed to move are below the force convergence criterion **epsforce**, which is specified in the input file.

In addition to the convergence parameters, the atomic positions and types and other methodological parameters are specified in the input file. Optionally, displacements from the atomic positions in the `inp` file can be specified in a file named `disp`. A sample *flair* `inp` file with comments is included in the Appendix.

2.4 VASP

The Vienna Ab initio Simulation Package (VASP) [11-14] is a computational software package that uses periodic boundary conditions and various quantum

mechanical electronic structure methods to model materials at the atomic scale. All VASP calculations presented in this dissertation used the projector-augmented wave (PAW) method [9-10] and the generalized gradient approximation (GGA) exchange-correlation potential of Perdew, Burke and Ernzerhof [15].

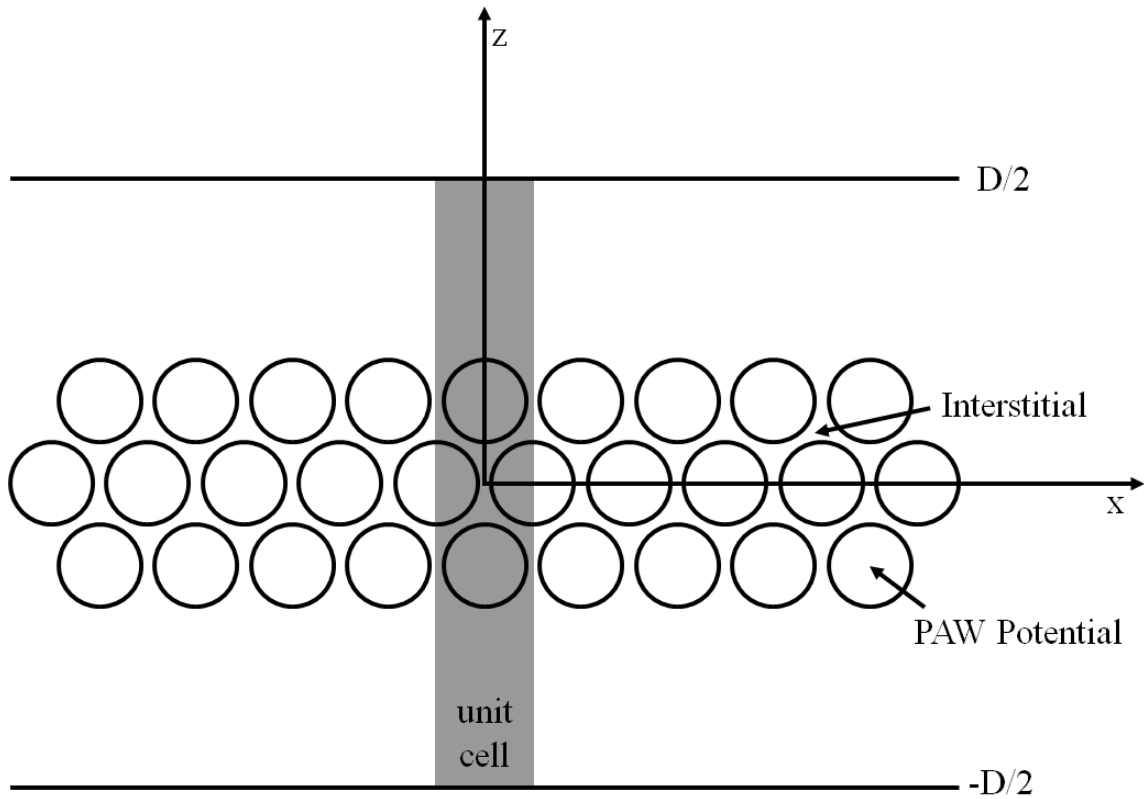


Figure 2.2: Regions in a VASP calculation.

Similarly to the FLAPW method, the PAW method also divides space into regions (shown in Figure 2.2); spheres around the atoms and an interstitial region. The spheres in this case are the area inside the core radii of the atoms where the PAW potentials are used to describe the electron density distribution. Plane waves are used to describe the electron density outside the core radii. One major difference in VASP and

the PAW method in general is that the core electrons are “frozen”, i.e. a fixed potential is used to represent the ionic cores.

Similarly to *flair*, VASP has both electronic and geometric “loops” and again there is an electronic “loop” for each geometric step. The main difference in VASP is that the PAW method, as described above, is used to calculate the ground state energy in the electronic steps.

The convergence criterion for the electronic steps is set by the parameter `EDIFF` in the input file `INCAR`. According to the VASP manual [16]: “The relaxation of the electronic degrees of freedom will be stopped if the total (free) energy change and the band structure energy change ('change of eigenvalues') between two steps are both smaller than `EDIFF`.”

Like in *flair*, the energy and charge density distribution are used to calculate the forces on all of the atoms. The ionic cores that have been allowed to relax are then moved in an attempt to minimize the forces and the “loop” continues until the convergence criteria are met. The geometric convergence criterion is specified with the parameter `EDIFFG` in the `INCAR` file. The value of `EDIFFG` can be either positive or negative. If `EDIFFG` is positive, the relaxation will be stopped when the change in total (free) energy between two geometric steps is smaller than `EDIFFG`. If `EDIFFG` is negative, the relaxation is stopped when the forces on all atoms that have been allowed to move are less than the magnitude of `EDIFFG`. Using the forces as the convergence criterion (negative `EDIFFG`) is more common.

Other methodological parameters are also specified in the `INCAR` file. Unlike *flair*, the atomic positions are specified in a separate file named `POSCAR` for VASP. The

atomic types are defined by the potentials in a file named `POTCAR`. In this case, PAW potentials were used for all calculations presented. However, VASP calculations can also be performed using ultrasoft pseudopotentials. The k-point mesh size is specified in a file named `KPOINTS`. These four files (`INCAR`, `KPOINTS`, `POSCAR`, and `POTCAR`) are the required input files for VASP. If they do not exist in the working directory, VASP will not run properly. Sample `INCAR`, `POSCAR`, and `KPOINTS` files with comments are included in the Appendix.

2.5 bSKAN

bSKAN is a software that can simulate Scanning Tunneling Microscopy (STM) images and Scanning Tunneling Spectroscopy (STS) spectra from the Kohn-Sham states obtained from ground-state DFT calculations. It was developed by Professor Werner Hofer at the University of Liverpool and can be obtained by contacting him. A complete discussion of the capabilities, theoretical background and program usage can be found in the bSKAN guide [17].

The simplest treatment of tunneling between the STM tip and the sample used in bSKAN is the Tersoff-Hamann approach. This method is based on the work of Tersoff and Hamann [18-19] and assumes that the tunneling current is proportional to the local density of states at the STM tip as described in the following equation [20]:

$$I(\mathbf{R}) \propto \sum_{E_n > E_F - eV_{bias}}^{E_n < E_F} |\psi(\mathbf{R}, E_n)|^2 =: n(\mathbf{R}, V_{bias}) \quad (2.4.1)$$

where I is the tunneling current, E_n the eigenstates of the crystal electrons, E_F the Fermi level, V_{bias} the bias voltage and n the electron density [20]. In other words, this method approximates the tunneling probability (current) at a given point to be directly proportional to the local density of states. This approach gives reliable results for many systems and has the advantage of being much less computational expensive than the Bardeen method.

In the Bardeen method, bSKAN takes independently calculated DFT wavefunctions for both the surface and the tip and uses perturbation theory to model the tunneling transition. The tunneling current is described by the following equation [20]:

$$I = \frac{4\pi e}{\hbar} \sum_{\mu, \nu} \left| \int_S (\chi_\nu^* \nabla \psi_\mu - \psi_\mu \nabla \chi_\nu^*) \right|^2 \delta(E_\nu - E_\mu - eV_{bias}) \quad (2.4.2)$$

where χ_ν are the eigenstates with energy E_ν of the STM tip, ψ_μ the eigenstates of the surface with energy E_μ . The integral extends over the separation surface S between sample and tip; the summation includes all eigenstates within a given interval from the Fermi level [20]. An illustration of the method is shown in Figure 2.3.

To model the effects of bias voltage and multiple scattering, the system can be reduced to a tunneling current between two leads, the surface and the tip, assumed to be in thermodynamic equilibrium [17]. The tunneling current is then found via a non-equilibrium Green's function approach [21].

In application, the `INSCAN` file contains the input parameters which bSKAN uses to determine what type of calculations to perform. Some of the relevant parameters are bias voltage (`BIAS VOLTAGE`), the vacuum boundary of the surface (`ZVACUUM`) and the limits of thermal broadening (`LIMITS`). Sample `INSCAN` files with comments are included

in the Appendix. In the first step, bSKAN takes the Kohn-Sham states and positions of the atomic cores from DFT and converts them to a 3D matrix of local density of states in a file named `CURMAT`. This file can then be evaluated to get either a 3D tunneling current map in a file named `CURRENT` or a constant current (tunneling probability) contour in a file named `PLOTCON`. A `PLOTCON` file can then be used to display a color contrast plot which is analogous to a constant current STM image.

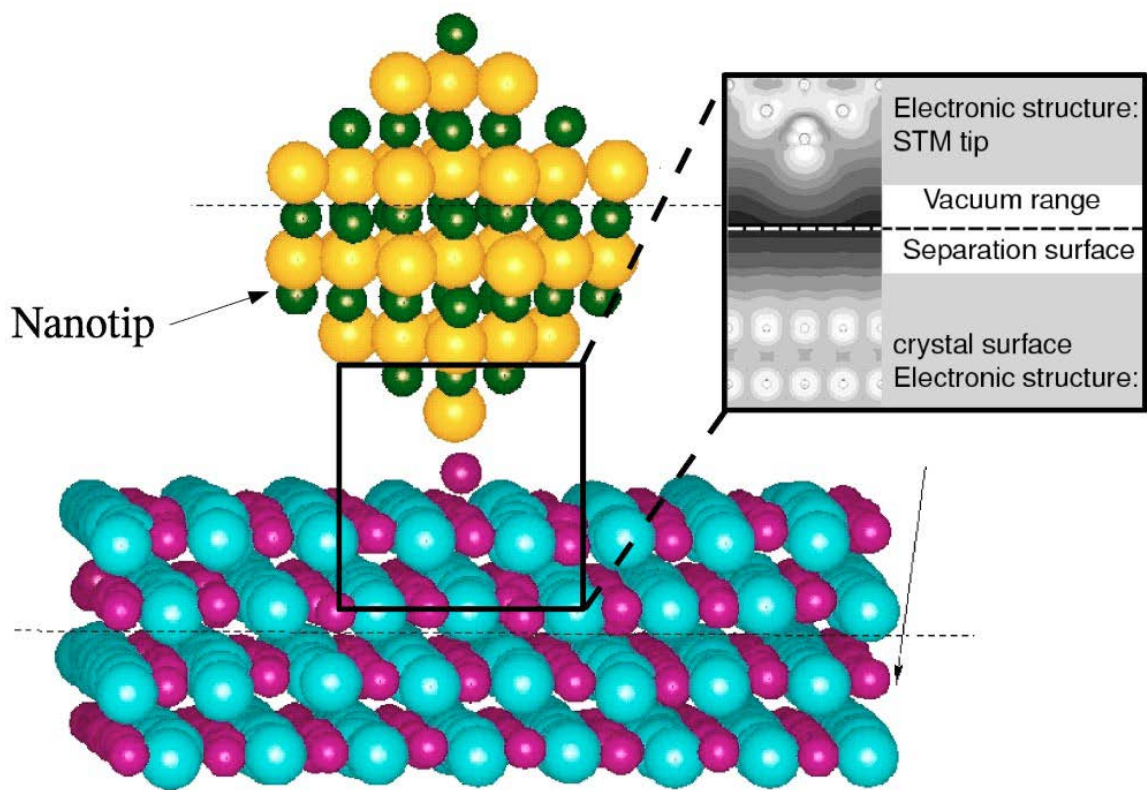


Figure 2.3: Theoretical modeling of the STM current within a perturbation approach. The surface and the tip are treated as separate systems, and their electronic structure is determined by DFT calculations. The current through the separation surface is then determined by numerical integration at the plane of the surface. (Reproduced from Reference [20] with permission.)

2.6 References

- [1] Thomas, L. H., The calculation of atomic fields. *Mathematical Proceedings of the Cambridge Philosophical Society* **1927**, 23 (05), 542-548.
- [2] Fermi, E., A statistical method for determining some properties of the atom. I. *Atti Accad. Naz. Lincei, Cl. Sci. Fis., Mat. Nat., Rend.* **1927**, 6, 602-7.
- [3] Hohenberg, P.; Kohn, W., Inhomogeneous Electron Gas. *Physical Review* **1964**, 136 (3B), B864-B871.
- [4] Kohn, W.; Sham, L. J., Self-Consistent Equations Including Exchange and Correlation Effects. *Physical Review* **1965**, 140 (4A), A1133-A1138.
- [5] Weinert, M.; Schneider, G.; Podloucky, R.; Redinger, J. *Flair*.
<http://www.uwm.edu/~weinert/flair.html>.
- [6] Weinert, M.; Schneider, G.; Podloucky, R.; Redinger, J., FLAPW: applications and implementations. *Journal of Physics-Condensed Matter* **2009**, 21 (8).
- [7] Weinert, M.; Wimmer, E.; Freeman, A. J., Total-energy all-electron density functional method for bulk solids and surfaces. *Physical Review B* **1982**, 26 (8), 4571-4578.
- [8] Wimmer, E.; Krakauer, H.; Weinert, M.; Freeman, A. J., Full-potential self-consistent linearized-augmented-plane-wave method for calculating the electronic structure of molecules and surfaces: O₂ molecule. *Physical Review B* **1981**, 24 (2), 864-875.
- [9] Blöchl, P. E., Projector augmented-wave method. *Physical Review B* **1994**, 50 (24), 17953-17979.

- [10] Kresse, G.; Joubert, D., From ultrasoft pseudopotentials to the projector augmented-wave method. *Physical Review B* **1999**, *59* (3), 1758-1775.
- [11] Kresse, G.; Furthmüller, J., Efficient iterative schemes for ab initio total-energy calculations using a plane-wave basis set. *Physical Review B* **1996**, *54* (16), 11169-11186.
- [12] Kresse, G.; Furthmüller, J., Efficiency of ab-initio total energy calculations for metals and semiconductors using a plane-wave basis set. *Computational Materials Science* **1996**, *6* (1), 15-50.
- [13] Kresse, G.; Hafner, J., Ab initio molecular dynamics for liquid metals. *Physical Review B* **1993**, *47* (1), 558-561.
- [14] Kresse, G.; Hafner, J., Ab initio molecular-dynamics simulation of the liquid-metal–amorphous-semiconductor transition in germanium. *Physical Review B* **1994**, *49* (20), 14251-14269.
- [15] Perdew, J. P.; Burke, K.; Ernzerhof, M., Generalized Gradient Approximation Made Simple. *Physical Review Letters* **1996**, *77* (18), 3865.
- [16] Kresse, G.; Marsman, M.; Furthmüller, J. VASP the GUIDE. <http://cms.mpi.univie.ac.at/vasp/vasp.pdf>.
- [17] Hofer, W. A. A Guide to simulation of STM images and spectra from first principles: bSKAN 3.6. http://www.liv.ac.uk/~whofer/stm/bskan_guide.pdf.
- [18] Tersoff, J.; Hamann, D. R., Theory and Application for the Scanning Tunneling Microscope. *Physical Review Letters* **1983**, *50* (25), 1998-2001.
- [19] Tersoff, J.; Hamann, D. R., Theory of the scanning tunneling microscope. *Physical Review B* **1985**, *31* (2), 805-813.

- [20] Hofer, W. A.; Foster, A. S.; Shluger, A. L., Theories of scanning probe microscopes at the atomic scale. *Reviews of Modern Physics* **2003**, 75 (4), 1287-1331.
- [21] Palotás, K.; Hofer, W. A., Multiple scattering in a vacuum barrier obtained from real-space wavefunctions. *Journal of Physics: Condensed Matter* **2005**, 17 (17), 2705.

Chapter 3

Shear Properties of Potassium Chloride Films on Iron

Obtained using Density Functional Theory

3.1 Introduction

The laws of friction were first systematically studied by Leonardo da Vinci and subsequently confirmed by Amontons [1]. The results of this work state that the friction coefficient μ , defined as the lateral sliding force (F) divided by the normal load (L), $= F/L$ is constant and independent of A the ('apparent' or macroscopic) contact area and V , the sliding velocity [1-2]. Thus, the value of the friction coefficient depends primarily on the materials that comprise the sliding interface. While the friction of a sliding interface lubricated by a fluid film is rather well understood [3-4], it is currently not possible to calculate a friction coefficient for a solid–solid interface from first principles.

Density functional theory (DFT) has been used to successfully calculate the mechanical properties of materials, including bulk modulus, Young's modulus, shear modulus, and Poisson's ratio and has been applied to a relatively wide range of materials including metals and ceramics [5-7]. Several different approaches exist, including linear response [8] and direct methods. Linear response approaches are, by construction, restricted to small displacements and therefore not amenable to examining the effects of large displacements that occur when materials deform plastically or during frictional processes where gross sliding occurs. Direct methods for calculating the elastic constants C_{ij} proceed by imposing selected distortions to the bulk unit cell and using DFT to

calculate the change in energy as a function of this distortion and thereby the relevant elastic constants. Based on the success of DFT in calculating the elastic properties of materials, the following explores how DFT can be extended to include larger atomic distortions and thus mimic the behavior of atoms undergoing sliding motion. In particular, the theoretical results are compared with experimental data for the sliding of a thin film of an alkali halide deposited onto metal substrates [9]. While alkali halides are not used commercially to form lubricant (so-called boundary-layer) films, they offer the advantage that they are sufficiently simple that they are amenable to analysis using DFT.

A large amount of experimental work has been carried out to examine the sliding of well-defined, nanometer sized tips on surfaces with sufficient sensitivity to detect atomic-level stick–slip motions caused by atoms sliding over each other [10]. These effects have been rationalized using a model first proposed by Tomlinson and Prandtl [11-12]. The sliding of atoms over the potential energy curve between the two contacting surfaces directly leads to the atomic stick–slip observed experimentally and the Tomlinson model has been successfully used to rationalize the velocity dependence of friction [13-15]. Thus, in principle, calculating the sliding potential using DFT can provide information on interfacial shear. Previous DFT calculations have yielded values of friction coefficients that are in reasonable accord with experiment [16-27]. However, the lateral force during sliding depends not only on the shear strength, but also on the real area of contact, which is often difficult to measure precisely. Measurements on well-defined surfaces in ultrahigh vacuum have demonstrated that a monolayer of an adsorbate, such as an alkali halide, interposed between two sliding surfaces acts as a solid lubricant film to reduce the interfacial friction [9]. By measuring the friction force for

KCl films grown on a wide range of substrates with different hardness values, it was found that the shear strength S depended linearly on pressure as $S = S_0 + \alpha P$, where P is the pressure in the contact. In particular, the value of S_0 , the zero-pressure limit of the interfacial shear strength ($P = 0$), was measured to be $65 \pm 5 \text{ MPa}$ [9]. Because of the relative simplicity of the KCl/metal system, this offers an opportunity to calculate the shear properties of a system for which reliable experimental results are available, thereby providing a stringent test of the ability of DFT calculations to mimic the interfacial sliding shear. Furthermore, the results of the DFT calculations provide insights into the shear process—the location of the shear plane, for example—that are difficult to determine experimentally. In the following, we present DFT results for the sliding of a KCl(100) film on a Fe(100) substrate, which is the orientation found from x-ray diffraction experiments of halide films on iron [28]. The calculation of the sliding of KCl on Fe(100) raises additional issues compared to the metal-on-metal or semiconductor–metal cases because of the long-range electrostatic interactions. Having reliable experimental data allows us to critically assess the accuracy of DFT for these types of problem.

It is noted that the calculation of reliable values of S_0 using DFT is the first step in exploring whether quantum calculations can predict the shear properties of interfaces and ultimately calculate friction coefficients. A full understanding will come from being able to correctly mimic the pressure dependence of shear and correctly calculate the value of α . Being able to properly calculate S_0 values is the first step.

3.2 Theoretical Methods

We model the KCl/Fe(100) system using a supercell geometry consisting of a seven-layer Fe(100) film with three layers of KCl on each side. A vacuum gap of ~ 15 Å is placed between repeating slabs in the direction of the surface normal. In this (100) orientation, each KCl (Fe) layer consists of one potassium and chlorine atom (and 2 Fe atoms) per surface unit cell. To test the accuracy of the DFT calculations, we have initially calculated the shear modulus of a pure, 13-layer KCl(100) film.

To mimic friction measurements in which a tip is pulled along the surface, the top layer is shifted laterally, allowing the other atomic positions to relax. This procedure is then repeated for different starting points from the relaxed positions, thus in principle allowing for hysteresis effects. As discussed later, this (time-consuming) procedure is not necessary for KCl/Fe(100), and a simpler procedure of considering adsorption of the film on high-symmetry positions only is sufficient. To start, the geometry of the undisplaced case was optimized by fixing the middle three layers of iron to their bulk positions and allowing all other atoms to relax until the forces on all unrestricted atoms was less than 10^{-2} eV Å⁻¹. For all shifted cases, the geometry was optimized by fixing the three central layers of iron to their bulk positions, allowing the surface atoms of the KCl film to move only in the direction of the surface normal (but fixing the lateral displacement) while allowing all other atoms to fully relax.

Two different electronic structure methods were used for the spin-polarized DFT calculations. The first is an implementation of the all-electron, full-potential linearized augmented plane-wave (FLAPW) method, *flair* [29-31]. Since this method explicitly

includes all electrons, the calculations are rather time consuming. To attempt to address this issue, we also use the projector augmented wave (PAW) method [32-33] as implemented in the Vienna *ab initio* simulation package, VASP [34-36]. The PAW potentials chosen in the VASP calculation include both the 3s and 3p as valence states for potassium, the 3p state for chlorine and the 3d, 4s and 4p electrons for iron so do not explicitly include all (core) electrons and is therefore computationally more efficient. Both methods used the same generalized gradient approximation (GGA) functional of Perdew, Burke and Ernzerhof [37] for exchange–correlation and similar selfconsistent convergence criteria of better than 10^{-5} eV. The plane-wave cut-off energies were initially set to 396 eV, and additional calculations were performed using a higher cut-off energy of 600 eV. The two methods show similar trends, although physically relevant numbers can (and do) differ significantly, as does the computational cost, *flair* being significantly more expensive than VASP.

3.3 Results and Discussion

3.3.1 KCl(100)

We first consider the shear properties of a pure KCl(100) slab calculated using both VASP and *flair*. The calculated bulk lattice spacing for KCl of 0.627 nm using *flair* agrees well with the experimental value of 0.629 nm. Figure 3.1 shows (half) the KCl slab used for the calculations, where the open circles show the equilibrium positions of the ions before displacement, and the filled circles display the positions after the outermost layer had been displaced by 20% of a lattice spacing along a $\langle 10 \rangle$ direction

where the unit cell volume remains constant as the outermost layer is displaced. The large circles represent Cl^- ions and the smaller ones the K^+ ions. Figure 3.2 shows the change in energy as a function of fractional lattice displacement α (equal to $\delta x/a_0$, where δx is the displacement and a_0 is the periodicity along the displacement direction) for distortions along the $\langle 10 \rangle$ direction calculated using *flair*. This curve is fit to an even-order polynomial of up to α^4 , with the fit shown as a solid line in Figure 3.2. The elastic constant is extracted from the second derivative of the curve at the origin D , and the elastic part of the curve is emphasized by a straight line indicating the tangent at the origin in the inset in Figure 3.2 showing that there are substantial deviations from elastic behavior along the $\langle 10 \rangle$ direction for $\alpha \gtrsim 0.06$. The shear modulus G is calculated from the equation $G = \frac{2nD}{a_0^3}$ where n is the number of KCl layers in the slab and a_0 is the KCl

lattice spacing. As seen in Figure 3.1, the displacement of the top layer causes the lower layers to distort also. In fact, this behavior continues for displacements of the top layer up to at least half a lattice constant. The calculated value of the shear modulus $G_{\langle 10 \rangle}$ is 11.0 ± 0.7 GPa, in excellent agreement with the experimental value of 10.8 GPa [38].

Shear calculations were also carried out for sliding along the $\langle 11 \rangle$ direction using *flair*. Results similar to the $\langle 10 \rangle$ direction were found, and the corresponding plot of energy versus α^2 reveals that the distortion is elastic up to $\alpha \sim 0.08$. In this case, the shear modulus, measured from the second derivative at the origin is 6.4 ± 0.4 GPa, again in excellent agreement with the experimental value of 6.24 GPa [38].

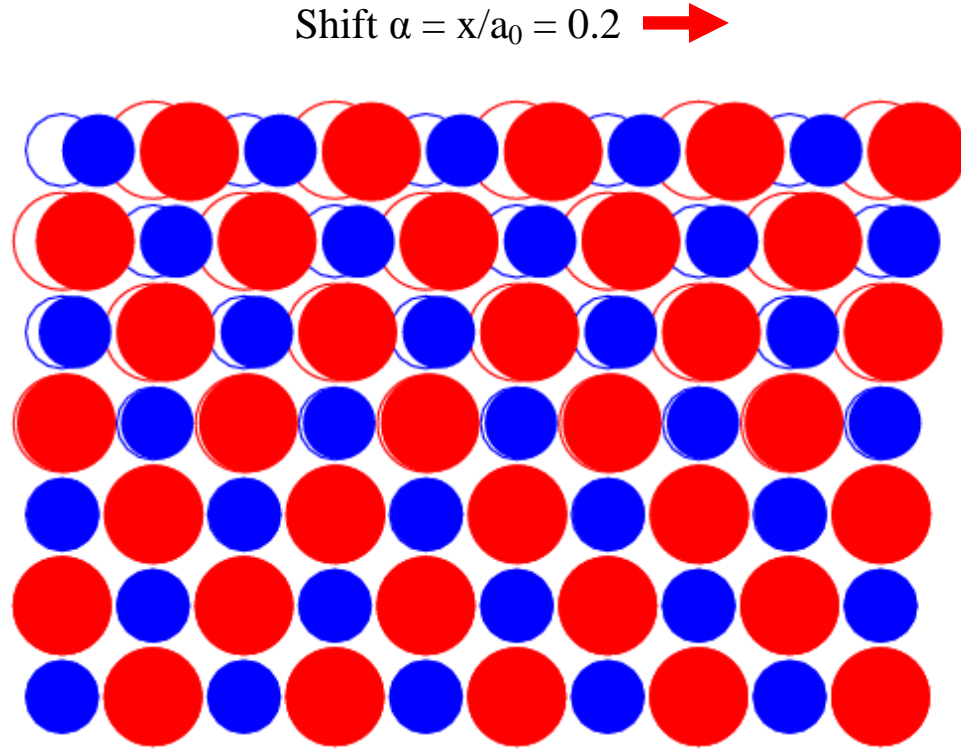


Figure 3.1: A depiction of the equilibrium geometry of a distorted KCl(100) slab (solid circles) for a displacement $\alpha = 0.2$ along $\langle 10 \rangle$ compared to the undistorted lattice (open circles). Cl (K) ions are large red (small blue) circles.

Calculations were also carried out using VASP. Energies were again calculated as a function of the displacement of the outer layer of the slab and the shear moduli calculated in a similar manner as described above for the *flair* calculations, resulting in values of $G_{\langle 10 \rangle}$ of 12.4 ± 0.5 GPa and $G_{\langle 11 \rangle}$ of 6.0 ± 0.8 GPa. While these values are in reasonable agreement with the experimental shear moduli [38], the agreement is poorer than with *flair*. Consequently, the discussion of the shear of a KCl film on an iron substrate is based mainly on calculations performed using *flair*; a brief comparison to results derived from VASP values is given later.

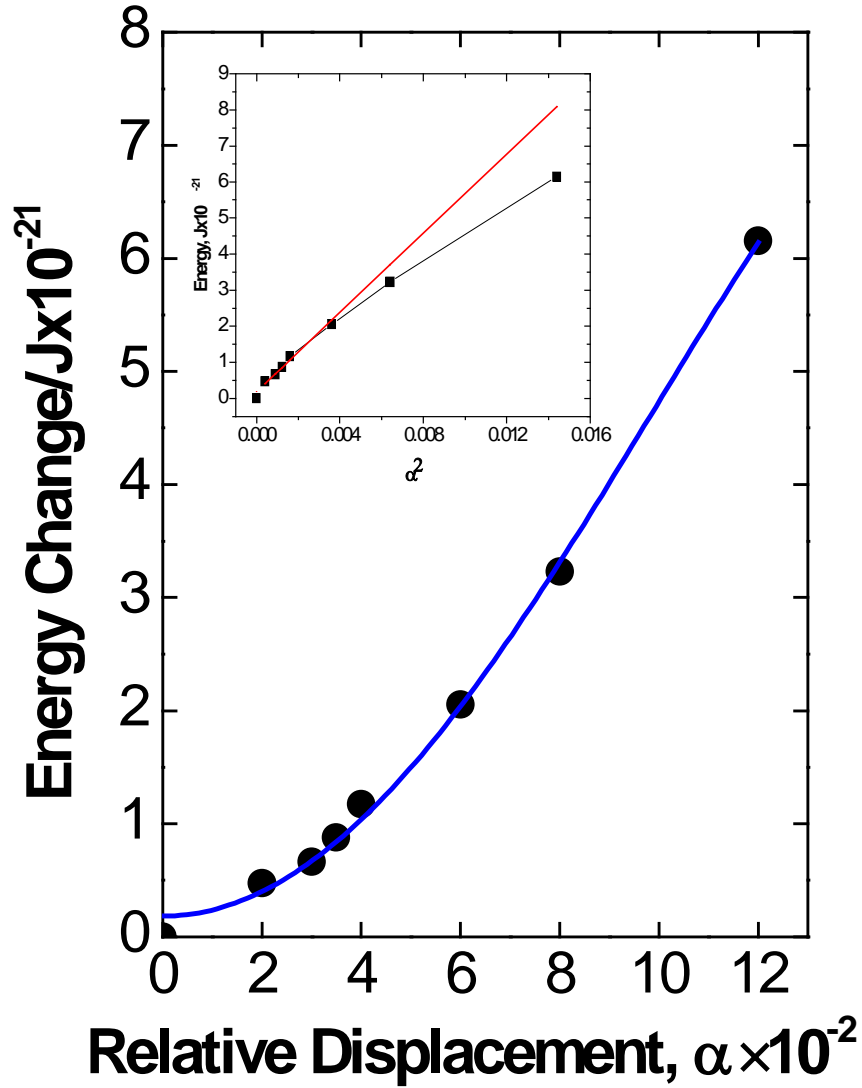


Figure 3.2: Plot of the calculated change in energy as a function of displacement of the outer layer of the slab α for shear along the $\langle 10 \rangle$ direction. Shown as an inset is a plot of calculated energy change as a function of α^2 to indicate the elastic region.

Finally, the large (factor of ~ 2) anisotropy is related to whether the distortion path moves ions over the atoms in the layer below (for the $\langle 10 \rangle$ distortion) or between them ($\langle 11 \rangle$). These results indicate that the mechanical properties of an ionic lattice such as KCl can be accurately reproduced by DFT calculations.

3.3.2 KCl/Fe(100)

To begin to address the question of how and why KCl acts as a lubricant film and to calculate shear properties, we carried out calculations for a three-layer KCl film on an iron surface. A calculation was performed to obtain the initial equilibrium configuration of the halide film on the surface by computing the energy of the film as a function of the distance between the KCl and Fe planes. As noted above, DFT showed a bulk lattice constant for KCl of 0.627 nm, and for iron of 0.282 nm, in good agreement with the experimental value of 0.287 nm. The interface was constructed to include one KCl unit and four Fe unit cells as indicated in Figure 3.3 to yield a $0.564 \times 0.564 \text{ nm}^2$ supercell, leading to a calculated lattice mismatch of 10%. The KCl lattice was constrained to the iron substrate lattice spacing in the x-y plane (parallel to the interface). The minimum energy separation between the KCl and Fe slabs was initially obtained by calculating the energy of KCl and Fe slabs as a function of their separation. This distance was then used to fully optimize the geometry by allowing all of the atoms to relax.

In order to mimic sliding, the outermost layer of the KCl slab was translated while allowing the other atoms to relax. The nomenclature for the location of the KCl film relative to the Fe(100) substrate is illustrated in Figure 3.3. For example, potassium and chloride ions located above an iron substrate atom is designated an ‘atop’ site, etc. The paths (A and B) for the sliding calculations described below are also indicated on Figure 3.3. The top layer was slid using both successive small increments and an initial large translation by 20% of a lattice spacing, initially maintaining all of the other atoms in their original positions, but by allowing them to move during the energy minimization. An

energy-minimization calculation was performed using *flair* to establish the optimum geometry caused by sliding the outermost layer.

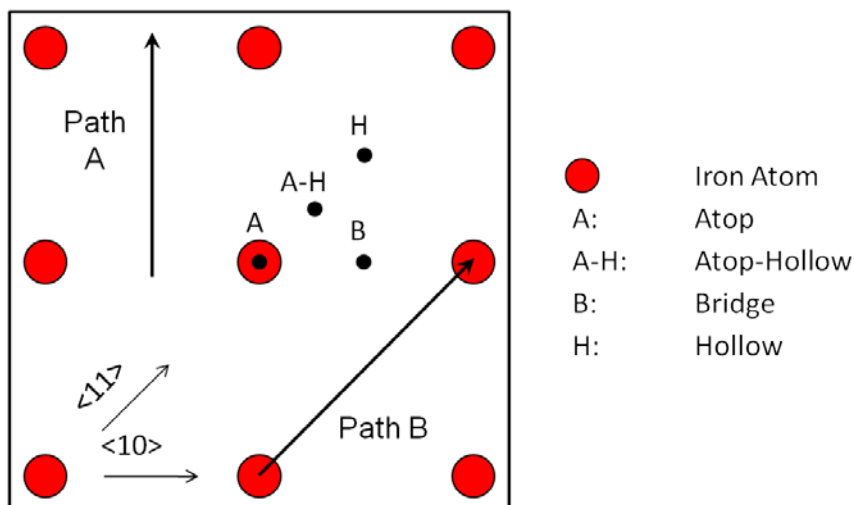


Figure 3.3: Schematic of the location of the ions above the Fe(100) lattice. Also indicated are the paths used for the sliding calculations.

While this approach is computationally expensive since the initial atoms positions are far from their expected final equilibrium locations, it was taken to avoid any unintended bias in the final result and could be compared to the results of the step-wise sliding (with which they coincided). The positions of the atoms were allowed to relax until the energies and forces converged. Since, after convergence, the forces on each of the atoms were close to zero, this corresponds to sliding with a zero applied pressure; thus the results are compared with the experimentally measured value of S_0 [9].

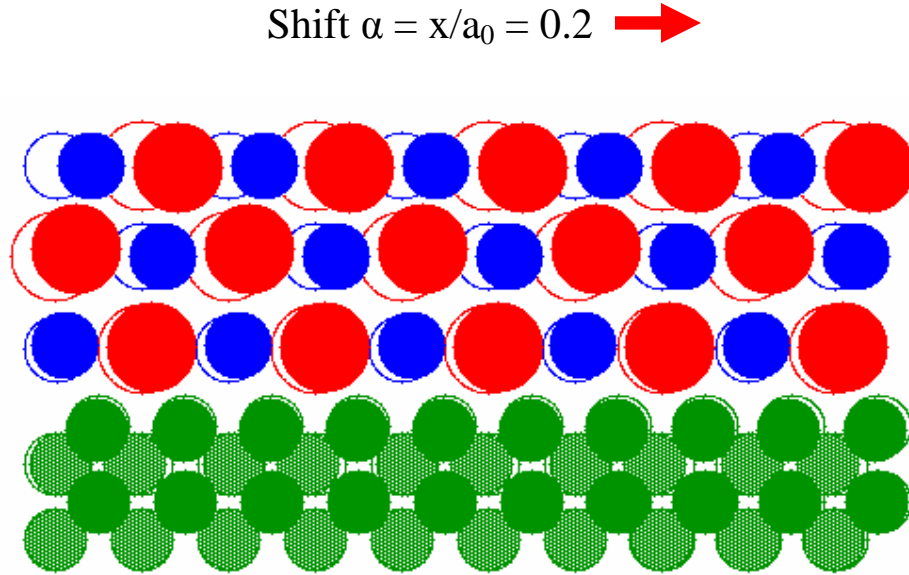


Figure 3.4: A depiction of the equilibrium geometry of a distorted KCl/Fe(100) slab (solid circles) for a displacement $\alpha = 0.2$ along $\langle 10 \rangle$ compared to the undistorted lattice (open circles). Cl (K) ions are depicted as large red (small blue) circles; Fe substrate atoms are depicted by green circles.

Figure 3.5 displays the results of the calculated energies as a function of sliding distance along path A (Figure 3.3), where the KCl ions move from a ‘bridge’ to a ‘four-fold’ site, to a ‘bridge’ site. Figure 3.4 shows a schematic diagram of the KCl slab on the Fe(100) substrate with a displacement of the outermost layer of 20% of a lattice spacing. The energy increases as the atoms in the KCl slab move from the ‘bridge’ to the ‘four-fold’ position, and decreases to its original value as it moves to the ‘bridge’ site once again. The shape of the potential energy curve is symmetric and the maximum increase in potential energy (at $\alpha = 0.25$) is ~ 7 meV. Figure 3.6 plots the final lateral equilibrium positions of each of the layers within the KCl film and the top iron layer, as a function of the imposed displacement of the outermost KCl layer. It is clear that both of the inner layers of the KCl film have moved almost the same distance as the translation imposed on the outermost layer, whereas the iron surface has moved only very slightly. These

results indicate that the KCl slab essentially moves as a single unit and that shear occurs at the KCl–Fe interface.

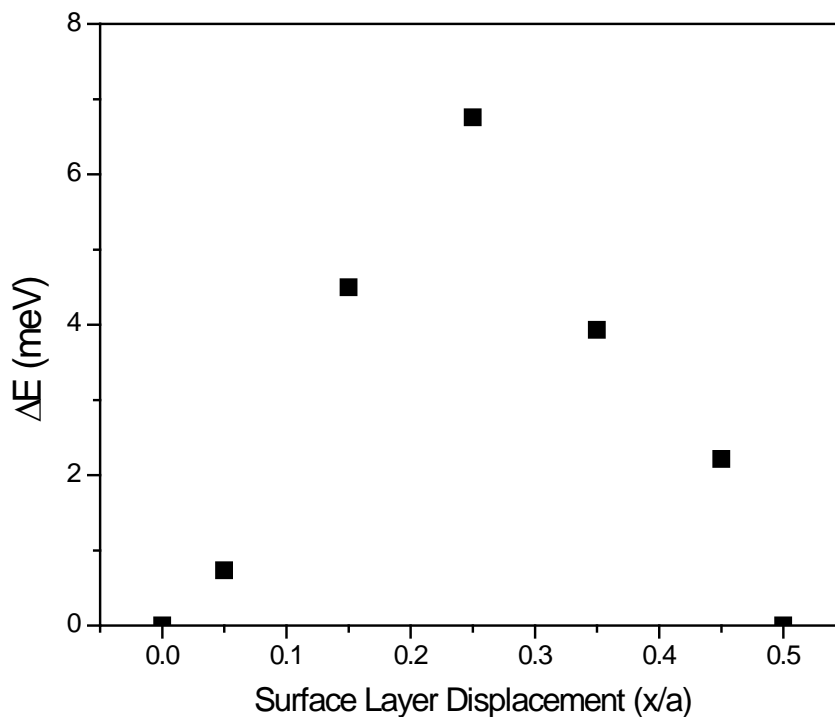


Figure 3.5: The change in energy as a function of the surface KCl layer displacement along the $\langle 10 \rangle$ direction, along Path A in Figure 3.3.

The results of a similar calculation, but now for sliding along path B, are displayed in Figure 3.7. The curve is again relatively symmetric and the maximum increase in potential energy (at $\alpha = 0.25$) is ~ 27 meV. The displacements of the layers of the KCl film and the outermost iron layer are again plotted as a function of the displacement of the top layer of the film in Figure 3.8. This reveals similar behavior as for sliding along path A; an increase in energy during sliding, and translation of layers in the halide film that follow that of the outermost layer, with only minimal displacement of the Fe surface. Again this indicates that sliding occurs at the iron–KCl interface.

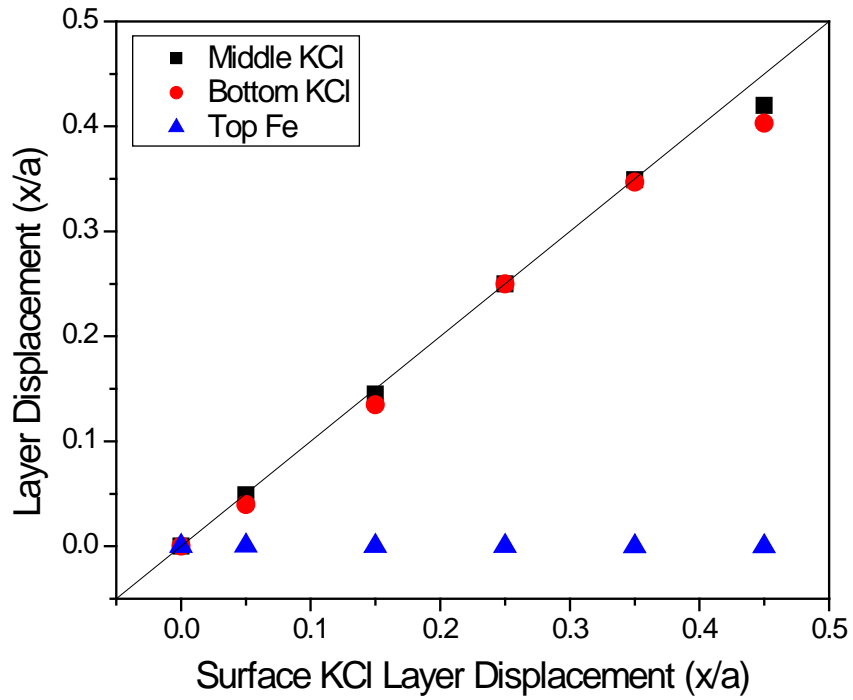


Figure 3.6: Displacements of the (■) middle KCl, (●) bottom KCl and (▲) top Fe layers along the $\langle 10 \rangle$ direction as a function of the surface KCl layer displacement along Path A (Figure 3.2), corresponding to the potential energy curve shown in Figure 3.5.

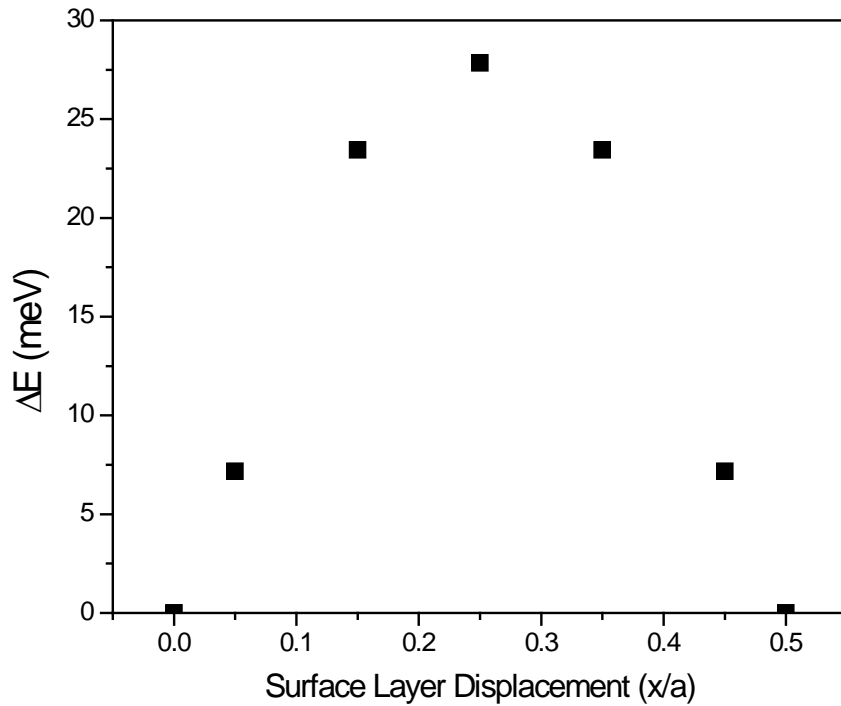


Figure 3.7: The change in energy as a function of the surface KCl layer displacement along the $\langle 11 \rangle$ direction, along Path B (Figure 3.3).

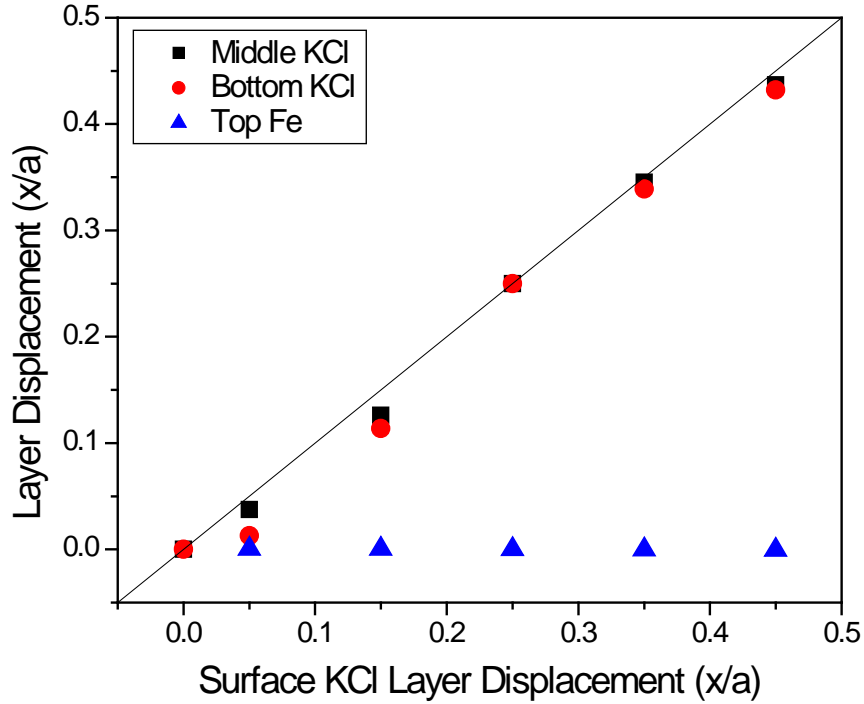


Figure 3.8: Displacements of the (■) middle KCl, (●) bottom KCl and (▲) top Fe layers along the $\langle 11 \rangle$ direction as a function of the surface KCl layer displacement along Path B (Figure 3.3), corresponding to the potential energy curve shown in Figure 3.6.

This shear behavior is in complete agreement with what would be expected from the relative values of the shear moduli ($\sim 6\text{--}11$ GPa) [38] compared to the measured interfacial shear strength, ~ 70 MPa [9]. Thus, at a shear stress required to completely slide the surface (~ 70 MPa), the elastic strain of the film is $\frac{\sim 70 \times 10^6}{\sim 9 \times 10^9} \approx 10^{-2}$. DFT calculation qualitatively reproduced the experimental behavior.

While in principle, the energy should be calculated for all possible paths on the surface to produce a range of plots such as those shown in Figures 3.5 and 3.7, the observation that the lattice is only very slightly laterally distorted during sliding allows the situation to be considerably simplified by calculating the equilibrium energies of the lattice located at various positions on the iron substrate, resulting in significant savings in

computational time. Thus, the energies of the equilibrium structures of a KCl film on various sites on the substrate were calculated and are given in Table 3.1. The K and Cl atoms in ‘atop’ sites are found to be the most stable configuration.

Site	<i>flair</i> : ΔE (meV)	VASP: ΔE (meV)
Atop	0	0
Atop-Hollow	15	6
Bridge	22	7
Hollow	28	9

Table 3.1: Energy differences for KCl slabs adsorbed on a Fe(100) substrate at various sites (see Figure 3.3) relative to the atop site calculated using *flair* and VASP.

The energy differences computed for the equilibrium structures of the KCl film are identical to those calculated for the sliding potentials shown in Figures 3.5 and 3.7. Thus, the height of the potential for sliding along a $\langle 10 \rangle$ direction (path A) from a ‘bridge’ over a ‘hollow’ site is ~ 7 meV (figure 3.5), while the energy difference from the equilibrium calculations (Table 3.1), is 6 meV. Similarly, for sliding along path B, from an ‘atop’ through a ‘four-fold’ site, the height of the potential energy curve is ~ 27 meV (Figure 3.7), while the energy difference between KCl slabs located at these sites is 28 meV (Table 3.1).

Similar calculations were also carried out using VASP. In this case, a similar phenomenon was found in which the slab slid uniformly over the iron substrate, but the calculated energy differences (cf, Table 3.1) along each of the paths indicated in Figure 3.3 were substantially lower, by about a factor of three, than those calculated using *flair*. The largest energy differences for adsorption at the various sites on the surface are less

than 3 kJ mol^{-1} . Thus, the accuracy required for sliding potentials on surfaces is much greater than that required for chemical reactions, for example, where activations energies are generally greater than 50 kJ mol^{-1} . This suggests that *flair* successfully reproduces the small energy corrugation encountered during the sliding of the thin KCl film, while VASP is less accurate. The origin of these discrepancies will be discussed in greater detail below. However, the accuracy afforded by VASP ($\sim \text{kJ mol}^{-1}$) is sufficient for most chemical problems, but with the additional benefit of computational efficiency. To understand these discrepancies in more detail, we performed extensive tests to ensure that both the VASP and *flair* results were converged; for example, the kinetic energy of the VASP wavefunction expansions was increased from the value of 396 eV used in most of the calculations to 600 eV, with essentially no changes in the calculated results. The energy differences between the VASP and *flair* calculations are reflected in the structural properties at the interface, particularly in the nearest-neighbor Fe–Cl bond lengths. The calculated Fe–K bond lengths for the different (atop, bridge, and hollow) configurations agree within $\sim 0.02 \text{ \AA}$, but the calculated Fe–Cl bond lengths differ significantly and vary depending on the coordination: the *flair* versus VASP values are 3.54 versus 3.78 \AA for the atop position; 3.99 versus 4.13 \AA for the bridge; and 4.24 versus 4.37 \AA for the hollow configuration. For comparison, Fe–K values for *flair* (VASP) are 3.87 \AA (3.90 \AA), 4.18 \AA (4.16 \AA), and 4.41 \AA (4.39 \AA) for the atop, bridge, and hollow configurations, respectively. Even with these large differences in the Fe–Cl distances, the two methods agree on the value of a corrugation of the free surface (the difference in height between the surface Cl and K ions) of $0.15 \pm 0.01 \text{ \AA}$, with the Cl ion being higher than the potassium. Similarly, in spite of the 0.23 \AA difference in Fe–Cl bond length in the atop

configuration, both *flair* and VASP give a corrugation of the Fe atoms at the interface for the atop configuration of 0.05 Å. On the other hand, because of the difference in Fe–Cl bond lengths, the corrugation of the interface KCl layer differs significantly (~ 0.17 – 0.21 Å) between the two sets of calculations, resulting in almost no corrugation (0.07, 0.03, and 0.02 Å for atop, bridge, and hollow, respectively) for the VASP calculation of the interfacial KCl layer.

Since the differences between the *flair* and VASP values given in Table 3.1 are strongly correlated to the calculated Fe–Cl distances, the questions naturally arise as to why the two methods differ and which is physically more correct. The two methods make different approximations, including the representation of the wavefunctions, the treatment of relativistic effects (not expected to be important here), and the core–valence interactions. In the FLAPW approach, the basis functions are optimally adapted to the local environment, but at the expense of increased computational cost compared to the more approximate PAW approach. This variational flexibility that allows for changes in the shape of the basis functions (including changes in the positions of nodes) is particularly important when the local bonding environment changes, e.g., different numbers of, and distances to, nearest-neighbor atoms, and when there are changes in the nature of the bonding ionic versus covalent versus metallic). From a chemical perspective, the Fe–Cl interaction should be stronger than Fe–K, as indicated by the short Fe–Cl bond lengths (~ 2.2 Å) in species such as FeCl, FeCl₂, and FeCl₃. Thus, differences between the Fe–Cl and Fe–K bond lengths are expected. While the *flair* calculations exhibit this behavior, the VASP ones do not. Having approximately the same Fe–K and Fe–Cl bond lengths in the bridge and hollow configurations results in the

interface KCl layer being flatter than the surface layer. The use of suitably modified PAW potentials might, in principle, remove the discrepancies between the two sets of calculations, but is beyond the scope of this work. Although the energy differences between the two calculational methods shown in Table 3.1 are small—and smaller than normally of interest—the stringent requirements on the energies involved in shear calculations require much more precise calculations than for other structural determinations.

Finally, the results of the calculated potentials can be used to calculate a shear strength, S_0 for comparison with the experimentally determined value (65 ± 5 MPa) [9]. It has recently been demonstrated that the lateral force calculated using the Tomlinson–Prandtl model [11-12] can depend not only on the height of the potential barrier and its periodicity, but also on the shape of the potential [39]. However, the potential energy curves shown in figures 3.5 and 3.7 are reasonably close to sinusoidal so that the lateral forces calculated from the limiting force in the Tomlinson–Prandtl model using a simple sinusoidal potential and normalized to the unit cell area to yield a shear strength. It is assumed that the initial configuration is at the most stable (‘atop’) site and the shear strength is then calculated from the height of the barriers for sliding along the $\langle 10 \rangle$ and $\langle 11 \rangle$ directions (Table 3.1). This leads to maximum heights of the potentials of 22 and 28 meV respectively. This approach leads to calculated values of the shear strength at zero pressure (S_0) along the $\langle 10 \rangle$ direction of 79.8 MPa, and along the $\langle 11 \rangle$ direction of 70.3 MPa for the energies calculated using *flair* (Table 3.1). Both of these values are in excellent agreement with the experimentally measured value of 65 ± 5 MPa [9]. The results also suggest that, in spite of the presence of an interface with four-fold symmetry,

the shear strength is quite isotropic. Note that similar calculations using VASP would lead to calculated shear strengths about a factor of three lower (~ 25 MPa).

These results demonstrate that DFT methods are capable of successfully calculating the interfacial shear strength during sliding at zero pressure (S_0) and can successfully reproduce the experimental value for a simple model lubricant film consisting of KCl on iron. In addition, the calculations reveal that shear occurs between the iron surface and KCl film where the film is only minimally laterally distorted. Thus, the height of the sliding potential can be calculated efficiently merely by calculating the energies at various high-symmetry ‘sites’ on the surface. This result will considerably simplify calculations of the effect of pressure on sliding. In this case, the sliding potential should, in principle, be calculated along various paths with various values of an imposed normal pressure. Such calculations would be computationally prohibitive. The ability to calculate the effect of pressure on the behavior of the film at a limited number of locations renders this problem more tractable. Being able to achieve this will enable friction coefficients of thin, boundary-layer lubricating films to be calculated from first principles using DFT.

3.4 Conclusions

Calculations of the shear of a KCl film on a metal (iron) substrate reveal that the small values of the sliding potential energies require very precise DFT calculations. In the case of sliding a KCl film, this may well occur since similar structures are being compared so that systematic errors may cancel out. The calculated value of the zero-

pressure limit of the shear strength (S_0) of a KCl film is very close to the experimentally measured value implying that DFT is capable of calculating interfacial shear properties. The DFT calculations indicate that the KCl film moves as a relatively rigid entity and that shear takes place between the iron substrate and the KCl film.

3.5 References

- [1] Amontons, G., *Mèm. Acad. R. A* **1699**, 257. (Amsterdam: Chez Gerard Kuyper, 1706)
- [2] Coulomb, C. A., *Mèm. Math. Phys.* **1785**, (Paris X), 161-342.
- [3] Dowson, D.; Higginson, G. R., A Numerical Solution to the Elasto-Hydrodynamic Problem. *Journal of Mechanical Engineering Science* **1959**, *1* (1), 6-15.
- [4] Dowson, D.; Higginson, G. R., The Effect of Material Properties on the Lubrication of Elastic Rollers. *Journal of Mechanical Engineering Science* **1960**, *2* (3), 188-194.
- [5] Ogata, S.; Li, J.; Hirosaki, N.; Shibutani, Y.; Yip, S., Ideal shear strain of metals and ceramics. *Physical Review B* **2004**, *70* (10), 104104.
- [6] Jhi, S.-H.; Louie, S. G.; Cohen, M. L.; Morris, J. W., Jr., Mechanical Instability and Ideal Shear Strength of Transition Metal Carbides and Nitrides. *Physical Review Letters* **2001**, *87* (7), 075503.

- [7] Shenoy, V. B.; Miller, R.; Tadmor, E. B.; Phillips, R.; Ortiz, M., Quasicontinuum Models of Interfacial Structure and Deformation. *Physical Review Letters* **1998**, *80* (4), 742-745.
- [8] Baroni, S.; Giannozzi, P.; Testa, A., Elastic Constants of Crystals from Linear-Response Theory. *Physical Review Letters* **1987**, *59* (23), 2662-2665.
- [9] Gao, F.; Furlong, O.; Kotvis, P.; Tysoe, W. T., Pressure Dependence of Shear Strengths of Thin Films on Metal Surfaces Measured in Ultrahigh Vacuum. *Tribol Lett* **2008**, *31* (2), 99-106.
- [10] Carpick, R. W.; Salmeron, M., Scratching the Surface: Fundamental Investigations of Tribology with Atomic Force Microscopy. *Chemical Reviews* **1997**, *97* (4), 1163-1194.
- [11] Tomlinson, G. A., CVI. A molecular theory of friction. *Philosophical Magazine Series 7* **1929**, *7* (46), 905-939.
- [12] Prandtl, L., Ein Gedankenmodell zur kinetischen Theorie der festen Körper. *ZAMM - Journal of Applied Mathematics and Mechanics / Zeitschrift für Angewandte Mathematik und Mechanik* **1928**, *8* (2), 85-106.
- [13] Gnecco, E.; Bennewitz, R.; Gyalog, T.; Loppacher, C.; Bammerlin, M.; Meyer, E.; Güntherodt, H. J., Velocity Dependence of Atomic Friction. *Physical Review Letters* **2000**, *84* (6), 1172-1175.
- [14] Riedo, E.; Gnecco, E.; Bennewitz, R.; Meyer, E.; Brune, H., Interaction Potential and Hopping Dynamics Governing Sliding Friction. *Physical Review Letters* **2003**, *91* (8), 084502.

- [15] Fusco, C.; Fasolino, A., Velocity dependence of atomic-scale friction: A comparative study of the one- and two-dimensional Tomlinson model. *Physical Review B* **2005**, *71* (4), 045413.
- [16] Koskilinna, J.; Linnolahti, M.; Pakkanen, T., Friction coefficient for hexagonal boron nitride surfaces from ab initio calculations. *Tribol Lett* **2006**, *24* (1), 37-41.
- [17] Koskilinna, J.; Linnolahti, M.; Pakkanen, T., Friction and a Tribochemical Reaction between Ice and Hexagonal Boron Nitride: A Theoretical Study. *Tribol Lett* **2008**, *29* (2), 163-167.
- [18] Koskilinna, J.; Linnolahti, M.; Pakkanen, T., Friction Paths for Cubic Boron Nitride: An Ab Initio Study. *Tribol Lett* **2007**, *27* (2), 145-154.
- [19] Koskilinna, J. O.; Linnolahti, M.; Pakkanen, T. A., Tribochemical Reactions between Methylated Diamond (111) Surfaces: A Theoretical Study. *Tribol Lett* **2005**, *20* (2), 157-161.
- [20] Liang, T.; Sawyer, W. G.; Perry, S. S.; Sinnott, S. B.; Phillpot, S. R., First-principles determination of static potential energy surfaces for atomic friction in MoS₂ and MoO₃. *Physical Review B* **2008**, *77* (10), 104105.
- [21] Matsuzawa, N. N.; Kishii, N., Theoretical Calculations of Coefficients of Friction between Weakly Interacting Surfaces. *The Journal of Physical Chemistry A* **1997**, *101* (51), 10045-10052.
- [22] Neitola, R.; Pakkanen, T. A., Ab Initio Studies on the Atomic-Scale Origin of Friction between Diamond (111) Surfaces. *The Journal of Physical Chemistry B* **2001**, *105* (7), 1338-1343.

- [23] Neitola, R.; Pakkanen, T. A., Ab Initio Studies on Nanoscale Friction between Fluorinated Diamond Surfaces: Effect of Model Size and Level of Theory. *The Journal of Physical Chemistry B* **2006**, *110* (33), 16660-16665.
- [24] Neitola, R.; Ruuska, H.; Pakkanen, T. A., Ab Initio Studies on Nanoscale Friction between Graphite Layers: Effect of Model Size and Level of Theory. *The Journal of Physical Chemistry B* **2005**, *109* (20), 10348-10354.
- [25] Overney, G.; Zhong, W.; Tomanek, D. In *Theory of elastic tip--surface interactions in atomic force microscopy*, Baltimore, Massachusetts (USA), AVS: Baltimore, Massachusetts (USA), 1991; pp 479-482.
- [26] Tománek, D.; Zhong, W.; Thomas, H., Calculation of an Atomically Modulated Friction Force in Atomic-Force Microscopy. *EPL (Europhysics Letters)* **1991**, *15* (8), 887.
- [27] Zhong, W.; Tománek, D., First-principles theory of atomic-scale friction. *Physical Review Letters* **1990**, *64* (25), 3054-3057.
- [28] Wu, G.; Gao, F.; Kaltchev, M.; Gutow, J.; Mowlem, J. K.; Schramm, W. C.; Kotvis, P. V.; Tysoe, W. T., An investigation of the tribological properties of thin KCl films on iron in ultrahigh vacuum: modeling the extreme-pressure lubricating interface. *Wear* **2002**, *252* (7–8), 595-606.
- [29] Wimmer, E.; Krakauer, H.; Weinert, M.; Freeman, A. J., Full-potential self-consistent linearized-augmented-plane-wave method for calculating the electronic structure of molecules and surfaces: O₂ molecule. *Physical Review B* **1981**, *24* (2), 864-875.

- [30] Weinert, M.; Wimmer, E.; Freeman, A. J., Total-energy all-electron density functional method for bulk solids and surfaces. *Physical Review B* **1982**, 26 (8), 4571-4578.
- [31] Weinert, M.; Schneider, G.; Podloucky, R.; Redinger, J. *Flair*.
<http://www.uwm.edu/~weinert/flair.html>.
- [32] Kresse, G.; Joubert, D., From ultrasoft pseudopotentials to the projector augmented-wave method. *Physical Review B* **1999**, 59 (3), 1758-1775.
- [33] Blöchl, P. E., Projector augmented-wave method. *Physical Review B* **1994**, 50 (24), 17953-17979.
- [34] Kresse, G.; Hafner, J., Ab initio molecular dynamics for liquid metals. *Physical Review B* **1993**, 47 (1), 558-561.
- [35] Kresse, G.; Furthmüller, J., Efficient iterative schemes for ab initio total-energy calculations using a plane-wave basis set. *Physical Review B* **1996**, 54 (16), 11169-11186.
- [36] Kresse, G.; Furthmüller, J., Efficiency of ab-initio total energy calculations for metals and semiconductors using a plane-wave basis set. *Computational Materials Science* **1996**, 6 (1), 15-50.
- [37] Perdew, J. P.; Burke, K.; Ernzerhof, M., Generalized Gradient Approximation Made Simple. *Physical Review Letters* **1996**, 77 (18), 3865-3868.
- [38] Norwood, M. H.; Briscoe, C. V., Elastic Constants of Potassium Iodide and Potassium Chloride. *Physical Review* **1958**, 112 (1), 45-48.

- [39] Furlong, O.; Manzi, S.; Pereyra, V.; Bustos, V.; Tysoe, W., Monte Carlo Simulations for Tomlinson Sliding Models for Non-Sinusoidal Periodic Potentials. *Tribol Lett* **2010**, *39* (2), 177-180.

Chapter 4

Pressure Dependence of Shear Strengths in Sliding, Boundary-Layer Friction

4.1 Introduction

The lateral force F_L in sliding friction is rigorously given by $F_L = SA_C$, where S is the shear strength of the sliding interface and A_C is the real area of contact. Measurements of the shear properties of pressurized bulk materials indicate that they depend on pressure [1] suggesting that interfacial shear during sliding is also pressure dependent, $S = S(P)$, where P is the pressure in the contact. A linear pressure dependence of shear strength has been assumed in many cases to rationalize the experimentally observed variation of the friction coefficient with normal load [2-7]. Load-dependent sliding potentials have been observed with atomic force microscopy (AFM) friction measurements, which also leads to a linear increase in shear strength with pressure [8-9]. Finally, many molecular dynamics (MD) simulations, which plot lateral sliding force versus normal load, reveal a linear variation between these quantities [10-18]. Since these calculations are invariably carried out for constant areas, these can be thought of as plots of shear strength versus pressure. In particular, MD simulations of a model sliding interface using Lennard-Jones interaction potentials proposed that the pressure dependence originated from the vertical motion that occurred during sliding as the atoms in the interface rode over each other [14]. In this case, the pressure dependence arose from the external work done by the vertical motion of the atoms against the normal

load and could be rationalized by a hard-sphere model to mimic the surface corrugation. A similar argument was made for the origin of the pressure dependence of the shear of polymers [3].

A linear variation in shear strength with pressure, $S(P) = S_0 + \alpha P$ could arise from a first-order Maclaurin's series expansion of the pressure dependence, with S_0 being the shear strength at $P = 0$, and α the coefficient of the first term in the expansion given by $\alpha = \left. \frac{dS}{dP} \right|_{P=0}$. This raises the question of whether a linear dependence of shear strength, if it exists, is rigorous or merely represents the first term in the expansion of a more complex function. As pointed out elsewhere [16], such a linear variation in shear strength with pressure ($P = \frac{F_N}{A_C}$, where F_N is the normal force) rigorously leads to an equation for the friction coefficient $\mu = \frac{S_0}{P} + \alpha$, without any assumptions regarding the nature of the contact. This is an attractive possibility since it would result in a friction coefficient that is relatively independent of load and may go some way toward rationalizing Amontons' law [16]. In this case, at limiting, high contact pressures, α represents the minimum attainable friction coefficient. Thus understanding the molecular origins of pressure-dependent shear strengths will potentially guide the design of low-friction films. Materials and chemical properties can be determined using first-principles quantum calculations using density functional theory (DFT) methods [19-22]. For example, such an approach enables mechanical properties to be calculated without any assumptions being made concerning the form of the inter-atomic interaction potentials, and the potentials used in MD simulations are invariably derived using DFT calculations. Thus, in principle, calculating shear properties as a function of pressure using DFT methods will provide fundamental insights into the existence and origin of pressure-

dependent shear strengths. However, the results of such calculations should be validated by comparison with experiment. Since the computational requirements for DFT calculations increase with the complexity of the system, experimental data should be available for systems that are sufficiently simple that accurate, first-principles DFT calculations can be performed. We have previously shown that DFT can reproduce the experimentally measured value of S_0 for a thin KCl film on a metal substrate [23]. In this case, the shear properties of a KCl film on a Fe(100) substrate were computed by laterally translating the outer layer of the KCl film and calculating the energies of the system as a function of sliding distance. The resulting potentials were used to calculate the values of S_0 and yielded a value of 79.8 MPa for sliding along the $\langle 10 \rangle$ and 70.3 MPa along the $\langle 11 \rangle$ directions [23]. The experimental shear strength has been measured for KCl evaporated onto metal substrates in ultrahigh vacuum to obtain and maintain clean, well-characterized films [24]. The experiment values are $S_0 = 65 \pm 5$ MPa and $\alpha = 0.14 \pm 0.02$ [24]. Thus the experimental and theoretical values of S_0 are in good agreement. However, in order to obtain such good agreement, it was found necessary to use a full-potential linearized augmented plane wave method (FLAPW) that explicitly included all electrons (including those in the core) to reproduce the small energy changes that occur during sliding (≤ 30 meV). (Since the metal and KCl films are in contact, the bonding is predominately covalent/ionic, and thus these calculations did not include van der Waals' interactions.) In order to calculate pressure-dependent shear strengths (and thereby calculate α), in principle, similar shear calculations should be performed by translating the outer surface of the KCl layer under various applied normal loads. In view of the computational expense of the FLAPW calculations, this would be prohibitive. However,

theory showed that shear occurred at the KCl–Fe interface without substantial shear distortion of the KCl film. This enabled the energies at the turning points of the shear potentials to be calculated to obtain the heights of the sliding potentials, which were in excellent agreement with those obtained by performing a full shear calculation [23]. We have exploited this observation in the following by calculating the energy of a KCl + Fe(100) slab as a function of applied normal pressure when it is located at various high-symmetry sites on the surface. The pressure-dependent height of the sliding potential is determined from the calculated energies to establish how the shear strength varies with pressure. The validity of the approach is ascertained by comparing theory and experiment. However, since theoretical pressure-dependent shear strength determinations rely on a number of DFT calculations (at different pressures), the resulting errors are likely to be larger than just for a single calculation. Nevertheless, the resulting form of the variation in shear strength with pressure, since it includes all interactions, should be accurate. An analysis of the theoretical results enables the physical origins of the pressure-dependent shear strength to be established.

4.2 Theoretical Methods

The KCl/Fe(100) system was previously modeled by a traditional approach using a supercell geometry that consisted of a seven-layer Fe(001) film with three layers of KCl on each side [23]. A vacuum gap of ~ 15 Å was placed between repeating slabs in the direction of the surface normal. In order to mimic the pressure dependence, the energy was initially calculated by displacing the outer layer of the KCl film by some amount.

However, since it is unlikely that the potassium and chloride ions will displace by equal amounts under the influence of a normal load, an alternative strategy was adopted. In this case, a bilayer of KCl was placed between Fe(100) slabs, which are seven iron layers thick. The distance d between the outer layers of the iron slab is changed to mimic the compression due to the applied normal load (see Figure 4.1).

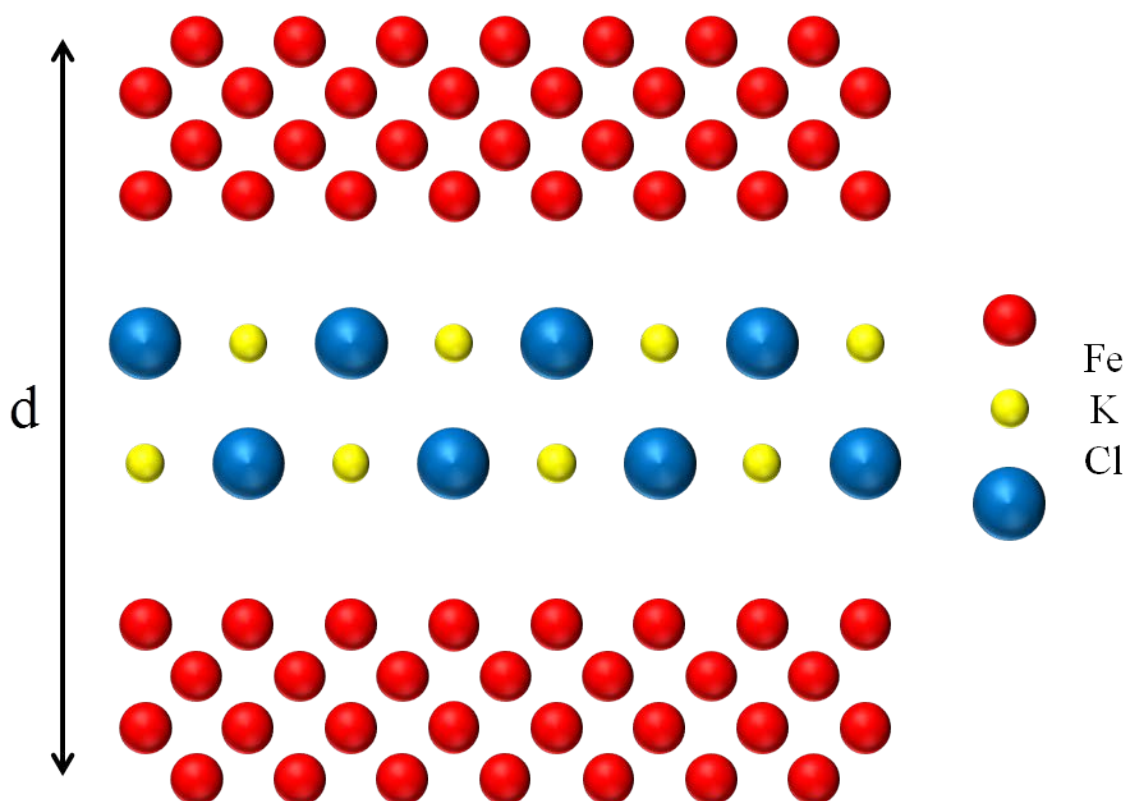


Figure 4.1: A schematic depiction of the KCl bilayer enclosed between two, four-atom thick iron slabs where the surfaces have a (100) orientation. Application of an external pressure is simulated by changing the distance d between the outermost iron layers in the composite slab.

This strategy is adopted since the previous DFT slab calculations showed that the iron in contact with the KCl slab moved much less than the potassium and chloride ions [23], as expected since iron has a larger Young's modulus and hardness than KCl. This

indicates that those iron atoms farther away from the surface will move a negligible amount from their equilibrium positions so that an applied pressure can be realistically imposed by uniformly moving the outer iron layers by varying the value of d . Based on the results for the KCl film on iron [23], calculations were performed for the ions in the KCl layer located (i) above an iron atom in the substrate (designated atop), (ii) above a bridge site in the Fe(100) substrate (designated bridge), and (iii) above the four-fold hollow site in the substrate (designated hollow). Initial calculations were carried out using a KCl bilayer since AFM experiments for alkali halides on a copper surface indicates that it adsorbs onto the surface as a bilayer [25]. The effect of film thickness on the shear properties will be explored elsewhere [26]. Finally, KCl(100)/Fe(100) is used for the initial structure calculations since X-ray diffraction results have demonstrated that the KCl film adopts this orientation on iron [27].

Spin-polarized DFT calculations were performed by an implementation of the all-electron, full-potential linearized augmented-plane wave (FLAPW) method, *flair* [28-30] using the generalized gradient approximation (GGA) functional of Perdew, Burke, and Ernzerhof [31] for exchange-correlation and self-consistent convergence criteria of better than 10^{-5} eV. Total energies were calculated by varying the distance d between the outermost iron layers (Figure 4.1). Van der Waals' interactions were not explicitly included in the calculation.

The geometry of the undisplaced case was optimized by fixing the middle three layers of iron to their bulk positions and allowing all other atoms to relax until the forces on all unrestricted atoms was less than 10^{-2} eV/Å. The resulting plots of energy versus d

are used to calculate the pressure-dependent shear strength and the strategy for accomplishing this is discussed below.

4.3 Results and Discussion

The plots of energy versus displacement for a KCl slab located on various sites on the Fe(100) substrate are displayed in Figure 4.2, and are plotted versus $d/2$ to take account of the presence of two iron layers in the slab. The corresponding applied pressure can be calculated from the first derivative of the energy versus distance curve, which requires the curves to be fit to an analytical function. The curves were fit to both Morse ($E(d) = E_0 + D_e(1 - \exp(-\alpha(d - d_0)))^2$) and harmonic potentials ($E(d) = E_0 + \frac{k}{2}(d - d_0)^2$), where E_0 is the energy minimum of the potential, at a slab distance d_0 . D_e is the dissociation energy, α is a constant, and k is the force constant of the harmonic potential. A slightly better fit was obtained using a harmonic potential, which is used for the subsequent analysis and the fitting parameters are given in Table 4.1. For clarity, the fits are compared in Figure 4.3. As found previously for the KCl slab on iron, the most stable position is for the K^+ and Cl^- ions located in atop positions [23]. This was ascribed to the ability of the halide ion to bond to the iron atom below [23]. The bonding is less favorable at bridge and hollow sites leading to a lower binding energy. Note that this is contrary to what might be expected on the basis of a simple hard-sphere model for which the four-fold hollow site might be expected to be the most stable.

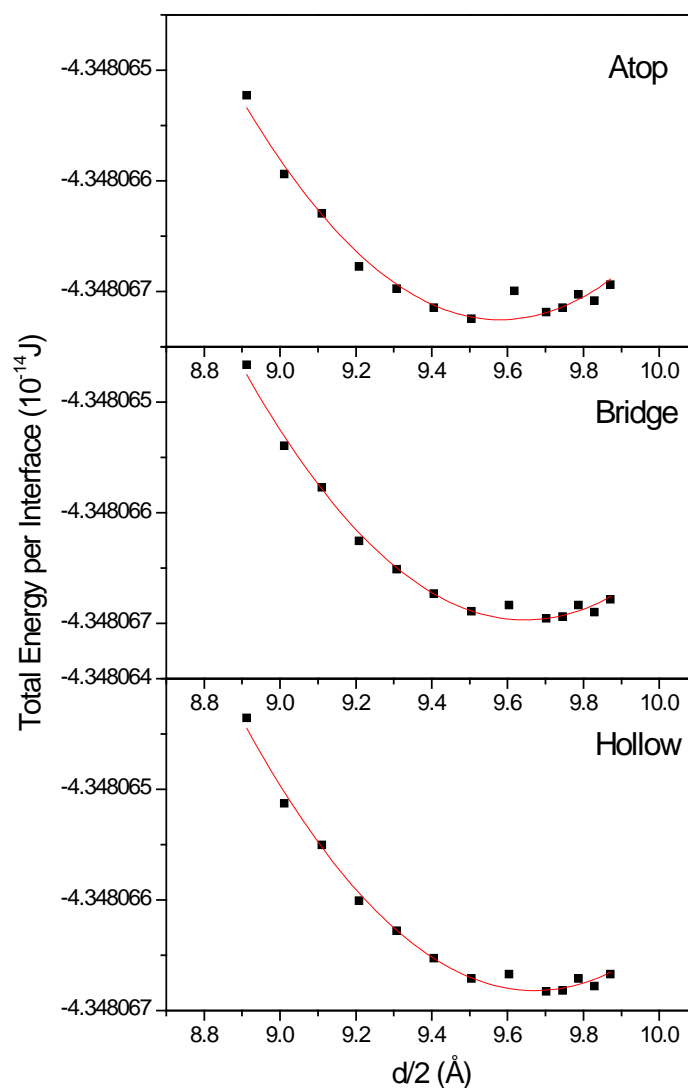


Figure 4.2: Plot of the total energy of the KCl+iron composite slab as a function of half of the separation between the outermost iron layers $d/2$ for the chlorine and potassium ions located (a) above iron atoms in the substrate (designated *atop*), (b) above a site between iron atoms in the substrate (designated *bridge*) and (c) above the four-fold hollow between four iron atoms (designated *hollow*). The energy is plotted *versus* $d/2$ to take into account the existence of two surfaces.

	E_0 (10^{-14} J)	d_0 (Å)	k (N/m)
Atop	-4.3480673	9.58	8.61
Bridge	-4.3480673	9.63	8.26
Hollow	-4.3480668	9.65	8.24

Table 4.1: The parameters of the fits to harmonic potentials to the data displayed in Figure 4.2.

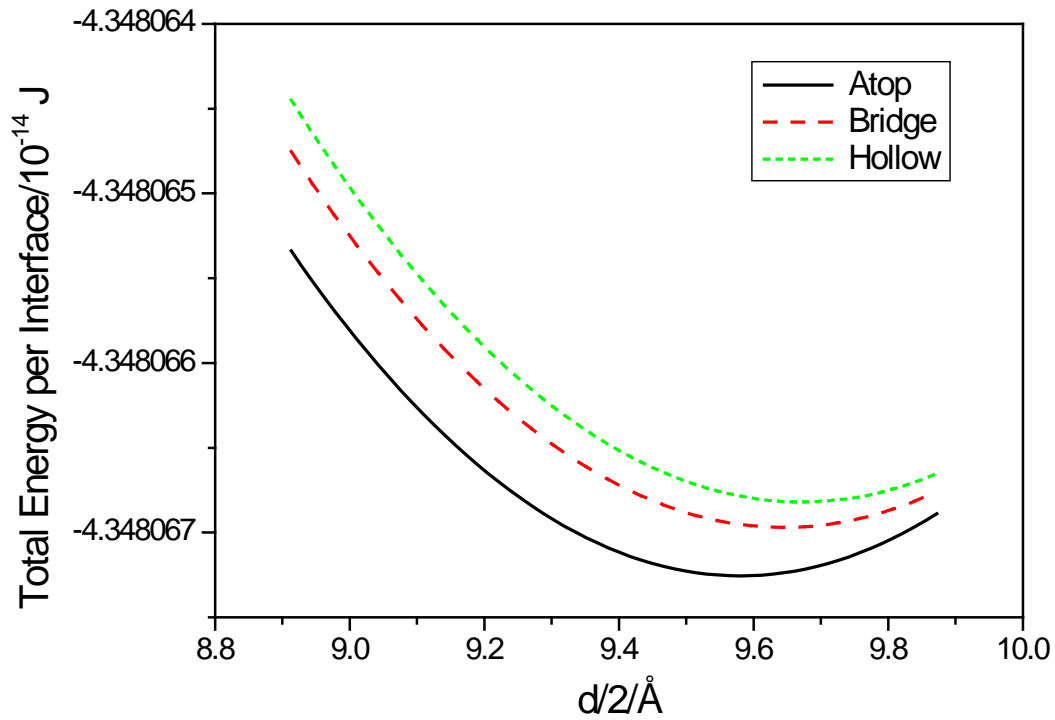


Figure 4.3: Plots of the fits to harmonic potentials to the data displayed in Figure 4.2.

The resulting sliding potential comprises two terms. The first is due to the difference in the values of E_0 at each site and yields the value of S_0 (the pressure-independent part of the shear strength). The second contribution arises from the different thicknesses Δd of the KCl film located at different sites, which requires additional work

$P\Delta d$ to be carried out against the normal force. If the sites at the minimum and maximum of the sliding potential are designated a and b , respectively, then $\Delta d = d_a - d_b = (d_0^a - d_0^b) + P\left(\frac{1}{k_b} - \frac{1}{k_a}\right)$ for a harmonic potential. The first term represents the corrugation of the surface and the second is due to the different compressibilities (k_a and k_b) of the KCl film at different sites. This then yields a formula for the pressure-dependent height of the sliding potential $\Delta E(P)$ that includes both effects as:

$$\Delta E(P) = (E_0^a - E_0^b) + (d_0^a - d_0^b)P + P^2\left(\frac{1}{k_b} - \frac{1}{k_a}\right) \quad (1)$$

and thus formally includes both linear and parabolic pressure dependence. The first term is used to yield a value of S_0 and the second two terms yield the pressure dependence. Since the atop site is the most stable (Figure 4.3), sliding can occur via the bridge site (along the $\langle 10 \rangle$ direction), or via the hollow site (along $\langle 11 \rangle$). Thus, the values of the second and third terms in Equation 1 are calculated as a function of pressure P for sliding along the $\langle 10 \rangle$ and $\langle 11 \rangle$ directions and the results are summarized in Figure 4.4. The linear terms are shown as filled squares (■) and the effect of adding the parabolic term is shown as filled circles (●). The energy change for sliding along the $\langle 11 \rangle$ direction is larger than for sliding along $\langle 10 \rangle$ reflecting the lower stability of the hollow site than the bridge site (see Figure 4.3). The data were plotted to a maximum pressure of 700 MPa, corresponding to the measured hardness of iron. This reveals that the parabolic term only slightly perturbs the linear term so that the third term in Equation 1 is much less than the second term. This indicates that the pressure dependence of the shear strength, at least in the case of KCl on Fe(100), is due predominantly to the atomic corrugation as the KCl film slides over the Fe(100) substrate, which requires additional external work to be done to move the slab against the applied normal load.

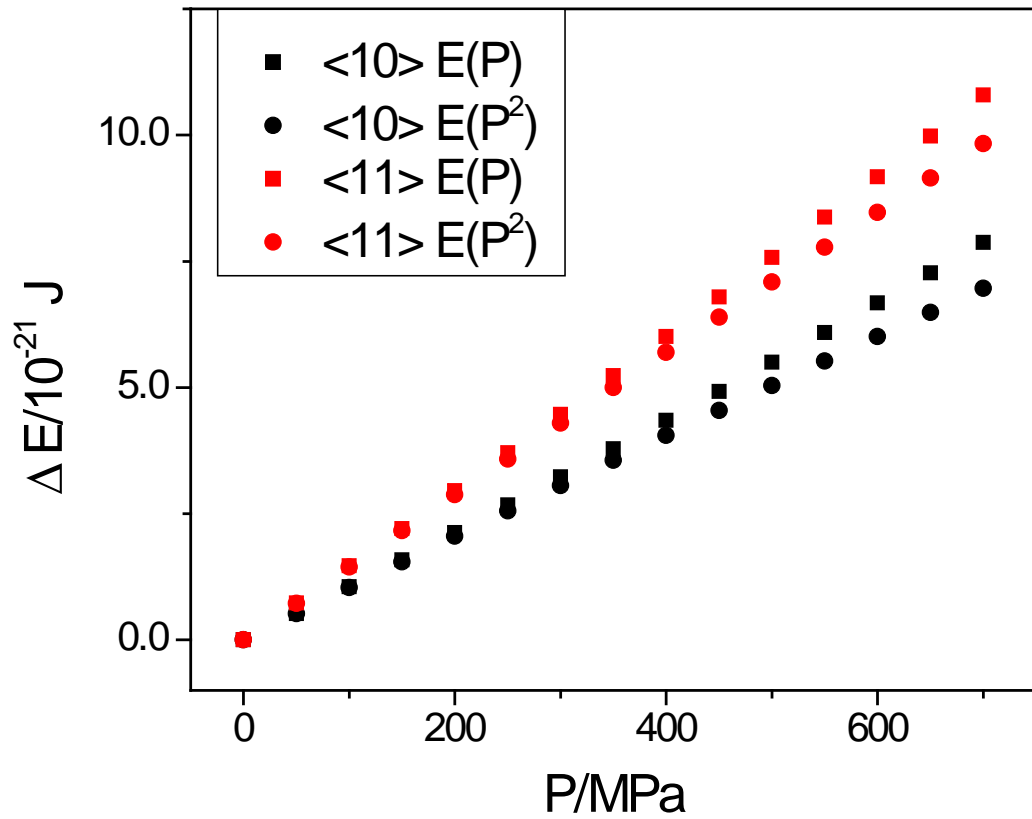


Figure 4.4: Plot of the height of the sliding potentials ΔE versus pressure for sliding along the $\langle 11 \rangle$ direction from an *atop* to a *hollow* to an *atop* site (in red, upper traces), or for sliding along the $\langle 10 \rangle$ direction from an *atop* to a *bridge* to an *atop* site (in black, lower traces). The portion of the data that vary linearly with P , calculated for a KCl film on iron are shown as solid squares (\blacksquare), while the effect of adding a quadratic pressure dependence is shown by the solid circles (\bullet).

Finally, the shear strength can be calculated from the height of the sliding potential shown in Figure 4.4 from the limiting force in the Tomlinson–Prandtl [9, 32–33] model using a simple sinusoidal potential and normalized to the unit cell area to yield a shear strength [23]. The results for sliding along both the $\langle 11 \rangle$ and $\langle 10 \rangle$ directions are displayed in Figure 4.5, which includes the value at zero pressure (from E_0). The values of shear strengths along the two directions are remarkably similar in spite of the

somewhat different values of ΔE (Figure 4.4) because of the different periodicities. The resulting values of $S_0 \langle 10 \rangle = 64 \pm 9$ MPa and $S_0 \langle 11 \rangle = 69 \pm 8$ MPa. The errors in the values of S_0 are estimated by propagating the standard deviations of the fitting parameters to the curves in Figures 4.2 and 4.3 (Table 4.1) to the calculation of the shear strength from the Tomlinson–Prandtl model [23]. The resulting values of S_0 are in excellent agreement with the experimental value of 65 ± 5 MPa, and is, in fact, slightly better than the agreement with the slab calculations [23]. This may be due to the better energy convergence obtained to the fit than by the energy minimization in the DFT calculation or because the model used for this study (Figure 4.1) more closely mimics the sliding interface.

The α values are similarly isotropic yielding $\alpha \langle 10 \rangle$ and $\alpha \langle 11 \rangle$ both equal to 0.05 ± 0.01 and are lower than, but within the same range as the experimental value of 0.14 ± 0.02 [24]. Again, the errors in the calculated values of α are estimated by propagating the standard deviations of the fitting parameters to the potential shown in Figures 4.2 and 4.3 (Table 4.1). The difference between the experimental and calculated values of α could be due to differences in the film thickness between the simulations and the experiment but it has recently been demonstrated that the thickness of the KCl film has a negligible effect on the shear parameters [26]. Alternatively, it may be due to the choice in substrate for the simulation (Fe(100)). Since the experiment is carried out using an annealed polycrystalline substrate, the surface will likely expose different surfaces.

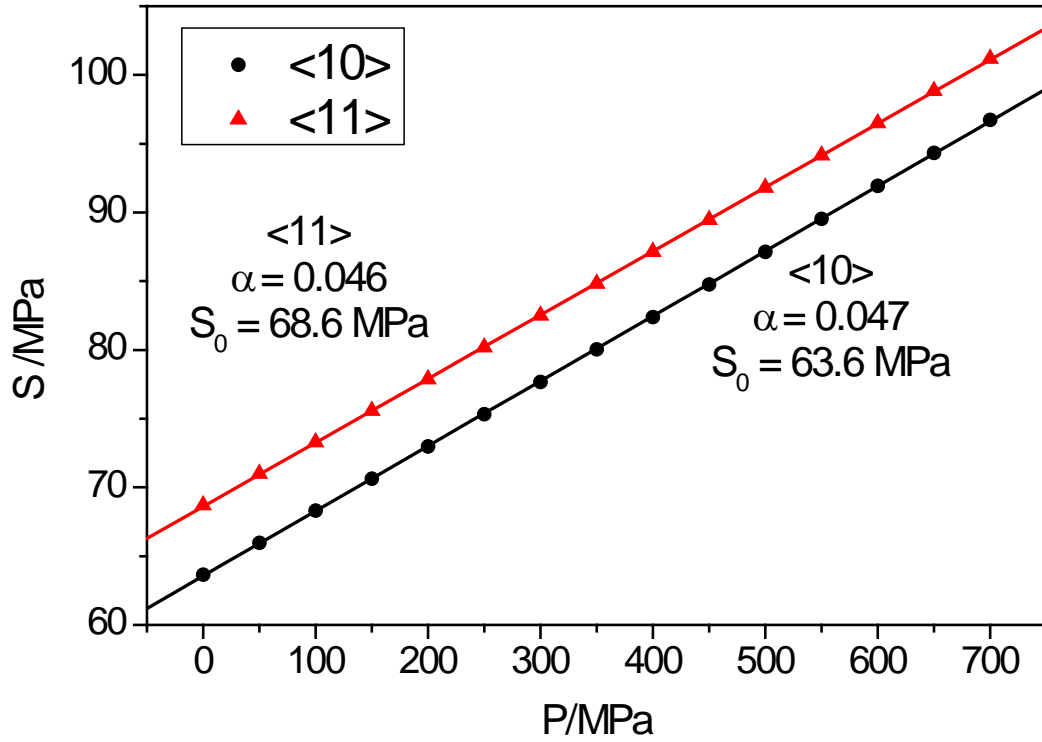


Figure 4.5: Calculated values of the pressure-dependent shear strength S for a bilayer KCl film on Fe(100) plotted as a function of pressure P for sliding along the $\langle 10 \rangle$ (●) and $\langle 11 \rangle$ (▲) directions.

Discrepancies might also arise since a Tomlinson/Prandtl model is used to calculate the friction force [23]. The friction force is calculated from the high-velocity limit as discussed in Reference 23. The high sliding speeds used in the experiment (4×10^{-3} m/s [24]) suggest that this condition should be fulfilled. The Tomlinson–Prandtl model also assumes that all of the energy is dissipated in surmounting the sliding potential and it has been suggested that this may not be the case [34]. However, at the sliding speed at which the data were collected (4×10^{-3} m/s), the time taken to transit a unit cell (of length 6.3×10^{-10} m) is ~ 0.15 μ s, which should be sufficiently long to dissipate essentially all of the energy.

Nevertheless, the results indicate that the value of S_0 arises from differences in binding energies of the KCl film at various sites on the iron substrate as found previously [23]. The pressure dependence is due to two effects. The first results in a linear variation in shear strength with contact pressure and arises due to the surface, atomic-scale corrugation that causes a vertical motion of the film. This effect has been identified previously from MD simulations using a Lennard-Jones 6–12 potential [14] and for organic films [3]. The second term arises from slightly different compliances of the film at different locations on the surface. This term is found to be significantly smaller than the corrugation term, at least for KCl on iron, leading to a linear dependence of the shear strength on pressure.

4.4 Conclusions

It is shown that first-principles DFT calculations are able to reasonably reproduce the parameters S_0 and α in the pressure-dependent shear strength of a simple model boundary film consisting of KCl, where the agreement with the experimental value of S_0 is excellent and with the value of α is reasonable. The system is modeled using a KCl bilayer enclosed between two Fe(100) slabs, where the energy varies harmonically as a function of the separation between the outermost layers. This enables a simple analytical model to be developed for the pressure-dependent shear strength of the film, which includes both linear and quadratic pressure dependences. However, it is found in the case of the KCl film, that the coefficient of the quadratic term is much lower than the linear term, leading to the linear shear-strength pressure dependence found experimentally.

Physically, this term arises because of the different heights of the film at different sites on the surface that requires additional external work to be done against the normal applied load. It is found that the most stable site occurs when the potassium and halide ions are located above iron atoms in the substrate due to bonding between iron and the halide ions, which is less favorable in other sites.

4.5 References

- [1] Bridgeman, P. W., Shearing phenomena at high pressures, particularly in inorganic compounds. *Proc. Am. Acad. Arts Sci.* **1986**, *71*, 387–460.
- [2] Briscoe, B. J.; Evans, D. C. B., The Shear Properties of Langmuir-Blodgett Layers. *Proceedings of the Royal Society of London. A. Mathematical and Physical Sciences* **1982**, *380* (1779), 389-407.
- [3] Sutcliffe, M. J.; Taylor, S. R.; Cameron, A., Molecular asperity theory of boundary friction. *Wear* **1978**, *51* (1), 181-192.
- [4] Singer, I. L.; Bolster, R. N.; Wegand, J.; Fayeulle, S.; Stupp, B. C., Hertzian stress contribution to low friction behavior of thin MoS₂ coatings. *Applied Physics Letters* **1990**, *57* (10), 995-997.
- [5] Schwarz, U. D.; Allers, W.; Gensterblum, G.; Wiesendanger, R., Low-load friction behavior of epitaxial C60 monolayers under Hertzian contact. *Physical Review B* **1995**, *52* (20), 14976-14984.
- [6] Briscoe, B. J.; Smith, A. C., The influence of dynamic loading on sliding friction. *Nature* **1979**, *278* (5706), 725-726.

- [7] Georges, J. M.; Mazuyer, D., Pressure effects on the shearing of a colloidal thin film. *Journal of Physics-Condensed Matter* **1991**, *3* (47), 9545-9550.
- [8] Riedo, E.; Gnecco, E.; Bennewitz, R.; Meyer, E.; Brune, H., Interaction potential and hopping dynamics governing sliding friction. *Physical Review Letters* **2003**, *91* (8).
- [9] Furlong, O. J.; Javier Manzi, S.; Daniel Pereyra, V.; Bustos, V.; Tysoe, W. T., Kinetic Monte Carlo theory of sliding friction. *Physical Review B* **2009**, *80* (15).
- [10] Harrison, J. A.; Gao, G.; Schall, J. D.; Knippenberg, M. T.; Mikulski, P. T., Friction between solids. *Philosophical Transactions of the Royal Society a-Mathematical Physical and Engineering Sciences* **2008**, *366* (1869), 1469-1495.
- [11] Mikulski, P. T.; Herman, L. A.; Harrison, J. A., Odd and even model self-assembled monolayers: Links between friction and structure. *Langmuir* **2005**, *21* (26), 12197-12206.
- [12] Gao, G. T.; Mikulski, P. T.; Harrison, J. A., Molecular-scale tribology of amorphous carbon coatings: Effects of film thickness, adhesion, and long-range interactions. *Journal of the American Chemical Society* **2002**, *124* (24), 7202-7209.
- [13] Mikulski, P. T.; Harrison, J. A., Packing-density effects on the friction of n-alkane monolayers. *Journal of the American Chemical Society* **2001**, *123* (28), 6873-6881.
- [14] He, G.; Robbins, M. O., Simulations of the kinetic friction due to adsorbed surface layers. *Tribology Letters* **2001**, *10* (1-2), 7-14.
- [15] Persson, B. N. J., *Sliding friction: physical principles and applications*. 2 ed.; Springer: Heidelberg, 2000.

- [16] Gao, J. P.; Luedtke, W. D.; Gourdon, D.; Ruths, M.; Israelachvili, J. N.; Landman, U., Frictional forces and Amontons' law: From the molecular to the macroscopic scale. *Journal of Physical Chemistry B* **2004**, *108* (11), 3410-3425.
- [17] Mo, Y.; Turner, K. T.; Szlufarska, I., Friction laws at the nanoscale. *Nature* **2009**, *457* (7233), 1116-1119.
- [18] Mo, Y.; Szlufarska, I., Roughness picture of friction in dry nanoscale contacts. *Physical Review B* **2010**, *81* (3).
- [19] Baroni, S.; Giannozzi, P.; Testa, A., Elastic constants of crystals from linear-response theory. *Physical Review Letters* **1987**, *59* (23), 2662-2665.
- [20] Jhi, S. H.; Louie, S. G.; Cohen, M. L.; Morris, J. W., Mechanical instability and ideal shear strength of transition metal carbides and nitrides. *Physical Review Letters* **2001**, *87* (7).
- [21] Ogata, S.; Li, J.; Hirotsaki, N.; Shibutani, Y.; Yip, S., Ideal shear strain of metals and ceramics. *Physical Review B* **2004**, *70* (10).
- [22] Shenoy, V. B.; Miller, R.; Tadmor, E. B.; Phillips, R.; Ortiz, M., Quasicontinuum models of interfacial structure and deformation. *Physical Review Letters* **1998**, *80* (4), 742-745.
- [23] Garvey, M.; Furlong, O. J.; Weinert, M.; Tysoe, W. T., Shear properties of potassium chloride films on iron obtained using density functional theory. *Journal of Physics-Condensed Matter* **2011**, *23* (26).
- [24] Gao, F.; Furlong, O.; Kotvis, P. V.; Tysoe, W. T., Pressure dependence of shear strengths of thin films on metal surfaces measured in ultrahigh vacuum. *Tribology Letters* **2008**, *31* (2), 99-106.

- [25] Filleter, T.; Paul, W.; Bennewitz, R., Atomic structure and friction of ultrathin films of KBr on Cu(100). *Physical Review B* **2008**, 77 (3).
- [26] Garvey, M.; Weinert, M.; Tysoe, W. T., On the film thickness dependence of shear strengths in sliding, boundary-layer friction. *Wear* **2012**, 274, 281-285.
- [27] Wu, G.; Gao, F.; Kaltchev, M.; Gutow, J.; Mowlem, J. K.; Schramm, W. C.; Kotvis, P. V.; Tysoe, W. T., An investigation of the tribological properties of thin KCl films on iron in ultrahigh vacuum: modeling the extreme-pressure lubricating interface. *Wear* **2002**, 252 (7–8), 595-606.
- [28] Weinert, M.; Schneider, G.; Podloucky, R.; Redinger, J. *Flair*.
<http://www.uwm.edu/~weinert/flair.html>.
- [29] Weinert, M.; Wimmer, E.; Freeman, A. J., Total-energy all-electron density functional method for bulk solids and surfaces. *Physical Review B* **1982**, 26 (8), 4571-4578.
- [30] Wimmer, E.; Krakauer, H.; Weinert, M.; Freeman, A. J., Full-potential self-consistent linearized-augmented-plane-wave method for calculating the electronic structure of molecules and surfaces: O₂ molecule. *Physical Review B* **1981**, 24 (2), 864-875.
- [31] Perdew, J. P.; Burke, K.; Ernzerhof, M., Generalized gradient approximation made simple. *Physical Review Letters* **1996**, 77 (18), 3865-3868.
- [32] Tomlinson, G. A., CVI. A molecular theory of friction. *Philosophical Magazine Series 7* **1929**, 7 (46), 905-939.

- [33] Prandtl, L., Ein Gedankenmodell zur kinetischen Theorie der festen Körper. *ZAMM - Journal of Applied Mathematics and Mechanics / Zeitschrift für Angewandte Mathematik und Mechanik* **1928**, 8 (2), 85-106.
- [34] Cannara, R. J.; Brukman, M. J.; Cimatu, K.; Sumant, A. V.; Baldelli, S.; Carpick, R. W., Nanoscale friction varied by isotopic shifting of surface vibrational frequencies. *Science* **2007**, 318 (5851), 780-783.

Chapter 5

Film Thickness Dependence of Shear Strengths in Sliding, Boundary-Layer Friction

5.1 Introduction

We have shown previously that the pressure-dependent shear properties of a thin, model boundary layer film consisting of KCl on iron can be calculated using first-principles density functional theory (DFT) [1-2]. First, in order to calculate the shear strength in the absence of an external load, three layers of KCl were placed on a seven layer thick iron slab [1] and the sliding potential was calculated using DFT by laterally displacing the outer layer of the KCl film and then allowing all of the other atoms in the slab to relax to their minimum energies. It was found that shear occurred at the KCl/Fe interface [1]. Thus, since the KCl slab moved rigidly with respect to the iron substrate, the height of the sliding potential for KCl on iron could be obtained without performing a full sliding calculation by simply calculating the energy of the slab located on various high-symmetry points on the surface, thereby resulting in a significant saving in computation time [1]. This simplification occurred because the shear force required to initiate sliding was much lower than the shear modulus of the halide film, with the result that the film was only minimally distorted during sliding, resulting in a shear plane located at the iron–KCl interface [1].

It has been shown experimentally in several cases that the shear strength varies linearly with contact pressure P and can be written as $S = S_0 + \alpha P$, where S_0 is the shear

strength at zero pressure and α is a proportionality constant [3-14]. Similar results have been found for the shear of bulk materials [15]. In particular, it was found experimentally, from friction measurements of a thin film of KCl on metal surfaces, that $S_0 = 65 \pm 5$ MPa and $\alpha = 0.14 \pm 0.02$ [16]. The experimental measurements were carried out for KCl deposited onto various metal substrates in ultrahigh vacuum where the background pressure was $\sim 1 \times 10^{-10}$ Torr. This ensured that the system was free of contaminants and that the frictional data were measured for a clean, continuous KCl film on an atomically clean metal substrate [16]. The metal foil substrates were all cleaned in ultrahigh vacuum and their cleanliness measured in situ using Auger spectroscopy ensuring that the initial substrates were also clean prior to KCl deposition. While the metal foil substrates were initially likely to be rather disordered, following the cleaning and vacuum annealing process, they are likely to become more ordered [17]. KCl is not used commercially as a boundary film, but it was chosen as a model since it is sufficiently simple that it is amenable to analysis by high-level, first-principles quantum calculations.

Based on the work discussed above for KCl on an iron substrate, it was subsequently possible to obtain a theoretical value of the pressure-dependent shear strength of a composite iron–KCl–iron sandwich by calculating the energy of the system as a function of applied pressure for various locations of the KCl slab with respect to the iron substrate, rather than having to carry out a more complex calculation in which the film was sheared while simultaneously imposing a normal load [2]. The calculation was carried out for two layers of KCl sandwiched between iron. The pressure dependence of the shear strength was calculated by compressing the slab from its equilibrium thickness

and by plotting the energy of the system as a function of the thickness of the iron–KCl–iron composite film. The energy was found to vary parabolically with film thickness and so was found to deform elastically over the range of pressures used in the experiment [16]. The normal pressure applied to the film was calculated from the first derivative of the plot of energy versus normal displacement. It was found that the resulting pressure dependence of the shear strength contained both linear (P^1) and quadratic (P^2) terms. The first pressure-dependent term arose from different equilibrium thicknesses of the film located at different positions on the substrate. This required additional work to be expended against the applied normal load, leading to a shear strength that depended linearly on pressure, in accord with the conclusions of previous work [3-9]. The second term arose from the slightly different compliances of the film located on different sites and resulted in a quadratic pressure dependence in the shear strength. It was found that this effect was much smaller than the one that resulted in the linear pressure dependence, thus proving a fundamental theoretical understanding of the experimentally observed linear dependence. The DFT calculations for a KCl bilayer sandwich gave $S_{0<10>} = 64 \pm 9$ and $S_{0<11>} = 69 \pm 8$ MPa, both in excellent agreement with experiment [2]. However, this calculation also predicted that both $\alpha_{<10>}$ and $\alpha_{<11>}$ had values of 0.05 ± 0.01 [2], somewhat lower than the experimentally measured value of 0.14 ± 0.02 [16]. As noted above, for computational economy, the DFT calculations were carried out using a KCl bilayer. One possible explanation for the difference between the experimental and theoretical values of α may be that it depends on the thickness of the KCl film, and this issue is explored in the following sections.

The model for determining the pressure-dependent shear strength exploited the harmonic variation in energy with slab thickness suggested by DFT calculations [2]. Extending this model to explicitly analyze the effect of film thickness on the pressure-dependent shear, the thickness of the film t at some contact pressure P is written as $P = Y(t - t_0)/(t_0)$, where Y is the Young's modulus of the material that forms the boundary film and t_0 is the film thickness at zero pressure. The values of Y and t_0 are obtained directly from the energy change as a function of slab thickness calculated by DFT as shown previously [2]. The shear dependence arises from differences in $t(\Delta t)$ at different locations of the film with respect to the substrate, so that the additional extra work carried out during sliding is $P\Delta t$. If a minimum and maximum in the sliding potential occur at points a and b , respectively, then the change in the film thickness during sliding is $t_b - t_a$. The above equation can be simply rewritten to give $t = t_0 + (Pt_0)/(Y)$. If the corresponding parameters at locations a and b are Y_a and t_0^a , and Y_b and t_0^b , respectively, then:

$$\Delta t = (t_b - t_a) = (t_0^b - t_0^a) + P \left(\frac{t_0^b}{Y_b} - \frac{t_0^a}{Y_a} \right) \quad (1)$$

The values of the film thickness and Young's modulus will vary depending on the location of the slab with respect to the substrate. In the case of KCl on iron, it was found that the energetically most stable – and also the geometrically lowest – site was that in which the potassium and chloride ions were located directly above an iron atom in the substrate. This is contrary to what might be expected based on a hard-sphere model, and arose because of chemical bonding between the iron atoms and the halide ions [1]. If the bonding between the film and the substrate is rather local, the thickness of the film might not be expected to strongly influence t_0 and Y . However, the second term explicitly

depends on the thickness of the film. Calculations for the bilayer slab revealed that the second term was much smaller than the first, thereby resulting in an overall linear variation of shear strength with pressure [2]. However, the existence of this term, and the possibility of longer-range bonding interactions warrant an examination of this effect.

5.2 Theoretical Methods

The KCl/Fe(100) system was previously modeled using a bilayer of KCl that was placed between Fe(100) slabs, which are seven iron layers thick [2] and the results are compared in the following to those for four layers of KCl placed between Fe(100) slabs. The calculations are performed for a (2×2) iron substrate cell with KCl placed epitaxially on the substrate and the calculations are carried out using periodic boundary conditions to mimic an infinite surface. This orientation is chosen since X-ray diffraction measurements of thicker KCl films have shown them to have a (100) orientation [18-19]. The calculated bulk lattice spacing for KCl of 0.627 nm agrees well with the experimental value of 0.629 nm. The experimental lattice spacing for iron is 0.287 nm, so that the lattice mismatch between KCl and iron is $\sim 11\%$. It is assumed in the calculation that the KCl film is strained to so that it is epitaxial with the iron substrate and the structure of the iron plus KCl system is optimized to yield the total energy. The structure of the iron–KCl–iron sandwich with four KCl layers used for the calculation is shown in Figure 5.1. Thus, the KCl film is strained to accommodate to the underlying iron lattice. Such pseudomorphic growth of strained films has been observed in other systems where the energy gain by forming an epitaxial film is larger than the energy

required to strain the lattice. As the films become thicker, the strain energy increases eventually resulting in a loss of epitaxy [20]. It has been shown previously that shear of the KCl/metal slab occurs at the film–metal interface since the shear modulus of the KCl film is larger than the shear strength of the interface [1]. Thus, such a configuration that uses the smallest (2×2) unit cell will lead to the maximum energy change due to shear between the film and substrate. The use of larger substrate unit cells that reduce the strain of the adsorbed film will result in lower heights of the sliding potentials and thus lower calculated shear strengths. Thus, a comparison of the calculated value of shear strength, in particular the value of S_0 (the shear strength at zero applied pressure) with the experimental value will provide information on the nature of the interface. The role of different asperity contact geometries on sliding has been simulated using molecular dynamics methods [21].

The effect of an applied normal load is modeled by varying the distance d between the outer layers of the iron slab (Figure 5.1); that is, by changing the distance between the topmost layer of the upper slab and the bottom layer of the lower slab. These outermost iron layers are chosen to be sufficiently far away from the sliding interface that they can be uniformly displaced to mimic an externally applied load. In addition, to maintain cyclic boundary conditions normal to the contacting surfaces, the slab for the DFT calculation contains two, symmetrically equivalent Fe–KCl interfaces.

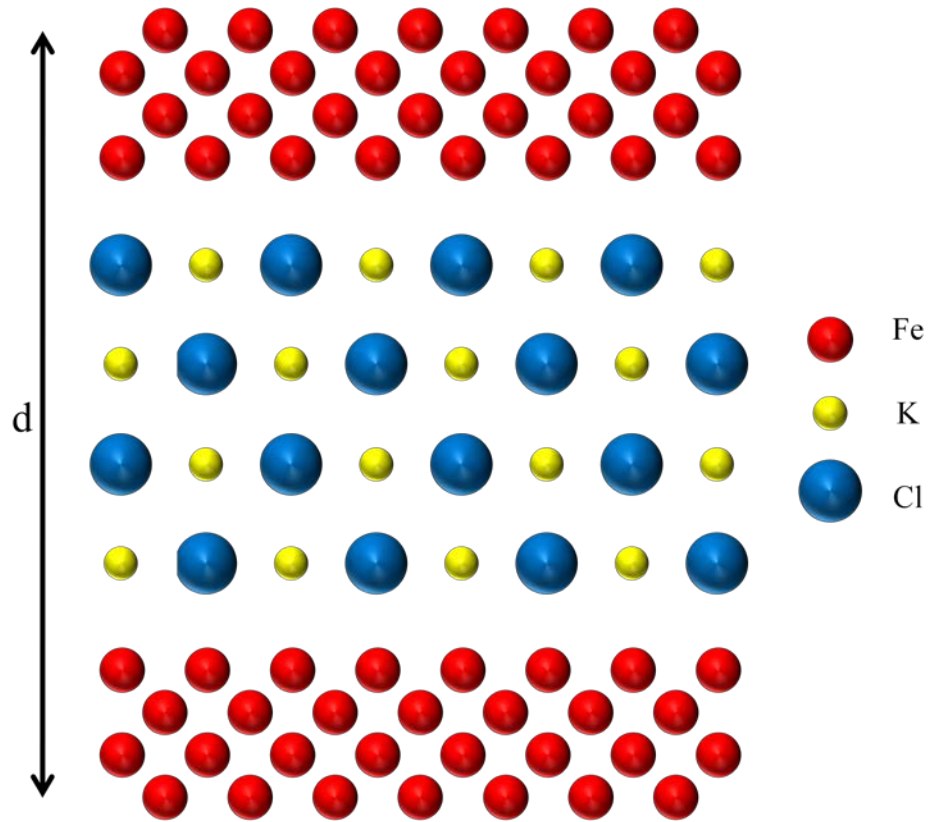


Figure 5.1: Depiction of the structure used for the density functional theory calculations showing four layers of KCl sandwiched between iron.

The energy of the slab was evaluated as a function of d using spin-polarized DFT calculations, which were performed by an implementation of the all-electron, full-potential linearized augmented-plane wave (FLAPW) method, *flair* [22-24] using the generalized gradient approximation (GGA) functional of Perdew et al. [25] for exchange-correlation and self-consistent convergence criteria of better than 10^{-5} eV. The geometry was optimized by allowing all atoms to relax until the forces on all unrestricted atoms were less than 10^{-2} eV/Å. The resulting plots of energy *versus* d are used to calculate the pressure-dependent shear strength and the strategy for accomplishing this is discussed below.

It was found previously that, for the KCl film on iron [1], the height of the sliding potential could be calculated from the energy of the slab located at high-symmetry points on the surface; the minimum and maximum energies at these positions correspond to turning points in the sliding potentials since the KCl layer was only minimally distorted during sliding. This occurs since shear occurs at the KCl–substrate interface as discussed above [1]. Accordingly, the calculations in this work were performed for a four-layer KCl film with the Cl^- and K^+ ions in the KCl layer located (i) above iron atoms in the substrate (designated *atop*), (ii) above bridge sites in the Fe(100) substrate (designated *bridge*) and (iii) above four-fold hollow sites in the substrate (designated *hollow*).

5.3 Results and Discussion

The shear of a model, four-layer KCl film sandwiched between iron slabs is compared with previous results for a two-layer slab to gauge the effect of film thickness on the shear properties of the film [2]. It was found previously for the two-layer slab that the value of S_0 calculated from the height of the sliding potential was in good agreement with experiment, while the predicted value of α was substantially lower than the experimentally measured value. In order to carry out DFT calculations most efficiently using periodic boundary conditions, it is assumed that the KCl film is commensurate (that is, is epitaxial) with the underlying iron and is modeled by a KCl slab on a (2×2) Fe(100) substrate. The resulting shear strength is taken to be directly proportional to the contact area. In the case of incommensurate interfaces, it has been shown that this assumption is not always valid [26-27]. The validity of the model and its underlying

assumptions are tested by comparing the theoretical predictions with experimental measurements of shear strength collected in ultrahigh vacuum for thin, well-characterized KCl films. Agreement between the calculated and measured values of shear strength will suggest that the assumptions made in the model are valid, at least for this particular system. Thus, the agreement between theory and experiment for the two-layer slab implies that the assumptions discussed above are valid for the model KCl boundary layer since it correctly reproduces the experimental value of S_0 . The discrepancy between the experimental and calculated values of α suggest that some modifications to the model are required that affect the value of α , while maintaining the key ingredients so that the value of S_0 remains unchanged. The following explores whether changing the film thickness can accomplish this since the experiments were performed by evaporating KCl onto metals substrates and by measuring the friction coefficient for films that just covered the substrate. However, because of the immobility of the halide film on the metal substrate, a second layer forms prior to completely saturating the first layer [19].

	E_0 (10^{-14} J)	d_0 (Å)	Y (Pa)
Atop	4.811837846	13.263	4.8635
Bridge	4.811837567	13.337	4.7658
Hollow	4.811837435	13.374	4.7196

Table 5.1: Harmonic potential fitting parameters to the data displayed in Figures 5.2 and 5.3.

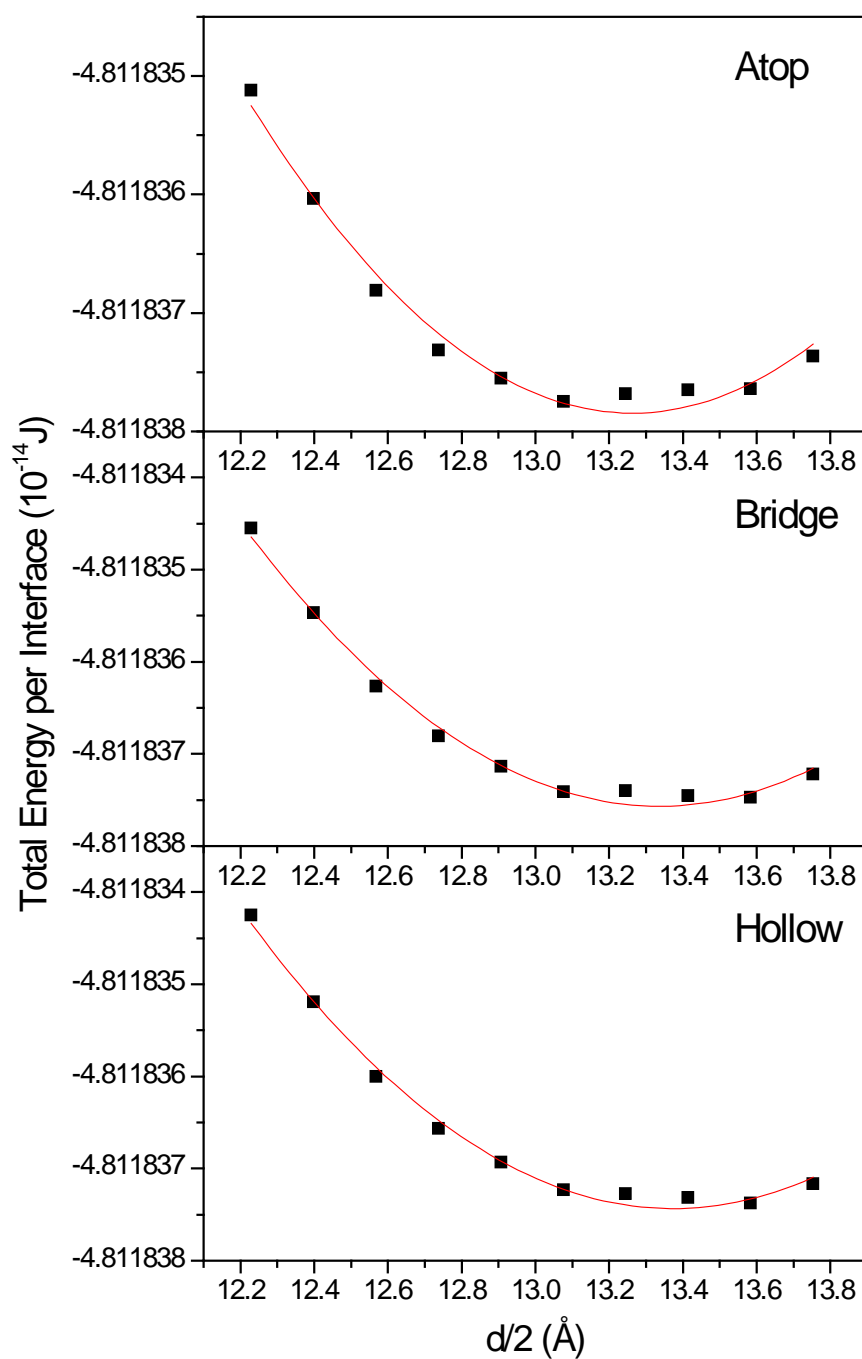


Figure 5.2: Plot of the energy of a four-layer KCl slab sandwiched between iron as a function of $d/2$, where d is the distance between the outermost edges of the slab. Results are shown for potassium and chloride ions on the KCl located on atop (top), bridge (middle), and hollow (bottom) sites on the iron substrate. Lines are harmonic potential fits to the data. (Fitting parameters are given in Table 5.1.)

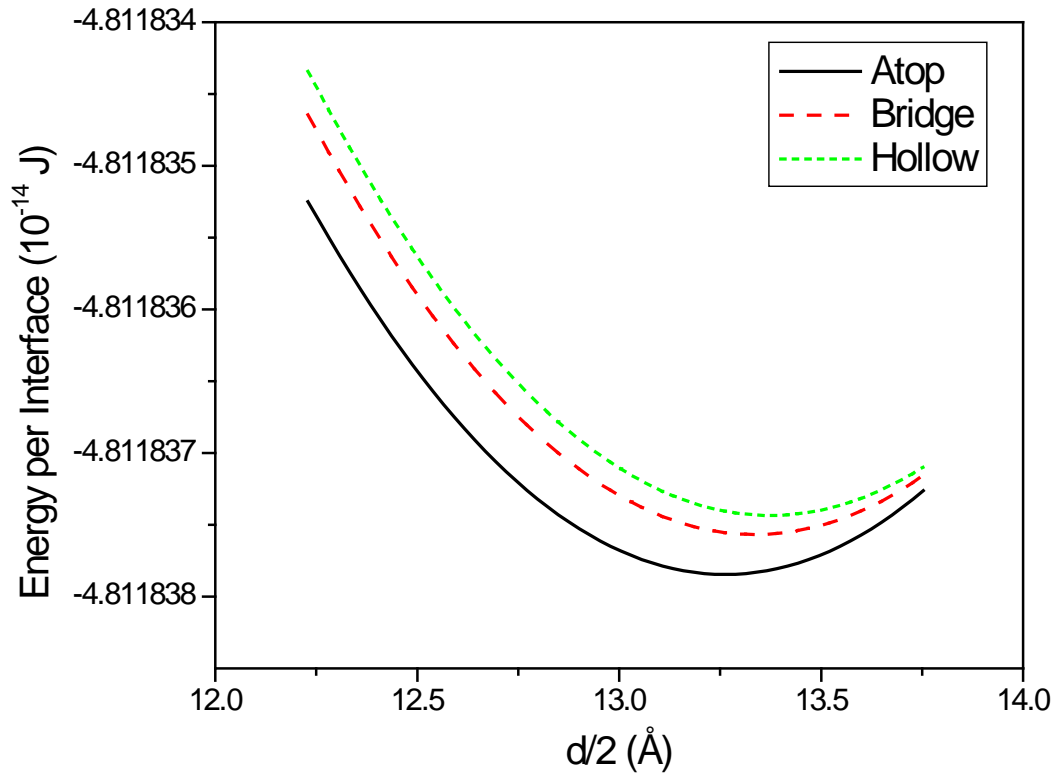


Figure 5.3: Plots of the fits to the results of the calculations shown in Figure 5.2 for the potassium and chloride ions on the KCl located on *atop*, *bridge* and *hollow* sites on the iron substrate. (Fitting parameters are given in Table 5.1.)

The potential energy curves as a function of $d/2$ (to take account of the presence of two interfaces in the model) for a four-layer KCl film placed between Fe(100) slabs are shown in Figure 5.2 for the potassium and chloride ions located at (a) *atop*, (b) *bridge* and (c) *hollow* positions. These are fit to a harmonic potential [2] and the fits are shown as solid lines through the data points and the resulting fitting parameters are summarized in Table 5.1. The resulting fits are replotted together on the same scale in Figure 5.3 for direct comparison. This reveals that the potential energy curves for the halide films located at different positions with respect to the surface are different, which gives rise to the pressure-dependent sliding potential as the atoms slide over each other. This

indicates that, as was found for the bilayer KCl film, the film is most stable when the potassium and chloride ions are located above iron atoms in the substrate. In the case of the bilayer films, this was found to be predominantly due to some bonding between the Cl^- ions in the film and the iron atoms in the substrate [1]. This bonding interaction was stronger at the atop sites than when the halide ions were located over bridge or four-fold sites. The different energies at the minima of the potentials yield pressure-independent sliding potentials, and thus values of S_0 . In addition, the value of $d/2$ at the minima of each of the potentials is different giving rise to different thicknesses of the film at different locations of the KCl slab with respect to the iron substrate. Additional work must be expended against the normal force to overcome this energy. Finally, the shapes of the curves are slightly different, resulting in slightly different Young's moduli of the film at different sites, corresponding to the second term in Equation (1). These effects give rise to a pressure-dependent energy difference while sliding from site a to b as:

$$\Delta E = (E_b - E_a) + P(t_0^b - t_0^a) + P^2 \left(\frac{t_0^b}{Y_b} - \frac{t_0^a}{Y_a} \right) \quad (2)$$

and thus predicts both a linear and a quadratic pressure dependence in the sliding potential.

The data in Figure 5.3 indicate, as noted above for the bilayer KCl film, that the *atop* location of the potassium and chloride ions is the most stable. Thus, the heights of the sliding potentials are calculated for sliding *via* the *bridge* site (from an *atop* to a *bridge* to an *atop* site, along the $\langle 10 \rangle$ direction), or *via* the *hollow* site (from an *atop* to a *hollow* to an *atop* site, along $\langle 11 \rangle$) and was done previously [2]. The pressure-dependent height of the potential as a function of normal pressure P is plotted in Figure 5.4, up to 700 MPa corresponding to the hardness of iron [28]. The linear terms (■) for sliding

along the $\langle 10 \rangle$ and $\langle 11 \rangle$ directions are shown and the corrections to those values arising from the quadratic terms in Equation (2) are also plotted (\bullet). As was found for the bilayer slab, the quadratic part of the sliding potential is much smaller than the linear part. Thus, the majority of the external work is expended in overcoming the atomic-scale roughness of the surface, and the differences in compliances at different slab locations, although they do play a role, are rather minor.

The resulting sliding potentials (Equation (2)) are used to calculate the shear strength as a function of pressure [2] and the results are displayed in Figure 5.5. Because the second term in Equation (2) is small, this results in a linear variation of shear strength with pressure, thereby enabling the values of S_0 and α to be calculated from the intercept and slopes of the curves, respectively. Note that, in spite of the quite large differences in the heights of the sliding potentials (Figure 5.4), the pressure-dependent shear strength curves are quite similar leading to rather isotropic shear for the Fe–KCl interface. This occurs because the differences in heights of the potentials are compensated by the different lattice periodicities along the $\langle 10 \rangle$ and $\langle 11 \rangle$ directions. The calculated values for the four-layer KCl slab are $S_{0\langle 10 \rangle} = 62 \pm 15$ and $S_{0\langle 11 \rangle} = 65 \pm 11$ MPa while $\alpha_{\langle 10 \rangle}$ and $\alpha_{\langle 11 \rangle} = 0.06 \pm 0.01$. The corresponding values for the bilayer slab are $S_{0\langle 10 \rangle} = 64 \pm 9$, $S_{0\langle 11 \rangle} = 69 \pm 8$ MPa, and $\alpha_{\langle 10 \rangle}$ and $\alpha_{\langle 11 \rangle}$ equal 0.05 ± 0.01 [2]. Within the error limits, the values for the bilayer and four-layer KCl slabs are identical and both are in reasonable agreement with the experimental values of $S_0 = 65 \pm 5$ MPa and $\alpha = 0.14 \pm 0.02$, although again the calculated values of α are somewhat lower than the experimental value.

The shear properties along the $\langle 10 \rangle$ and $\langle 11 \rangle$ directions are identical within experimental error suggesting that the calculated shear properties of the KCl film are isotropic. Since the experiments were carried out using annealed metal foil substrates [16], in principle, the shear properties should be averaged over all substrates orientations for the theoretical data to be compared with experiment. Since, in the case of the KCl film, the shear is isotropic, such averaging is not necessary in this case, although this is likely not to be generally true for other films.

The calculated values of S_0 and α indicate that the thickness of the alkali halide (in this case, KCl) slab has a negligible effect on the shear properties of the film. Equation (2) suggests that there should be an explicit dependence on films thickness in the quadratic term but the results in Figure 5.3 indicate that this term is much smaller than the linear term, so that its overall contribution to the pressure-dependent shear strength (at least for a model KCl film) is negligible. The results also suggest that both the pressure independent part of the potential (that yields S_0) and the linear pressure-dependent term (that yields α) are not strongly affected by changing the thickness of the film implying that the interaction between the slab and the substrate is dominated by local effects.

Thus, while the calculated value of α is not in good agreement with experiment, suggesting that other sources for this discrepancy should be sought, the values of S_0 do agree with experiment. As discussed above, the calculations assume that the KCl film is in registry with the iron substrate [2]. This enables calculations to be carried out using periodic boundary conditions as required for the DFT calculations and the assumption to be made that the lateral friction force scales with contact area. It could be argued that the discrepancy between the calculated and measured values of α arises because the interface

is not commensurate. This, however, would result in lower values of S_0 , whereas the calculated and experimental values are in good agreement, suggesting that the commensurate model is valid.

5.4 Conclusions

First-principles DFT calculations are used to determine the shear properties of four-layer KCl films sandwiched between slabs of iron by considering the potential energy curves calculated for a KCl film located at high-symmetry sites with respect to the iron substrate. These calculations are compared to similar ones for bilayer slabs in order to gauge the effects of film thickness on the shear properties. The resulting calculated values for the four-layer slab are $S_{0<10>} = 62 \pm 15$ and $S_{0<11>} = 65 \pm 11$ MPa, and $\alpha_{<10>} = 0.06 \pm 0.01$ and $\alpha_{<11>} = 0.06 \pm 0.01$. These values are in excellent agreement with previous results for the bilayer slab and in reasonable agreement with experiment. These results suggest that the slab thickness does not have a profound effect on the tribological properties of the film, and that the local bonding between the KCl slab and the iron substrate plays an important role. The results further imply that the assumptions of the model, namely that the film is in registry with the substrate is true for the tribological interface.

5.5 References

- [1] Garvey, M.; Furlong, O. J.; Weinert, M.; Tysoe, W. T., Shear properties of potassium chloride films on iron obtained using density functional theory. *Journal of Physics-Condensed Matter* **2011**, *23* (26).
- [2] Garvey, M.; Weinert, M.; Tysoe, W. T., On the Pressure Dependence of Shear Strengths in Sliding, Boundary-Layer Friction. *Tribology Letters* **2011**, *44* (1), 67-73.
- [3] Briscoe, B. J.; Evans, D. C. B., The Shear Properties of Langmuir-Blodgett Layers. *Proceedings of the Royal Society of London. A. Mathematical and Physical Sciences* **1982**, *380* (1779), 389-407.
- [4] Sutcliffe, M. J.; Taylor, S. R.; Cameron, A., Molecular asperity theory of boundary friction. *Wear* **1978**, *51* (1), 181-192.
- [5] Singer, I. L.; Bolster, R. N.; Wegand, J.; Fayeulle, S.; Stupp, B. C., Hertzian stress contribution to low friction behavior of thin MoS₂ coatings. *Applied Physics Letters* **1990**, *57* (10), 995-997.
- [6] Schwarz, U. D.; Allers, W.; Gensterblum, G.; Wiesendanger, R., Low-load friction behavior of epitaxial C₆₀ monolayers under Hertzian contact. *Physical Review B* **1995**, *52* (20), 14976-14984.
- [7] Briscoe, B. J.; Smith, A. C., The influence of dynamic loading on sliding friction. *Nature* **1979**, *278* (5706), 725-726.

- [8] Riedo, E.; Gnecco, E.; Bennewitz, R.; Meyer, E.; Brune, H., Interaction potential and hopping dynamics governing sliding friction. *Physical Review Letters* **2003**, *91* (8).
- [9] Furlong, O. J.; Javier Manzi, S.; Daniel Pereyra, V.; Bustos, V.; Tysoe, W. T., Kinetic Monte Carlo theory of sliding friction. *Physical Review B* **2009**, *80* (15).
- [10] Harrison, J. A.; Gao, G.; Schall, J. D.; Knippenberg, M. T.; Mikulski, P. T., Friction between solids. *Philosophical Transactions of the Royal Society a-Mathematical Physical and Engineering Sciences* **2008**, *366* (1869), 1469-1495.
- [11] Mikulski, P. T.; Herman, L. A.; Harrison, J. A., Odd and even model self-assembled monolayers: Links between friction and structure. *Langmuir* **2005**, *21* (26), 12197-12206.
- [12] Gao, G. T.; Mikulski, P. T.; Harrison, J. A., Molecular-scale tribology of amorphous carbon coatings: Effects of film thickness, adhesion, and long-range interactions. *Journal of the American Chemical Society* **2002**, *124* (24), 7202-7209.
- [13] Mikulski, P. T.; Harrison, J. A., Packing-density effects on the friction of n-alkane monolayers. *Journal of the American Chemical Society* **2001**, *123* (28), 6873-6881.
- [14] He, G.; Robbins, M. O., Simulations of the kinetic friction due to adsorbed surface layers. *Tribology Letters* **2001**, *10* (1-2), 7-14.
- [15] Bridgeman, P. W., Shearing phenomena at high pressures, particularly in inorganic compounds. *Proc. Am. Acad. Arts Sci.* **1986**, *71*, 387-460.

- [16] Gao, F.; Furlong, O.; Kotvis, P. V.; Tysoe, W. T., Pressure dependence of shear strengths of thin films on metal surfaces measured in ultrahigh vacuum. *Tribology Letters* **2008**, *31* (2), 99-106.
- [17] Furlong, O.; Miller, B.; Tysoe, W., Shear-Induced Surface-to-Bulk Transport at Room Temperature in a Sliding Metal–Metal Interface. *Tribology Letters* **2011**, *41* (1), 257-261.
- [18] Gao, F.; Kotvis, P. V.; Tysoe, W. T., The frictional properties of thin inorganic halide films on iron measured in ultrahigh vacuum. *Tribology Letters* **2003**, *15* (3), 327-332.
- [19] Gao, F.; Kotvis, P. V.; Tysoe, W. T., The frictional behavior of thin halide films on iron. *Tribology Transactions* **2004**, *47* (2), 208-217.
- [20] Bauer, E., Epitaxy of metals on metals. *Applications of Surface Science* **1982**, *11–12* (0), 479-494.
- [21] Luan, B. Q.; Robbins, M. O., The breakdown of continuum models for mechanical contacts. *Nature* **2005**, *435* (7044), 929-932.
- [22] Wimmer, E.; Krakauer, H.; Weinert, M.; Freeman, A. J., Full-potential self-consistent linearized-augmented-plane-wave method for calculating the electronic structure of molecules and surfaces: O₂ molecule. *Physical Review B* **1981**, *24* (2), 864-875.
- [23] Weinert, M.; Wimmer, E.; Freeman, A. J., Total-energy all-electron density functional method for bulk solids and surfaces. *Physical Review B* **1982**, *26* (8), 4571-4578.

- [24] Weinert, M.; Schneider, G.; Podloucky, R.; Redinger, J., FLAPW: applications and implementations. *Journal of Physics-Condensed Matter* **2009**, *21* (8).
- [25] Perdew, J. P.; Burke, K.; Ernzerhof, M., Generalized gradient approximation made simple. *Physical Review Letters* **1996**, *77* (18), 3865-3868.
- [26] Muser, M. H., Structural lubricity: Role of dimension and symmetry. *Europhysics Letters* **2004**, *66* (1), 97-103.
- [27] Muser, M. H.; Wenning, L.; Robbins, M. O., Simple microscopic theory of Amontons's laws for static friction. *Physical Review Letters* **2001**, *86* (7), 1295-1298.
- [28] Wu, G.; Gao, F.; Kaltchev, M.; Gutow, J.; Mowlem, J. K.; Schramm, W. C.; Kotvis, P. V.; Tysoe, W. T., An investigation of the tribological properties of thin KCl films on iron in ultrahigh vacuum: modeling the extreme-pressure lubricating interface. *Wear* **2002**, *252* (7-8), 595-606.

Chapter 6

Pressure Dependence of the Shear Strengths of the Tungsten Carbide–Potassium Chloride Interface

6.1 Introduction

First-principles density functional theory (DFT) calculations have been used to explore sliding friction [1-11], in particular, to understand the experimentally observed pressure-dependent shear strength of model KCl boundary films grown on metal substrates [12-15]. In the experiments, it was found that the shear strength S varied linearly with contact pressure P as $S = S_0 + \alpha P$, with the parameters $S_0 = 65 \pm 5$ MPa and $\alpha = 0.14 \pm 0.02$ for KCl films [16]. The contact pressure was varied by changing the substrate. For the tungsten carbide tribopair used in the experiment, it was demonstrated that the tips of the contacting asperities deformed plastically thereby allowing the contact pressure to be equated to the hardness of the substrate material, H_S [17]. The shear strength was obtained by plotting the friction coefficient versus $1/H_S$; a linear dependence was found, and the parameters S_0 and α were obtained from a fit to the experimental data [16].

The value of S_0 was previously calculated using DFT for a conventional slab geometry in which a thin KCl film was in registry with a Fe(001) substrate. This orientation was chosen based on X-ray diffraction results of the KCl film [18]. In the calculation, the outer layer of the KCl slab was displaced laterally, while all of the other atoms in the KCl slab and the iron substrate were allowed to relax to their equilibrium

positions. It was found that the KCl slab moved rigidly over the iron substrate; shear occurred between the KCl and the iron, since the shear modulus of KCl is much larger than the shear strength of the interface. This conclusion allowed the height of the sliding potential in various sliding directions to be efficiently calculated from the energies of the slab located at various high-symmetry positions with respect to the substrate, without having to calculate the full sliding potential. This approach yielded a value of S_0 that was in reasonable agreement with experiment [10-11].

The observation that the heights of the sliding potentials could be calculated from the energies of the slab located at high-symmetry sites with respect to the substrate was exploited to calculate the pressure dependence of the shear strength. Since pressure-dependent shear strengths have been proposed from experiment [19-25] and invoked by theory [26-31], these calculations were performed with the dual goals of understanding the origin of the pressure dependence and to attempt to quantitatively reproduce the experimental values of the parameters S_0 and α . The calculations were performed using a configuration in which a KCl slab was sandwiched between two iron slabs [10]. The distance d between the outermost iron layers was varied to mimic the effect of an applied normal load and the energy of the slab, located at various high-symmetry points on the surface, was calculated as a function of d . The energy was found to vary harmonically over the pressure ranges expected in a tribological contact on metal substrates. The differences in the energies at the minima of the potentials were used to calculate S_0 , again yielding values in good agreement with experiment. It was also found that the vertical positions at the minima in the potentials were different for slabs located at different sites on the surface. Such a corrugation of the surface Δd results in additional work being

carried out against the normal pressure P , equal to $P\Delta d$, resulting in the experimentally observed linear variation in shear strength with pressure [16]. It was also found that the compliance of the film varied slightly when the slab was located at different high-symmetry positions on the surface, which would lead to a quadratic pressure dependence. However, this effect was found to be much smaller than the linear term, resulting in an overall linear pressure dependence of the shear strength, as found experimentally. The resulting values of α calculated by DFT methods ($\alpha_{\langle 10 \rangle}$ and $\alpha_{\langle 11 \rangle}$ equal 0.05 ± 0.01) were lower than, but within the same range as the experimental value of $\alpha = 0.14 \pm 0.02$.

The DFT calculations were performed using periodic boundary conditions, thereby requiring that the KCl film be in registry with the substrate. The agreement between experiment and theory implies that this is a reasonable approximation for the case of a KCl boundary film. Calculations for an interface with the atoms in registry yield an upper limit to the shear strength since all of the atoms in contact move over the sliding potential simultaneously. For an incommensurate interface, however, different atoms at the interface ride over the potentials at different positions, thereby lowering the shear strengths. If this occurred in the experiment, the calculated shear strength would have been much higher than that measured experimentally. In addition, a lack of commensurability between the atoms in the contacting interface would lead to a shear strength that does not scale linearly with contact area [32-35], an assumption implicit in our calculations.

Since the results of the calculations revealed that shear occurred between the metal (in the case of the calculations, iron) and the KCl film, this would lead to KCl being transferred to the tribopin, which is not found experimentally [12]. Furthermore, if

shear occurred between the film and the substrate, the shear strength would be expected to depend on the details of the bonding between the film and substrate, while it does not appear to do so. Also, the contact area between the film and substrate is much larger than that between the tribopin and the outermost surface of the film. If the shear strengths of the two interfaces are comparable, the tip-film contact will shear in preference to that between the film and substrate. Shear between the tip and film would account for the lack of sensitivity of the shear strength to the nature of the bonding between the film and substrate since sliding is controlled by the interaction between the tip and the film surface, which is the same for all experiments. In view of these considerations, the following explores the pressure-dependent shear strength of the tungsten carbide–KCl contact, using similar strategies as those developed for the KCl–Fe interface [10]. Thus, a bilayer film of KCl is sandwiched between slabs of tungsten carbide and the energy is calculated as a function of the separation between the outermost layers of the slab for KCl located at various high-symmetry points on the tungsten carbide surface. These are then fit to harmonic potentials to obtain pressure-dependent sliding potentials, which are in turn used to calculate pressure-dependent shear strengths for comparison with experiment.

The structure of tungsten carbide has been explored previously using DFT calculations [36-40]. This work is mainly concerned with the interactions between tungsten carbide and potassium chloride, and therefore will not attempt to verify the properties of bulk tungsten carbide beyond the necessary determination of the optimum lattice parameters.

6.2 Theoretical Methods

The size of the quasi-commensurate supercell needed to model the interface between the most stable, hexagonal (0001) face of WC and cubic (001) face of the rock salt structure of KCl renders it too computationally expensive to calculate, especially since each high-symmetry site requires multiple calculations to determine the pressure dependence of the energies at various sites. Work therefore focuses on the $(1\bar{1}00)$ and $(10\bar{1}0)$ faces of WC which have almost square surface unit cells since the c/a ratio of WC is close to unity [41]. The locations of the two planes with respect to the basal plane are illustrated in Figure 6.1. Due to the periodic boundary conditions, a stacking fault is introduced in the middle of the WC layer to insure that both KCl/WC interfaces within a cell are identical.

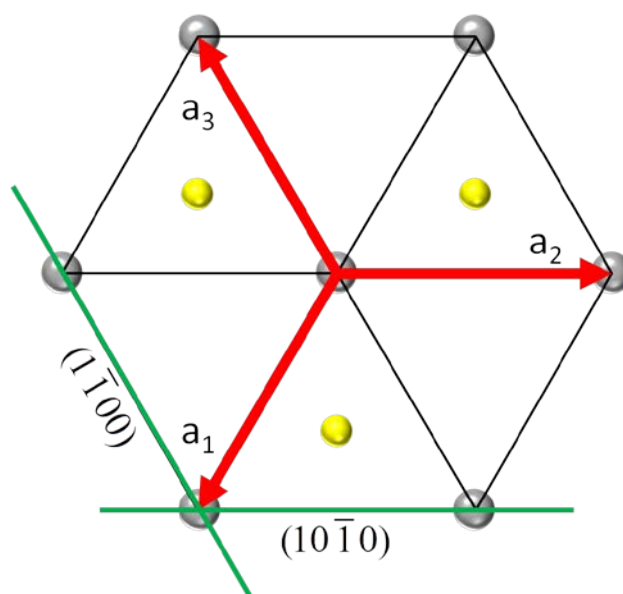


Figure 6.1: Locations of the $(1\bar{1}00)$ and $(10\bar{1}0)$ planes of WC shown with respect to the basal plane of WC. Larger silver and smaller yellow spheres indicate W and C atoms respectively.

The method used previously for calculating the pressure dependence of the sliding potentials for the Fe(001)/KCl system [10] is used here for the two WC/KCl interfaces. In this method, a bilayer of KCl is inserted between five-layer supercells of WC, and the energy calculated as a function of the spacing between the outermost layers d to mimic the imposition of a contact pressure. A schematic of WC/KCl/WC sandwich is shown in Figure 6.2. The total energy calculated for the system is divided by two to account for the fact that there are two identical WC/KCl interfaces per supercell. This total energy per interface is then plotted as a function of $d/2$ to mimic the effect of a normal load on the sliding potential.

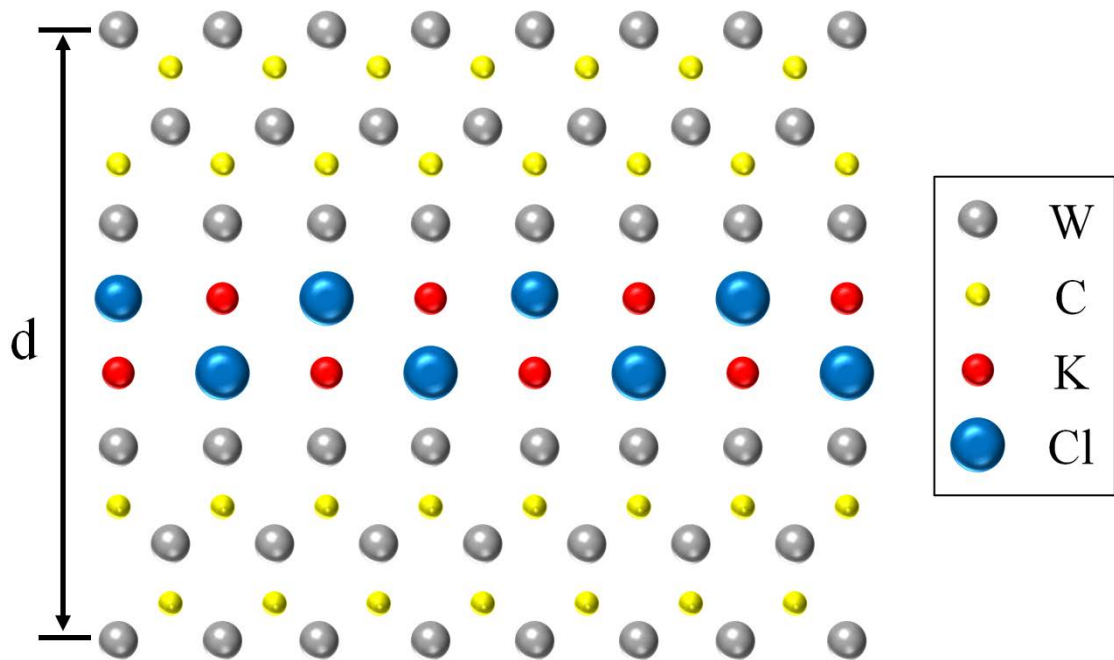


Figure 6.2: A schematic depiction of a KCl bilayer enclosed between two, tungsten carbide slabs where the KCl slab has the (100) plane in contact with the WC layers, and the WC surface exposes either the $(1\bar{1}00)$ or $(10\bar{1}0)$ planes. The application of an external load is simulated by changing the distance d between the outermost tungsten layers in the composite slab.

All DFT calculations were performed with *flair* [42-44], which is an implementation of the all-electron, full-potential linearized augmented-plane wave (FLAPW) method. The generalized gradient approximation (GGA) functional of Perdew et al. [45] is used for exchange–correlation and self-consistent convergence criteria of better than 3×10^{-5} eV were used. The geometries were considered to be converged when the forces on all atoms were $<3 \times 10^{-3}$ eV/Å .

6.3 Results

The calculated structure of the hexagonal tungsten carbide unit cell is compared with the results of previous calculations [36-40] and the experimental lattice spacing [41] in Table 6.1. The values of the a and c lattice parameters are in good agreement with previous calculations and experiment. The resulting value of the ratio c/a is close to unity and yields the pseudo-square unit cell on the $(1\bar{1}00)$ and $(10\bar{1}0)$ faces of WC.

A KCl bilayer slab (Figure 2) is then placed at various sites between WC slabs, with the separation between the outer layers set to some value d (Figure 2). It has been demonstrated previously that the calculated shear strengths do not depend strongly on the thickness of the KCl layer, warranting the use of a bilayer in the calculations used here [11]. The high-symmetry sites selected for the calculation are indicated in Figure 3 for the $(1\bar{1}00)$ (Figure 6.3a) and $(10\bar{1}0)$ (Figure 6.3b) tungsten carbide faces. Calculations were performed for the potassium and chloride ions located at atop tungsten sites (A(W)), bridge sites that have carbon atoms below (B(C)), bridge sites with tungsten atoms below (B(W)), and for a hollow site (H).

	a (Å)	c (Å)	c/a
Present work	2.94	2.88	0.98
DFT [36]	2.92	2.84	0.97
DFT [37]	2.932	2.853	0.973
DFT [38]	2.915	2.839	0.974
DFT [39]	2.92	2.85	0.98
DFT [40]	2.979	2.905	0.975
Experimental [41]	2.907	2.837	0.976

Table 6.1: The lattice parameters of hexagonal tungsten carbide calculated using DFT compared with the results of previous DFT calculations and the experimental values.

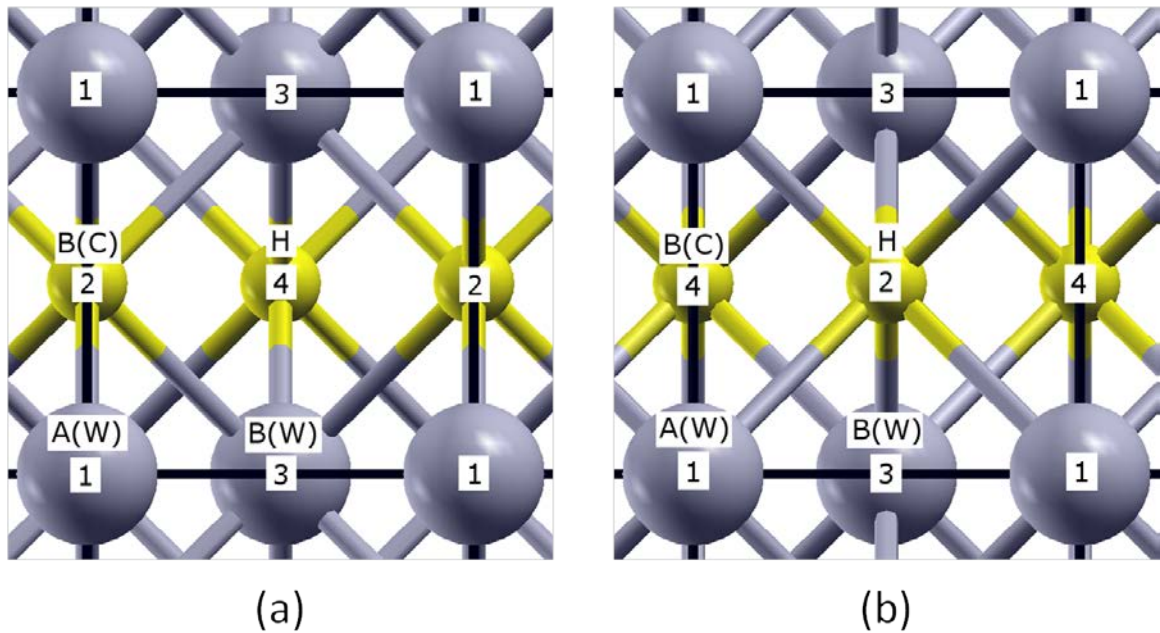


Figure 6.3: Top view of (a) the $(1\bar{1}00)$ and (b) the $(10\bar{1}0)$ tungsten carbide faces. The high-symmetry sites for potassium and chloride ions for which the calculations are performed are indicated as A(W) for an atop tungsten site, B(C) for a bridge site that has a carbon atom below it in the lattice, B(W) for a bridge site that has a tungsten atom below it, and H for a hollow site. Each atom is numbered from 1 to 4 to indicate the layer in which the atom is located (e.g. tungsten atoms labeled as 1 are at the surface, atoms with 2, 3 or 4 are in the second, third or fourth layer below the surface respectively). Larger silver and smaller yellow spheres indicate W and C atoms respectively.

The results for the energy change of the system as a function of $d/2$ (where the division takes account of the presence of two WC slabs) for the ions in the KCl slab located at various sites (as indicated in Figure 6.3a) are displayed in Figure 6.4 for adsorption on the $(1\bar{1}00)$ face. It is found that the majority of the compression occurs at the interface between the KCl film and the WC substrate and within the KCl film itself. The W–K bond length changes by $\sim 19\%$ at the largest compression and the W–Cl bond by $\sim 13\%$. The K–Cl bond within the film changes by $\sim 11\%$ under similar compressions. The change in interlayer spacing of the topmost layer of the WC is $< 1\%$ reflecting the much higher elastic modulus of WC than KCl, and the lower layers of the WC substrate shift by a negligible amount. This implies that the use of five layers of WC to model the substrate should be sufficient to mimic its bulk properties.

The calculations were also performed with a fixed lattice substrate lattice constant. In principle, the in-plane dimensions of the substrate could relax with the application of a normal force. However, these small displacements of the much less compliant WC substrate suggest that this should be negligible.

The shapes of the energy change versus vertical displacement were fit to harmonic and Morse potentials. As found previously for KCl located between iron films [10], in all cases the energy is well fit by a harmonic potential, indicating that the films deform elastically under load, where the energy is given by $E(d) = E_0 + \frac{k}{2}(d - d_0)^2$, where E_0 is the minimum energy at the position d_0 and k is a force constant. Corresponding plots for the KCl film located between WC slabs at various sites on the $(10\bar{1}0)$ face (as indicated in Figure 6.3b) are displayed in Figure 6.5. Again, this shows harmonic behavior and fits to the data are again indicated by solid lines.

6.4 Discussion

The general behavior of the KCl bilayer slab sandwiched between WC is similar to that found for KCl sandwiched between iron [9-11] and shows elastic behavior as a function of separation between the outermost layers of the slab (Figures 6.4 and 6.5). The fits to the data shown in Figure 6.4 (for the ions in the KCl layer contacting the $(1\bar{1}00)$ face of WC) are combined in Figure 6.6 to facilitate comparison between the plots. This clearly shows that the energies (given by the minima of the potentials) are different for KCl located at different sites, with KCl located at the A(W) (the potassium and chloride ions located above a tungsten site, Figure 6.3a) being the most stable. The energy differences between this site and the other sites on the surface are given in Table 6.2. This corrugation in the sliding potential energy gives rise to the pressure-independent part of the shear strength (S_0). Figure 6.6 also clearly shows differences in the values of d at which this minimum occurs. Thus, as the atoms slide over each other at the interface, this also leads to different equilibrium spacings and the change in the value, Δd requires extra work to be done against the applied normal load, leading to a pressure-dependent shear strength and the value of α .

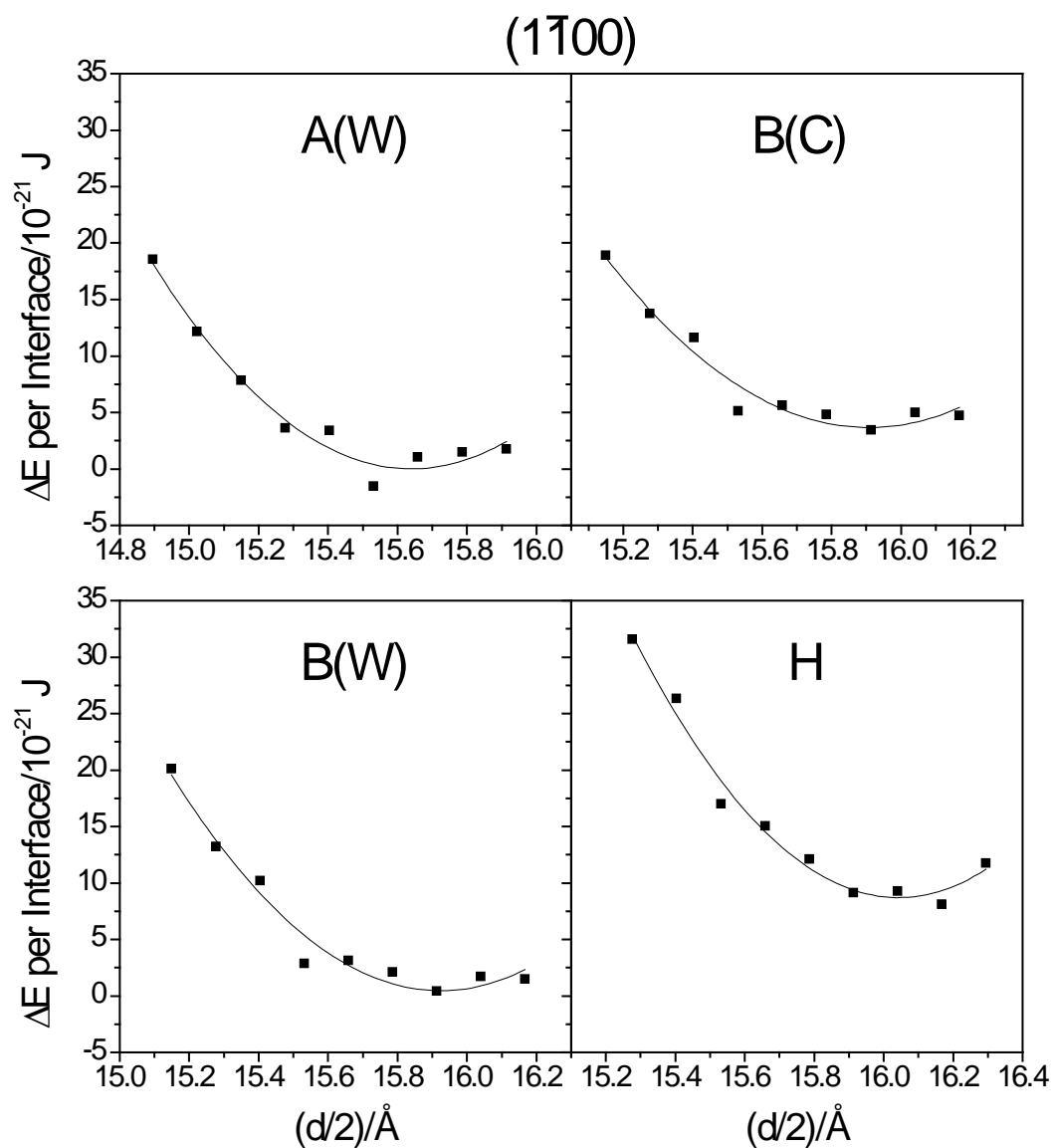


Figure 6.4: Plot of the total energy of the KCl+tungsten carbide composite slab as a function of half of the separation between the outermost tungsten carbide layers $d/2$ for a KCl(100) slab located on various sites with respect to the WC (1100) surface.

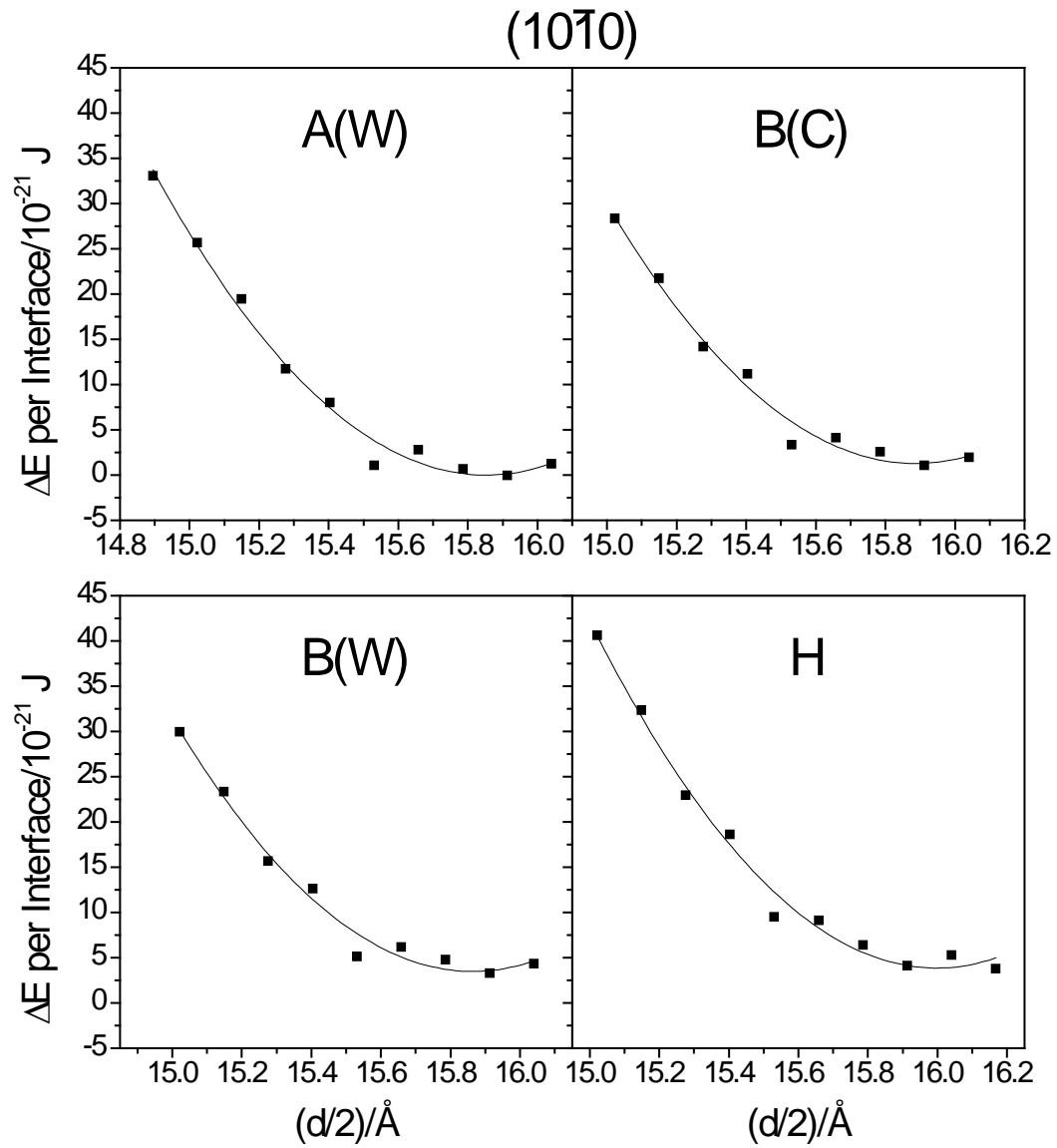


Figure 6.5: Plot of the total energy of the KCl+tungsten carbide composite slab as a function of half of the separation between the outermost tungsten carbide layers $d/2$ for the KCl(100) slab located on various sites with respect to the WC (10 $\bar{1}$ 0) surface.

Site	ΔE_0 (10^{-21} J)	d_0 (Å)	k (N/m)
(1 $\bar{1}$ 00)			
A(W)	0.0	15.64	6.55
B(W)	0.46	15.92	6.37
B(C)	3.67	15.91	5.23
H	8.71	16.04	7.91
(10 $\bar{1}$ 0)			
A(W)	0.0	15.85	7.35
B(W)	3.49	15.87	7.50
B(C)	1.28	15.89	7.31
H	3.86	16.00	7.72

Table 6.2: Parameters of the harmonic fitting potentials for the data displayed in Figures 6.4 and 6.5.

The best-fit curves for KCl located at various sites on the WC(10 $\bar{1}$ 0) face (as indicated in Figure 6.3b) are displayed in Figure 6.7. Again, the A(W) site is the most stable and Table 6.2 contains the fitting parameters and the energy difference between the most stable A(W) site and the others; again, differences in the equilibrium slab distances for the KCl ions located at different sites will give rise to the pressure dependence as found previously for KCl on an iron substrate. There are also differences in the compliances of the slabs on different faces and on different sites and these values are in the same range as found for KCl sandwiched between Fe(001) slabs [10]. As noted above, these variations give rise to a quadratic dependence of the shear strength on pressure, but this effect is much smaller than the linear variation that arises from the change in equilibrium thickness, and can to a good approximation be neglected. The

general behavior found for sliding of the WC tribopin over the surface is similar to that for sliding against Fe(001) [9-11].

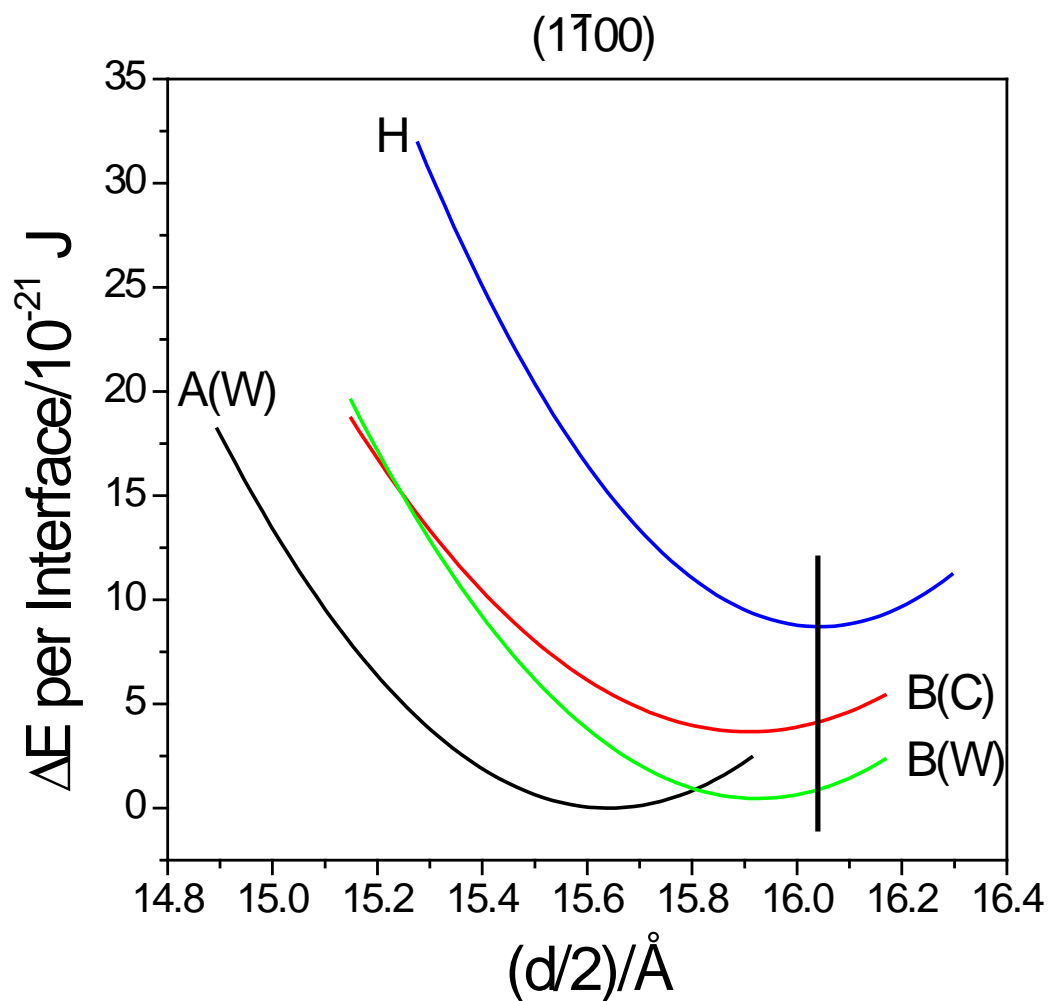


Figure 6.6: Plots of the fits to harmonic potentials to the data displayed in Figure 6.4.

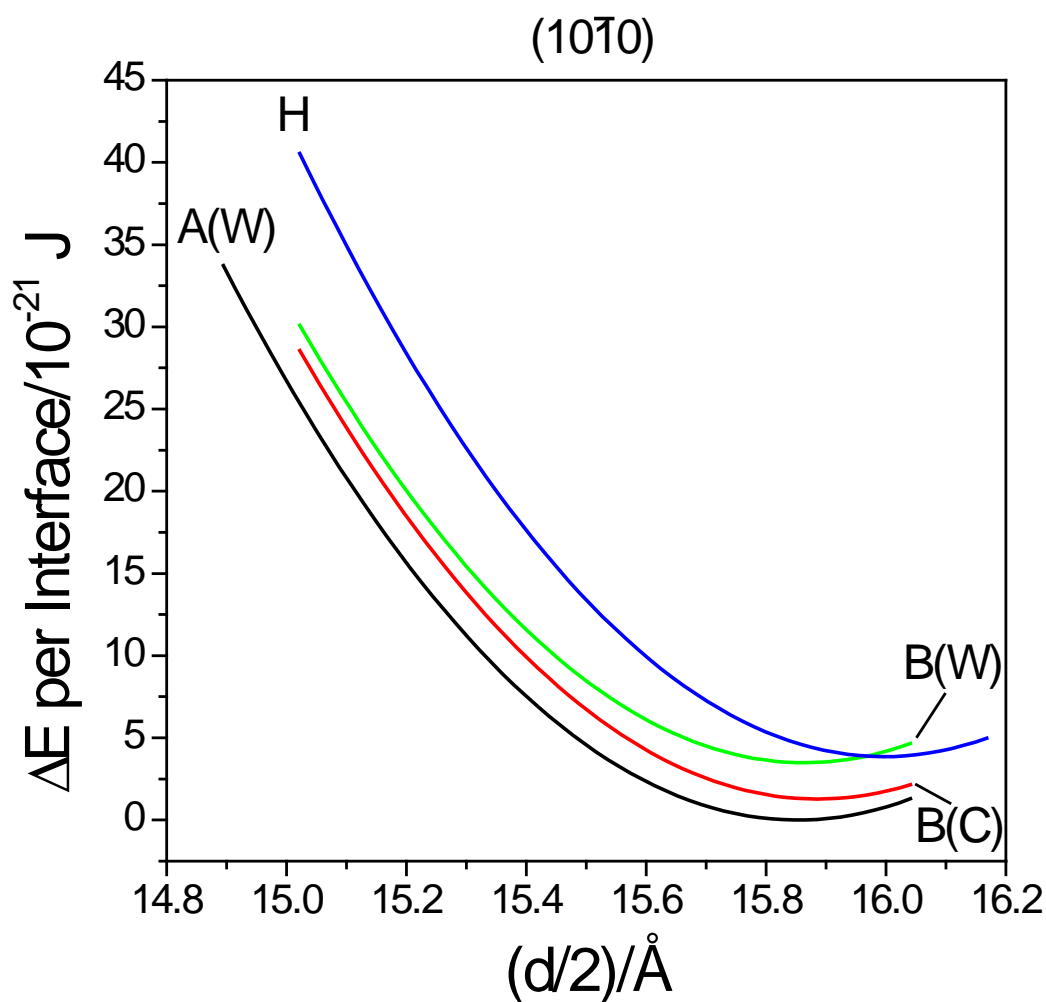


Figure 6.7: Plots of the fits to harmonic potentials to the data displayed in Figure 6.5.

The most stable sites for both faces of WC are the atop sites over a tungsten atom, while the least stable sites are the hollow sites (Figures 6.5 and 6.6). It would intuitively be expected that the highest-coordination adsorption sites would be the most stable. However, similar effects were found for KCl slabs adsorbed on Fe(001), and were ascribed to some bonding between the iron atoms in the slab and the chloride ions in the film [9]. A similar phenomenon appears to take place with KCl in contact with WC and

this is emphasized by the nearest-neighbor distances between the atoms at the interfaces between WC(1 $\bar{1}$ 00) and WC(10 $\bar{1}$ 0) and KCl shown in Table 3. For both faces, the W–Cl distances are shortest for the A(W) sites, indicative of bonding between the tungsten and chloride ions. Analogously, the distances are largest for the hollow sites due to weaker bonding.

The values of S_0 are calculated as described previously [9-10] from the high-velocity limit of the Tomlinson sliding model [46] from the heights of the potentials obtained from the energy differences between the most stable (A(W)) sites and the other sites to obtain the shear strengths for sliding along various directions for a KCl slab in contact with the WC(1 $\bar{1}$ 00) and (10 $\bar{1}$ 0) faces. The results are summarized in Table 6.4. The resulting values of S_0 vary from ~9 to 125 MPa and so are in the same general range as found for KCl sliding against Fe(001). However, while the calculated S_0 values for KCl on iron were rather isotropic [9], clearly on WC they are not. Nevertheless, the results indicate that shear strengths at the KCl/WC and KCl/Fe(001) interfaces are of the same magnitude, and that both are much less than the shear modulus of KCl [9]. Since the shear strengths at the WC/KCl and Fe/KCl interfaces are of the same magnitude, while the contact area between the tip and the film is much lower than between the film and the substrate, sliding must take place between the tip and the outermost surface of the KCl film. This is in accord with experimental results where no transfer film was found when sliding a tungsten carbide tip against a KCl film, whereas one was detected while sliding against a layered compound, FeCl₂ [12]. In the latter case, the presence of a transfer film indicates that shear occurs within the film. For FeCl₂, therefore, the shear properties of the film are expected to be rather independent of the nature of the material

that comprises the substrate and the moving contact. Indeed, this has been found to be the case, where the values of the friction coefficients of reactively formed or evaporated FeCl_2 films measured in ultrahigh vacuum (of ~ 0.08 [12]) were similar to those found for small chlorinated hydrocarbons dissolved in a poly α -olefin measured in a pin and V-block apparatus of between ~ 0.07 and 0.11 , where they react to form a ferrous chloride film [47]. In all cases, the friction coefficient is for FeCl_2 films coating both surfaces sliding against each other.

Site	d_{W-Cl} (Å)	d_{K-Cl} (Å)
(1100)		
A(W)	3.46	3.76
B(W)	3.85	3.92
B(C)	3.82	3.94
H	4.02	4.06
(10 $\bar{1}$ 0)		
A(W)	3.80	3.96
B(W)	3.87	3.94
B(C)	3.87	3.94
H	4.02	4.06

Table 6.3: Vertical distances between planes containing interfacial tungsten and potassium, and chlorine atoms.

Assuming that the crystallites on the surface are randomly azimuthally oriented, average values for S_0 can be obtained as 70 ± 10 MPa for the KCl slab on the WC(1100) face and 51 ± 13 MPa on the WC(10 $\bar{1}$ 0) face. These values are both within the range measured experimentally (of 65 ± 5 MPa). However, only a limited number of the available faces of WC were studied, and the faces that are exposed on the pin used for the

experiment are not known, so that caution must be exercised in arriving at firm conclusions. Nevertheless, the observation that the shear strengths calculated for a film that is in registry with the WC tribopin are within the range of the measured values suggests that this situation corresponds reasonably closely to the true experimental contact conditions. That is, if the atoms in the tip and film were out of registry, it would be expected that the shear strengths calculated for an in-registry film would be much higher than the measured values. Unfortunately, there are no experimental techniques that will allow the atomic structure at a sliding, solid–solid interface to be determined directly. Nevertheless, the correspondence between the experimental and theoretical shear results for this model system implies that, as the tip contacts the substrate at high pressures (the hardness of the substrate), the atoms at the interface are forced into registry.

Epitaxial or commensurate films (where the atoms in the film are in registry with the substrate) form when the energy gain by bonding to the most favorable sites on the substrate exceeds the strain energy required to compress (or expand) the film [48]. The strain energy increases with film thickness, so that films tend to grow epitaxially up to some critical film thickness, above which the film adopts its bulk lattice structure. This behavior is seen in high-resolution atomic force microscope (AFM) images of alkali halides on metal substrates, where the initial layers grow in registry with the substrate, while individual bulk crystallites form as the film becomes thicker [49]. In the friction experiment, it is found that the friction coefficient decreases from the value for the clean substrate with increasing alkali halide coverage and reaches a minimum value when the surface becomes completely covered by the halide film. The pressure-dependent shear

strengths were measured at this alkali halide coverage. This implies that the film is sufficiently thin that when the tip comes into contact with the outermost layer of the thin KCl film, the potassium and halide ions adjust so that they are in registry with atoms in the tribopin.

Path	S_0 (MPa)	α
(1 $\bar{1}$ 00)		
A(W) - B(C) - A(W)	75 ± 11	0.09 ± 0.04
A(W) - B(W) - A(W)	9 ± 12	0.10 ± 0.03
A(W) - H - A(W)	125 ± 8	0.10 ± 0.02
(10 $\bar{1}$ 0)		
A(W) - B(C) - A(W)	26 ± 14	0.01 ± 0.04
A(W) - B(W) - A(W)	70 ± 14	0.00 ± 0.04
A(W) - H - A(W)	55 ± 10	0.04 ± 0.02

Table 6.4: Calculated values of S_0 and α for several paths on the WC(1 $\bar{1}$ 00) and WC(10 $\bar{1}$ 0) surfaces.

The resulting values of α for the (1 $\bar{1}$ 00) and (10 $\bar{1}$ 0) faces are also summarized in Table 6.4. They clearly depend strongly both on the face in contact with the KCl slab and the sliding direction, while for KCl on iron, α values were quite isotropic [10]. Since the pressure dependence occurs because of the atomic-scale corrugation at the interface that causes additional work to be done against the normal load, it is no longer appropriate to simply average over all values. Thus, as the tip slides over the surface, rigid WC will move to surmount the highest point. This is illustrated in Figure 6.6. Here, sliding between KCl and WC(1 $\bar{1}$ 00) along a direction from the most stable A(W) sites across the hollow site (H) will cause a vertical motion from a $d/2$ value of ~ 15.64 Å, corresponding

to the equilibrium spacing at the most stable (A(W)) site, to a value of $\sim 16.04 \text{ \AA}$ (indicated by a vertical line in Figure 6.6) as the tip moves over the hollow (H) site. The external work performed as the tip moves a vertical distance of $\sim 0.40 \text{ \AA}$ against the normal load leads to a pressure-dependent shear strength. The asperity contact will move vertically by this amount as long as there are some $(1\bar{1}00)$ crystallites that are oriented such that sliding occurs along the A(W)–H–A(W) path. The KCl film sliding in other directions on WC($1\bar{1}00$) crystallites at the interface will then be less compressed. Thus, the energies of the interface while sliding via the bridge sites (B(C) and B(W)) will change by an amount indicated by the vertical line drawn in Figure 6.6. These energies are slightly higher than the minimum values used to calculate S_0 , and will therefore yield values that are slightly higher than those given in Table 6.4, but they will still be of the same magnitude as the experimental value ($65 \pm 5 \text{ MPa}$). This implies that the appropriate predicted value of a for a randomly oriented KCl/WC($1\bar{1}00$) interface should be 0.10 ± 0.03 , in better agreement with the experimentally measured values of 0.14 ± 0.02 [13-14]. Clearly, the values of the calculated shear parameters depend in detail on the structure of the tribopair (the exposed surface and orientations) but the results show that they are in the same range as the experimental ones, and that DFT calculations provide insights into the physical origins of the frictional behavior of boundary films and their interfacial structures.

6.5 Conclusions

The sliding potentials for a KCl bilayer film sandwiched between WC slabs are calculated as a function of pressure to mimic the sliding of the tribopin against the surface. Calculations are carried out for KCl on the pseudo-square ($1\bar{1}00$) and ($10\bar{1}0$) faces of tungsten carbide and the effect of pressure is gauged by varying the distance between the outermost layers of the WC slabs. While the shear strengths at zero applied load (S_0) are rather anisotropic, the average values are 70 ± 10 MPa for the KCl slab on the WC($1\bar{1}00$) face and 51 ± 13 MPa on the WC($10\bar{1}0$) face, in reasonable agreement with the experimental value of 65 ± 5 MPa. This implies that the atoms in the contact between the tribopin and the outermost atoms of the KCl film are in registry in the contact. This value of the shear strength is much lower than the shear modulus of KCl [9] and indicates that sliding occurs between the tribopin and the outermost layer of the film. This conclusion is also in agreement with experiment, where no transfer film is found for KCl on an iron substrate.

6.6 References

- [1] Koskilinna, J. O.; Linnolahti, M.; Pakkanen, T. A., Friction paths for cubic boron nitride: An ab initio study. *Tribology Letters* **2007**, 27 (2), 145-154.
- [2] Koskilinna, J. O.; Linnolahti, M.; Pakkanen, T. A., Friction coefficient for hexagonal boron nitride surfaces from ab initio calculations. *Tribology Letters* **2006**, 24 (1), 37-41.

- [3] Neitola, R.; Ruuska, H.; Pakkanen, T. A., Ab initio studies on nanoscale friction between graphite layers: Effect of model size and level of theory. *Journal of Physical Chemistry B* **2005**, *109* (20), 10348-10354.
- [4] Matsuzawa, N. N.; Kishii, N., Theoretical calculations of coefficients of friction between weakly interacting surfaces. *Journal of Physical Chemistry A* **1997**, *101* (51), 10045-10052.
- [5] Liang, T.; Sawyer, W. G.; Perry, S. S.; Sinnott, S. B.; Phillpot, S. R., First-principles determination of static potential energy surfaces for atomic friction in MoS₂ and MoO₃. *Physical Review B* **2008**, *77* (10).
- [6] Smith, G.; Modine, N.; Waghmare, U.; Kaxiras, E., First-principles study of static nanoscale friction between MoO₃ and MoS₂. *Journal of Computer-Aided Materials Design* **1998**, *5* (1), 61-71.
- [7] Tomanek, D.; Zhong, W., Palladium-Graphite Interaction Potentials Based on First-Principles Calculations. *Physical Review B* **1991**, *43* (15), 12623-12625.
- [8] Tomanek, D.; Zhong, W.; Thomas, H., Calculation of an Atomically Modulated Friction Force in Atomic-Force Microscopy. *Europhysics Letters* **1991**, *15* (8), 887-892.
- [9] Garvey, M.; Furlong, O. J.; Weinert, M.; Tysoe, W. T., Shear properties of potassium chloride films on iron obtained using density functional theory. *Journal of Physics-Condensed Matter* **2011**, *23* (26).
- [10] Garvey, M.; Weinert, M.; Tysoe, W. T., On the Pressure Dependence of Shear Strengths in Sliding, Boundary-Layer Friction. *Tribology Letters* **2011**, *44* (1), 67-73.

- [11] Garvey, M.; Weinert, M.; Tysoe, W. T., On the film thickness dependence of shear strengths in sliding, boundary-layer friction. *Wear* **2012**, 274–275 (0), 281-285.
- [12] Gao, F.; Kotvis, P. V.; Tysoe, W. T., The friction, mobility and transfer of tribological films: potassium chloride and ferrous chloride on iron. *Wear* **2004**, 256 (11-12), 1005-1017.
- [13] Gao, F.; Kotvis, P. V.; Tysoe, W. T., The frictional behavior of thin halide films on iron. *Tribology Transactions* **2004**, 47 (2), 208-217.
- [14] Gao, F.; Kotvis, P. V.; Tysoe, W. T., The frictional properties of thin inorganic halide films on iron measured in ultrahigh vacuum. *Tribology Letters* **2003**, 15 (3), 327-332.
- [15] Gao, F.; Wu, G.; Stacchiola, D.; Kaltchev, M.; Kotvis, P. V.; Tysoe, W. T., The tribological properties of monolayer KCl films on iron in ultrahigh vacuum: Modeling the extreme-pressure lubricating interface. *Tribology Letters* **2003**, 14 (2), 99-104.
- [16] Gao, F.; Furlong, O.; Kotvis, P. V.; Tysoe, W. T., Pressure dependence of shear strengths of thin films on metal surfaces measured in ultrahigh vacuum. *Tribology Letters* **2008**, 31 (2), 99-106.
- [17] Tabor, D., *The Hardness of Metals*. Clarendon Press: Oxford, 1951.
- [18] Wu, G.; Gao, F.; Kaltchev, M.; Gutow, J.; Mowlem, J. K.; Schramm, W. C.; Kotvis, P. V.; Tysoe, W. T., An investigation of the tribological properties of thin KCl films on iron in ultrahigh vacuum: modeling the extreme-pressure lubricating interface. *Wear* **2002**, 252 (7-8), 595-606.

- [19] Bridgeman, P. W., Shearing phenomena at high pressures, particularly in inorganic compounds. *Proc. Am. Acad. Arts Sci.* **1986**, *71*, 387–460.
- [20] Briscoe, B. J.; Evans, D. C. B., The Shear Properties of Langmuir-Blodgett Layers. *Proceedings of the Royal Society of London. A. Mathematical and Physical Sciences* **1982**, *380* (1779), 389-407.
- [21] Sutcliffe, M. J.; Taylor, S. R.; Cameron, A., Molecular asperity theory of boundary friction. *Wear* **1978**, *51* (1), 181-192.
- [22] Singer, I. L.; Bolster, R. N.; Wegand, J.; Fayeulle, S.; Stupp, B. C., Hertzian stress contribution to low friction behavior of thin MoS₂ coatings. *Applied Physics Letters* **1990**, *57* (10), 995-997.
- [23] Schwarz, U. D.; Allers, W.; Gensterblum, G.; Wiesendanger, R., Low-load friction behavior of epitaxial C₆₀ monolayers under Hertzian contact. *Physical Review B* **1995**, *52* (20), 14976-14984.
- [24] Briscoe, B. J.; Smith, A. C., The influence of dynamic loading on sliding friction. *Nature* **1979**, *278* (5706), 725-726.
- [25] Riedo, E.; Gnecco, E.; Bennewitz, R.; Meyer, E.; Brune, H., Interaction potential and hopping dynamics governing sliding friction. *Physical Review Letters* **2003**, *91* (8).
- [26] Furlong, O. J.; Javier Manzi, S.; Daniel Pereyra, V.; Bustos, V.; Tysoe, W. T., Kinetic Monte Carlo theory of sliding friction. *Physical Review B* **2009**, *80* (15).
- [27] Mikulski, P. T.; Harrison, J. A., Packing-density effects on the friction of n-alkane monolayers. *Journal of the American Chemical Society* **2001**, *123* (28), 6873-6881.

- [28] Gao, G. T.; Mikulski, P. T.; Harrison, J. A., Molecular-scale tribology of amorphous carbon coatings: Effects of film thickness, adhesion, and long-range interactions. *Journal of the American Chemical Society* **2002**, *124* (24), 7202-7209.
- [29] He, G.; Robbins, M. O., Simulations of the kinetic friction due to adsorbed surface layers. *Tribology Letters* **2001**, *10* (1-2), 7-14.
- [30] Harrison, J. A.; Gao, G.; Schall, J. D.; Knippenberg, M. T.; Mikulski, P. T., Friction between solids. *Philosophical Transactions of the Royal Society a-Mathematical Physical and Engineering Sciences* **2008**, *366* (1869), 1469-1495.
- [31] Mikulski, P. T.; Herman, L. A.; Harrison, J. A., Odd and even model self-assembled monolayers: Links between friction and structure. *Langmuir* **2005**, *21* (26), 12197-12206.
- [32] Hirano, M.; Shinjo, K., Atomistic Locking and Friction. *Physical Review B* **1990**, *41* (17), 11837-11851.
- [33] Muser, M. H., Structural lubricity: Role of dimension and symmetry. *Europhysics Letters* **2004**, *66* (1), 97-103.
- [34] Muser, M. H.; Robbins, M. O., Conditions for static friction between flat crystalline surfaces. *Physical Review B* **2000**, *61* (3), 2335-2342.
- [35] Peyrard, M.; Aubry, S., Critical behaviour at the transition by breaking of analyticity in the discrete Frenkel-Kontorova model. *Journal of Physics C: Solid State Physics* **1983**, *16* (9), 1593.

- [36] Zhong, Y.; Zhu, H.; Shaw, L. L.; Ramprasad, R., The equilibrium morphology of WC particles - A combined ab initio and experimental study. *Acta Materialia* **2011**, 59 (9), 3748-3757.
- [37] Kong, X.-S.; You, Y.-W.; Xia, J. H.; Liu, C. S.; Fang, Q. F.; Luo, G. N.; Huang, Q.-Y., First principles study of intrinsic defects in hexagonal tungsten carbide. *Journal of Nuclear Materials* **2010**, 406 (3), 323-329.
- [38] Gaston, N.; Hendy, S., Hydrogen adsorption on model tungsten carbide surfaces. *Catalysis Today* **2009**, 146 (1-2), 223-229.
- [39] Marinelli, F.; Jelea, A.; Allouche, A., Interactions of H with tungsten carbide surfaces: An ab initio study. *Surface Science* **2007**, 601 (2), 578-587.
- [40] Juslin, N.; Erhart, P.; Traskelin, P.; Nord, J.; Henriksson, K. O. E.; Nordlund, K.; Salonen, E.; Albe, K., Analytical interatomic potential for modeling nonequilibrium processes in the W-C-H system. *Journal of Applied Physics* **2005**, 98 (12).
- [41] Wyckoff, R. W. G., *Crystal Structures*. 2 ed.; Interscience Publishers: 1963; Vol. 1.
- [42] Weinert, M.; Wimmer, E.; Freeman, A. J., Total-energy all-electron density functional method for bulk solids and surfaces. *Physical Review B* **1982**, 26 (8), 4571-4578.
- [43] Wimmer, E.; Krakauer, H.; Weinert, M.; Freeman, A. J., Full-potential self-consistent linearized-augmented-plane-wave method for calculating the electronic structure of molecules and surfaces: O₂ molecule. *Physical Review B* **1981**, 24 (2), 864-875.

- [44] Weinert, M.; Schneider, G.; Podloucky, R.; Redinger, J., FLAPW: applications and implementations. *Journal of Physics-Condensed Matter* **2009**, *21* (8).
- [45] Perdew, J. P.; Burke, K.; Ernzerhof, M., Generalized gradient approximation made simple. *Physical Review Letters* **1996**, *77* (18), 3865-3868.
- [46] Tomlinson, G. A., CVI. A molecular theory of friction. *Philosophical Magazine Series 7* **1929**, *7* (46), 905-939.
- [47] Gao, F.; Furlong, O.; Kotvis, P. V.; Tysoe, W. T., Tribological properties of films formed by the reaction of carbon tetrachloride with iron. *Tribology Letters* **2005**, *20* (2), 171-176.
- [48] Bauer, E., Epitaxy of metals on metals. *Applications of Surface Science* **1982**, *11–12* (0), 479-494.
- [49] Filleter, T.; Paul, W.; Bennewitz, R., Atomic structure and friction of ultrathin films of KBr on Cu(100). *Physical Review B* **2008**, *77* (3).

Chapter 7

Identifying Molecular Species on Surfaces by Scanning

Tunneling Microscopy: Methyl Pyruvate on Pd(111)

7.1 Introduction

Spectroscopic methods have been extensively used to provide elemental and structural information on adsorbates on surfaces. In particular, reflection-absorption infrared spectroscopy (RAIRS) is perhaps the most chemically sensitive technique by providing detailed information on adsorbate structure and orientation from the vibrational frequencies and by exploiting the surface selection rules [1]. However, because the infrared absorbances of the adsorbates are generally not accurately known, surface vibrational spectroscopy provides little information on the relative abundances of the species being detected. Scanning tunneling microscopy (STM) provides detailed information on adsorbate coverage, distribution and mobility because the molecules are imaged directly, but it is often difficult to identify the nature of the species being imaged without some detailed, *a priori* knowledge of the system [2]. This is often not a problem for adsorbates on relatively unreactive surfaces such as gold, copper, or silver. However, for adsorbates that are modified by reaction with the surface, identification of the various surface species can become difficult. Scanning tunneling spectroscopies can provide information on the electronic or vibrational energies of adsorbates but thermal broadening mandates that the experiments be carried out at very low temperatures [3-5]. In the following, the adsorption of methyl pyruvate on Pd(111) is studied by using a

combination of the results of previous surface spectroscopic measurements [6] to provide a restricted subset of possible adsorbate structures on Pd(111), and by simulating the shapes of the STM images of these surface structures calculated using density functional theory (DFT) to compare with the experimental images.

Methyl pyruvate is a key prochiral reactant in the Orito reaction for its enantiospecific hydrogenation to methyl lactate on cinchona-alkaloid-modified catalysts surfaces [7-41]. The surface chemistry of methyl pyruvate has been explored on noble-metal surfaces [6, 32, 42-43]. Two molecular species have been identified on Pd(111); a flat-lying keto species found at low coverages, which converted to an upright species as the coverage increased [6, 43]. However, a relatively weak infrared signal detected following methyl pyruvate adsorption at 80 K provided some evidence of tautomerization to the enol form [6], that has also been identified on Pt(111) [42]. The structures of the flat-lying and vertical keto forms of methyl pyruvate were further investigated using DFT [43], which yielded calculated heats of adsorption for the two forms of methyl pyruvate that agreed well with their desorption activation energies measured by temperature-programmed desorption (TPD). These calculations were therefore extended in the following to include the enol and enolate forms of the methyl pyruvate. The results of the DFT calculations formed the basis for simulating STM images. The simulations were first carried out using the simpler Tersoff-Hamann method [44-45], which computes the tunneling probability for a spherically symmetric tip potential. These were followed by more detailed calculations that include specific tip structures using the Bardeen method [46].

The ultimate goal of this work is to identify the nature of the interactions between a model chiral modifier, naphthyl ethylamine (NEA) [47], and a prochiral reactant, methyl pyruvate. Here the prochiral reactant interacts with the chiral modifier to orient it such that the subsequent hydrogenation reaction preferentially yields one enantiomer. Understanding the nature of such interactions is central to understanding the way in which chiral modifiers function. As part of this process, the structure of NEA alone has been examined on Pd(111) [47], where *exo* and *endo* conformers were identified. Analogous prochiral interactions have been explored between trifluoroacetophenone (TFAP) and NEA [48], where docking complexes were identified.

7.2 Experimental Methods

The Pd(111) substrate was cleaned using a standard procedure consisting of cycles of argon ion sputtering and annealing in 3×10^{-8} Torr of oxygen at 1000 K. Methyl pyruvate (Alfa Aesar, 98%) was purified by several freeze-pump-thaw cycles. While dosing, the Pd(111) sample was held at ~ 120 K and the methyl pyruvate was dosed onto the Pd(111) surface through a variable leak valve. Following methyl pyruvate adsorption, images were acquired at a sample temperature of ~ 120 K using an electrochemically etched tip made from recrystallized tungsten wire. A sample temperature of 120 K was selected to facilitate surface reactions of methyl pyruvate while maintaining the sample temperature below ~ 250 K, where the onset of thermal decomposition of the adsorbed methyl pyruvate was found by infrared spectroscopy [6]. The tip was conditioned by a controlled interaction with a clean Au(111) single crystal

surface. This is expected to result in a gold-terminated tip.[49] Experiments were performed using a scanning tunneling microscope (RHK UHV350 dual AFM/STM) housed in an ultrahigh vacuum (UHV) chamber operating at a base pressure below 2×10^{-10} Torr following bakeout, as described elsewhere [50]. The presented images were not processed except for background subtraction and contrast adjustment.

7.3 Theoretical Methods

DFT calculations were performed with the projector augmented wave (PAW) method [51-52] as implemented in the Vienna *ab initio* simulation package, VASP [53-55]. The exchange-correlation potential was described using the generalized gradient approximation (GGA) of Perdew, Burke and Ernzerhof [56]. A cutoff of 400 eV was used for the planewave basis set, and the wave functions and electron density were converged to within 1×10^{-5} eV. The first Brillouin zone was sampled with a $4 \times 4 \times 1$ Γ -centered k -point mesh. Geometric relaxations were considered to be converged when the force was < 0.02 eV/Å on all unrestricted atoms.

STM topography simulations were performed with the Bardeen approach to tunneling [57-58] and a scattering method developed to first order in the Green's functions [46] as implemented in bSKAN 3.7.

7.4 Results

7.4.1 STM Images

Figure 7.1 shows a typical high-resolution ($20 \times 20 \text{ nm}^2$) STM image of a relatively low coverage of methyl pyruvate adsorbed on Pd(111) at 120 K, collected using a tunneling voltage of -94 mV . Similar images were obtained with more negative biases (-200 , -300 , -400 , -500 , and -600 mV), but a deterioration of the image was observed after prolonged scanning, whereas stable images were observed when scanning at -94 mV . Image deterioration was also observed when using positive biases. Methyl pyruvate is not randomly distributed on the surface and clusters are observed. Nevertheless, relatively isolated methyl pyruvate species can be identified at the edges of the agglomerates.

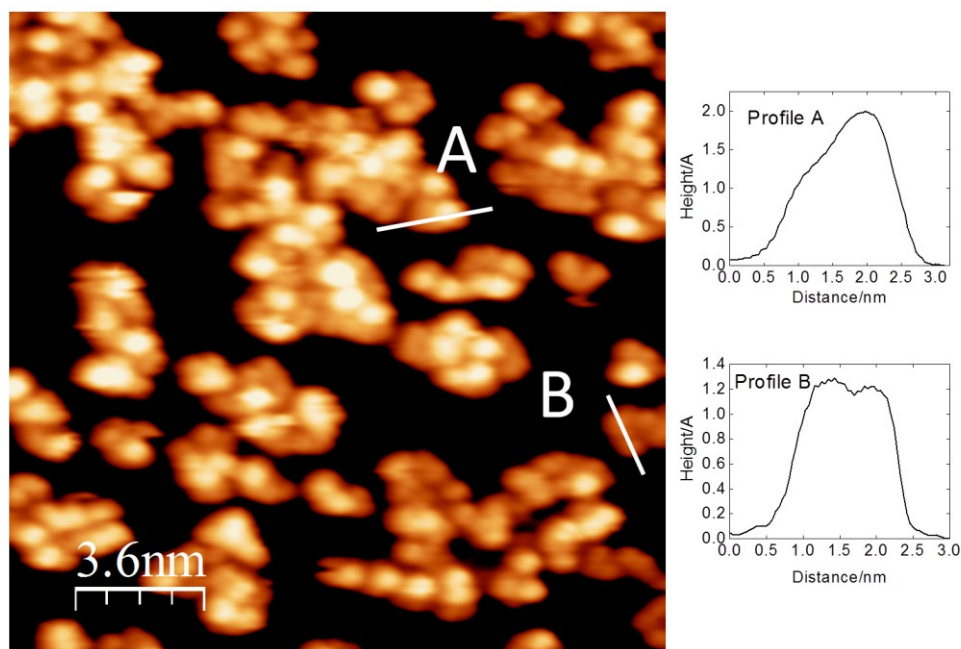


Figure 7.1: Methyl pyruvate on Pd(111) imaged at 120K ($I_t = 8.35 \text{ nA}$, $V_b = -94 \text{ mV}$). Two species, designated **A** and **B** are identified on the surface, and line profiles along the long axes of the images are shown on the figure.

Two profiles can be discerned. The first is labeled **A**, and shows a bright and a dim part in the elongated image. This is emphasized by the line profile measured along the long axis of the image where the bright region is ~ 2 Å above the substrate, showing a shoulder corresponding to the dimmer portion. The second profile, designated **B**, shows an elongated structure with two lobes of equal intensity. This is illustrated by the line profile for species **B** along the long axis of the image showing two maxima with heights of ~ 1.2 Å above the background separated by ~ 5 Å.

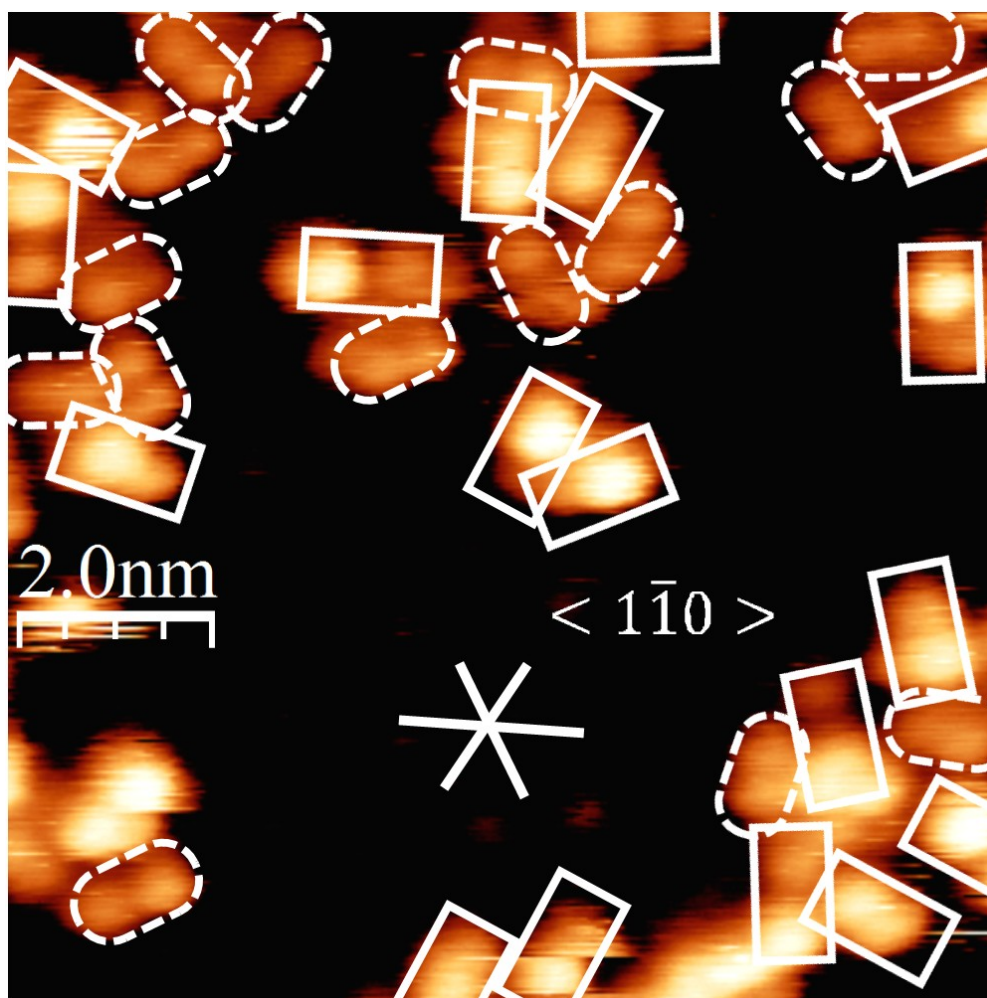


Figure 7.2: A coverage of ~ 0.03 ML of methyl pyruvate on Pd(111) imaged at 120K ($I_t = 8.13$ nA, $V_b = -91$ mV). Species **A** are identified by solid rectangles and species **B** by dashed ovals. The $\langle 1\bar{1}0 \rangle$ directions of the underlying Pd(111) lattice are indicated.

To more clearly identify the two species, higher resolution images were collected at lower coverages ($\Theta(\text{methyl pyruvate}) \approx 0.03 \text{ ML}$, where coverages are referenced to the palladium atom density on the (111) surface). A typical image is displayed in Figure 7.2. High-resolution images of the Pd(111) substrate allow the underlying crystallographic directions to be determined and the resulting $\langle 1\bar{1}0 \rangle$ (close-packed) directions are indicated in the figure. Because species **A** is higher than species **B** (Figure 7.1), species **A** were identified by setting a threshold height in the image of 1.5 \AA , which eliminated any profiles of type **B** because their images are lower than this cutoff height. The orientations of the images were then assigned by assuming that the dimmer regions close to the bright spot separated by $\sim 7 \text{ \AA}$ are due to species **A**. The remainder of the images were assigned to species **B**. The results are highlighted in Figure 2 and enclosed by solid rectangles (Species **A**) and dotted ovals (Species **B**), where $\sim 60\%$ of the adsorbates comprise species **A** and $\sim 40\%$ species **B**. Both types of image (**A** and **B**) either have their long axes along the close-packed $\langle 1\bar{1}0 \rangle$ directions or are rotated by $\sim 30^\circ$ from the close-packed directions (along the $\langle 1\bar{2}1 \rangle$ directions). This suggests the presence of two, distinct methyl pyruvate-derived species at low coverages at a sample temperature of $\sim 120 \text{ K}$. The first species has STM images showing lobes of equal intensities with their long axes oriented either along the $\langle 1\bar{1}0 \rangle$ or $\langle 1\bar{2}1 \rangle$ directions, designated species **B**. The second, slightly more abundant species also has an elongated shape, but shows a brighter and a dimmer portion again oriented along both the $\langle 1\bar{1}0 \rangle$ and $\langle 1\bar{2}1 \rangle$ directions, designated species **A**.

Two keto forms of methyl pyruvate have been previously identified on Pd(111) by infrared spectroscopy: a flat-lying species present at lower coverages, which converts

to a second, perpendicular form due to surface crowding as the surface coverage increases [6, 59]. The assignment to these species was confirmed using DFT [43] and the calculated heats of adsorption agreed well with the measured desorption activation energies. Therefore, at first sight this would suggest that the two structures measured by STM (Figures 7.1 and 7.2) should correspond to the flat-lying and upright forms of the keto form of methyl pyruvate. However, the coverage used to collect the images in Figures 7.1 and 7.2 is sufficiently low to exclude the formation of the perpendicular species and the flat-lying form should predominate. The DFT calculations discussed in greater detail below indicate that the enol tautomer of methyl pyruvate is also relatively stable on the surface. As noted above, surface infrared spectra collected for methyl pyruvate on Pd(111) had suggested the formation of some enol species [6].

The experimental images are assigned by comparison with predictions from STM simulations and comparison with previous spectroscopic results [6] and will reveal the presence of both the flat-lying keto form of methyl pyruvate, as identified previously, as well as the enol form. The flat-lying keto species are found to be either aligned along the close-packed directions or rotated by $\sim 30^\circ$ (ellipses with dashed lines). They are assigned to the features with profile line **B** in Figure 7.1, which confirms that the DFT calculations and simulated images correctly predict the presence of a species known to be present on the surface.

This is extended to identifying the second species as an enol, which is found to be aligned both along the close-packed $\langle 1\bar{1}0 \rangle$ directions and also rotated by $\sim 30^\circ$ from the close-packed directions, corresponding to species **A** (enclosed by rectangles with solid lines).

7.4.2 DFT Calculations of Methyl Pyruvate Derived Surface Species

Previous DFT calculations of flat-lying, keto methyl pyruvate on Pd(111) [43] established the structure of the most stable, flat-lying configuration. They showed that the trans (**2**, Figure 7.3) form of methyl pyruvate is significantly less stable than the cis form (**1**, Figure 7.3). On the basis of these previous results [43], more precise calculations were performed here for flat-lying *cis*-methyl pyruvate (**1**) for initial configurations with the C-C bond between the carbonyl carbons located above atop (A), bridge (B) and three-fold hollow (H) sites on Pd(111) with initial angles of 0 and 30° with respect to the $\langle 1\bar{1}0 \rangle$ directions, where the letters A, B and H are used to label the surface species. These initial configurations were allowed to relax to minimize the energy. Calculations were thus performed for A0cis, A30cis, B0cis, B90cis and H60cis methyl pyruvate where the number indicates the azimuthal angles with respect to the $\langle 1\bar{1}0 \rangle$ directions. The results are summarized in Table 7.1, which presents the adsorption energies that were calculated in the usual way from the difference between the energy of methyl pyruvate adsorbed on Pd(111) and the sum of the energies of gas-phase methyl pyruvate and a clean Pd(111) surface. The results indicate, in agreement with previous calculations [43], that species **1** on the atop sites is the most stable, with a long axis oriented at $32 \pm 5^\circ$ with respect to the $\langle 1\bar{1}0 \rangle$ directions (A30cis). This species is slightly more stable than methyl pyruvate oriented at $2 \pm 5^\circ$ respect to the $\langle 1\bar{1}0 \rangle$ directions (A0cis).

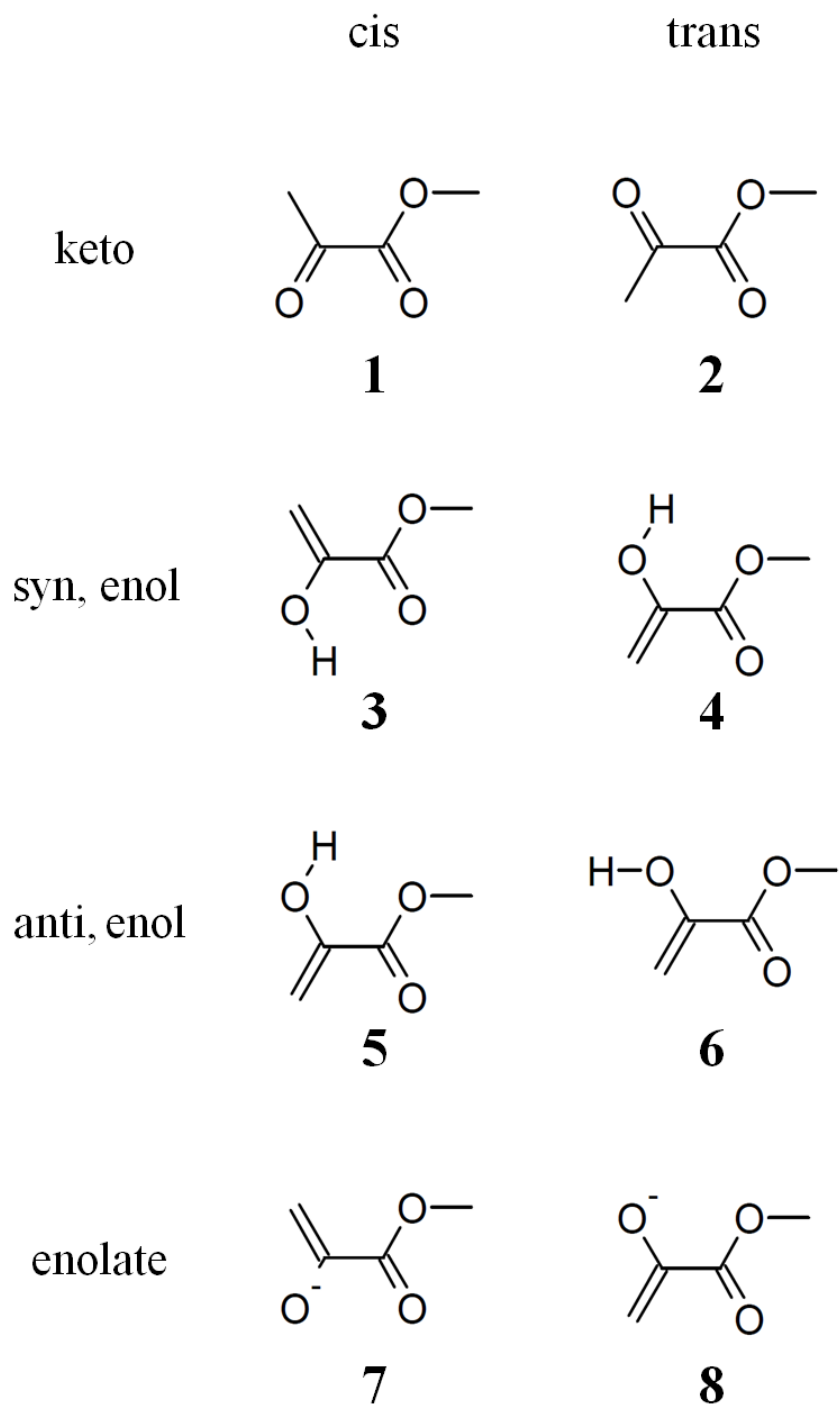


Figure 7.3: Structures of various forms of methyl pyruvate: *cis* keto (1), *trans* keto (2), *cis syn*-enol (3), *trans syn*-enol (4), *cis anti*-enol (5), *trans anti*-enol (6), *cis* enolate (7), and *trans* enolate (8).

Species	Adsorption Energy (kJ/mol)	Relaxed azimuthal angle relative to $\langle 1\bar{1}0 \rangle$ ($^\circ$)	Equilibrium population at 120 K
A0cis	-44.6	2 ± 5	0.34
A30cis	-45.2	32 ± 5	0.62
B0cis	-10.5	1 ± 5	0.00
B90cis	-42.2	37 ± 5	0.03
H60cis	-30.1	6 ± 5	0.00

Table 7.1: Adsorption energies of flat-lying *cis*-methyl pyruvate (1) on Pd(111) calculated using density functional theory, the relaxed azimuthal angles with respect to the close-packed $\langle 1\bar{1}0 \rangle$ directions, and the Boltzmann population calculated from the relative energies at a sample temperature of 120 K. The most stable species are highlighted.

Similar calculations were carried out for the enol tautomer of methyl pyruvate. There are several possible conformations of the enol form of methyl pyruvate. The first arises due to rotation about the C-C bond giving *cis* (**3** and **5**, Figure 7.3) and *trans* (**4** and **6**, Figure 7.3) geometries, as found for the keto tautomer. In the enol, rotation can also occur about the C-OH bond to provide the *syn* (**3** and **4**, Figure 7.3) conformations in which the OH group is directed towards the carbonyl group, and the *anti* (**5** and **6**, Figure 7.3) conformations, in which it is directed away from it. Calculations were performed for the enol tautomers with the molecular plane both parallel and perpendicular to the surface, for both the *cis* and *trans* conformations. Initial structures were constructed with the COH and C=O groups located over physically realistic atop, bridge and three-fold hollow sites for *syn* and *anti* conformation of the OH group. Calculations were thus performed for both perpendicular and flat-lying species with AA-**4** and -**6**, BB-**4** and -**6**, HH-**4** and -**6**, AB-**4** and -**6**, BA-**4** and -**6**, AA-**3** and -**5**, BB-**3** and -**5**, HH-**3** and -**5**, AB-**3** and -**5**, and BA-**3** and **5** structures, where the first letter indicates the initial adsorption site of the COH group and the second the location of the carbonyl group (before the

structure was allowed to relax). The numbers indicate the conformations shown in Figure 7.3. The heats of adsorption were again calculated from the energy difference between the adsorbed species on Pd(111) and gas-phase methyl pyruvate and the clean Pd(111) surface.

System	Adsorption Energy (kJ/mol)	System	Adsorption Energy (kJ/mol)
Flat-lying syn enol (3 and 4)		Perpendicular syn enol (3 and 4)	
AA trans	-45.1	AA trans	+34.5
BB trans	-58.3	BB trans	+32.4
HH trans	-61.7	HH trans	+33.7
AB trans	-54.6	AB trans	+34.2
BA trans	-41.4	BA trans	+31.7
AA cis	-46.0	AA cis	+5.0
BB cis	-57.3	BB cis	+3.3
HH cis	-59.9	HH cis	+4.9
AB cis	-62.2	AB cis	+6.5
BA cis	-45.9	BA cis	+3.0

Table 7.2: Adsorption energies of the enol form of flat-lying and perpendicular *syn,cis*- (3) and *syn,trans*- (4) methyl pyruvate on Pd(111) calculated using DFT.

The results are presented in Table 7.2 for the syn conformers of all of the above structures, which show that the perpendicular enol forms of methyl pyruvate are energetically unfavorable. Similar calculations were carried out for the anti conformer and the results are summarized in Table 7.3. Again, all of the flat-lying species are stable, whereas the perpendicular species are not. However, the syn conformer are consistently more stable than the anti ones, by an average of ~20 kJ/mol, because the syn

conformations are stabilized by an intramolecular hydrogen bonding interaction between the OH group and the carbonyl (Figure 7.3). An examination of the resulting structures indicates that the adsorption energies are dominated by the vinyl-surface interaction, which is a maximum when the vinyl carbon atoms are located over atop palladium sites in agreement with the bonding geometry found for ethylene on Pd(111) [60-64]. Ethylene is rehybridized on Pd(111) and adsorbs as a di- σ species; the bonding in the enol form of methyl pyruvate is dominated by this interaction. The calculated azimuthal angles of the syn cis enol forms (**3**) with respect to the $\langle 1\bar{1}0 \rangle$ directions, and the relative populations at 120 K are displayed in Table 7.4. This reveals that the calculated azimuthal angles (~ 0 and 30°) are in accord with the orientations found for both species **A** and **B** (Figure 7.2).

System	Adsorption Energy (kJ/mol)	System	Adsorption Energy (kJ/mol)
Flat-lying anti enol (5 and 6)		Perpendicular anti enol (5 and 6)	
AA trans	-25.8	AA trans	+34.5
BB trans	-47.9	BB trans	+32.4
HH trans	-52.4	HH trans	+33.7
AB trans	-32.0	AB trans	+34.2
BA trans	-32.6	BA trans	+31.7
AA cis	-25.3	AA cis	+14.4
BB cis	-35.3	BB cis	+22.3
HH cis	-37.5	HH cis	+23.2
AB cis	-26.3	AB cis	+20.9
BA cis	-31.9	BA cis	+15.2

Table 7.3: Adsorption energies of the enol form of flat-lying and perpendicular *anti,cis*- (**5**) and *anti,trans*- (**6**) methyl pyruvate on Pd(111) calculated using DFT.

Species	Relaxed azimuthal angle relative to $\langle 1\bar{1}0 \rangle$ ($^\circ$)	Equilibrium population at 120 K
AA cis	5 ± 5	0.00
BB cis	29 ± 5	0.01
HH cis	38 ± 5	0.09
AB cis	4 ± 5	0.90
BA cis	3 ± 5	0.00

Table 7.4: The relaxed azimuthal angles with respect to the close-packed $\langle 1\bar{1}0 \rangle$ directions and the Boltzmann population calculated from the relative energies at a sample temperature of 120 K for the flat-lying enol form of *syn*, *cis* methyl pyruvate (**3**) on Pd(111).

System	Adsorption Energy (kJ/mol)	System	Adsorption Energy (kJ/mol)
Flat-lying enolate (7 and 8)		Perpendicular enolate (7 and 8)	
AA trans	-40.7	AA trans	+42.3
BB trans	-49.1	BB trans	+31.0
HH trans	-37.0	HH trans	+31.7
AB trans	-51.9	AB trans	+41.3
BA trans	-44.9	BA trans	+37.5
AA cis	-47.6	AA cis	+15.2
BB cis	-23.0	BB cis	+27.9
HH cis	-50.5	HH cis	+10.6
AB cis	-47.0	AB cis	+14.8
BA cis	-51.9	BA cis	+9.7

Table 7.5: Adsorption energies of the enolate form of flat-lying and perpendicular *cis* (**7**) and *trans* (**8**) methyl pyruvate on Pd(111) calculated using density functional theory.

Alcohols are quite labile on Pd(111) tending to form the corresponding alkoxide [65-66]. Accordingly, the structures of the corresponding enolate form of methyl pyruvate were explored (**7** and **8**, Figure 7.3). The energies are displayed in Table 7.5 for flat and perpendicular enolate species (**7** and **8**) using the same notation as used above for the enol form. Again, the perpendicular geometries are unstable, while all of the flat-lying species are stable on the surface. Thus, the most stable enolate species are those with the C-O-Pd and second carbonyl groups located above hollow sites (HH-**7**), or over a bridge and atop site (BA-**7**) with cis conformations.

From the relative energies of the cis and trans isomers and their tautomers, the most likely surface species can be determined. The keto form is much more stable in the gas phase than either the enol or enolate species, and it is the most stable on the Pd(111) surface as the cis isomer. A cis-trans isomerization for a methyl pyruvate molecule adsorbed on the surface would be expected to have a large barrier and therefore would be unlikely. This would suggest that only cis isomers of methyl pyruvate are likely to be observed on the Pd(111) surface. A keto-enol tautomerization of an adsorbed keto species would then lead to a cis isomer of the enol form of methyl pyruvate. This is in accord with the DFT calculations that show that the cis isomers of the enol form of methyl pyruvate are the most stable in the syn conformation (Species **3**, Table 7.2) and are more stable than the anti form (**5**) due to intramolecular hydrogen bonding. In particular, these conformations are more stable than the enolate forms, **7** and **8** (Table 7.5); DFT calculations suggest that species **3** should be stable on the surface. It also has orientations with respect to the $\langle 1\bar{1}0 \rangle$ directions that correspond to those found experimentally (Figure 7.2).

7.4.3 Simulations of the STM Images

The above calculations and a comparison of the calculated orientation with respect to the underlying lattice suggest that the most abundant species for the keto conformation should have the carbonyl groups located above palladium atoms in the cis conformation (**1**) with azimuthal angles of ~ 0 and 30° with respect to the $\langle 1\bar{1}0 \rangle$ directions (Table 7.1). In the case of the enol form, species **3** is the most stable with the HH and AB structures being the most abundant (Tables 7.2 and 7.4). The STM images of these structures were then simulated to establish whether they are in accord with those measured on Pd(111) at high resolution (Figure 7.2). This was done in two steps. In the first, the images of all stable structures were simulated using the Tersoff-Hamann method [44-45] because this is computationally efficient. This confirmed that the shapes of the images of the most stable keto and enol structures were in general accord with the measured ones. However, in order to provide a more stringent simulation and to explore how the shapes of the images depend on tip structure, the Bardeen method [46, 67] was also used. Since the tungsten tips were functionalized by gold to render them more chemically inert, gold-terminated tungsten tips were constructed from gold pyramids on W(110) and W(111) surfaces (depicted in Figure 7.4 (a) and (b)). However, adsorbates may also transfer to the tips during scanning. To simplify the modeling of such tips and because the functional groups in methyl pyruvate are methyl and carbonyl groups, the tips were functionalized with CO (depicted for gold on W(110) and W(111), respectively, in Figure 7.4(c) and (d)), and methyl groups, displayed in Figure 7.4 (e) and (f), respectively.

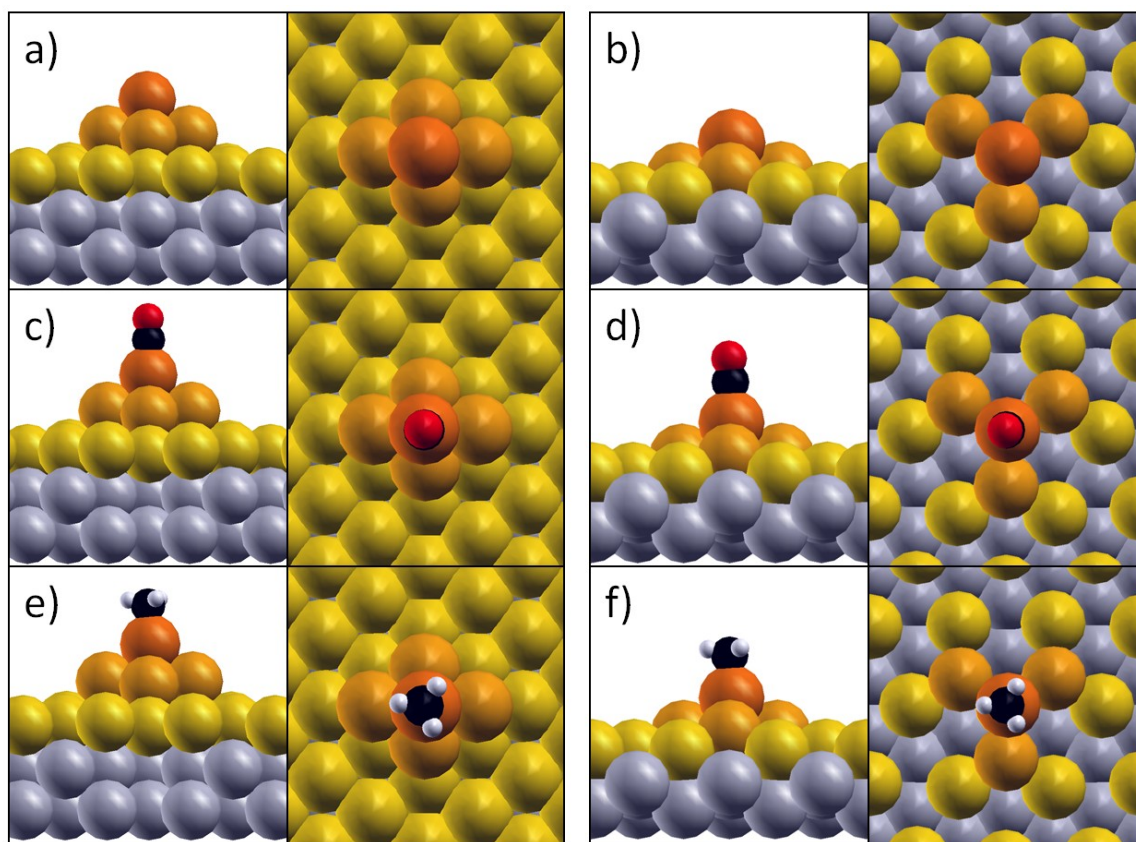


Figure 7.4: Depictions of the most stable structures of the various tips used to simulate the STM images of methyl-pyruvate derived species on Pd(111) showing (a) a gold pyramid on a W(110) substrate, (b) a gold pyramid on a W(111) substrate, (c) a CO functionalized gold pyramid on a W(110) substrate, (d) a CO functionalized gold pyramid on a W(111) substrate, (e) a CH₃ functionalized gold pyramid on a W(110) substrate, and (f) a CH₃ functionalized gold pyramid on a W(111) substrate.

The images for flat-lying species (**1**) were first simulated because it has been identified by previous spectroscopic measurements [6]. In particular, being able to correctly simulate the image for the known, flat-lying keto form will provide a stringent test of the simulation method. The results of the simulations are displayed in Figure 7.5 for clean and functionalized tips. All images show the characteristic two-lobed structures with the long axes oriented at ~ 0 and $\sim 30^\circ$ to the close-packed directions. Although there are slight differences in the relative intensities of the lobes in the images for the different

tip structures, they all correspond closely to the shapes for species **B** seen in the experimental images in Figure 7.2 (highlighted by dotted ellipses). This is emphasized by the line profile along a simulated image plotted in Figure 7.5(g). This is very similar to the experimental profile, showing two peaks of equal height (of ~ 1.2 Å) separated by ~ 5 Å (Figure 7.1). Comparison of the molecule to the shapes of the simulated STM images (Figure 7.5) indicates that the bright portions of the images correspond to the location of the methyl groups. The DFT calculations suggest that the population of species **1** oriented at 30° to the $\langle 1\bar{1}0 \rangle$ directions should be greater than that which is parallel to the close-packed directions (Table 7.1), and this is borne out by the small sample shown in Figure 7.2 and in other images. However, because the methyl pyruvate species tend to agglomerate (Figure 7.1), it was not possible to carry out a detailed statistical analysis. In addition, as shown in Figures 7.8 to 7.13 in the Supporting Figures section, there are no significant changes in the shapes of the simulated images with bias voltage for the keto species, as found experimentally. Thus, the presence of a flat lying, *cis* keto species (**1**), identified previously using surface infrared spectroscopy [6], is confirmed by STM based on the relative energies, molecular orientation and the correspondence between the simulated and experimental images and is in accord with previous calculations [43]. This result indicates that the simulation methods used here provide calculated images that are in good agreement with a known structure.

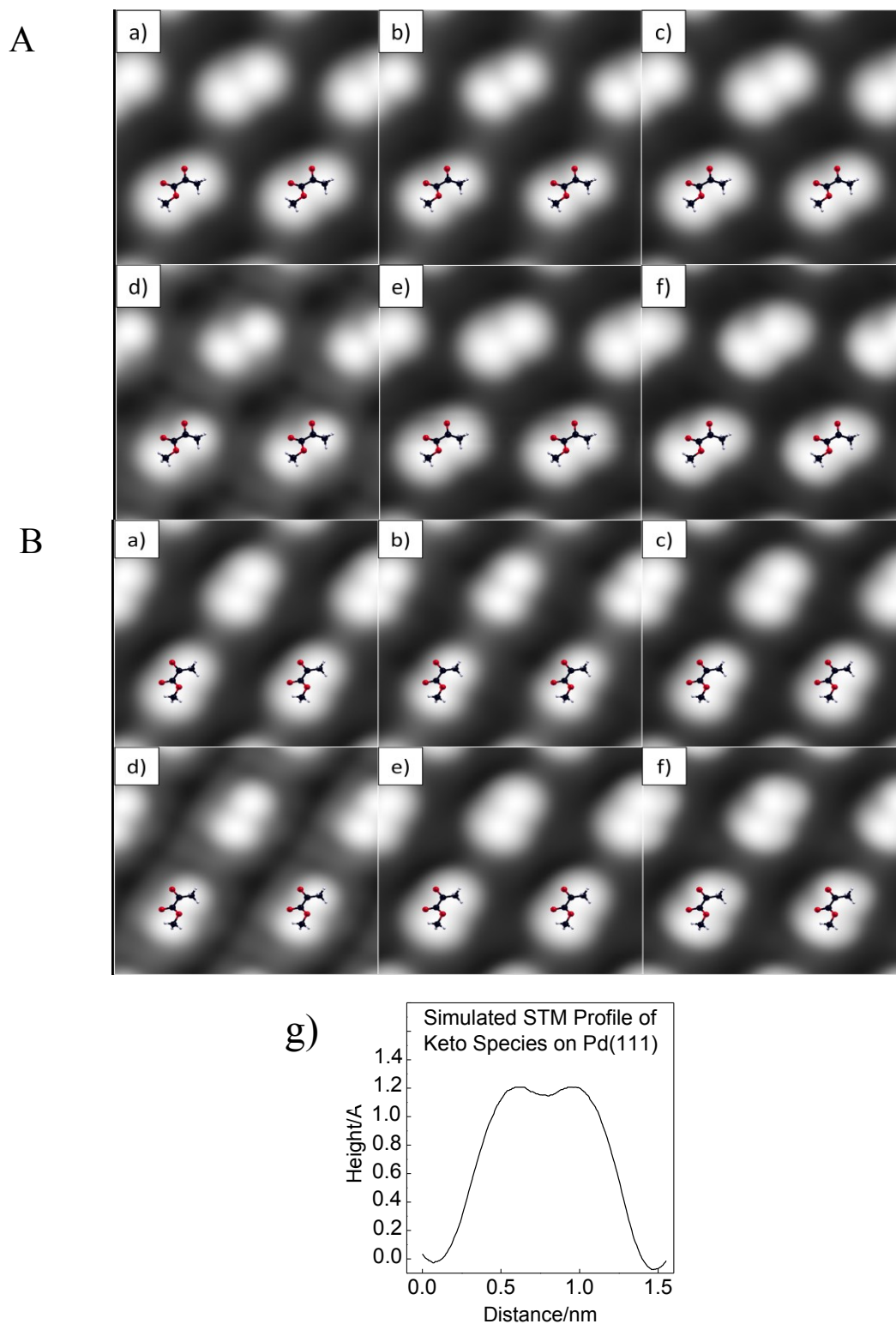


Figure 7.5: (A) Simulated STM images of the keto form of methyl pyruvate (**1**) with the carbonyl groups located on atop sites oriented at 30° with respect to the $\langle \bar{1}10 \rangle$ directions (A30cis) using the Bardeen method with the following tips: (a) Au on W(110), (b) CH_3 on Au on W(110), (c) CO on Au on W(110), (d) Au on W(111), (e) CH_3 on Au on

W(111), and (f) CO on Au on W(111). (B) STM images of the keto form of methyl pyruvate (**1**) with the carbonyl groups located on atop sites oriented at 0° with respect to the $\langle 1\bar{1}0 \rangle$ directions (A0cis) simulated by the Bardeen method with the following tips: (a) Au on W(110), (b) CH₃ on Au on W(110), (c) CO on Au on W(110), (d) Au on W(111), (e) CH₃ on Au on W(111), and (f) CO on Au on W(111). (g) Profile measured along the long axis of the simulated image.

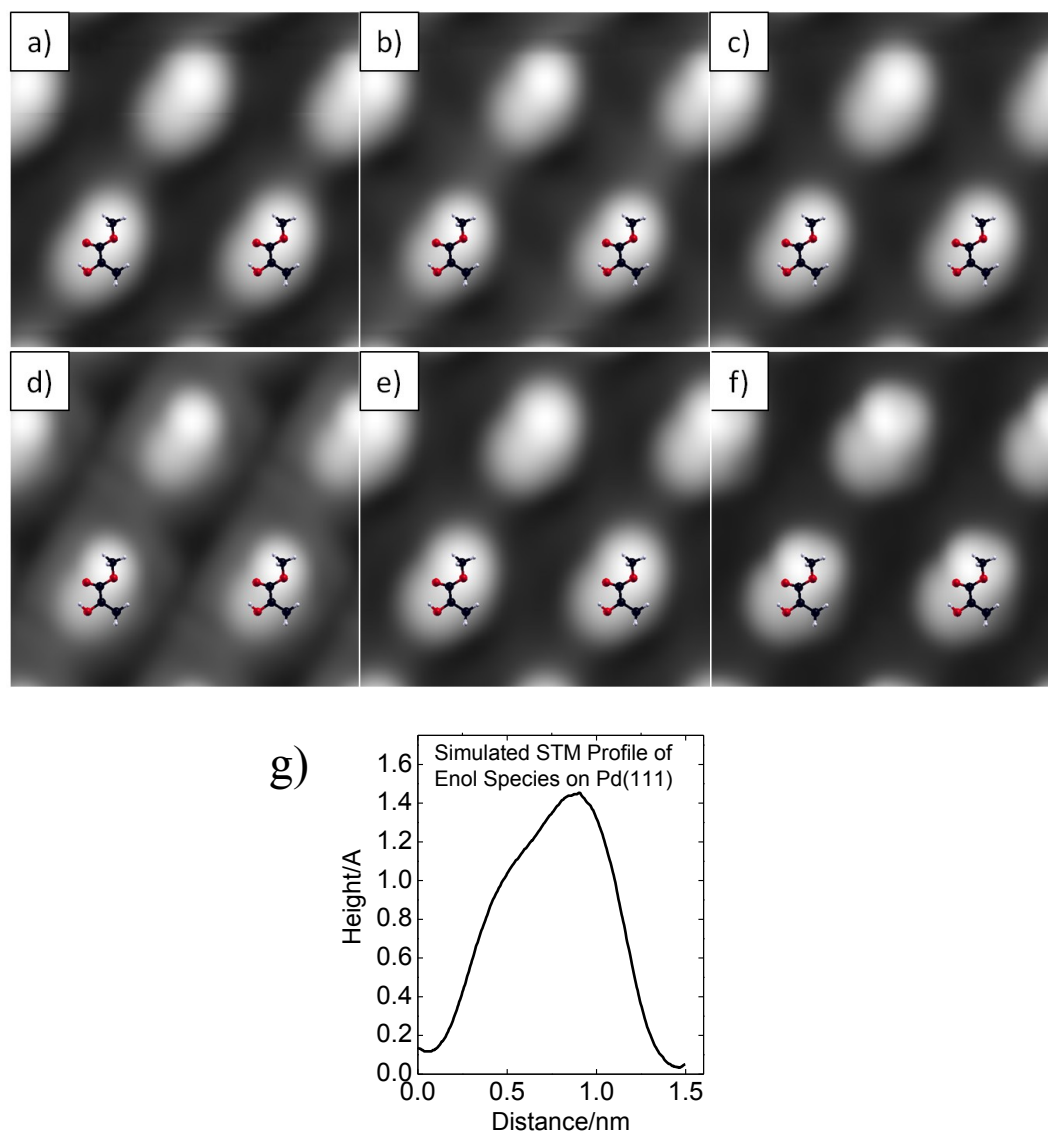


Figure 7.6: STM images of the enol form of methyl pyruvate (**3**) with the carbonyl and alcohol groups located on atop and bridge sites (AB cis) simulated by the Bardeen method with the following tips: (a) Au on W(110), (b) CH₃ on Au on W(110), (c) CO on Au on W(110), (d) Au on W(111), (e) CH₃ on Au on W(111), (f) CO on Au on W(111). (g) Profile measured along the long axis of the simulated image.

This is extended to examining the nature of the second species, suggested from the above DFT calculations to be species **3**. The simulated images for the enol species with various tips (Figure 7.4) are shown in Figure 7.6. Whereas again there are some slight variations in the calculated images as the tip changes, all of the images display a characteristic bright region with a dimmer part corresponding to the shapes of species **A** (defined by solid rectangles, Figure 7.2). There are also only relatively minor changes in the simulated images with tip bias. (See Figures 7.14 to 7.19.) Fig. 7.6(g) shows a profile along the long axis of the simulated image, emphasizing the presence of bright (high) and dimmer (low) regions, with a simulated height of the bright region of ~ 1.5 Å, in good agreement with the experimental profile.

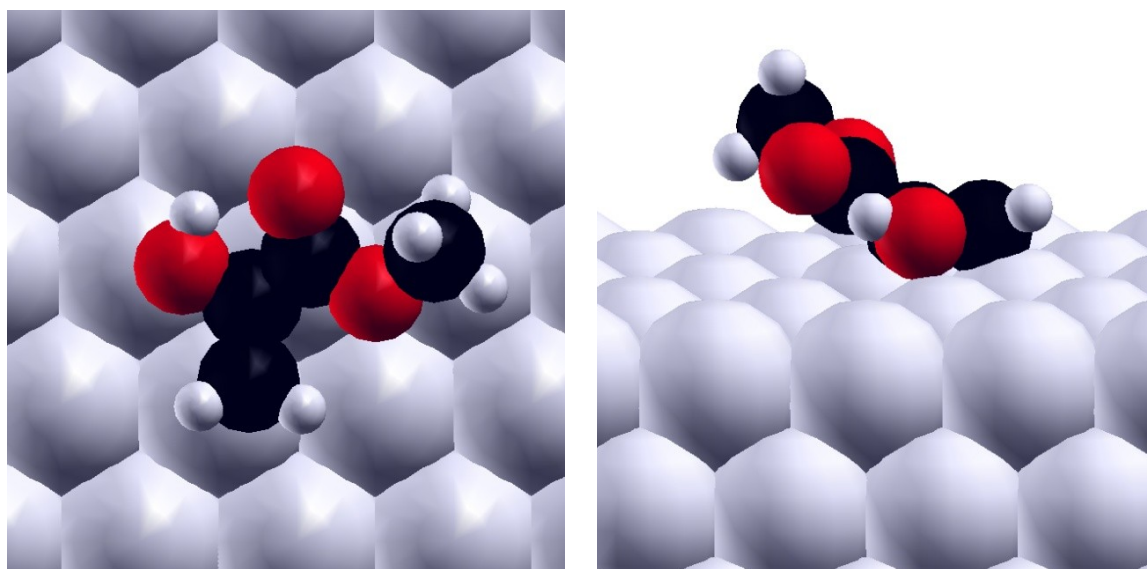


Figure 7.7: Proposed structure of flat-lying AB *syn,cis* enol (**3**) form of methyl pyruvate on Pd(111).

The superimposed calculated structures in the simulated images in Figure 7.6 indicate that the bright region corresponds to the presence of the methyl group in the

methoxy, while the dimmer region is due to the vinyl group. This general conclusion is in accord with the simulated (Figure 7.5) and experimental (Figure 7.2) images of the keto form, where again the methyl and methoxy species images as bright spots. The most stable structure of the cis, syn enol tautomer of methyl pyruvate is displayed in Figure 7.7.

7.5 Discussion

Two distinct forms of methyl pyruvate were identified on Pd(111). The first species is a flat-lying, cis keto form of methyl pyruvate (**1**) that has been identified previously using surface infrared spectroscopy [6], and the assignment was confirmed by comparing the heat of adsorption calculated by DFT with the desorption activation energy measured by TPD [43]. The STM images showed a second species that cannot be assigned to the keto form of methyl pyruvate and is instead assigned to the enol tautomer (**3**). Note that a weak feature at $\sim 1558\text{ cm}^{-1}$ was assigned to the C=C stretching vibration of an enol species on Pd(111) [6], close to the vibrational frequency assigned to enol species in Ni(111) [42]. However, STM (Figure 7.2) suggested that the enol species is present at quite high relative coverages on Pd(111) at 120 K. There may be several origins for this difference. First, the C=C vibrational modes are much less intense than C=O modes so that a high proportion of the enol species would only have weak infrared intensities, in particular since the C=C bond is oriented close to parallel to the surface (Figure 7.7). Second, the infrared data were collected at a lower temperature ($\sim 80\text{ K}$) than that used for the STM images ($\sim 120\text{ K}$). The activation energy to convert the

initially adsorbed keto form to an enol may be sufficiently high that its formation at 80 K is kinetically limited. Subsequent infrared spectra were only collected after heating to much higher temperature (~ 175 K).

Only the keto form of methyl pyruvate was found to desorb from the surface, and there was no evidence from TPD of the presence of enol species [6], and only flat-lying and perpendicular forms of methyl pyruvate, as well as decomposition products, were observed. This is understandable because the heat of adsorption of the enol form of methyl pyruvate is ~ 15 kJ/mol higher than the keto form, and the enol tautomer is much less stable than the keto in the gas phase. This would result in a high desorption activation energy for direct enol desorption. A lower energy pathway would be for the enol to rapidly convert to the keto form during the desorption sweep and desorb as the keto form. Alternatively, it could completely thermally decompose.

The agglomeration of the species found at even relatively low coverages on the surface (Figure 7.1) is in accord with the presence of both the keto and enol forms, likely due to hydrogen bonding interactions between the -OH group of the enol form and carbonyl groups. This prevents the shapes of the images within the clusters from being resolved, raising the possibility of the existence of other forms of methyl pyruvate or changes in molecular structure due to these interactions. However, surface infrared spectroscopy suggests the presence of a single form of flat-lying methyl pyruvate at low coverages [6], suggesting that this is not a major issue.

This work also indicated that both the Tersoff–Hamann and Bardeen simulation methods reliably reproduced the shapes of the experimentally measured STM images. This offers a powerful strategy for identifying the presence of surface species on reactive

surfaces such as palladium when combined with surface spectroscopic methods. As pointed out previously [42], the presence of an enol species is attractive in terms of NEA-modified enantioselective catalysis. First, hydrogen-bonding interactions between the amine group on NEA and the C-O-H group of an enol will be stronger than with the carbonyl groups of the keto form. Second, C=C bond hydrogenation is facile on palladium surfaces [68]. The interaction between methyl pyruvate and NEA is discussed in Chapter 8.

7.6 Conclusions

The STM images of methyl pyruvate adsorbed on Pd(111) at 120 K were assigned by comparison with the structures calculated using DFT and images simulated using the Bardeen method using model gold-coated tungsten tips that are also functionalized by CO and methyl groups, combined with the results of previous spectroscopic measurements. Two distinct methyl-pyruvate-derived species were identified at low coverages and assigned by comparing both the orientations of the simulated structures with those found experimentally and the calculated image shapes with experiment.

The first species, previously identified using RAIRS, was a flat-lying, keto form of *cis*-methyl pyruvate (**1**). It was characterized by two-lobed structures with the long axes of the structures oriented at ~ 0 and $\sim 30^\circ$ to the close-packed directions, and the simulated images agreed well with those found experimentally. It was found that the simulated structures were not strongly dependent on the tip structure or tip bias voltage, as found experimentally.

This approach was used to identify the nature of the second species as the enol

form of cis-methyl pyruvate (**3**) with the carbonyl groups located on atop and bridge sites. The orientation of the structures with respect to the underlying Pd(111) lattice as well as the calculated image shapes was in good agreement with the experimental images.

7.7 Supporting Figures

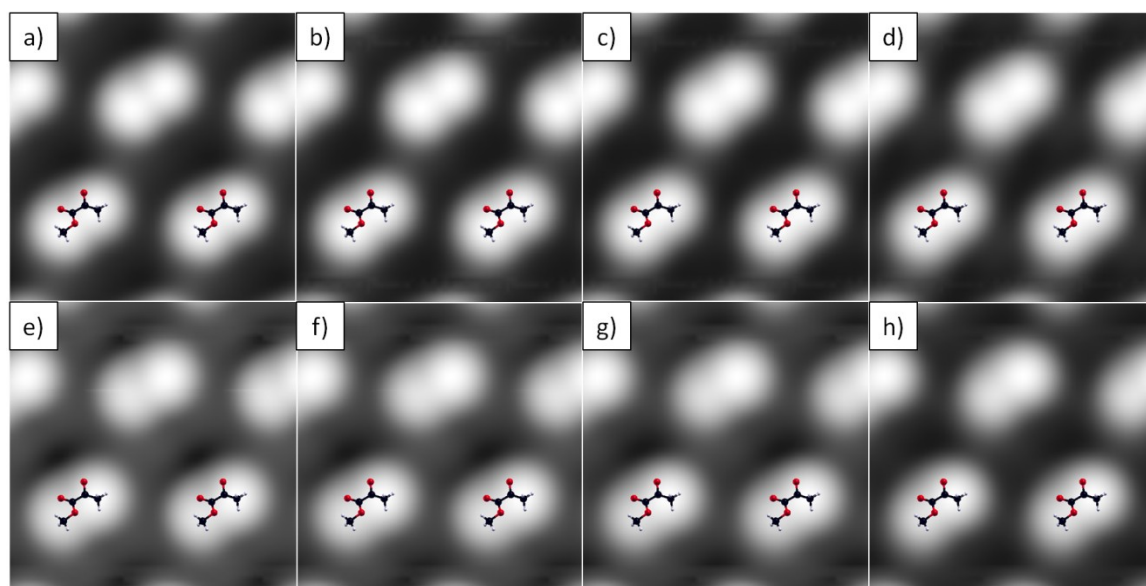


Figure 7.8: STM images of the keto form of methyl pyruvate with the carbonyl groups located on atop sites oriented at 30° with respect to the $\langle \bar{1}\bar{1}0 \rangle$ direction imaged with Au on W(110) tip at varied bias: a) -0.1 V, b) -0.2 V, c) -0.3 V, d) -0.4 V e) +0.1 V, f) +0.2 V, g) +0.3 V, h) +0.4 V.

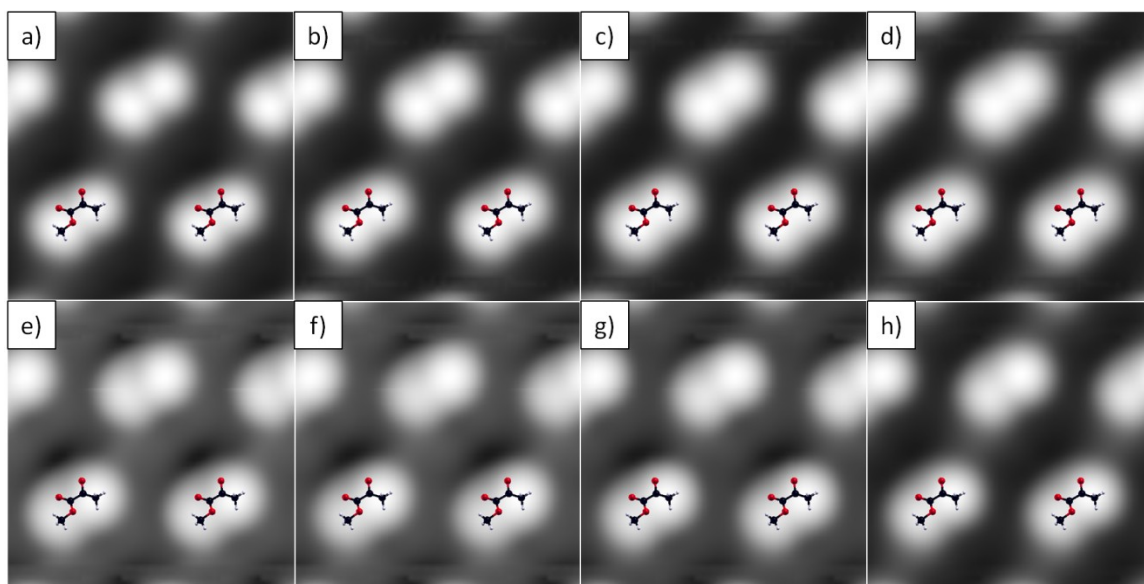


Figure 7.9: STM images of the keto form of methyl pyruvate with the carbonyl groups located on atop sites oriented at 30° with respect to the $\langle 1\bar{1}0 \rangle$ direction imaged with a CH_3 group on Au on W(110) tip at varied bias: a) -0.1 V, b) -0.2 V, c) -0.3 V, d) -0.4 V, e) +0.1 V, f) +0.2 V, g) +0.3 V, h) +0.4 V.

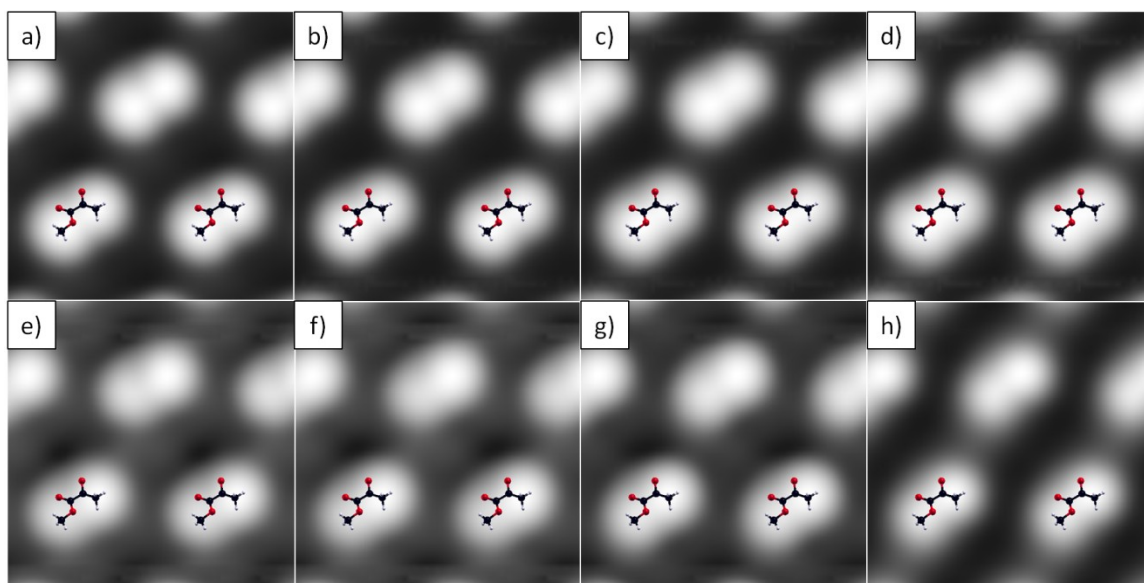


Figure 7.10: STM images of the keto form of methyl pyruvate with the carbonyl groups located on atop sites oriented at 30° with respect to the $\langle 1\bar{1}0 \rangle$ direction imaged with a CO group Au on W(110) tip at varied bias: a) -0.1 V, b) -0.2 V, c) -0.3 V, d) -0.4 V, e) +0.1 V, f) +0.2 V, g) +0.3 V, h) +0.4 V.

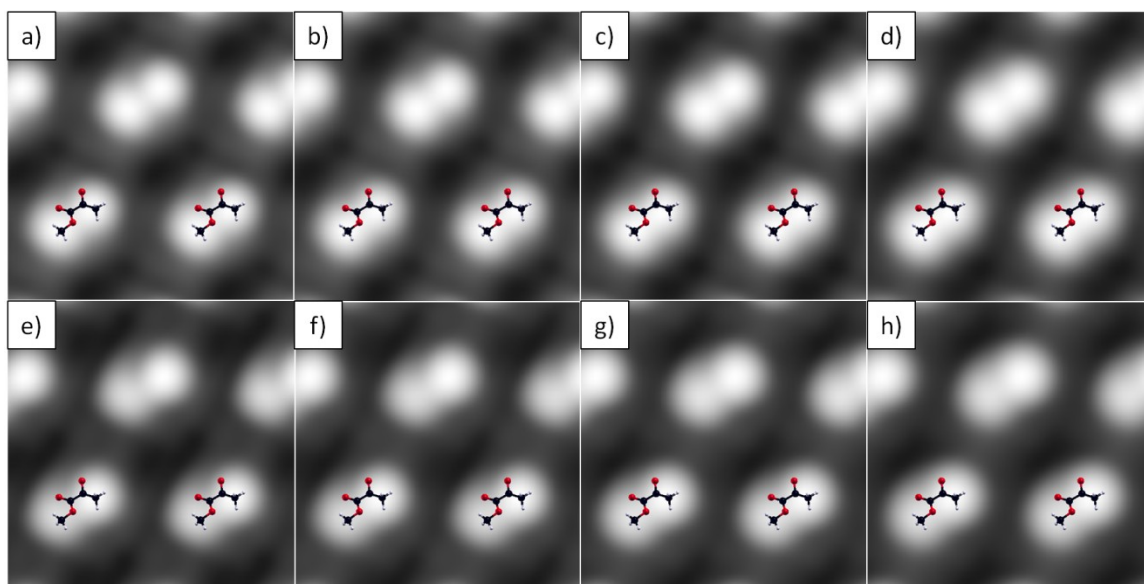


Figure 7.11: STM images of the keto form of methyl pyruvate with the carbonyl groups located on atop sites oriented at 30° with respect to the $\langle \bar{1}\bar{1}0 \rangle$ direction imaged with Au on W(111) tip at varied bias: a) -0.1 V, b) -0.2 V, c) -0.3 V, d) -0.4 V, e) +0.1 V, f) +0.2 V, g) +0.3 V, h) +0.4 V.

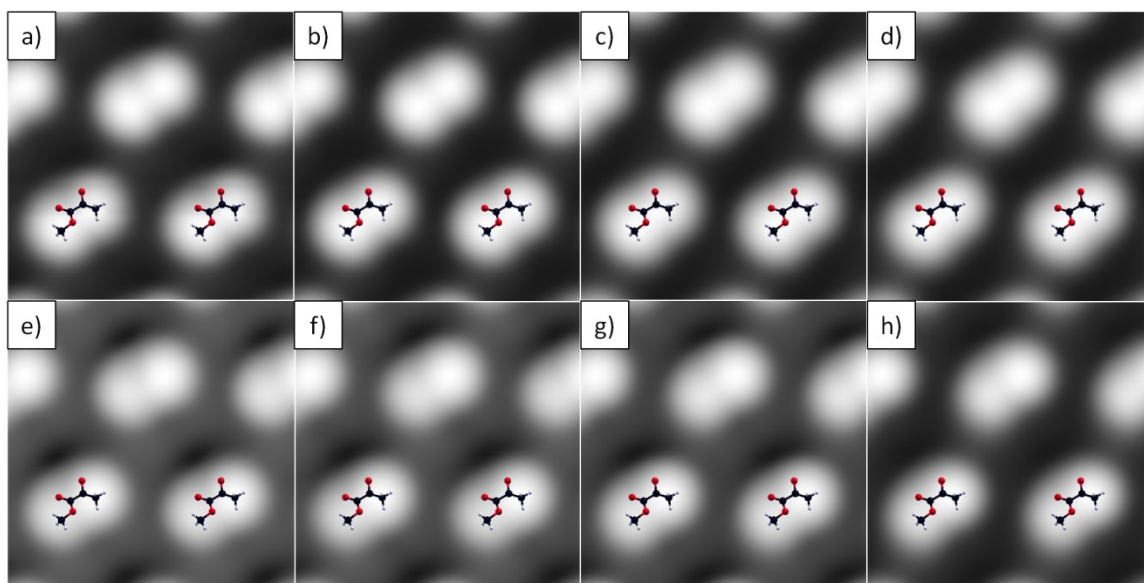


Figure 7.12: STM images of the keto form of methyl pyruvate with the carbonyl groups located on atop sites oriented at 30° with respect to the $\langle \bar{1}\bar{1}0 \rangle$ direction imaged with a CH_3 group on Au on W(110) tip at varied bias: a) -0.1 V, b) -0.2 V, c) -0.3 V, d) -0.4 V, e) +0.1 V, f) +0.2 V, g) +0.3 V, h) +0.4 V.

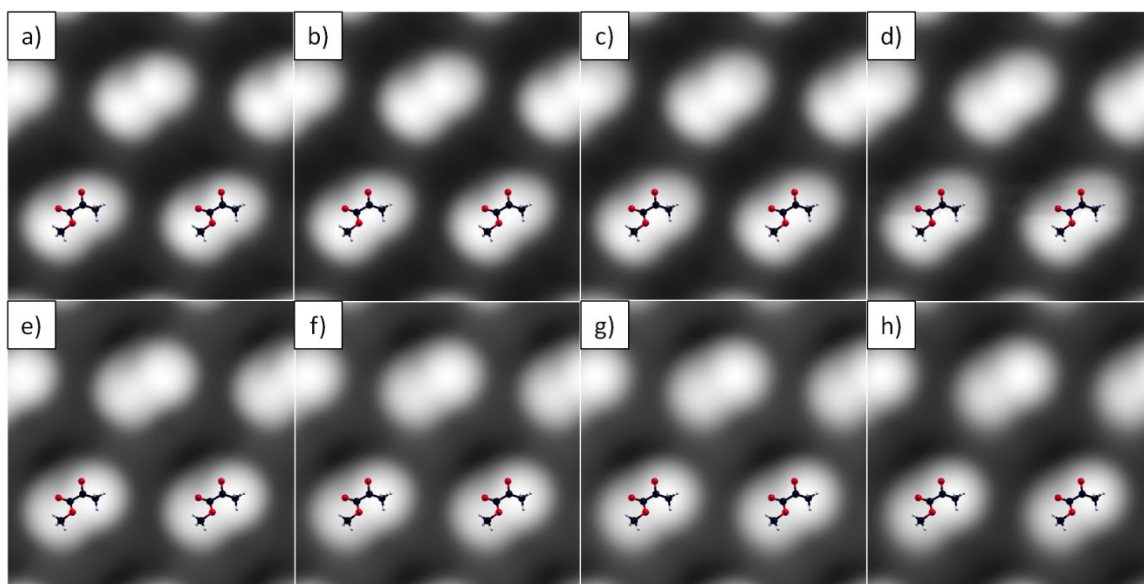


Figure 7.13: STM images of the keto form of methyl pyruvate with the carbonyl groups located on atop sites oriented at 30° with respect to the $\langle \bar{1}\bar{1}0 \rangle$ direction imaged with a CO group on Au on W(111) tip at varied bias: a) -0.1 V, b) -0.2 V, c) -0.3 V, d) -0.4 V, e) +0.1 V, f) +0.2 V, g) +0.3 V, h) +0.4 V.

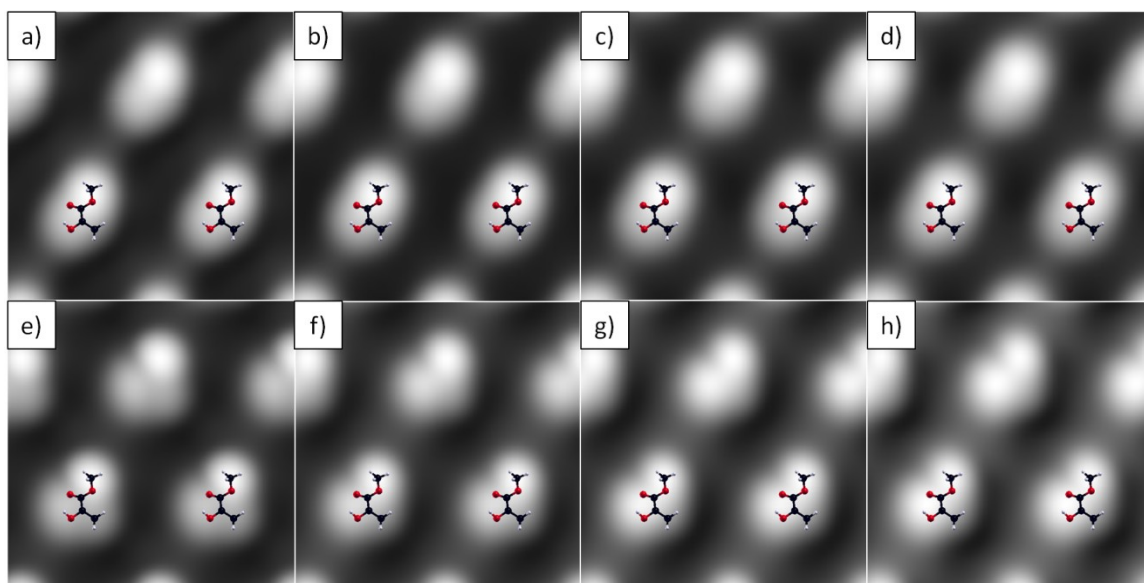


Figure 7.14: STM images of the most stable enol form of methyl pyruvate with the carbonyl groups located on bridge and atop sites (AB cis) imaged with a Au on W(110) tip at varied bias: a) -0.1 V, b) -0.2 V, c) -0.3 V, d) -0.4 V, e) +0.1 V, f) +0.2 V, g) +0.3 V, h) +0.4 V.

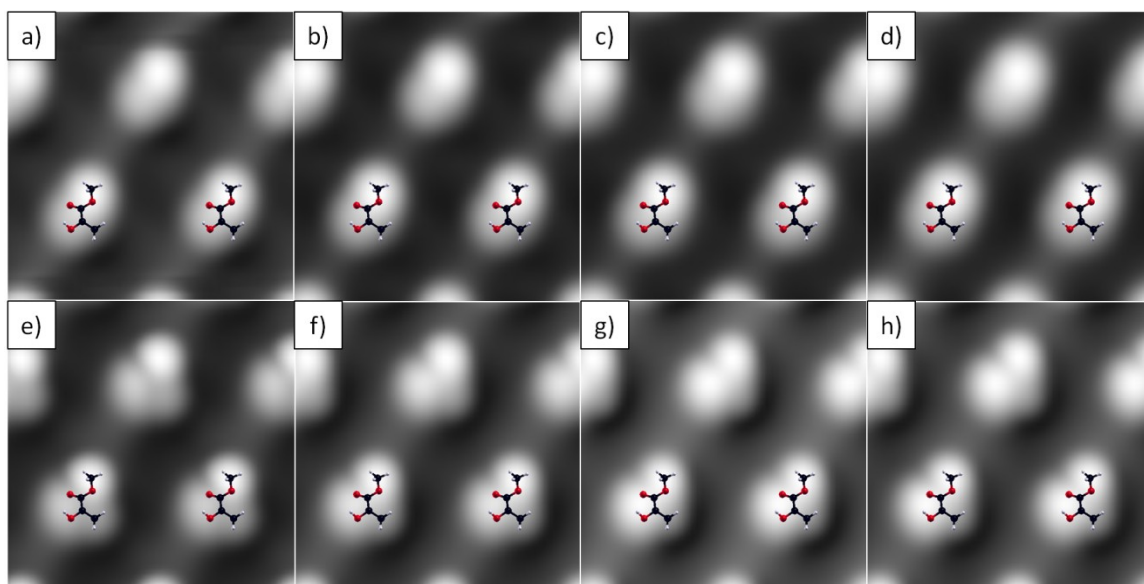


Figure 7.15: STM images of the enol form of methyl pyruvate with the carbonyl groups located on bridge and atop sites (AB cis) imaged with a CH₃ group on Au on W(110) tip at varied bias: a) -0.1 V, b) -0.2 V, c) -0.3 V, d) -0.4 V, e) +0.1 V, f) +0.2 V, g) +0.3 V, h) +0.4 V.

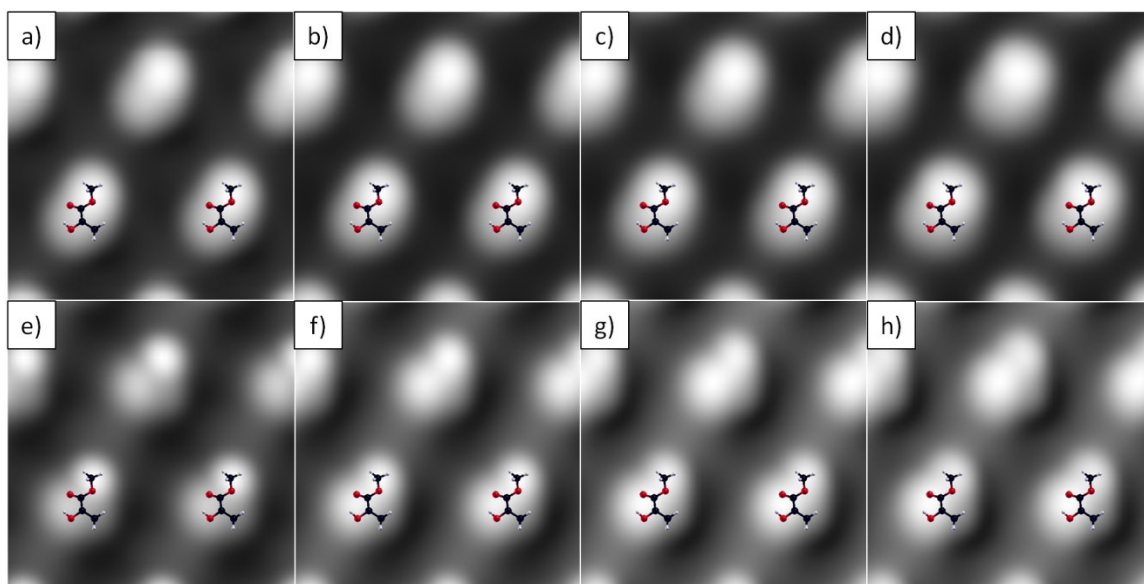


Figure 7.16: STM images of the enol form of methyl pyruvate with the carbonyl groups located on bridge and atop sites (AB cis) imaged with a CO group on Au on W(110) tip at varied bias: a) -0.1 V, b) -0.2 V, c) -0.3 V, d) -0.4 V, e) +0.1 V, f) +0.2 V, g) +0.3 V, h) +0.4 V.

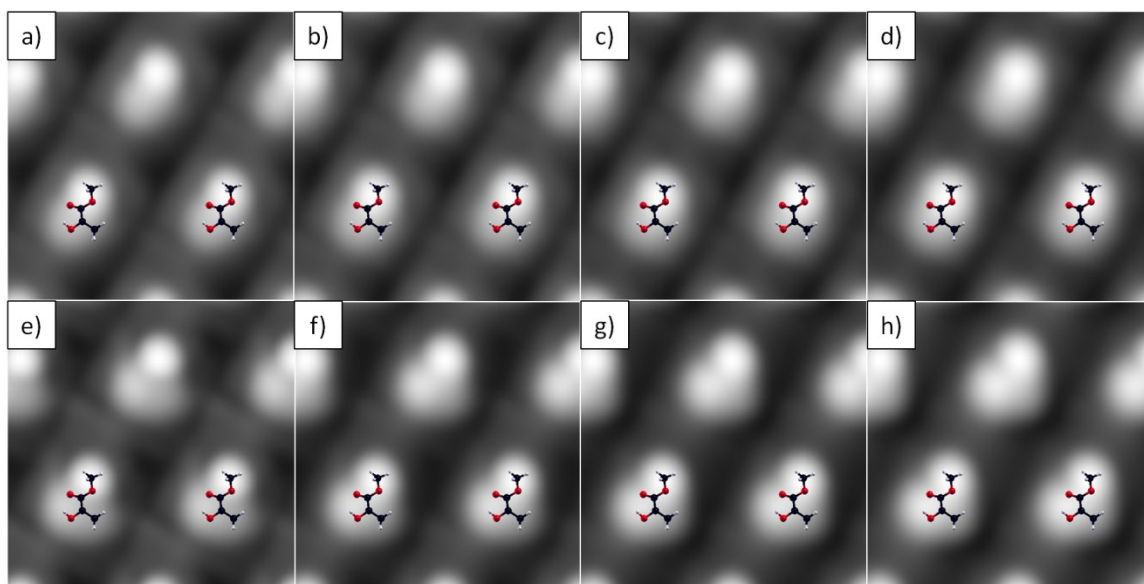


Figure 7.17: STM images of the enol form of methyl pyruvate with the carbonyl groups located on bridge and atop sites (AB cis) imaged with a Au on W(111) tip at varied bias: a) -0.1 V, b) -0.2 V, c) -0.3 V, d) -0.4 V, e) +0.1 V, f) +0.2 V, g) +0.3 V, h) +0.4 V.

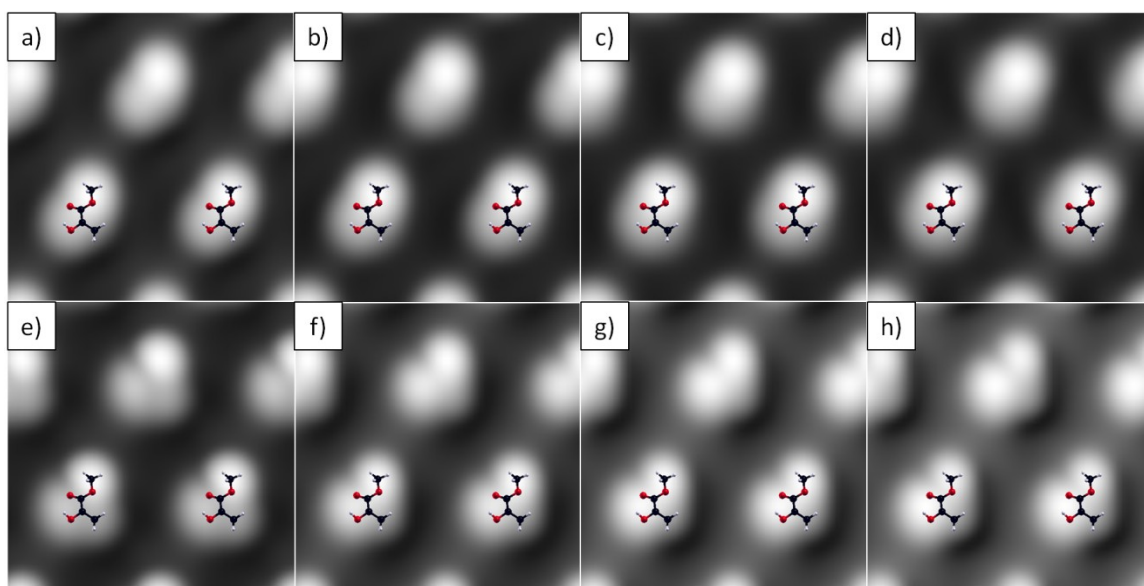


Figure 7.18: STM images of the enol form of methyl pyruvate with the carbonyl groups located on bridge and atop sites (AB cis) imaged with a CH₃ group on Au on W(111) tip at varied bias: a) -0.1 V, b) -0.2 V, c) -0.3 V, d) -0.4 V, e) +0.1 V, f) +0.2 V, g) +0.3 V, h) +0.4 V.

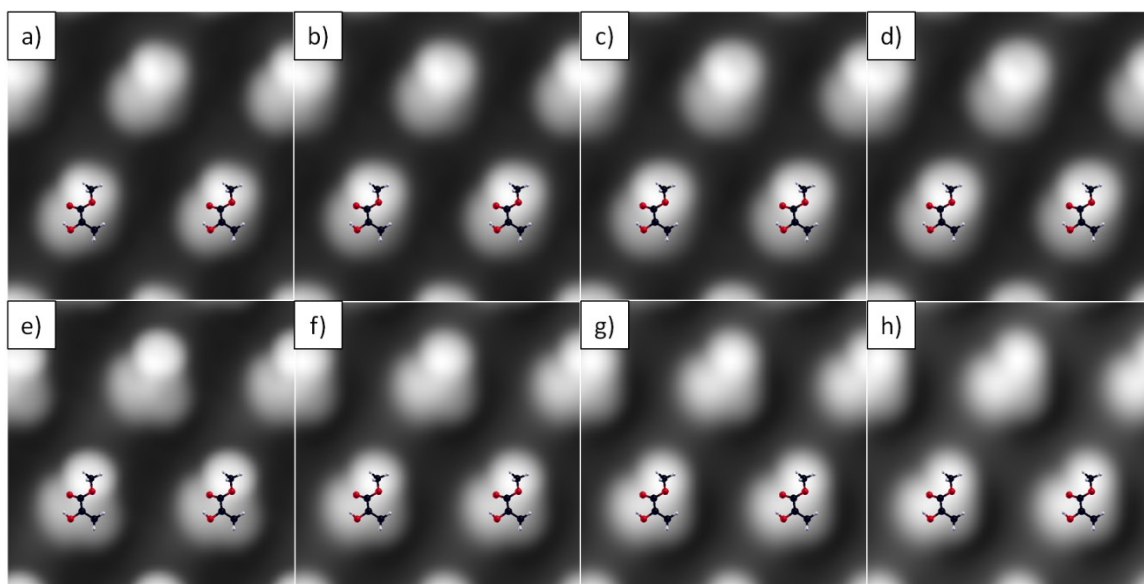


Figure 7.19: STM images of the enol form of methyl pyruvate with the carbonyl groups located on bridge and atop sites (AB cis) imaged with a CO group on Au on W(111) tip at varied bias: a) -0.1 V, b) -0.2 V, c) -0.3 V, d) -0.4 V, e) +0.1 V, f) +0.2 V, g) +0.3 V, h) +0.4 V.

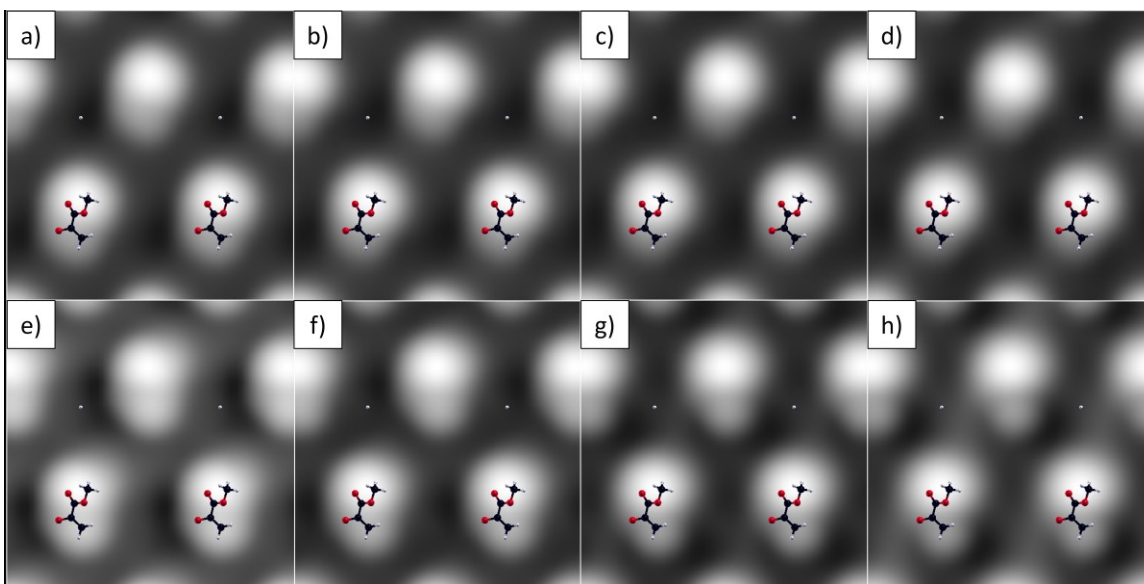


Figure 7.20: STM images of the enolate form of methyl pyruvate with the carbonyl groups located on bridge and atop sites (BA cis) imaged with a Au on W(110) tip at varied bias: a) -0.1 V, b) -0.2 V, c) -0.3 V, d) -0.4 V, e) +0.1 V, f) +0.2 V, g) +0.3 V, h) +0.4 V.

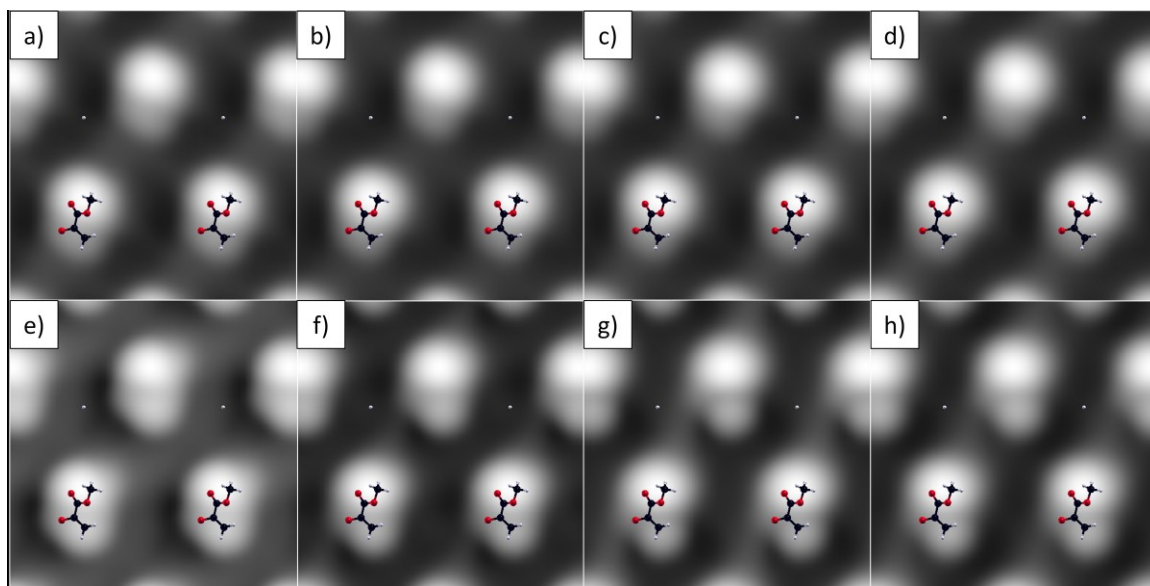


Figure 7.21: STM images of the enolate form of methyl pyruvate with the carbonyl groups located on bridge and atop sites (BA cis) imaged with a CH₃ group on Au on W(110) tip at varied bias: a) -0.1 V, b) -0.2 V, c) -0.3 V, d) -0.4 V, e) +0.1 V, f) +0.2 V, g) +0.3 V, h) +0.4 V.

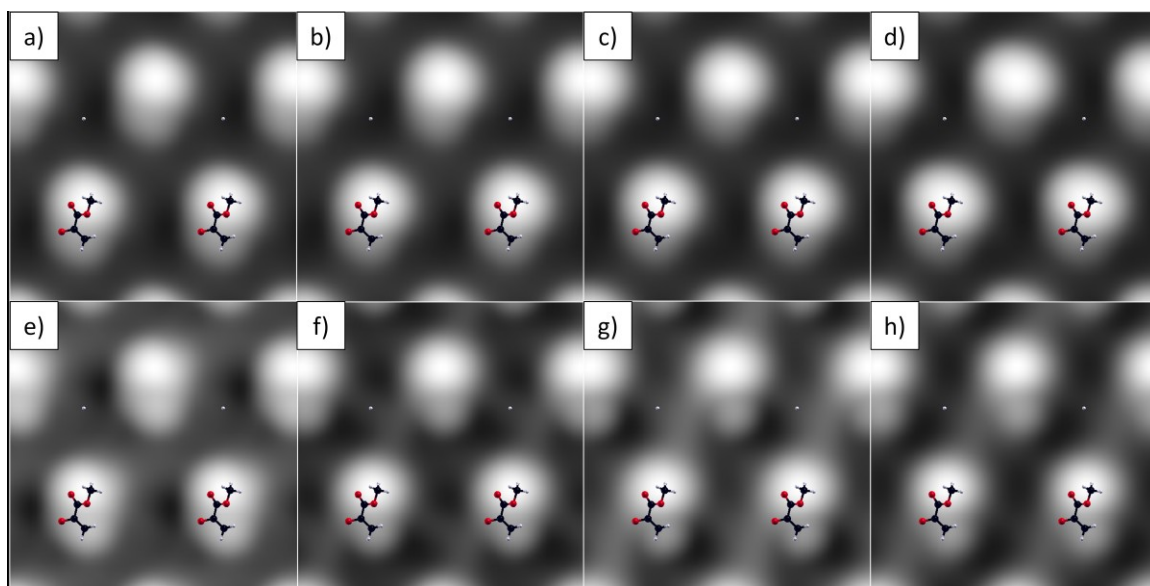


Figure 7.22: STM images of the of the enolate form of methyl pyruvate with the carbonyl groups located on bridge and atop sites (BA cis) imaged with a CO group on Au on W(110) tip at varied bias: a) -0.1 V, b) -0.2 V, c) -0.3 V, d) -0.4 V, e) +0.1 V, f) +0.2 V, g) +0.3 V, h) +0.4 V.

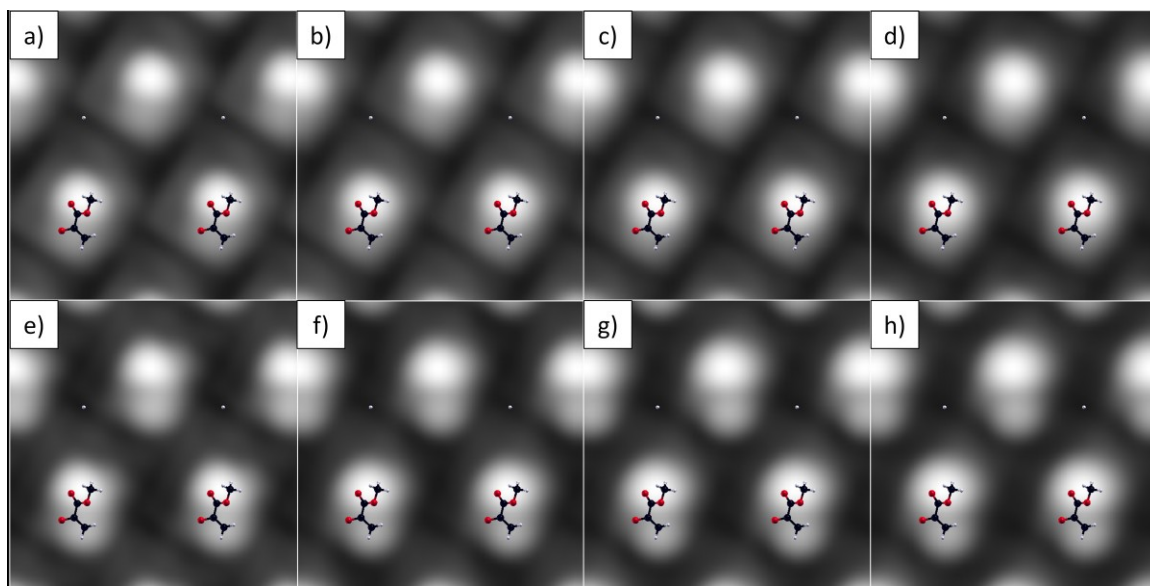


Figure 7.23: STM images of the enolate form of methyl pyruvate with the carbonyl groups located on bridge and atop sites (BA cis) imaged with a Au on W(111) tip at varied bias: a) -0.1 V, b) -0.2 V, c) -0.3 V, d) -0.4 V, e) +0.1 V, f) +0.2 V, g) +0.3 V, h) +0.4 V.

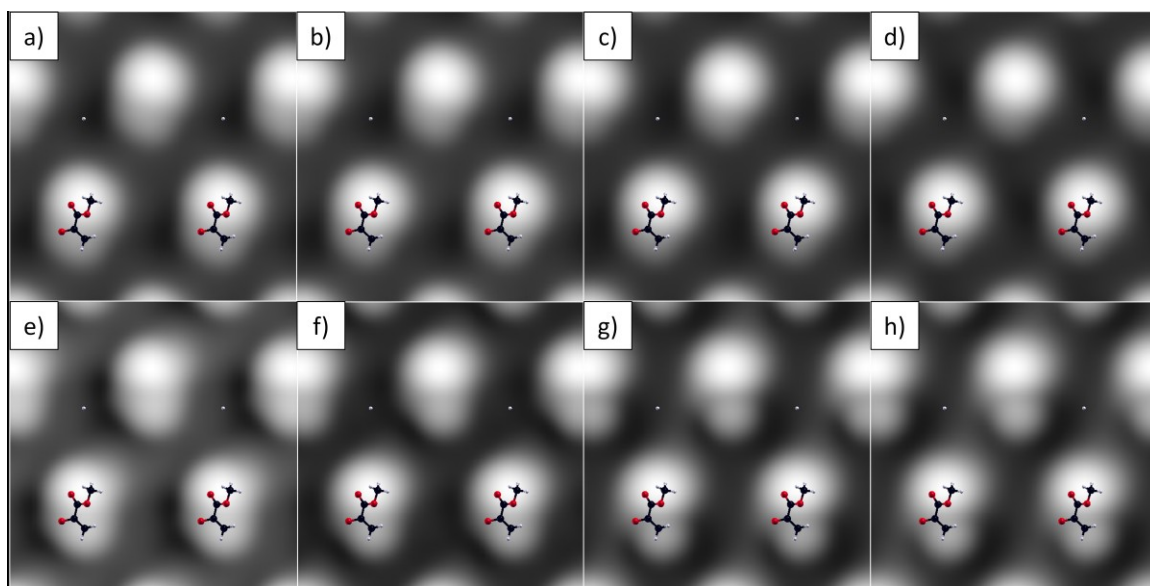


Figure 7.24: STM images of the enolate form of methyl pyruvate with the carbonyl groups located on bridge and atop sites (BA cis) imaged with a CH₃ group on Au on W(111) tip at varied bias: a) -0.1 V, b) -0.2 V, c) -0.3 V, d) -0.4 V, e) +0.1 V, f) +0.2 V, g) +0.3 V, h) +0.4 V.

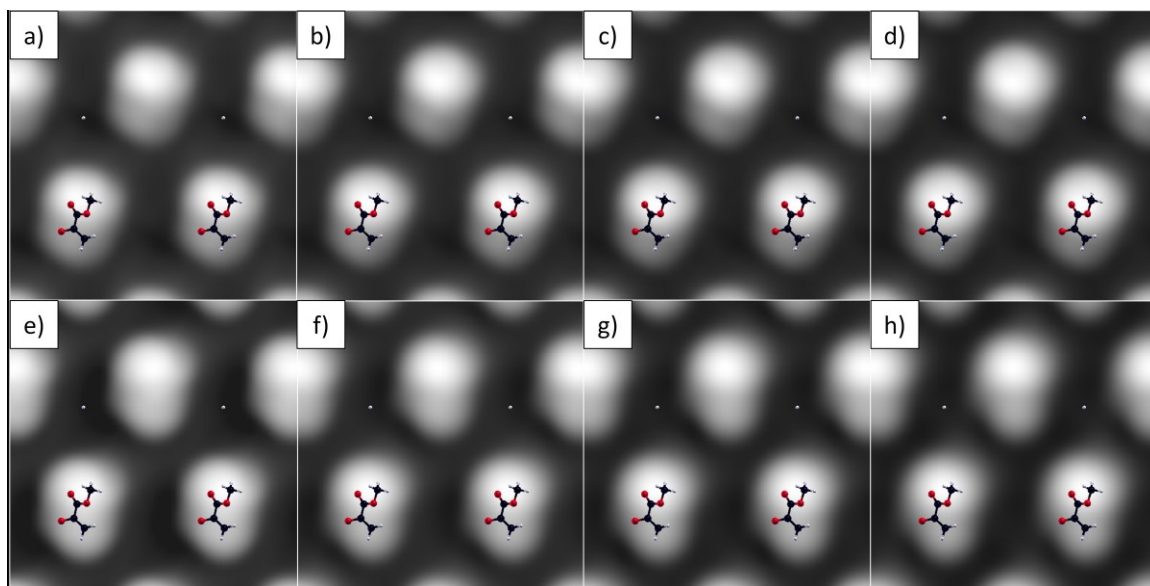


Figure 7.25: STM images of the enolate form of methyl pyruvate with the carbonyl groups located on bridge and atop sites (BA cis) imaged with a CO group on Au on W(111) tip at varied bias: a) -0.1 V, b) -0.2 V, c) -0.3 V, d) -0.4 V, e) +0.1 V, f) +0.2 V, g) +0.3 V, h) +0.4 V.

7.8 References

- [1] Greenler, R. G., Infrared Study of Adsorbed Molecules on Metal Surfaces by Reflection Techniques. *The Journal of Chemical Physics* **1966**, 44 (1), 310-315.
- [2] Chen, C. J., *Introduction to scanning tunneling microscopy*. Oxford University Press: New York, 1993.
- [3] Morgenstern, M., Scanning Tunneling Spectroscopy : Local Density of States and Spin Distribution of Interacting Electron Systems. In *Scanning Probe Microscopy : Characterization, Nanofabrication and Device Application of Functional Materials*, Vilarinho, P. M.; Rosenwaks, Y.; Kingon, A., Eds. Springer Netherlands: 2005; Vol. 186, pp 251-273.

- [4] Feenstra, R. M., Scanning tunneling spectroscopy. *Surface Science* **1994**, 299–300 (0), 965-979.
- [5] Zandvliet, H. J. W.; van Houselt, A., Scanning Tunneling Spectroscopy. *Annual Review of Analytical Chemistry* **2009**, 2 (1), 37-55.
- [6] Burkholder, L.; Tysoe, W. T., Structure and Reaction Pathways of Methyl Pyruvate on Pd(111). *The Journal of Physical Chemistry C* **2009**, 113 (34), 15298-15306.
- [7] Behzadi, B.; Ferri, D.; Baiker, A.; Ernst, K. H., Adsorption mode of the chiral modifier cinchonidine on Au(111). *Applied Surface Science* **2007**, 253 (7), 3480-3484.
- [8] Lavoie, S.; Laliberte, M. A.; McBreen, P. H., Adsorption states and modifier-substrate interactions on Pt(111) relevant to the enantioselective hydrogenation of alkyl pyruvates in the Orito reaction. *Journal of the American Chemical Society* **2003**, 125 (51), 15756-15757.
- [9] Orito, Y.; Imai, S.; Niwa, S., Asymmetric hydrogenation of α -keto esters using a platinum-alumina catalyst modified with cinchona alkaloid. *J. Chem. Soc. Jpn.* **1980**, (4), 670-2.
- [10] Orito, Y.; Imai, S.; Niwa, S.; Nguyengiahung, Asymmetric Hydrogenation of Methyl Benzoylformate Using Platinum-Carbon Catalysts Modified with Cinchonidine. *Journal of Synthetic Organic Chemistry Japan* **1979**, 37 (2), 173-174.

- [11] Orito, Y.; Imai, S.; Niwa, S., Asymmetric Hydrogenation of Methyl Pyruvate Using Pt-C Catalyst Modified with Cinchonidine. *J. Chem. Soc. Jpn.* **1979**, (8), 1118-1120.
- [12] Huck, W.-R.; Bürgi, T.; Mallat, T.; Baiker, A., Asymmetric hydrogenation on platinum: nonlinear effect of coadsorbed cinchona alkaloids on enantiodifferentiation. *Journal of Catalysis* **2003**, 216 (1-2 (40th Anniversary Commemorative Issue)), 276-287.
- [13] Zaera, F., Chiral Modification of Solid Surfaces: A Molecular View. *J. Phys. Chem. C* **2008**, 112 (42), 16196-16203.
- [14] Kacprzak, K.; Gawroński, J., Cinchona Alkaloids and Their Derivatives: Versatile Catalysts and Ligands in Asymmetric Synthesis. *Synthesis* **2001**, (07), 0961-0998.
- [15] Baiker, A., Design of new chiral modifiers for heterogeneous enantioselective hydrogenation: a combined experimental and theoretical approach. In *Chiral Catalyst Immobilization and Recycling*, Vos, D. E. D.; Vankelecom, I. F. J.; Jacobs, P. A., Eds. Wiley-VCH: Weinheim, 2000; pp 155-171.
- [16] Kraynov, A.; Suchopar, A.; D'Souza, L.; Richards, R., Determination of geometric orientation of adsorbed cinchonidine on Pt and Fe and quiphos on Pt nanoclusters via DRIFTS. *Physical Chemistry Chemical Physics* **2006**, 8 (11), 1321-1328.
- [17] Wells, R. P. K.; McGuire, N. R.; Li, X. B.; Jenkins, R. L.; Collier, P. J.; Whyman, R.; Hutchings, G. J., The effect of water on the enantioselective hydrogenation of

- ethyl pyruvate and butane-2,3-dione using cinchona-modified Pt/Al₂O₃. *Physical Chemistry Chemical Physics* **2002**, 4 (12), 2839-2845.
- [18] Margitfalvi, J. L.; Hegedüs, M.; Tfirst, E., Enantio-differentiation over heterogeneous catalysts. The shielding effect model. In *Proceedings of the 11th International Congress on Catalysis, 40th anniversary, Baltimore, MD, USA, June 30-July 5, 1996 (Studies in Surface Science and Catalysis Vol. 101, Part A)*, Hightower, J. W.; Delgass, W. N.; Iglesia, E.; Bell, A. T., Eds. Elsevier: Amsterdam, 1996; pp 241-250.
- [19] Augustine, R. L.; Tanielyan, S. K.; Doyle, L. K., Enantioselective heterogeneous catalysis. I. A working model for the catalyst:modifier:substrate interactions in chiral pyruvate hydrogenations. *Tetrahedron: Asymmetry* **1993**, 4 (8), 1803-27.
- [20] Schwalm, O.; Minder, B.; Weber, J.; Baiker, A., Enantioselective hydrogenation of α -keto esters over Pt/alumina modified with cinchonidine: theoretical investigation of the substrate-modifier interaction. *Catal. Lett.* **1994**, 23 (3-4), 271-79.
- [21] Blaser, H. U.; Jalett, H. P.; Muller, M.; Studer, M., Enantioselective hydrogenation of α -ketoesters using cinchona modified platinum catalysts and related systems: A review. *Catalysis Today* **1997**, 37 (4), 441-463.
- [22] Margitfalvi, J. L.; Tálas, E., Enantioselective hydrogenation of ethyl pyruvate over cinchonidine-Pt/Al₂O₃ catalysts containing anchored silicium organic moieties. *Applied Catalysis A-General* **1999**, 182 (1), 65-74.

- [23] Pfaltz, A.; Heinz, T., Enantioselective Hydrogenation of Ethyl Pyruvate over Pt/Alumina - Systematic Variation of the Modifier Structure. *Topics in Catalysis* **1997**, *4* (3), 229-239.
- [24] Studer, M.; Blaser, H. U.; Exner, C., Enantioselective hydrogenation using heterogeneous modified catalysts: An update [Review]. *Advanced Synthesis & Catalysis* **2003**, *345* (1-2), 45-65.
- [25] Sutherland, I. M.; Ibbotson, A.; Moyes, R. B.; Wells, P. B., Enantioselective hydrogenation. I. Surface conditions during methyl pyruvate hydrogenation catalyzed by cinchonidine-modified platinum/silica (EUROPT-1). *J. Catal.* **1990**, *125* (1), 77-88.
- [26] Meheux, P. A.; Ibbotson, A.; Wells, P. B., Enantioselective hydrogenation. II. Variation of activity and optical yield with experimental variables in methyl pyruvate hydrogenation catalyzed by cinchona-modified platinum/silica (EUROPT-1). *J. Catal.* **1991**, *128* (2), 387-96.
- [27] Bond, G.; Wells, P. B., Enantioselective hydrogenation. IV. Hydrogen isotope exchange in 10,11-dihydrocinchonidine and in quinoline catalyzed by platinum group metals. *J. Catal.* **1994**, *150* (2), 329-34.
- [28] LeBlond, C.; Wang, J.; Andrews, A. T.; Sun, Y.-K., Establishment and maintenance of an optimal chiral surface in cinchona-modified 1% Pt/Al₂O₃ for enantioselective hydrogenation of α -keto esters. *Top. Catal.* **2000**, *13* (3), 169-174.

- [29] Ma, Z.; Lee, I.; Zaera, F., Factors Controlling Adsorption Equilibria from Solution onto Solid Surfaces: The Uptake of Cinchona Alkaloids on Platinum Surfaces. *J. Am. Chem. Soc.* **2007**, *129*, 16083-16090.
- [30] Bürgi, T.; Baiker, A., Heterogeneous Enantioselective Hydrogenation over Cinchona Alkaloid Modified Platinum: Mechanistic Insights into a Complex Reaction. *Accounts of Chemical Research* **2004**, *37* (11), 909-917.
- [31] Garland, M.; Blaser, H. U., A heterogeneous ligand-accelerated reaction: enantioselective hydrogenation of ethyl pyruvate catalyzed by cinchona-modified platinum/aluminum oxide catalysts. *Journal of the American Chemical Society* **1990**, *112* (19), 7048-7050.
- [32] Schneider, M. S.; Urakawa, A.; Grunwaldt, J. D.; Bürgi, T.; Baiker, A., Identification of catalyst surface species during asymmetric platinum-catalysed hydrogenation in a "supercritical" solvent. *Chem Commun* **2004**, (6), 744-745.
- [33] Ferri, D.; Bürgi, T.; Baiker, A., In Situ ATR-IR Study of the Adsorption of Cinchonidine on Pd/Al₂O₃: Differences and Similarities with Adsorption on Pt/Al₂O₃. *Journal of Catalysis* **2002**, *210* (1), 160-170.
- [34] Lai, J. F.; Ma, Z.; Mink, L.; Mueller, L. J.; Zaera, F., Influence of Peripheral Groups on the Physical and Chemical Behavior of Cinchona Alkaloids. *J. Phys. Chem. B* **2009**, *113* (34), 11696-11701.
- [35] Ma, Z.; Lee, I.; Kubota, J.; Zaera, F., In-situ characterization of the adsorption of cinchona chiral modifiers on platinum surfaces. *Journal of Molecular Catalysis A: Chemical* **2004**, *216* (2), 199-207.

- [36] Meier, D. M.; Ferri, D.; Mallat, T.; Baiker, A., Molecular insight into the dynamics of chiral modification of Pt/alumina. *Journal of Catalysis* **2007**, *248* (1), 68-76.
- [37] Szöllősi, G.; Cserényi, S.; Fülöp, F.; Bartók, M., New data to the origin of rate enhancement on the Pt-cinchona catalyzed enantioselective hydrogenation of activated ketones using continuous-flow fixed-bed reactor system. *Journal of Catalysis* **2008**, *260* (2), 245-253.
- [38] Mink, L.; Ma, Z.; Olsen, R.; James, J.; Sholl, D.; Mueller, L.; Zaera, F., The Physico-chemical Properties of Cinchona Alkaloids Responsible for their Unique Performance in Chiral Catalysis. *Topics in Catalysis* **2008**, *48* (1), 120-127.
- [39] Zaera, F., Regio-, Stereo-, and Enantioselectivity in Hydrocarbon Conversion on Metal Surfaces. *Accounts of chemical research* **2009**, *42* (8), 1152-1160.
- [40] Ma, Z.; Zaera, F., The Role of the Solvent in the Adsorption-Desorption Equilibrium of Cinchona Alkaloids between Solution and a Platinum Surface: Correlations among Solvent Polarity, Cinchona Solubility, and Catalytic Performance. *J. Phys. Chem. B* **2005**, *109* (1), 406-414.
- [41] LeBlanc, R. J.; Chu, W.; Williams, C. T., Surface Raman characterization of cinchonidine-modified platinum in ethanol: effects of liquid-phase concentration and co-adsorbed hydrogen. *Journal of Molecular Catalysis A: Chemical* **2004**, *212* (1-2), 277-289.
- [42] Lavoie, S.; Laliberté, M.-A.; Mahieu, G.; Demers-Carpentier, V.; McBreen, P., Keto-Enol Driven Assembly of Methyl Pyruvate on Pt(111). *Journal of the American Chemical Society* **2007**, *129* (38), 11668-11669.

- [43] Burkholder, L.; Garvey, M.; Weinert, M.; Tysoe, W. T., Structure of Methyl Pyruvate and alpha-(1-Naphthyl)ethylamine on Pd(111). *J. Phys. Chem. C* **2011**, *115* (17), 8790-8797.
- [44] Tersoff, J.; Hamann, D. R., Theory and Application for the Scanning Tunneling Microscope. *Physical Review Letters* **1983**, *50* (25), 1998-2001.
- [45] Tersoff, J.; Hamann, D. R., Theory of the scanning tunneling microscope. *Physical Review B* **1985**, *31* (2), 805-813.
- [46] Palotás, K.; Hofer, W. A., Multiple scattering in a vacuum barrier obtained from real-space wavefunctions. *Journal of Physics: Condensed Matter* **2005**, *17* (17), 2705.
- [47] Boscoboinik, J. A.; Bai, Y.; Burkholder, L.; Tysoe, W. T., Structure and Distribution of S-alpha-(1-Naphthyl)-ethylamine on Pd(111). *J. Phys. Chem. C* **2011**, *115* (33), 16488-16494.
- [48] Demers-Carpentier, V.; Goubert, G.; Masini, F.; Lafleur-Lambert, R.; Dong, Y.; Lavoie, S.; Mahieu, G.; Boukouvalas, J.; Gao, H.; Rasmussen, A. M. H.; Ferrighi, L.; Pan, Y.; Hammer, B.; McBreen, P. H., Direct Observation of Molecular Preorganization for Chirality Transfer on a Catalyst Surface. *Science* **2011**, *334* (6057), 776-780.
- [49] Landman, U.; Luedtke, W. D.; Burnham, N. A.; Colton, R. J., Atomistic Mechanisms and Dynamics of Adhesion, Nanoindentation, and Fracture. *Science* **1990**, *248* (4954), 454-461.
- [50] Burkholder, L.; Stacchiola, D. o.; Boscoboinik, J. A.; Tysoe, W. T., Enantioselective Chemisorption on Model Chirally Modified Surfaces: 2-Butanol

- on α -(1-Naphthyl)ethylamine/Pd(111). *The Journal of Physical Chemistry C* **2009**, *113* (31), 13877-13885.
- [51] Kresse, G.; Joubert, D., From ultrasoft pseudopotentials to the projector augmented-wave method. *Physical Review B* **1999**, *59* (3), 1758-1775.
- [52] Blöchl, P. E., Projector augmented-wave method. *Physical Review B* **1994**, *50* (24), 17953-17979.
- [53] Kresse, G.; Hafner, J., Ab initio molecular dynamics for liquid metals. *Physical Review B* **1993**, *47* (1), 558-561.
- [54] Kresse, G.; Furthmüller, J., Efficient iterative schemes for ab initio total-energy calculations using a plane-wave basis set. *Physical Review B* **1996**, *54* (16), 11169-11186.
- [55] Kresse, G.; Furthmüller, J., Efficiency of ab-initio total energy calculations for metals and semiconductors using a plane-wave basis set. *Computational Materials Science* **1996**, *6* (1), 15-50.
- [56] Perdew, J. P.; Burke, K.; Ernzerhof, M., Generalized Gradient Approximation Made Simple. *Physical Review Letters* **1996**, *77* (18), 3865.
- [57] Hofer, W. A.; Redinger, J., Scanning tunneling microscopy of binary alloys: first principles calculation of the current for PtX (100) surfaces. *Surface Science* **2000**, *447* (1-3), 51-61.
- [58] Hofer, W. A., Challenges and errors: interpreting high resolution images in scanning tunneling microscopy. *Progress in Surface Science* **2003**, *71* (5-8), 147-183.

- [59] Burkholder, L.; Tysoe, W. T., Structure and reaction pathways of methyl lactate on Pd(111). *Surface Science* **2009**, *603* (17), 2714-2720.
- [60] Kaltchev, M.; Thompson, A. W.; Tysoe, W. T., Reflection-absorption infrared spectroscopy of ethylene on palladium (111) at high pressure. *Surface Science* **1997**, *391* (1-3), 145-149.
- [61] Pallassana, V.; Neurock, M.; Lusvardi, V. S.; Lerou, J. J.; Kragten, D. D.; van Santen, R. A., A Density Functional Theory Analysis of the Reaction Pathways and Intermediates for Ethylene Dehydrogenation over Pd(111). *The Journal of Physical Chemistry B* **2002**, *106* (7), 1656-1669.
- [62] Pallassana, V.; Neurock, M., Electronic Factors Governing Ethylene Hydrogenation and Dehydrogenation Activity of Pseudomorphic PdML/Re(0001), PdML/Ru(0001), Pd(111), and PdML/Au(111) Surfaces. *Journal of Catalysis* **2000**, *191* (2), 301-317.
- [63] Mittendorfer, F.; Thomazeau, C.; Raybaud, P.; Toulhoat, H., Adsorption of Unsaturated Hydrocarbons on Pd(111) and Pt(111): A DFT Study. *The Journal of Physical Chemistry B* **2003**, *107* (44), 12287-12295.
- [64] Zheng, T.; Stacchiola, D.; Poon, H. C.; Saldin, D. K.; Tysoe, W. T., Determination of the structure of disordered overlayers of ethylene on clean and hydrogen-covered Pd(111) by low-energy electron diffraction. *Surface Science* **2004**, *564* (1-3), 71-78.
- [65] Davis, J. L.; Barteau, M. A., Decarbonylation and decomposition pathways of alcohol's on Pd(111). *Surface Science* **1987**, *187* (2-3), 387-406.

- [66] Gao, F.; Wang, Y. L.; Burkholder, L.; Hirschmugl, C.; Saldin, D. K.; Poon, H. C.; Sholl, D.; James, J.; Tysoe, W. T., The structure and reactivity of 2-butanol on Pd(111). *Surface Science* **2008**, *602* (13), 2264-2270.
- [67] Bardeen, J., Tunnelling from a Many-Particle Point of View. *Physical Review Letters* **1961**, *6* (2), 57-59.
- [68] Stacchiola, D.; Azad, S.; Burkholder, L.; Tysoe, W. T., An Investigation of the Reaction Pathway for Ethylene Hydrogenation on Pd(111). *The Journal of Physical Chemistry B* **2001**, *105* (45), 11233-11239.

Chapter 8

Studying Enantioselectivity on Chirally Modified Surfaces Using Computational Methods: Identifying NEA and Methyl Pyruvate Docking Complexes on Pd(111)

8.1 Introduction

The chiral modifier *S*- α -(1-naphthyl)-ethylamine (NEA) has been studied previously on Pd(111) where it was found to adsorb in two different geometries [1]. DFT calculations showed that the molecule is anchored to the surface by the naphthyl ring and two rotamers, identified as *exo* and *endo*, were found to be stable [2]. McBreen *et al.* have reported similar observations for NEA on Pt(111) [3].

The surface chemistry of methyl pyruvate has been studied on noble-metal surfaces [2, 4-7]. Two forms of methyl pyruvate at low coverages on Pd(111) at 120K were identified in Chapter 7. From DFT calculations and STM simulations, these were determined to be flat-lying keto and enol form of methyl pyruvate. This is similar to the suggestion by McBreen *et al.* that methyl pyruvate can undergo keto-enol tautomerization on Pt(111) at room temperature [6].

The observation of docking complexes via a 1:1 interaction between a chiral modifier and a prochiral reactant have recently been reported on Pt(111) [3, 8].

8.2 Experimental Methods

The Pd(111) substrate was cleaned using a standard procedure consisting of cycles of argon ion sputtering and annealing in 3×10^{-8} Torr of oxygen at 1000 K. The sample was cooled to ~ 270 K immediately before dosing NEA to minimize contamination from the background and decomposition of NEA. (S)-(-)- α -(1-naphthyl)ethylamine (Acros Organics, 99% purity) was dosed from a home-built Knudsen source described elsewhere [9]. Because of the high vapor pressure of NEA, the Knudsen source was cooled to ~ 200 K for at least 60 min before dosing. Methyl pyruvate (Alfa Aesar, 98% purity) was purified by several freeze-pump-thaw cycles. After dosing NEA, the sample was cooled to ~ 120 K and held at that temperature for all imaging. Methyl pyruvate was dosed onto the Pd(111) surface through a variable leak valve while maintaining a sample temperature of ~ 120 K. Following methyl pyruvate adsorption, images were acquired at a sample temperature of ~ 120 K using an electrochemically etched tip made from recrystallized tungsten wire. This was conditioned by a controlled interaction with a clean Au(111) single crystal surface. This is expected to result in a gold-terminated tip [10]. Experiments were performed using a scanning tunneling microscope (RHK UHV350 dual AFM/STM) housed in an ultrahigh vacuum (UHV) chamber operating at a base pressure below 2×10^{-10} Torr following bakeout, as described elsewhere [11].

8.3 Theoretical Methods

Density functional theory (DFT) calculations were performed with the projector augmented wave (PAW) method [12-13] as implemented in VASP [14-16]. The exchange-correlation potential was described using the generalized gradient approximation (GGA) of Perdew, Burke and Ernzerhof [17]. A cutoff of 400 eV was used for the planewave basis set, and the wavefunctions and electron density were converged to within 1×10^{-5} eV. The first Brillouin zone was sampled with a $3 \times 3 \times 1$ Γ -centered k-point mesh. Geometric relaxations were considered to be converged when the force was less than 0.02 eV/Å on all unrestricted atoms.

STM topography simulations were performed with the Bardeen approach to tunneling [18-19] and a scattering method developed to first order in the Green's functions [20] as implemented in bSKAN 3.7.

8.4 Results

8.4.1 STM Images

Images of NEA and methyl pyruvate coadsorbed on Pd(111) were obtained at low coverage and low temperature. Figure 8.1 shows a typical high-resolution image containing NEA and methyl pyruvate. Based on assignments from previous work [1], *exo* and *endo* conformers of NEA are identified. They are indicated by solid white circles (*exo*) and dashed white circles (*endo*) in Figure 8.1. One of the *exo*-NEA molecules is isolated from other features except for a methyl pyruvate molecule that is

adjacent to the bright portion of the NEA. Lines are drawn through the long axes of the dim portion of the NEA and the methyl pyruvate and the angle between the lines is indicated on Figure 8.1 which will be discussed later.

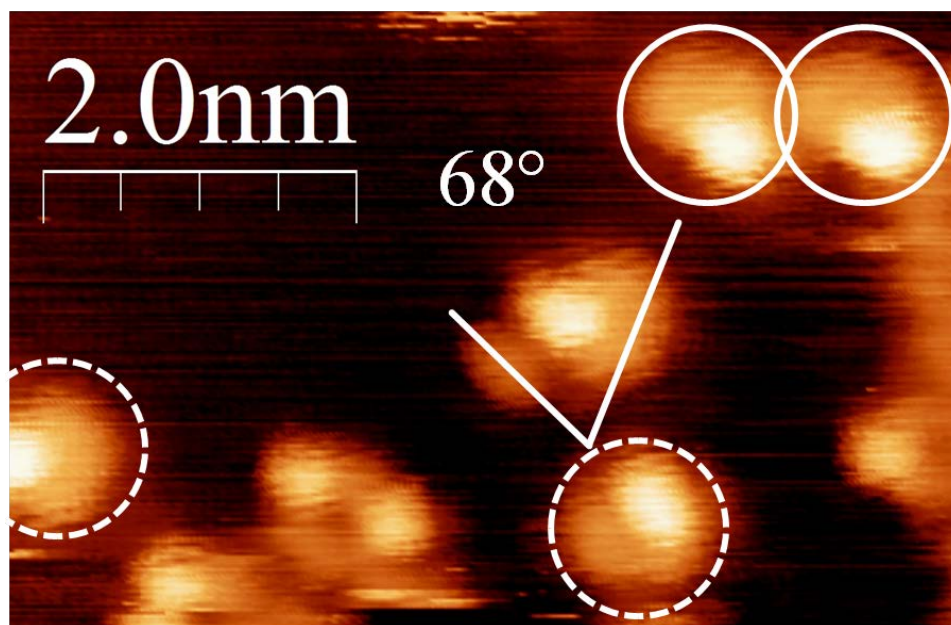


Figure 8.1: NEA and methyl pyruvate on Pd(111) imaged at 120K ($I_t = 183$ pA, $V_b = -154$ mV). Solid and dashed white circles are used to identify *exo*-NEA and *endo*-NEA, respectively. Two intersecting lines are drawn through the long axes of an *exo*-NEA molecule and a methyl pyruvate molecule.

Figure 8.2 shows a typical high-resolution image containing mostly isolated NEA molecules and methyl pyruvate. As in Figure 8.1, the *exo* and *endo* conformers of NEA in Figure 8.2 are identified based on assignments from Boscoboinik, *et al.* [1]. These are again indicated by solid white circles (*exo*) and dashed white circles (*endo*). In this image, one of the isolated NEA molecules has two methyl pyruvate molecules adjacent to the bright portion. Lines are again drawn through the long axes of the NEA and methyl pyruvate molecules and the corresponding angles are indicated on Figure 8.2.

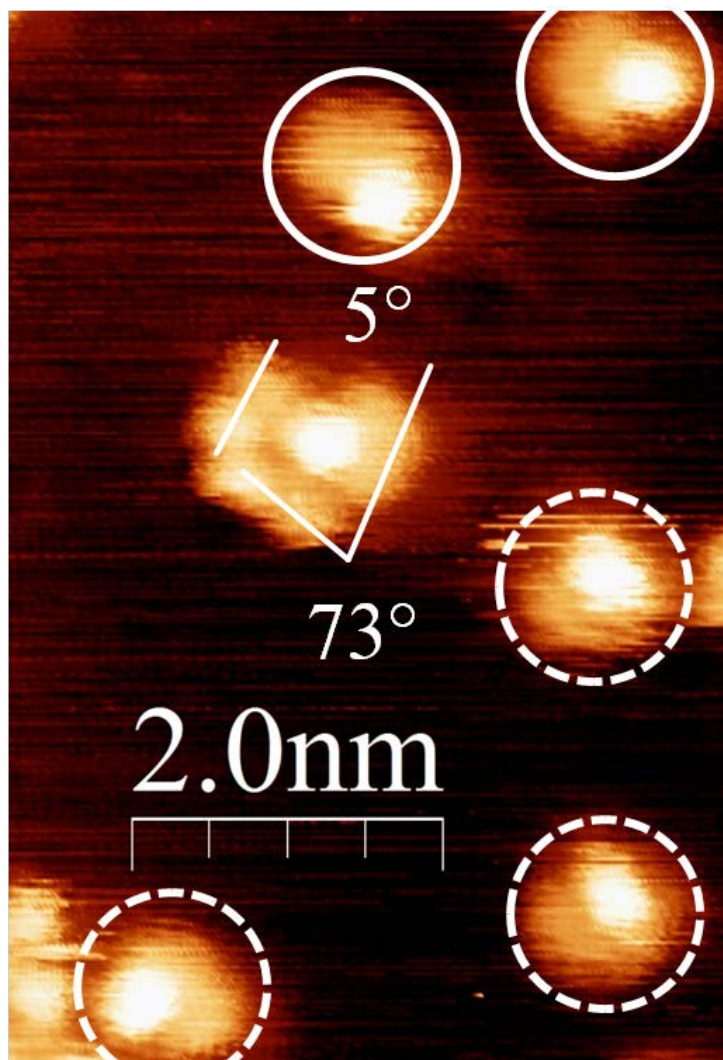


Figure 8.2: NEA and methyl pyruvate on Pd(111) imaged at 120K ($I_t = 280$ pA, $V_b = -154$ mV). Solid and dashed white circles are used to identify *exo*-NEA and *endo*-NEA, respectively. Three lines are drawn through the long axes of an *exo*-NEA molecule and two methyl pyruvate molecules.

8.4.2 DFT Calculations of NEA/Methyl Pyruvate Docking Complexes

Previous DFT calculations of methyl pyruvate on Pd(111) have shown that the two most likely species present are a flat-lying, keto form [2, 5] with the C-C bond between the carbonyl carbons located over an atop site and rotated 30° (keto A30) from the $\langle 1\bar{1}0 \rangle$ directions and a flat-lying syn enol form [5] with the alcohol oxygen located

at an atop site and the carbonyl oxygen located at a bridge site in the initial configuration (enol *syn* AB).

On Pd(111), Burkholder *et al.* found that NEA is most stable when adsorbed with the naphthyl group on the dibridge[7] adsorption site [2]. Rotation of the ethylamine group gives rise to two conformers identified as endo and exo [2].

Based on these results, DFT calculations were performed for combinations of the two most likely forms of methyl pyruvate with the two forms of NEA; keto A30 methyl pyruvate with *endo*-NEA, keto A30 methyl pyruvate with *exo*-NEA, enol *syn* AB methyl pyruvate with *endo*-NEA, and enol *syn* AB methyl pyruvate with *exo*-NEA.

For each combination of NEA and methyl pyruvate species, calculations were performed with the methyl pyruvate molecule located at a range of sites around the ethylamine group of the NEA molecule. The carbonyl and alcohol oxygen atoms of the methyl pyruvate species were oriented towards the amine group on the NEA molecule.

Eight reasonable starting geometries were identified for keto A30 methyl pyruvate near the ethylamine group of endo NEA. The converged geometries of the calculations are shown in Figure 8.3. The adsorption energy for the calculations is defined as follows:

$$E_{ads} = E_{tot} - E_{Pd} - E_{MP} - E_{NEA}$$

where E_{tot} is the total energy of the combined methyl pyruvate and NEA on Pd(111) calculation and E_{Pd} , E_{MP} , and E_{NEA} are the total energies the Pd(111) substrate, gas-phase methyl pyruvate, and gas-phase NEA, respectively. The interaction energy is defined as follows:

$$E_{int} = E_{ads} - E_{ads,NEA} - E_{ads,MP}$$

where E_{ads} is the adsorption energy of the system as defined above and $E_{ads,NEA}$ and $E_{ads,MP}$ are the adsorption energies of the NEA and methyl pyruvate species, respectively, calculated separately on Pd(111). The adsorption energies and interaction energies for the eight geometries shown in Figure 8.3 are listed in Table 8.1.

Next, eight reasonable starting geometries were identified for keto A30 methyl pyruvate near the ethylamine group of the other rotamer, *exo* NEA. The converged geometries of those calculations are shown in Figure 8.4. The adsorption and interaction energies were calculated as described above and are listed in Table 8.2 for the geometries shown in Figure 8.4.

For the combination of enol *syn* AB methyl pyruvate and *endo* NEA, seven reasonable starting geometries were identified where the alcohol and carbonyl groups of methyl pyruvate were near the ethylamine group of NEA. The converged geometries of those calculations are shown in Figure 8.5. The adsorption and interaction energies were calculated as described above and are listed in Table 8.3 for the geometries shown in Figure 8.5.

Finally, seven reasonable starting geometries were identified for enol *syn* AB methyl pyruvate near the ethylamine group of *exo* NEA. The converged geometries of those calculations are shown in Figure 8.6. The adsorption and interaction energies were calculated as described above and are listed in Table 8.4 for the geometries shown in Figure 8.6.

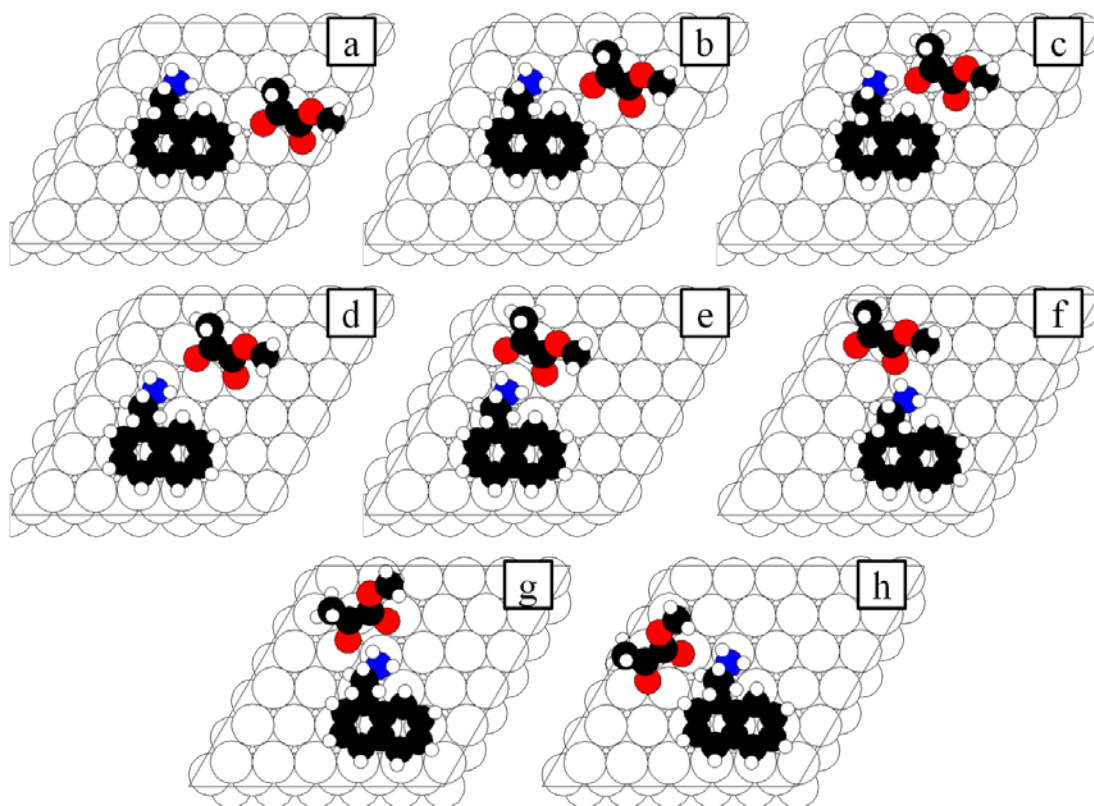


Figure 8.3: Converged geometries for the eight combinations of R-endo NEA and keto methyl pyruvate on Pd(111) calculated with DFT. They are identified as: (a) Geo01, (b) Geo02, (c) Geo03, (d) Geo04, (e) Geo05, (f) Geo06, (g) Geo07, and (h) Geo08.

System	E_{ads} (kJ/mol)	E_{int} (kJ/mol)
R-endo NEA + MP keto A30		
Geo01	-252.2	+18.5
Geo02	-267.6	+3.1
Geo03	-238.5	+32.2
Geo04	-268.9	+1.9
Geo05	-267.0	+3.8
Geo06	-243.8	+26.9
Geo07	-257.2	+13.6
Geo08	-259.7	+11.0

Table 8.1: Adsorption and interaction energies of R-endo NEA and keto methyl pyruvate on Pd(111) calculated using DFT for the geometries shown in Figure 8.3.

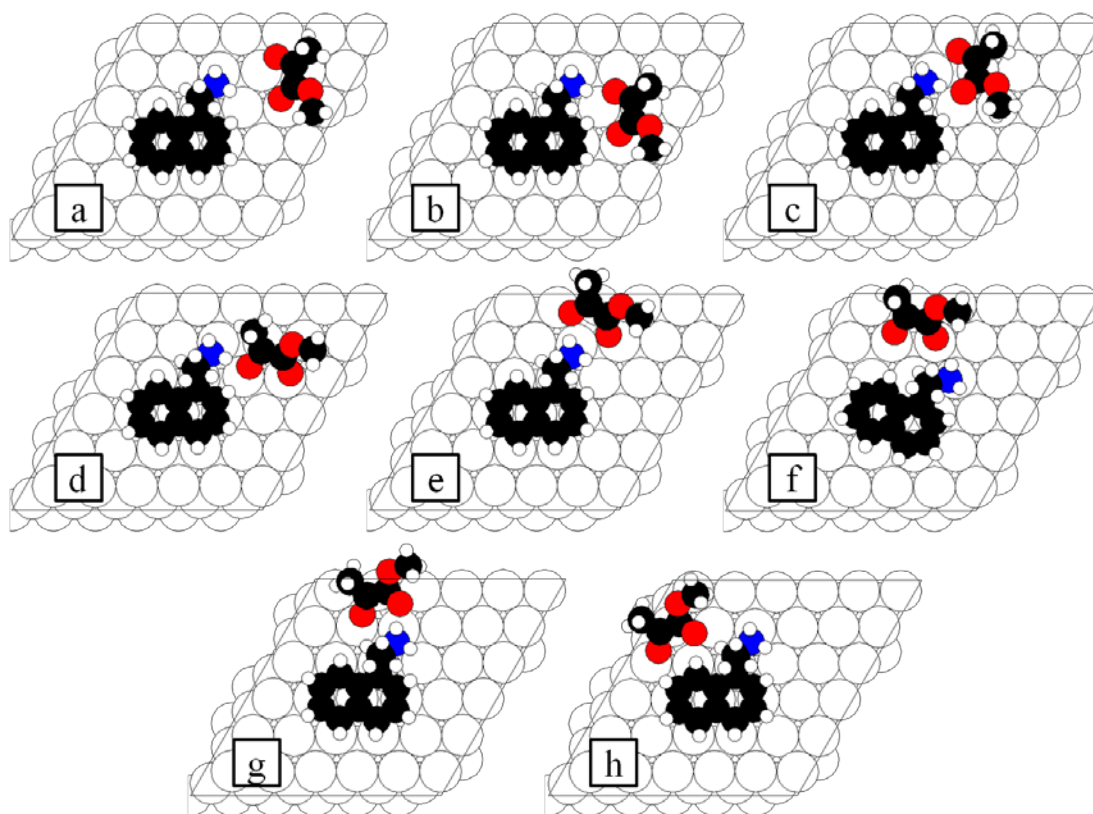


Figure 8.4: Converged geometries for the eight combinations of R-exo NEA and keto methyl pyruvate on Pd(111) calculated with DFT. They are identified as: (a) Geo01, (b) Geo02, (c) Geo03, (d) Geo04, (e) Geo05, (f) Geo06, (g) Geo07, and (h) Geo08.

System	E_{ads} (kJ/mol)	E_{int} (kJ/mol)
R-exo NEA + MP keto A30		
Geo01	-263.1	+9.2
Geo02	-271.9	+0.5
Geo03	-258.1	+14.3
Geo04	-251.2	+21.1
Geo05	-262.5	+9.8
Geo06	-260.8	+11.5
Geo07	-257.3	+15.0
Geo08	-235.1	+37.3

Table 8.2: Adsorption and interaction energies of R-exo NEA and keto methyl pyruvate on Pd(111) calculated using DFT for the geometries shown in Figure 8.4.

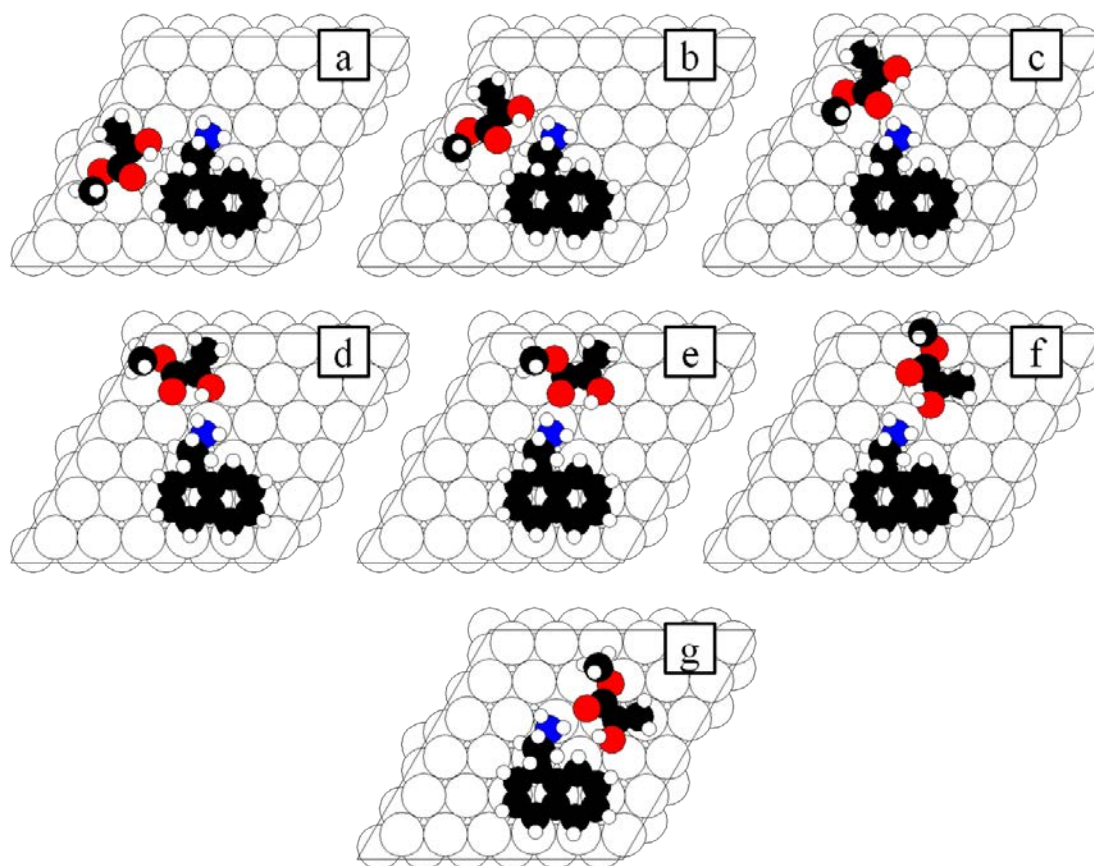


Figure 8.5: Converged geometries for the seven combinations of R-endo NEA and enol syn methyl pyruvate on Pd(111) calculated with DFT. They are identified as: (a) Geo01, (b) Geo02, (c) Geo03, (d) Geo04, (e) Geo05, (f) Geo06, and (g) Geo07.

System	E_{ads} (kJ/mol)	E_{int} (kJ/mol)
R-endo NEA + MP enol syn AB		
Geo01	-229.7	+55.9
Geo02	-246.4	+39.2
Geo03	-286.3	-0.7
Geo04	-265.8	+19.8
Geo05	-286.5	-0.9
Geo06	-272.8	+12.7
Geo07	-272.7	+12.9

Table 8.3: Adsorption and interaction energies of R-endo NEA and enol syn methyl pyruvate on Pd(111) calculated using DFT for the geometries shown in Figure 8.5.

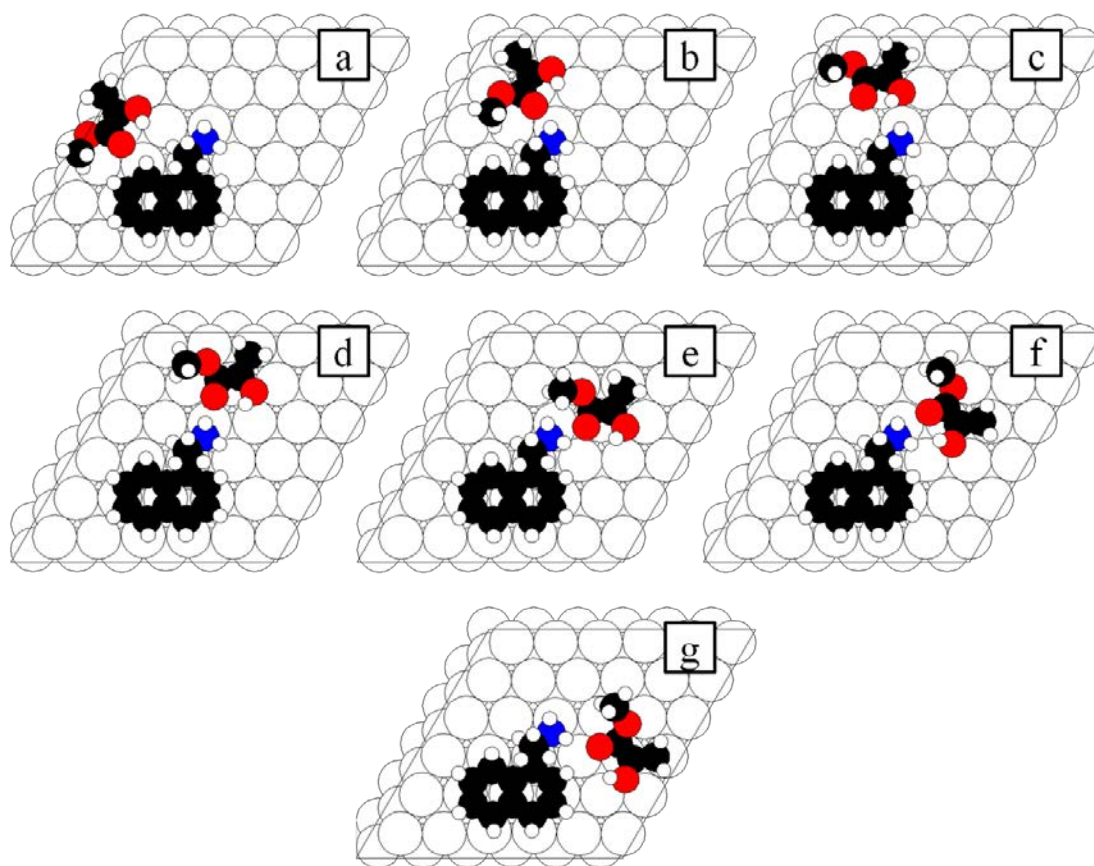


Figure 8.6: Converged geometries for the seven combinations of R-exo NEA and enol syn methyl pyruvate on Pd(111) calculated with DFT. They are identified as: (a) Geo01, (b) Geo02, (c) Geo03, (d) Geo04, (e) Geo05, (f) Geo06, and (g) Geo07.

System	E_{ads} (kJ/mol)	E_{int} (kJ/mol)
R-endo NEA + MP enol syn AB		
Geo01	-273.9	+13.3
Geo02	-288.1	-0.9
Geo03	-269.8	+17.4
Geo04	-292.5	-5.2
Geo05	-265.1	+22.1
Geo06	-277.3	+10.0
Geo07	-292.7	-5.5

Table 8.4: Adsorption and interaction energies of R-exo NEA and enol syn methyl pyruvate on Pd(111) calculated using DFT for the geometries shown in Figure 8.6.

The adsorption energies for the combinations range from \sim 230 kJ/mol to \sim 293 kJ/mol indicating that all complexes are relatively strongly bound to the surface. However, both species have been shown to have relatively large adsorption energies in previous work (\sim 220 kJ/mol for NEA [2], \sim 45 kJ/mol for keto methyl pyruvate, and \sim 60 kJ/mol for enol methyl pyruvate [5]). Also, the goal is to find combinations that would be likely to form and therefore be observed in STM images of the coadsorbed species. The interaction energy is a good indicator of this since it is the difference between the adsorption energy of the combined species and the individual species calculated in separate cells (i.e. infinitely separated). This should be an approximation of the energy gained (or lost) when the two species come together to form a docking complex on the surface for a given geometry.

It can be seen that most of the interaction energies are not favorable for the formation of a complex. For both endo and exo NEA with keto A30 methyl pyruvate all of the calculated geometries are higher in energy than the separated species. There are two geometries (Geo03 and Geo05 in Figure 8.5 and Table 8.3) for endo NEA with enol syn methyl pyruvate that gain energy relative to the separated species, but the gain is small. However, in the case of the last combination, exo NEA with enol syn methyl pyruvate, we find two geometries (Geo04 and Geo07 in Figure 8.6 and Table 8.4) that result in modest gains in energy. The NEA and methyl pyruvate species in these combinations are also the more energetically favorable species from individual calculations.

8.4.3 STM Simulations of NEA/Methyl Pyruvate Docking Complexes

From the observations above regarding the interaction energies, it appears that the most likely combinations to form a “docking complex” are the Geo04 and Geo07 geometries of exo NEA combined with enol syn methyl pyruvate. Because of this, STM simulations were performed for those geometries. Figures 8.7 and 8.8 show the simulated STM images for the Geo07 and Geo04 combinations, respectively, of exo NEA and enol syn methyl pyruvate.

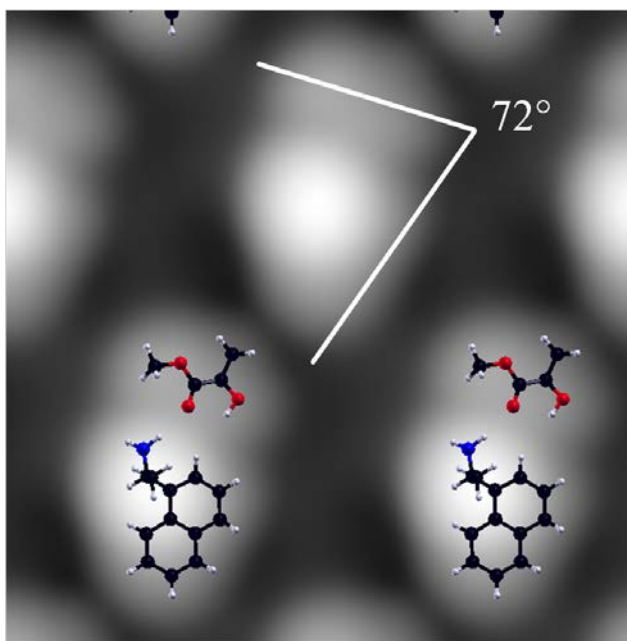


Figure 8.7: STM simulation of R-exo NEA and enol syn methyl pyruvate on Pd(111) obtained from the DFT calculated structure Geo07 in Figure 8.6. Intersecting lines are drawn through the long axes of the NEA and methyl pyruvate molecules and the angle between those lines is indicated.

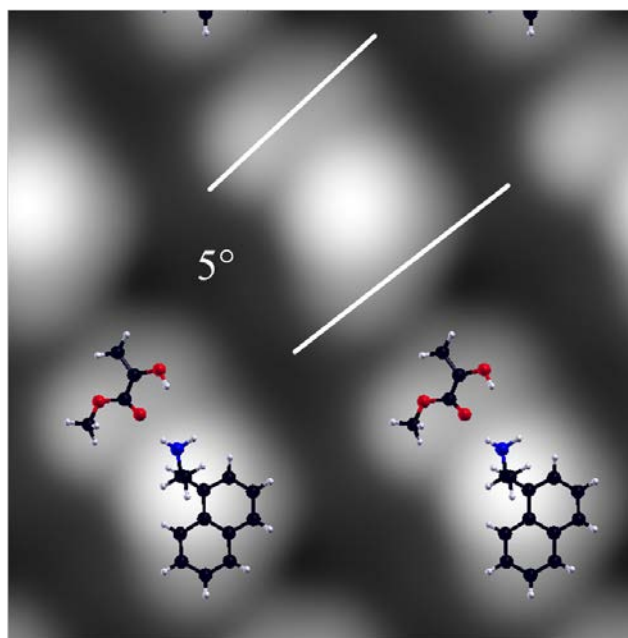


Figure 8.8: STM simulation of R-exo NEA and enol syn methyl pyruvate on Pd(111) obtained from the DFT calculated structure Geo04 in Figure 8.6. Lines are drawn through the long axes of the NEA and methyl pyruvate molecules and the angle between those lines is indicated.

8.5 Discussion

Two stable docking complex geometries have been identified for syn enol methyl pyruvate located near the ethylamine group of exo NEA. Based on their adsorption and interaction energies, they are the most stable of the calculated geometries and would gain ~5 kJ/mol of energy upon formation relative to the isolated species. STM simulations of the two geometries were performed to compare the visual appearance and relative orientations of the two species in both cases.

The first experimentally observed docking complex in Figure 8.1 appears to have the same general shapes as the simulated image of the Geo07 exo NEA with syn enol methyl pyruvate complex shown in Figure 8.7. The angle between the long axes of the

NEA and methyl pyruvate species is also in good agreement between the two images ($\sim 68^\circ$ experimentally versus $\sim 72^\circ$ simulated).

The second STM image, shown in Figure 8.2, contains a docking complex that appears to have two methyl pyruvate species adjacent to the bright protrusion, which has been shown previously to correspond to the ethylamine group of NEA. The long axis of one of the methyl pyruvate species is oriented at $\sim 73^\circ$ relative to the long axis of the NEA molecule, again in good agreement with the Geo07 exo NEA with syn enol methyl pyruvate complex shown in Figure 8.7. The other methyl pyruvate species is oriented with the long axis rotated $\sim 5^\circ$ with respect to the long axis of the NEA molecule, in good agreement with the Geo04 exo NEA with syn enol methyl pyruvate complex shown in Figure 8.8.

Based on the relative stability of the Geo04 and Geo07 exo NEA with syn enol methyl pyruvate complexes, the general visual agreement of their simulated images with the experimentally observed complexes, and the good agreement with the relative orientations between the NEA and methyl pyruvate species, the following assignments are made. The docking complex observed in Figure 8.1 is proposed to have the structure of the Geo07 exo NEA with syn enol methyl pyruvate complex converged geometry shown in Figure 8.6. The docking complex observed in Figure 8.2 is proposed to have a structure similar to a combination of the Geo04 and Geo07 exo NEA with syn enol methyl pyruvate complex converged geometries shown in Figure 8.6.

The structures of the two docking complexes are analyzed to explore the origin of the prochiral interaction. Indeed, both geometries show potential for hydrogen-bonding interactions between the NEA and methyl pyruvate species. Specifically, both

geometries have the carbonyl oxygen, a good H-bond acceptor, in close proximity to the amine group of the NEA, a good H-bond donor. In addition to having a prochiral interaction in which hydrogenation of the methyl pyruvate to methyl lactate would result in enantiospecific chemistry, the interaction with the enol form of methyl pyruvate is much larger than with the keto form. That is, the interaction is not only enantiospecific, but also favors one tautomer over the other. In the case of the enol form of methyl pyruvate, methyl lactate is formed by hydrogenation of a C=C bond, rather than hydrogenation of a C=O bond for the keto form.

Group VIII metals, for example platinum and palladium, are good hydrogenation catalysts for carbon-carbon double bonds, which, in turn, are hydrogenated more than C=O bonds. This implies that the interaction between NEA and methyl pyruvate results not only in the formation of a prochiral adsorbate but also a chemospecific interaction to form a more reactive enol form of methyl pyruvate. It has been demonstrated that this combination results in the large enantioselectivities found for enantioselective catalysts [21].

8.6 Conclusions

Two docking complexes between NEA and methyl pyruvate have been observed in STM images on Pd(111). Based on DFT calculations and STM simulations, the docking complexes are identified as occurring between exo NEA and syn enol methyl pyruvate. Potential hydrogen-bonding interactions are identified in both proposed docking complex geometries.

8.7 References

- [1] Boscoboinik, J. A.; Bai, Y.; Burkholder, L.; Tysoe, W. T., Structure and Distribution of S- α -(1-Naphthyl)-ethylamine on Pd(111). *The Journal of Physical Chemistry C* **2011**, *115* (33), 16488-16494.
- [2] Burkholder, L.; Garvey, M.; Weinert, M.; Tysoe, W. T., Structure of Methyl Pyruvate and α -(1-Naphthyl)ethylamine on Pd(111). *J. Phys. Chem. C* **2011**, *115* (17), 8790-8797.
- [3] Demers-Carpentier, V.; Goubert, G.; Masini, F.; Lafleur-Lambert, R.; Dong, Y.; Lavoie, S.; Mahieu, G.; Boukouvalas, J.; Gao, H.; Rasmussen, A. M. H.; Ferrighi, L.; Pan, Y.; Hammer, B.; McBreen, P. H., Direct Observation of Molecular Preorganization for Chirality Transfer on a Catalyst Surface. *Science* **2011**, *334* (6057), 776-780.
- [4] Burkholder, L.; Tysoe, W. T., Structure and Reaction Pathways of Methyl Pyruvate on Pd(111). *The Journal of Physical Chemistry C* **2009**, *113* (34), 15298-15306.
- [5] Garvey, M.; Bai, Y.; Boscoboinik, J. A.; Burkholder, L.; Sorensen, T. E.; Tysoe, W. T., Identifying Molecular Species on Surfaces by Scanning Tunneling Microscopy: Methyl Pyruvate on Pd(111). *The Journal of Physical Chemistry C* **2013**, *117* (9), 4505-4514.
- [6] Lavoie, S.; Lalibert , M.-A.; Mahieu, G.; Demers-Carpentier, V.; McBreen, P., Keto-Enol Driven Assembly of Methyl Pyruvate on Pt(111). *Journal of the American Chemical Society* **2007**, *129* (38), 11668-11669.

- [7] Schneider, M. S.; Urakawa, A.; Grunwaldt, J.-D.; Burgi, T.; Baiker, A., Identification of catalyst surface species during asymmetric platinum-catalysed hydrogenation in a "supercritical" solvent. *Chemical Communications* **2004**, 0 (6), 744-745.
- [8] Demers-Carpentier, V.; Rasmussen, A. M. H.; Goubert, G.; Ferrighi, L.; Dong, Y.; Lemay, J.-C.; Masini, F.; Zeng, Y.; Hammer, B.; McBreen, P. H., Stereodirection of an α -Ketoester at Sub-molecular Sites on Chirally Modified Pt(111): Heterogeneous Asymmetric Catalysis. *Journal of the American Chemical Society* **2013**, 135 (27), 9999-10002.
- [9] Boscoboinik, J. A. Small Organic Molecules on Transition Metal Surfaces and Monte Carlo Simulations of Bimetallic Surface Alloys. Ph.D. Dissertation, University of Wisconsin-Milwaukee, Milwaukee, WI, 2010.
- [10] Landman, U.; Luedtke, W. D.; Burnham, N. A.; Colton, R. J., Atomistic Mechanisms and Dynamics of Adhesion, Nanoindentation, and Fracture. *Science* **1990**, 248 (4954), 454-461.
- [11] Burkholder, L.; Stacchiola, D. o.; Boscoboinik, J. A.; Tysoe, W. T., Enantioselective Chemisorption on Model Chirally Modified Surfaces: 2-Butanol on α -(1-Naphthyl)ethylamine/Pd(111). *The Journal of Physical Chemistry C* **2009**, 113 (31), 13877-13885.
- [12] Blöchl, P. E., Projector augmented-wave method. *Physical Review B* **1994**, 50 (24), 17953-17979.

- [13] Kresse, G.; Joubert, D., From ultrasoft pseudopotentials to the projector augmented-wave method. *Physical Review B* **1999**, *59* (3), 1758-1775.
- [14] Kresse, G.; Furthmüller, J., Efficient iterative schemes for ab initio total-energy calculations using a plane-wave basis set. *Physical Review B* **1996**, *54* (16), 11169-11186.
- [15] Kresse, G.; Furthmüller, J., Efficiency of ab-initio total energy calculations for metals and semiconductors using a plane-wave basis set. *Computational Materials Science* **1996**, *6* (1), 15-50.
- [16] Kresse, G.; Hafner, J., Ab initio molecular dynamics for liquid metals. *Physical Review B* **1993**, *47* (1), 558-561.
- [17] Perdew, J. P.; Burke, K.; Ernzerhof, M., Generalized Gradient Approximation Made Simple. *Physical Review Letters* **1996**, *77* (18), 3865.
- [18] Hofer, W. A., Challenges and errors: interpreting high resolution images in scanning tunneling microscopy. *Progress in Surface Science* **2003**, *71* (5–8), 147-183.
- [19] Hofer, W. A.; Redinger, J., Scanning tunneling microscopy of binary alloys: first principles calculation of the current for PtX (100) surfaces. *Surface Science* **2000**, *447* (1–3), 51-61.
- [20] Palotás, K.; Hofer, W. A., Multiple scattering in a vacuum barrier obtained from real-space wavefunctions. *Journal of Physics: Condensed Matter* **2005**, *17* (17), 2705.

- [21] Diezi, S.; Ferri, D.; Vargas, A.; Mallat, T.; Baiker, A., The Origin of Chemo- and Enantioselectivity in the Hydrogenation of Diketones on Platinum. *Journal of the American Chemical Society* **2006**, *128* (12), 4048-4057.

Chapter 9

Conclusions

9.1 Summary

This dissertation has presented several examples of the application of computational chemistry methods to the interpretation and analysis of experimentally obtained results. This is an area of crucial and growing importance to fundamental research. Using a combination of computational and experimental methods allows researchers to probe properties of materials and systems that cannot be directly studied with current experimental methods. The two main areas covered in this dissertation, tribology and analysis of surface adsorbates by scanning tunneling microscopy (STM), can benefit from this approach.

Research in tribology can often focus on surfaces and interfaces that are not well defined. Also, many tribological phenomena of interest are dynamic processes that occur at interfaces which cannot be directly interrogated by experiment. Using computational models such as density functional theory (DFT) and molecular dynamics can help to elucidate the underlying structure and interactions at these interfaces.

The tribological applications presented in Chapters 3-5 have recently been cited in a review article [1] featured on the cover of the Journal of Vacuum Science & Technology. The authors write [1], “We expect that use of DFT for friction studies will increase in popularity both as a means of providing reference data to fit empirical

potentials and to explore frictional mechanisms on their own.” This is further evidence of the importance of this work.

In Chapter 3, it has been shown that the corrugation of the sliding potential of potassium chloride on iron, though small, can be reproduced with high precision DFT calculations. The height of sliding potentials can be determined effectively by calculating the energy at high-symmetry sites along a sliding path, greatly reducing the computational effort that would be required to calculate step-wise displacements along the sliding direction. The calculated value of the zero-pressure limit of the shear strength (S_0) of a KCl film was found to be in good agreement with the experimental value.

Expanding on the method developed in Chapter 3, the potentials at high-symmetry sites are calculated as a function of compression in Chapter 4. It was found that the energy varied harmonically with vertical distance and the calculated parameter S_0 was in excellent agreement with the experimental value. The pressure dependence was found to arise from the difference in separation between the film and the interface at different sites which requires additional work to be done against the applied normal load.

To further refine the model, the effect of varying the potassium chloride film thickness was explored in Chapter 5. A four-layer KCl film was calculated by the same method as the two-layer film and the results were compared. The values of S_0 and α were found to be in excellent agreement with the previous two-layer results. This suggests that the thickness of the KCl film does not appreciably affect its tribological properties, and that the local interactions at the interface play an important role.

In Chapter 6, to more accurately model the expected sliding interface, tungsten carbide is modeled with potassium chloride using the previously developed method.

Calculations were performed for KCl films in registry with the $(1\bar{1}00)$ and $(10\bar{1}0)$ faces of WC. The values of S_0 were found to be anisotropic and the averages for the two faces were found to be in good agreement with the experimental value. This implies that the assumption that the KCl and WC are in registry at the interface is correct. The calculated (and experimental) values of the shear strength are much lower than the shear modulus of KCl which indicates that sliding occurs between the WC tribopin and the outermost layer of the film. This is also in agreement with experiment, where no transfer film is found for KCl on an iron substrate.

Scanning tunneling microscopy takes advantage of the quantum mechanical behavior of electrons. Images obtained by a scanning tunneling microscope can often be difficult to interpret visually. Density functional theory calculations of possible structures can be used to simulate STM images which can then be compared to the experimental images. Also, the exact nature of the STM tip used to obtain the images is often unknown. Simulation of the images using varying tip models can help elucidate the structure and possibly the chemical composition of the experimental tip.

In Chapter 7, STM images of methyl pyruvate adsorbed on Pd(111) were assigned by comparison with the structures calculated using DFT and images simulated using bSKAN, combined with the results of previous spectroscopic measurements. Two distinct methyl-pyruvate-derived species were identified at low coverages and assigned by comparing both the orientations and shapes of the simulated structures with those found experimentally.

The first species was a flat-lying, keto form of *cis*-methyl pyruvate. It was characterized by two-lobed structures with the long axes of the structures oriented at $\sim 0^\circ$

and $\sim 30^\circ$ to the close-packed directions, and the simulated images agreed well with those found experimentally. It was found that the simulated structures were not strongly dependent on the tip structure or tip bias voltage, as found experimentally.

This approach was used to identify the nature of the second species as the enol form of *cis*-methyl pyruvate with the carbonyl groups located on atop and bridge sites. The orientation of the structures with respect to the underlying Pd(111) lattice as well as the calculated image shapes were in good agreement with the experimental images.

In Chapter 8, two docking complexes between NEA and methyl pyruvate were observed in STM images on Pd(111). Based on DFT calculations and STM simulations, the docking complexes were identified as occurring between *exo*-NEA and *syn* enol methyl pyruvate. Potential hydrogen-bonding interactions were identified in both proposed docking complex geometries.

9.2 References

- [1] Dong, Y.; Li, Q.; Martini, A., Molecular Dynamics Simulation of Atomic Friction: A Review and Guide. *Journal of Vacuum Science & Technology A: Vacuum, Surfaces, and Films* **2013**, *31* (3), 030801-24.

Appendix

The following sections present sample input files for *flair*, VASP, and bSKAN, job submission files and Bash shell scripts. Each file is preceded by a short description and then the filename as used by the author is given. The contents of the file are given next and are enclosed by a dashed line above and below. Filenames, input keywords, Linux commands and file contents are shown in `Courier New` font. The following is an example of the format:

Description: This will contain a short description of the file or files to follow.

Filename: `example_filename`

The contents of the file will be given here.

Comments are preceded by either "`#`" or "`!`" and can be at the beginning of a line or some point after the non-commented text.

Sample *flair* Input File

Description: The following is an example *flair* input file for bulk tungsten carbide.

Filename: inp

```
-----
WC                                     ! title

&input cartesian=f /

    0.5    -0.5    0.0                ! lattice vector a1
    0.5     0.5    0.0                ! lattice vector a2
    0.0     0.0    1.0                ! lattice vector a3
2.94 A                                ! overall lattice constant
    1.0   -3.0    0.98                ! scale factors for each direction
                                       ! if scale < 0, then take square
                                       ! root, i.e., -3.0 = sqrt(3.0)

    2                                     ! number of atoms
    74    0.0   0.0   0.0
    6     2/3  1/3  1/2

&allatoms dx=0.028 lnonsph=4 /
&atom id=74 element='W' rmt=2.5 /
&atom id=6  element='C' rmt=1.0 /

&comp gmax=12.0
      kmax=3.5
      jspins=1
/

&conv itmax_scf=120 /

&kpt  tkb=0.001 div1=8 kshift=t origin=0,0,1 /
&mpi  eigdir="/tmp/Mike" /
&mix  alpha=0.3 /

&geo l_geo=t maxstep=20 /                ! perform geometry optimization
                                       ! with 20 steps max
&relax 000 111 /                        ! freeze x,y,z for atom type 1 and
                                       ! relax x,y,z for atom type 2
&exco gga='pbe' /                        ! use pbe for exchange-correlation
-----
```

Sample VASP Input Files

Description: The following VASP input files are for a Au(111) 2x2 supercell with four layers of gold and $\sim 22\text{\AA}$ vacuum gap in the z direction.

Filename: INCAR

```
-----
SYSTEM = 2x2x4 Au(111)    # title

PREC   = Normal
ENCUT  = 400              # planewave basis cutoff (eV)
ALGO   = Fast             # electronic minimization algorithm
LREAL  = Auto

NELMDL = -3
ISMEAR = -1              # Fermi smearing
SIGMA  = 0.03            # width of smearing (eV)

NELMIN = 4               # do a minimum of four electronic steps
EDIFF  = 1E-5            # electronic convergence (eV)
EDIFFG = -0.01           # accuracy of ions (forces in eV/Å)
NSW    = 100             # maximum number of ionic steps
IBRION = 1               # minimization algorithm: 1 = RMM-DIIS

LPLANE = .TRUE.          # parallelization over plane wave coefficients
LSCALU = .TRUE.
NSIM   = 4               # number of bands optimized at the same time
NPAR   = 1               # parallelization over bands
-----
```

Filename: KPOINTS

```
-----
K-Points      ! comment line
0              ! number of k-points = 0 -> automatic generation scheme
Gamma         ! generate a Gamma centered grid
9 9 1         ! subdivisions along reciprocal lattice vectors
-----
```

Filename: POSCAR

2x2x4 Au(111)

1.0

5.9228000000	0.0000000000	0.0000000000
2.9614000000	5.1292952600	0.0000000000
0.0000000000	0.0000000000	29.6140000000

16

Selective

Direct

0.0000000000	0.0000000000	0.0000000000	F	F	F
0.0000000000	0.5000000000	0.0000000000	F	F	F
0.5000000000	0.0000000000	0.0000000000	F	F	F
0.5000000000	0.5000000000	0.0000000000	F	F	F
0.1666666667	0.1666666667	0.0816496581	F	F	F
0.1666666667	0.6666666667	0.0816496581	F	F	F
0.6666666667	0.1666666667	0.0816496581	F	F	F
0.6666666667	0.6666666667	0.0816496581	F	F	F
0.3333333333	0.3333333333	0.1632993162	T	T	T
0.3333333333	0.8333333333	0.1632993162	T	T	T
0.8333333333	0.3333333333	0.1632993162	T	T	T
0.8333333333	0.8333333333	0.1632993162	T	T	T
0.0000000000	0.0000000000	0.2449489743	T	T	T
0.0000000000	0.5000000000	0.2449489743	T	T	T
0.5000000000	0.0000000000	0.2449489743	T	T	T
0.5000000000	0.5000000000	0.2449489743	T	T	T

Sample bSKAN Input Files

Description: The following INCSAN file along with the sample geometry (ASAMPLE file) and wavefunctions (WAVSAMPLE file) from a VASP calculation can be used to calculate a 3D matrix of local density of states (CURMAT file) with bSKAN using the Tersoff-Hamann method as described in Chapter 2. Once the CURMAT file has been generated, the line containing `CURRENT = 0.0` can be uncommented and bSKAN will then produce a 3D tunneling current map in a file named CURRENT. If a nonzero value is set for the keyword CURRENT, a current contour of that value (in local DOS units) is written to the output file PLOTCON.

Filename: INSCAN

```
-----
# The first lines define the operation of the program

TERSOFF HAMANN          ! method command
LIMITS = -0.05  0.05    ! defines the limits of thermal broadening
GRIDPOINTS = 61         ! number of gridpoints of the surface
BIAS = -0.01            ! bias voltage ( sample -> tip)
ZVACUUM      = 11.2     ! vacuum boundary of the sample surface
NKELDYSH     = 1        ! first order scattering approach

PIVOT = 0.0000  0.0000  ! pivot (lower left corner) point
TOP = 0.0000  0.0000    ! top position on the surface

# the following lines are for evaluation, they require that the current
# matrix (in CURMAT) has already been calculated

# CURRENT = 0.001        ! current (only for evaluations)
# CURRENT = 0.0          ! in this case the whole current matrix is
#                        ! written to a formatted (OpenDx) file

# PLOTS = 5              ! performing horizontal plots of the current
# FPLOT = PLT            ! name of plotfiles (3 characters root)
# ZPLOT = 1 11 21 31 41 ! z-index for the defintion of planes
-----
```

Description: The following INCSAN file along with sample geometry (ASAMPLE file), tip geometry (ATIP file), sample wavefunctions (WAVSAMPLE file), and tip wavefunctions (WAVTIP file) from a VASP calculation can be used to calculate a 3D matrix of local density of states (CURMAT file) with bSKAN using the Bardeen method as described in Chapter 2. Once the CURMAT file has been generated, the line containing `CURRENT = 0.0` can be uncommented and bSKAN will then produce a 3D tunneling current map in a file named `CURRENT`. If a nonzero value is set for the keyword `CURRENT`, a current contour of that value (in local DOS units) is written to the output file `PLOTCON`.

Filename: INSCAN

```
-----
# The first lines define the operation of the program

NUMERICAL                ! method command
LIMITS = -0.05  0.05      ! defines the limits of thermal broadening
GRIDPOINTS = 61           ! number of gridpoints of the surface
BIAS = -0.01              ! bias voltage ( sample -> tip)
ZVACUUM      = 11.2       ! vacuum boundary of the sample surface
NKELDYSH      = 1         ! first order scattering approach

PIVOT = 0.0000  0.0000    ! pivot (lower left corner) point
TOP = 0.0000  0.0000      ! top position on the surface

# the following lines are for evaluation, they require that the current
# matrix (in CURMAT) has already been calculated

# CURRENT = 0.001          ! current (only for evaluations)
# CURRENT = 0.0            ! in this case the whole current matrix is
#                          ! written to a formatted (OpenDx) file

# PLOTS = 5                ! performing horizontal plots of the current
# FPLOT = PLT              ! name of plotfiles (3 characters root)
# ZPLOT = 1 11 21 31 41    ! z-index for the definition of planes
-----
```

Example Job Submission Files

Description: The following job file can be used to submit a job through an LSF scheduler which will execute `flair_inv` (*flair* for systems with inversion symmetry, also known as *flair* real) on 16 cores and will write the time the job finished and the directory it is located in to a file named `job.JOBID` (where `JOBID` is the job ID number assigned by the LSF scheduler) in the user's `$HOME/finished` directory.

Filename: `flair_inv.job`

```
-----
#!/bin/bash
module load intel-compiler/11.1.080-v1
module load openmpi/1.3.2-v1

#BSUB -J Flair
#BSUB -n 16
#BSUB -o output.%J
openmpi_wrapper /sharedapps/uwm/LS/ics-11.1/flair/3.23-v1/flair_inv_mpi

cat >$HOME/finished/job.$LSB_JOBID <<!
Job $LSB_JOBID finished `date`
It is located at $LS_SUBCWD
!
-----
```


Description: The following file can be used to submit a job through an LSF scheduler to execute vasp on 64 cores and will write the time the job finished and the directory it is located in to a file named `job.JOBID` (where `JOBID` is the job ID number assigned by the LSF scheduler) in the user's `$HOME/finished` directory.

Filename: `vasp.job`

```
-----  
#!/bin/bash  
module load intel-compiler/11.1.080-v1  
module load openmpi/1.3.2-v1  
  
#BSUB -J Vasp  
#BSUB -n 64  
#BSUB -o output.%J  
openmpi_wrapper /sharedapps/uwm/LS/ics-11.1/vasp/4.6-v1/vasp  
  
cat >$HOME/finished/job.$LSB_JOBID <<!  
Job $LSB_JOBID finished `date`  
It is located at $LS_SUBCWD  
!  
-----
```

Description: The following job file can be used to submit a job through an LSF scheduler to execute the script `multistep.sh` (see Useful Shell Scripts below) on 64 cores and will write the time the job finished and the directory it is located in to a file named `job.JOBID` (where `JOBID` is the job ID number assigned by the LSF scheduler) in the user's `$HOME/finished` directory.

Filename: `multistep.job`

```
-----
#!/bin/bash
module load intel-compiler/11.1.080-v1
module load openmpi/1.3.2-v1

#BSUB -J vasp-multi
#BSUB -n 64
#BSUB -o output.%J
multistep.sh

cat >$HOME/finished/job.$LSB_JOBID <<!
Job $LSB_JOBID finished `date`
It is located at $LS_SUBCWD
!
-----
```

Useful Shell Scripts

Description: The following script copies the jobfile `vasp.job` from the user's `$HOME/jobfiles` directory to the current directory and submits the job to the LSF scheduler on the number of cores specified by the argument given after the filename (e.g. `vasp.sh 64` will submit the job to run on 64 cores).

Filename: `vasp.sh`

```
-----
#!/bin/bash
cp $HOME/jobfiles/vasp.job .
bsub -n $1 < vasp.job
-----
```

Description: The following script runs the parallel version of VASP in multiple steps with different convergence criteria defined in `INCAR1`, `INCAR1R`, `INCAR2`, `INCAR3`, and `INCAR4` (which must be located in the user's `$HOME/jobsteps` directory). The `OUTCAR` file is checked for convergence after each step and the next step is started after the current step has converged.

Filename: `multistep.sh`

```
-----
#!/bin/bash
# This script runs vasp multiple times with inreasingly more
# precise geometric convergence criteria  mg jan.2012

# initializing loop counting variables
i=1 j=1 k=1 l=1

# make backup of original POSCAR
cp POSCAR POSCAR.orig

# copy step1 INCAR to local dir
```

```

cp ~/jobsteps/INCAR1 ./INCAR

# loop for first step convergence
# -----
while [ $i -le 3 ]
do
    echo "Loop 1."$i
    # run vasp
    openmpi_wrapper /sharedapps/uwm/LS/ics-11.1/vasp/4.6-v1/vasp

    # check for geometric convergence
    GEO_CONV=$(grep -c "structural" OUTCAR)
    if [ $GEO_CONV -eq 1 ]
    then
        echo "Converged!"
        mv-for-multi.sh 1.$i
        i=3
    else
        echo "Not Converged!"
        mv-for-multi.sh 1.$i
        cp ~/jobsteps/INCAR1R ./INCAR
    fi

    i=`expr $i + 1`
done
# -----
# end of loop for first step convergence

# copy step2 INCAR to local dir
cp ~/jobsteps/INCAR2 ./INCAR

# loop for second step convergence
# -----
while [ $j -le 3 ]
do
    echo "Loop 2."$j
    # run vasp
    openmpi_wrapper /sharedapps/uwm/LS/ics-11.1/vasp/4.6-v1/vasp

    # check for geometric convergence
    GEO_CONV=$(grep -c "structural" OUTCAR)
    if [ $GEO_CONV -eq 1 ]
    then
        echo "Converged!"
        mv-for-multi.sh 2.$j
        j=3
    else
        echo "Not Converged!"
        mv-for-multi.sh 2.$j
    fi

    j=`expr $j + 1`
done
# -----
# end of loop for second step convergence

# copy step3 INCAR to local dir

```

```

cp ~/jobsteps/INCAR3 ./INCAR

# loop for third step convergence
# -----
while [ $k -le 3 ]
do
    echo "Loop 3."$k
    # run vasp
    openmpi_wrapper /sharedapps/uwm/LS/ics-11.1/vasp/4.6-v1/vasp

    # check for geometric convergence
    GEO_CONV=$(grep -c "structural" OUTCAR)
    if [ $GEO_CONV -eq 1 ]
    then
        echo "Converged!"
        mv-for-multi.sh 3.$k
        k=3
    else
        echo "Not Converged!"
        mv-for-multi.sh 3.$k
    fi

    k=`expr $k + 1`
done
# -----
# end of loop for third step convergence

# copy step4 INCAR to local dir
cp ~/jobsteps/INCAR4 ./INCAR

# loop for fourth step convergence
# -----
while [ $l -le 3 ]
do
    echo "Loop 4."$l
    # run vasp
    openmpi_wrapper /sharedapps/uwm/LS/ics-11.1/vasp/4.6-v1/vasp

    # check for geometric convergence
    GEO_CONV=$(grep -c "structural" OUTCAR)
    if [ $GEO_CONV -eq 1 ]
    then
        echo "Converged!"
        mv-for-multi.sh 4.$l
        l=3
    else
        echo "Not Converged!"
        mv-for-multi.sh 4.$l
    fi

    l=`expr $l + 1`
done
# -----
# end of loop for fourth step convergence
-----

```

Description: The following script moves relevant VASP output files to a directory complete in the current directory after the completion of steps in the above multistep script multistep.sh. When it moves the files, it appends the job ID and loop index from multistep.sh. It is similar in function to the script mv-outputs.sh below.

Filename: mv-for-multi.sh

```
-----
#!/bin/sh
#This script moves the output files during a multistep VASP run
#mg jan.2012

COMPLETE=$(find . -name complete | wc -w)
JOB_ID=$LSB_JOBID

if [ $COMPLETE = 0 ]

then
    mkdir complete

fi

sleep 60
mv vasprun.xml ./complete/vasprun_${JOB_ID}.$1.xml
cp CONTCAR POSCAR
mv CONTCAR ./complete/CONTCAR_${JOB_ID}.$1
mv OUTCAR ./complete/OUTCAR_${JOB_ID}.$1
-----
```

Description: The following script moves important output files from a VASP calculation to a directory `complete` in the current directory. It copies the file `CONTCAR` to `POSCAR` and then moves the files `vasprun.xml`, `CONTCAR`, `OUTCAR` and `output.JOBID` (where `JOBID` is the job ID number assigned by the LSF scheduler) to the directory `./complete` with the LSF scheduler job ID appended to the end of the original filenames. If there is not exactly one LSF output file in the directory, it exits and gives the following error message: "Sorry, this script only works when there is one BSUB output file in the directory."

Filename: `mv-outputs.sh`

```
-----
#!/bin/sh
#This script moves the output files from a successful VASP run

NUM_OUTPUT=$(ls output.* | wc -w)
COMPLETE=$(find . -name complete | wc -w)
JOB_ID=$(cat output.* | grep -m 1 Job | awk -v RS=":" '/Job/ {printf "%.5s\n",$2}')

# old way of getting job id from output file, only works if jobid is 5 digits
# JOB_ID=$(awk '/Subject: Job/ {printf "%.5s\n",$3}' output.*)

#echo $NUM_OUTPUT
#echo $COMPLETE
#echo $JOB_ID
#echo $USER_TIME
#echo $USER_TIME_TWO
#echo $ELAPSED_TIME

if [ $NUM_OUTPUT = 1 ]

then
```

```
if [ $COMPLETE = 0 ]

then
    mkdir complete

fi

mv vasprun.xml ./complete/vasprun_${JOB_ID}.xml
cp CONTCAR POSCAR
mv CONTCAR ./complete/CONTCAR_${JOB_ID}
mv OUTCAR ./complete/OUTCAR_${JOB_ID}
mv output.${JOB_ID} ./complete/

else
    echo "Sorry, this script only works when there is one BSUB output file in the directory."

fi
```

Description: The following script summarizes relevant information from a *flair* output file named `out` and writes it to the screen.

(This script was written by Professor Michael Weinert.)

Filename: `summary`

```
-----
#!/bin/bash
# gets the summary information from the flair out file for each atomic
# step
# at present, gets distance, energy and force

if [ $# -eq 1 ]
then
    fn=$1
else
    fn=out
fi

if [ ! -f "${fn}" ] # check whether file exists
then
    echo " ${fn} does not exist - try again"
    exit
fi

# first check if spin-polarized
let ispins=1
[[ $(grep -q "distance of spin densities" ${fn}) ]] || ispins=2

# let ic=1
# [[ $(grep -q "step=" ${fn}) ]] || ic=$(grep "step=" ${fn} | head -1 | cut -d'=' -f3 | cut -d')' -f1 )

if [ $(grep -c "step=" ${fn}) -gt 0 ]
then
    let ic=$(grep "step=" ${fn} | head -1 | cut -d'=' -f3 | cut -d')' -f1 )
```

```

else
  let ic=1
fi

# echo "ic: ${ic} "

while grep -q "step=${ic})" ${fn}
do
#   get the free energy for the last iteration of the atomic step
  llm=`grep "step=${ic})" ${fn} | grep free | tail -1`
#   get the iteration number, and then the distance (and print)
  ( grep "it= `echo $llm | cut -d=' ' -f2 | cut -d',' -f1`:" ${fn} | grep distance \
    || \
    grep "it= `echo $llm | cut -d=' ' -f2 | cut -d',' -f1`:" ${fn} | grep distance \
    || \
    grep `echo $llm | cut -d'(' -f2 | cut -d',' -f1` ${fn} | grep distance ) | \
    tail -${ispins}
#   print out the free energy
  echo "$llm"
#   get the maximum force for this step
  grep "maximum force" ${fn} | grep " ${ic}:"
  echo " "
  let ic=ic+1
done

if [ ${ic} -eq 1 ]
then
  grep "distance of charge densities" ${fn} | tail -1
  grep "distance of spin densities" ${fn} | tail -1
  grep free ${fn} | tail -1
fi

```

Description: The following script gives the current cluster usage (for UWM HPCC Avi) as a percentage of the total cpus that are committed to jobs and the total number of cpus currently in use for the user running the script. If the user is using more than 256 cpus, they are warned that this is over their limit.

Filename: usage.sh

```
-----  
#!/bin/bash  
bhosts | awk '/compute/ {used_cpu += $5} END {used_cpu /= 11.36; print "Current Cluster Usage = " used_cpu " %"}'  
bjobs | awk '/compute/ {total ++};  
END {if (total<=256) print "My current usage is "total " cpus";  
else printf "My current usage is " total " cpus " "\033[47;0;31;1m" "(Over my limit!) :(" "\033[47;0;30;m" "\n" }'  
-----
```

Curriculum Vitae

Michael T. Garvey

Place of Birth: Neenah, WI

Education

Ph.D. in Chemistry, University of Wisconsin-Milwaukee 2013

Dissertation Title: “Applying Computational Methods to Interpret
Experimental Results in Tribology and Enantioselective Catalysis”

Advisor: Distinguished Professor Wilfred T. Tysoe

B.S., University of Wisconsin-Oshkosh 2007

Majors: Chemistry and Physics

Employment

**University of Wisconsin-Milwaukee, Department of Chemistry and Biochemistry
Milwaukee, WI**

Research Assistant 2012-2013

Advanced Opportunity Program Fellow 2009-2012

Research Assistant 2008-2009

Teaching Assistant 2007-2008

Awards and Fellowships

Keith Hall Award for Excellence in Graduate Research – 2012

Advanced Opportunity Program Fellowship – 2009-2012

Graduate School Fellowship (Declined) – 2009

Louise A. Arndt Fellowship – 2009

Gilbert F. and Katherine L. Pollnow Chemistry Scholarship for Outstanding Achievement in Physical Chemistry – 2006

Publications

2013

Garvey, M.; Bai, Y.; Tysoe, W. T., Studying Enantioselectivity on Chirally Modified Surfaces Using Computational Methods: Identifying NEA and Methyl Pyruvate Docking Complexes on Pd(111). *In Preparation*

Garvey, M.; Weinert, M.; Tysoe, W. T., Pressure Dependence of the Shear Strengths of the Tungsten Carbide–Potassium Chloride Interface. *Tribology Letters* **2013**, *50* (1), 105-113.

<http://dx.doi.org/10.1007/s11249-013-0109-y>

Garvey, M.; Bai, Y.; Boscoboinik, J. A.; Burkholder, L.; Sorensen, T. E.; Tysoe, W. T., Identifying Molecular Species on Surfaces by Scanning Tunneling Microscopy: Methyl Pyruvate on Pd(111). *The Journal of Physical Chemistry C* **2013**, *117* (9), 4505-4514.

<http://dx.doi.org/10.1021/jp3106309>

Calaza, F.; Li, Z.; Garvey, M.; Neurock, M.; Tysoe, W. T., Reactivity and Selectivity in the Au/Pd(111) Alloy-Catalyzed Vinyl Acetate Synthesis. *Catalysis Letters* **2013**, *143* (8), 756-762.

<http://dx.doi.org/10.1007/s10562-013-1042-2>

2012

Garvey, M.; Weinert, M.; Tysoe, W. T., On the film thickness dependence of shear strengths in sliding, boundary-layer friction. *Wear* **2012**, *274-275*, 281-285.

<http://dx.doi.org/10.1016/j.wear.2011.09.008>

Garvey, M.; Boscoboinik, J. A.; Burkholder, L.; Walker, J.; Plaisance, C.; Neurock, M.; Tysoe, W. T., Structure of the Au/Pd(100) Alloy Surface. *Journal of Physical Chemistry C* **2012**, *116* (7), 4692-4697.

<http://dx.doi.org/10.1021/jp2107445>

2011

Garvey, M.; Furlong, O. J.; Weinert, M.; Tysoe, W. T., Shear properties of potassium chloride films on iron obtained using density functional theory. *Journal of Physics-Condensed Matter* **2011**, *23* (26).

<http://dx.doi.org/10.1088/0953-8984/23/26/265003>

Garvey, M.; Weinert, M.; Tysoe, W. T., On the Pressure Dependence of Shear Strengths in Sliding, Boundary-Layer Friction. *Tribology Letters* **2011**, *44* (1), 67-73.

<http://dx.doi.org/10.1007/s11249-011-9827-1>

Boscoboinik, J.; Kestell, J.; Garvey, M.; Weinert, M.; Tysoe, W. T., Creation of Low-Coordination Gold Sites on Au(111) Surface by 1,4-phenylene Diisocyanide Adsorption. *Topics in Catalysis* **2011**, *54* (1-4), 20-25.

<http://dx.doi.org/10.1007/s11244-011-9642-9>

Burkholder, L.; Garvey, M.; Weinert, M.; Tysoe, W. T., Structure of Methyl Pyruvate and alpha-(1-Naphthyl)ethylamine on Pd(111). *Journal of Physical Chemistry C* **2011**, *115* (17), 8790-8797.

<http://dx.doi.org/10.1021/jp202291h>

2010

Boscoboinik, J. A.; Calaza, F. C.; Garvey, M. T.; Tysoe, W. T., Identification of Adsorption Ensembles on Bimetallic Alloys. *The Journal of Physical Chemistry C* **2010**, *114* (4), 1875-1880.

<http://dx.doi.org/10.1021/jp9078794>

Invited Presentation

April 2012 “Modeling the Pressure Dependence of Shear Strength in Sliding,
Boundary-Layer Friction”
Milwaukee Tribology Consortium, Milwaukee, WI

Oral Presentations

June 2013 “Studying Enantioselectivity on Chirally Modified Surfaces with
Experimental and Computational Methods”
2013 Great Lakes Regional Meeting of the American Chemical Society,
La Crosse, WI

November 2011 “Modeling the Pressure Dependence of Shear Strength in Sliding,
Boundary-Layer Friction”
American Vacuum Society 58th International Symposium and
Exhibition, Nashville, TN